Studies of diffraction with the ATLAS detector

Maciej Trzebinski

To cite this version:

Maciej Trzebinski. Studies of diffraction with the ATLAS detector. Other [cond-mat.other]. Université Paris Sud - Paris XI; Institut de Physique Nucleaire de l'Academie Polonaise des Sciences, 2013. English. NNT : 2013PA112134 . tel-00908126

Thèse de doctorat co-tutelle
de l'Université Paris 11
et
de l'Institut de Physique Nuclaire de l'Académie Polonaise des Sciences

spécialité
Champs, Particules, Matière

présentée par

Maciej TRZEBIŃSKI

pour obtenir le grade de docteur
de l'Université Paris 11
et
de l'Institut de Physique Nuclaire de l'Académie Polonaise des Sciences

Etude de la diffraction dans l'experience ATLAS au LHC

Thèse soutenue le 20 Septembre 2013 devant le jury composé de:

Jochen BARTELS (**rapporteur**)
Janusz CHWASTOWSKI (**directeur de thèse**)
Patrick FASSNACHT (**rapporteur**)
Joel FELTESSE (**président**)
Robi PESCHANSKI
Christophe ROYON (**directeur de thèse**)
Achille STOCCHI

Thèse préparée
au Service de Physique des Particules du CEA de Saclay
et
à l'Institut de Physique Nucléaire de l'Académie Polonaise des Sciences de Cracovie

Contents

1 State of the Art **7**

1.1 The Standard Model . . . 8

1.1.1 Feynman Diagrams . . . 10

1.1.2 Quantum Chromodynamics . . . 12

1.1.3 The Parton Model . . . 13

1.2 Diffractive Physics . . . 15

1.2.1 Soft Diffraction . . . 17

1.2.2 Hard Diffraction . . . 18

1.3 Jet-Gap-Jet Production . . . 22

2 Experimental Apparatus **31**

2.1 Large Hadron Collider . . . 31

2.1.1 LHC Magnets . . . 33

2.1.2 LHC Operation . . . 35

2.1.3 LHC Beam Size . . . 37

2.1.4 Proton Trajectories . . . 38

2.2 The ATLAS Detector . . . 49

2.2.1 Inner Detector . . . 50

2.2.2 Calorimeters . . . 52

2.2.3 Muon System . . . 56

2.2.4 Forward Detectors . . . 58

2.2.5 Data Acquisition and Trigger . . . 60

2.2.6 The ALFA Detector . . . 61

2.2.7 The AFP Detector . . . 73

3 Jet-Gap-Jet Measurement **87**

3.1 Data . . . 91

3.2 Trigger . . . 92

3.3 Jets . . . 94

3.4 Gap Definition . . . 95

3.4.1 Track Reconstruction . . . 95

3.4.2 Gap computed using Reconstructed Tracks . . . 97

3.4.3 Clusters . . . 101

3.4.4 Conclusions . . . 101

3.5 Data – Monte Carlo Comparison 106
3.6 Jet-Gap-Jet Measurement 108
    3.6.1 Event Displays 109
3.7 Summary 114

4 Double Pomeron Exchange Jet-Gap-Jet Production 115
4.1 Monte Carlo Generator 116
4.2 Experimental Environment 117
    4.2.1 Forward Protons 117
    4.2.2 Background Suppression 118
4.3 Test of the BFKL Model at the LHC 119
4.4 Conclusions 120

5 Exclusive Production with Forward Detectors 123
5.1 Central Exclusive Jet Production 123
    5.1.1 Forward Protons 124
    5.1.2 Monte Carlo Samples 129
    5.1.3 Trigger 130
    5.1.4 Signal Selection 131
    5.1.5 Results 140
    5.1.6 Summary 140
5.2 Exclusive $\pi^+\pi^-$ Production 144
    5.2.1 Production Mechanism 144
    5.2.2 Predictions for the ATLAS Experiment 146
    5.2.3 Summary 150

6 Summary 155

Appendices

Appendix A Transport Programs 159
A.1 Proton Transport 160
    A.1.1 Influence of the Interaction Vertex Position 160
    A.1.2 Influence of the Proton Transverse Momentum 163
A.2 Geometrical Acceptance 166
A.3 Differences between MAD-X PTC and FPTracker 167
A.4 Conclusions 170

Appendix B Parametrisation and Unfolding Tool 173
B.1 Transport Parametrisation 173
B.2 Unfolding Procedure 175

Bibliography 175

Contents

Diffraction has always been an important part of the studies performed in experiments involving hadron interactions. This is true also for the LHC, where a large community works on both theoretical and experimental aspects of possible diffractive measurements.

This work presents my contribution to the development of the diffractive programme of the ATLAS experiment at the LHC. The obtained results are important both for the general, motivational aspects concerning the possible measurements and their significance, as well as for more technical details crucial for the experimental set-up, its performance and data quality.

Chapter 1 of the thesis contains an introduction in the field of diffractive physics. It begins with a presentation of the Standard Model and introduces necessary definitions. A soft diffraction which contributes to minimum bias interactions, present in pile-up events and thus important to all measurements performed at the LHC at high luminosity is described. Next, hard diffraction and its types, which are most interesting from the Quantum Chromodynamics (QCD) point of view and the mechanism governing the Pomeron exchange, are discussed. Finally, the Jet-Gap-Jet (JGJ) production mechanism is described as a way of testing the predictions of one of the important ingredient of the Standard Model – the BFKL evolution equations.

Chapter 2 briefly introduces the Large Hadron Collider, presenting the main points of its programme, the key aspects of its design and properties of the LHC experiments. A large part of this Chapter is devoted to the studies of proton behaviour in the vicinity of the ATLAS Interaction Point (IP1). This work, performed by Author, was crucial to understand the behaviour of the elastically and diffractivelly scattered protons for different LHC optics. In the second part of the Chapter, a more detailed description of the ATLAS experiment is given, including sub-detectors, trigger and data processing. A large part is devoted to my contribution to the ATLAS forward detectors – the Absolute Luminosity For ATLAS (ALFA) and ATLAS Forward Proton (AFP) projects. A strong stress is put on the topics related to the detector geometric acceptances for different LHC working modes. In addition, in the AFP case, the optimal LHC collimator settings as well as the probability to trigger the particle shower for various designs of the detector pocket are discussed.

The measurement of JGJ process is discussed in detail in Chapter 3. This measurement is based on data collected by the ATLAS detector in low pile-up runs in 2010. Such conditions were considered in order to have clean events not polluted by additional interactions originating from pile-up. At the beginning of this Chapter, the optimal method of gap reconstruction is studied. A first proposed method is based on tracks reconstructed in the ATLAS Inner Detector whereas a second one uses the signal from the calorimeters. After the discussion of the trigger conditions, the comparison between Monte Carlo and data is shown. Once a good agreement between MC and data is obtained, the observation of Jet-Gap-Jet signal is presented.

In Chapter 4, a possible extension of JGJ measurement is discussed, as this process can also be measured in Double Pomeron Exchange. The advantage is that the fraction of Jet-Gap-Jet to inclusive jet events in DPE processes is larger than the corresponding fraction in Non-Diffractive processes, since in DPE events, one is not penalized by the gap survival probability. In this Chapter the potential of using the AFP detector as a proton tagging device for DPE JGJ measurement is evaluated. The visible cross section after the requirement of double proton tag as a function of detector distance from the beam and the optimal gap size are discussed. Finally, a possible result assuming 300 pb^{-1} of collected data is shown.

Chapter 5 is devoted to a special class of diffractive processes – exclusive production. In the first Section, the case of exclusive jet production is described. This process cannot be measured in the ATLAS experiment without the AFP stations. To make this measurement possible, several requirements need to be introduced in order to obtain acceptable signal-to-background ratio. After the selection, the statistics expected to be collected with 40 fb^{-1} of data was shown to be enough to improve the best constraints known from the Tevatron by one order of magnitude. In the second part of this Chapter, the exclusive $\pi^+\pi^-$ production is studied. This is an example of soft exclusive process, which can be measured in the existing forward detectors – the ALFA stations. Two different measurements are discussed, the first one based on the tracks reconstructed in the Inner Detector (for pions with pseudorapidity, $|\eta| < 2.5$) whereas the second one considers signals from the forward calorimeters ($2.5 < |\eta| < 4.9$). The obtained results indicate that there should be enough statistics to make a significant measurement for an integrated luminosity of 100 μb^{-1}, which corresponds to the amount of data already collected by the ALFA detector.

In the Appendices some important technicalities are discussed. In the first one, the comparison between two different proton tracking programs, MAD-X and FPTRACKER, is done. In Appendix B the proton transport and four-momentum unfolding method is discussed. The knowledge of the proton kinematics after the interaction plays a major role in most diffractive physics analysis.

The presented results are based on the work performed during my PhD studies. The majority of phenomenological studies were presented during conferences and workshops and published. This thesis is based on the following publications and ATLAS notes:

[1] **M. Trzebiński**, R. Staszewski, J. Chwastowski, *LHC High β^* Runs: Transport and Unfolding Methods*, ISRN High Energy Physics, vol. 2012 (2012) 491460,

[2] R. Staszewski, P. Lebiedowicz, **M. Trzebiński**, J. Chwastowski, A. Szczurek, *Exclusive $\pi^+\pi^-$ Production at the LHC with Forward Proton Tagging*, Acta Physica Polonica B

42 (2011) 1861,

[3] R. Staszewski, **M. Trzebiński**, J. Chwastowski, *Dynamic Alignment Method of the Forward Proton Detectors at the LHC*, Adv. in High Energy Physics, vol. 2012 (2012), Article ID 428305,

[4] C. Marquet, C. Royon, **M. Trzebiński**, R. Zlebcik, *Gaps between jets in double-Pomeron-exchange processes at the LHC*, Phys. Rev. D **87**, (2013) 034010,

[5] **M. Trzebiński**, *Towards a Total Cross Section Measurement with the ALFA Detector at ATLAS*, Acta Physica Polonica B **44** (2013),

[6] **M. Trzebiński**, *Probing the BFKL Pomeron with Future ATLAS Forward Detectors*, in Proceedings of the XI LISHEP – Workshop on High Energy Physics in the Near Future, Rio de Janeiro, 2013, edited by F. Caruso, V. Oguri and A. Santoro, eConf CC1303172,

[7] **M. Trzebiński**, J. Chwastowski, T. Sykora, *Transport of Protons with High Energy Loss Through the LHC Magnetic Lattice for the High β^* Optics*, ATLAS-COM-LUM-2011-004,

[8] **M. Trzebiński**, R. Staszewski, J. Chwastowski, *ForwardProtonParam: Tool for finding parametrisation equations and unfolding proton four-momentum at the IP*, in preparation,

[9] **M. Trzebiński**, J. Chwastowski, *Monte Carlo Studies for ALFA Runs at $\sqrt{s}$=8 TeV: Some Aspects of Optics, Beam Profiles, Elastic and Diffractive Event Patterns and Rates*, ATLAS-COM-LUM-2012-012,

[10] S. Jakobsen, O. Kepka, P. Newman, **M. Trzebiński**, *Diffractive physics program with ALFA in low-β^* run in proton-proton interactions at $\sqrt{s}$=8 TeV*, ATLAS-COM-PHYS-2012-1435,

[11] L. Adamczyk *et al.* (**M. Trzebiński**), *AFP: A Proposal to Install Proton Detectors at 220 m around ATLAS to Complement the ATLAS High Luminosity Physics Program*, ATLAS-COM-LUM-2011-006,

[12] O. Kepka, C. Royon, L. Schoeffel, R. Staszewski, **M. Trzebiński**, R. Zlebcik, *Physics Cases within the AFP project*, ATL-COM-PHYS-2012-775.

Chapter 1

State of the Art

The fundamental questions about the origin of our Universe and about its basic components remain unanswered for ages. One of the goals of physics is to find these answers. The branch of physics called High Energy Physics (HEP) addresses these questions by studying the behaviour of Nature at the smallest possible level, where its elementary ingredients interact. The knowledge that was learned during the past decades about the behaviour of matter is gathered inside the theory called *the Standard Model.* The Standard Model has a great success in describing our World, however one has to remember that it has certain drawbacks and is not a complete theory. For example, it does not incorporate gravitation as described by general relativity.

Scientists have managed to reduce the principles governing the behaviour of all known forms of matter to a set of fundamental laws and theories. At present, the basic behaviour of matter is best understood in terms of kinematics and interactions of elementary particles. One aim of particle physics is to unify all theories into one Theory of Everything in which all known laws could be special cases and from which the behaviour of all matter and energy can be derived.

In order to be able to investigate experimentally the smallest parts of matter, one has to use an adequate apparatus. Historically, the first method was the observation by bare eye. The eye resolution (how close two objects can be before they blur into one) is about 0.03 mm. To increase it one can use optical devices like a magnifying glass or a microscope. The limitation in resolution of these instruments comes from the fact that the light wavelengths should be smaller than what is studied, in order to be able to see some object. The microscopes using light in the visible wavelength spectrum can magnify objects up to 1500 times. When polarised ultraviolet light is used, the magnification can be increased to 3500 times. Since the use of shorter light waves is not convenient, an idea of using electrons instead of photons was introduced. The electron microscope can magnify object about 10 000 000 times, which gives a resolution of $\sim$ 50 picometers. This gives a possibility to look as deep as to see the structure of molecules.

To answer the question about the possibility of studying matter at even smaller level, one has to realise that the wavelength of a particle is related to its energy, according to the de Broglie principle:

$$\lambda \sim 1/E.$$

From this equation one can conclude that, in order to be able to observe matter with better resolution (shorter wavelengths), the energy of the probing particles has to be higher. To investigate matter at the level of the size of the nucleus ($\sim$ 1 femtometer), one has to build a special device that is able to produce particles with high enough energies – the particle accelerator. The general idea of making an observation using particle accelerators can be summarised in three steps:

1. accelerate a particle to such energy that the corresponding wavelength is smaller than the target size,
2. probe the target – smash a particle to it,
3. observe the outcome of the collision.

The properties (like mass, multiplicity, energy, scattered angle, *etc.*) of the outgoing particles are defined at the time of the collision (interaction). Therefore, by colliding high energy particles and measuring the output, one will be able to obtain informations about Nature at subatomic level.

1.1 The Standard Model

The already mentioned Standard Model theory contains the recent knowledge of matter behaviour at the subatomic level. Our Universe is built from several fundamental objects. There are twenty four known, elementary fermions[1]:

- six quarks (down (d), up (u), strange (s), charm (c), bottom or beauty (b) and top (t)),
- six leptons (electron (e), electron neutrino (ν_e), muon (μ), muon neutrino (ν_μ), tau (τ) and tau neutrino (ν_τ))

and twelve corresponding antiparticles with the same properties but different electric charge.

These particles differ in mass, charge and forces with which they interact. Their main properties are described in Table 1.1. It is worth to stress that the particles with a non-integer charge cannot exist (be observed) freely at in Nature – they must form an object. Free quarks cannot be observed, but only a quark-antiquark or a three (anti)quark composites. The former ones are called mesons, whereas the latter ones baryons. In general, the particles composed of quarks (so mesons and baryons) are called hadrons.

All known forces in Nature are compound of the four elementary ones:

---

[1] The particles with a fractional spin.

Table 1.1: Main properties of the Standard Model particles.

particle	charge	interaction		
		strong	weak	electromagnetic
quarks (u, c, t)	+2/3	✓	✓	✓
quarks (d, s, b)	-1/3	✓	✓	✓
leptons (e, μ, τ)	-1	X	✓	✓
leptons (ν_e, ν_μ, ν_τ)	0	X	✓	X

- strong,
- weak,
- electromagnetic,
- gravitation.

These forces differ in terms of relative strength and their range. For each of them at least one *force carrier* exists[2]. In the Standard Model, the force carriers are bosons – elementary particles with an integer spin. The known elementary bosons: gluon (g), photon (γ), W^+, W^- and Z^0 are responsible for hard, electromagnetic and weak interactions. The recently discovered Higgs (H) boson [13, 14] plays a special role in the Standard Model – it explains why the other elementary particles have mass. The main properties of the force carriers are described in Table 1.2.

Table 1.2: The main properties of the Standard Model force carriers.

force	carrier	relative strength	range [m]
strong	gluon (g)	1	10^{-15}
electromagnetic	photon (γ)	10^{-2}	∞
weak	W^+, W^-, Z^0	10^{-13}	10^{-18}
gravitation	graviton	10^{-38}	∞

The scheme of interactions between elementary particles is presented in Figure 1.1. It illustrates several interesting facts:

- quarks can interact (couple) directly with all other particles except leptons,

---

[2] In fact, the force carrier of the gravitation force, the graviton, was not discovered experimentally, therefore it should be treated as a hypothetical particle.

- leptons couple with photons, W^+, W^-, Z^0 and Higgs,
- the only particles which can interact with themselves (the so-called *self-coupling*) are the gluons, the Higgs boson and the W^+, W^- bosons.

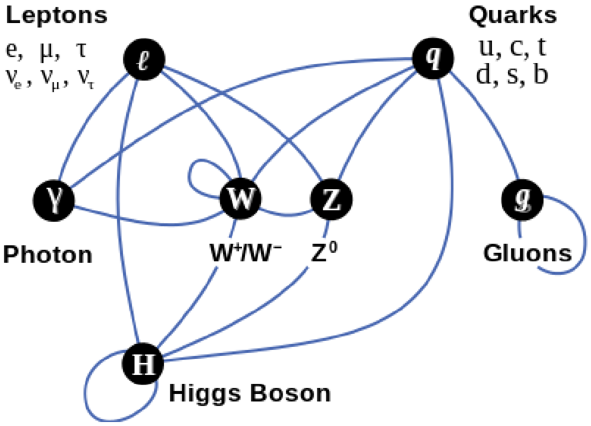

Figure 1.1: Interactions between the Standard Model elementary components.

1.1.1 Feynman Diagrams

A mathematical description of the interactions between particles is rather complicated. Fortunately, a convenient way to formulate these interactions was proposed by Richard Feynman [15]. In this approach the behaviour of an elementary particle is represented by a certain pictogram, as listed in Table 1.3. As an example, a process in which an electron (e^-) and a positron (e^+) annihilate into a photon (γ) from which a quark (q) anti-quark ($\bar{q}$) pair is created, is presented in Figure 1.2.

Another example is shown in Figure 1.3 – due to the proton-proton collision several new particles are produced. This situation is presented as seen by the detector (laboratory) where the interaction itself is undetectable (1.3a), and from a theoretical point of view – with a Feynman diagram (1.3b).

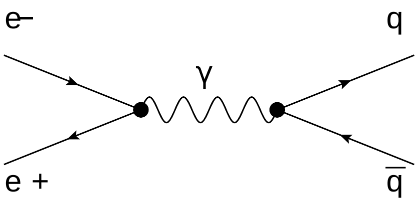

Figure 1.2: Exemplary process in which an electron (e^-) and a positron (e^+) annihilate and a quark (q) anti-quark ($\bar{q}$) pair is created, drawn using the Feynman diagram technique.

Table 1.3: Pictograms.

Pictogram	Name	Description
——▶——	quark line	This line represents quarks and leptons. If it is not clear from the overall context, the description (*e.g.* an up quark, an electron) is explicitly written near the line.
——◀——	anti-quark line	This line represents anti-quarks and anti-leptons.
∿∿∿∿∿	photon line	This line represents a photon, $W^{\pm}$ or Z^0 particles.
– – – – –	boson line	This line represents $W^{\pm}$ or Z^0 bosons.
ℓℓℓℓℓℓ	gluon line	This line represents gluons.
●	vertex	This pictogram represents an interaction vertex.
⬭	bulb	This special pictogram carries the message that the real process is complicated and therefore it is not desirable to describe it using simple lines.

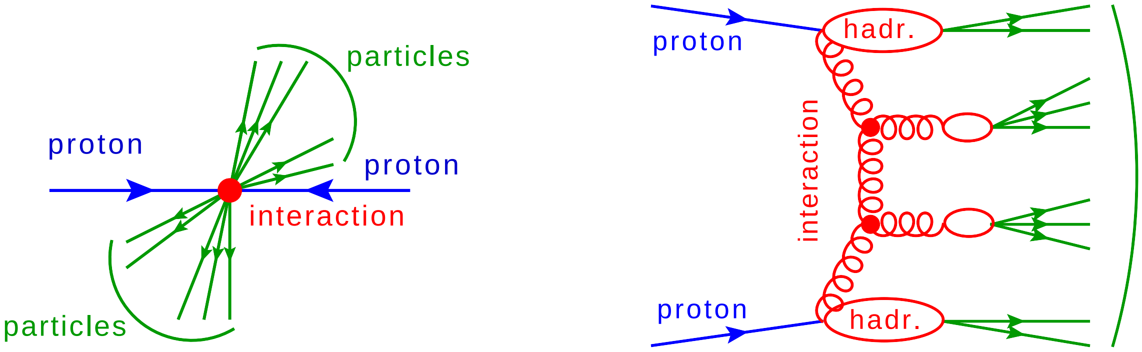

(a) laboratory frame view

(b) enhanced interaction view

Figure 1.3: Proton-proton collision from which some particles are produced shown from: a) the detector (laboratory) point of view and b) from the theoretical point of view.

To describe a scattering process of two particles to two particles the so-called *Mandelstam variables* are widely used. These variables are defined as:

$$\begin{aligned} s &= (p_1 + p_2)^2 = (p_3 + p_4)^2, \\ t &= (p_1 - p_3)^2 = (p_2 - p_4)^2, \\ u &= (p_1 - p_4)^2 = (p_2 - p_3)^2, \end{aligned}$$

where the p_1 and p_2 are the four-momenta of the incoming and p_3 and p_4 of the outgoing particles.

The interaction can happen in one of s, t or u channels. Each channel represent events is which the interaction involves the exchange of an intermediate particle with squared four-momentum equal s, t or u, respectively. An example of diagrams corresponding to these exchanges are drawn in Fig. 1.4.

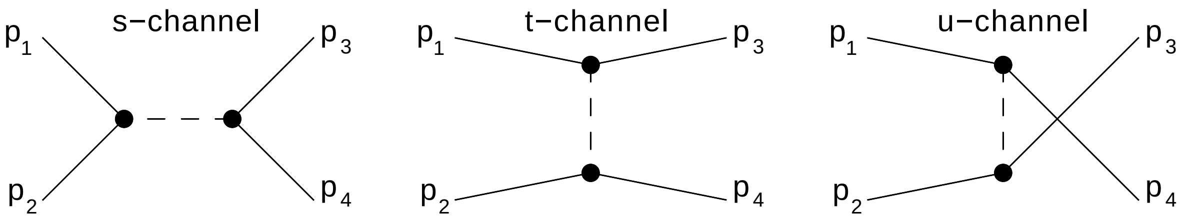

Figure 1.4: Feynman diagrams for interactions in s (**left**), t (**middle**) and u (**right**) channels.

1.1.2 Quantum Chromodynamics

The majority of particle interactions involving hadrons are ruled by strong force. The theory describing their behaviour is called *Quantum Chromodynamics* (QCD) [16]. This theory introduces a new property of matter – the *colour*. Such a property was needed in order to explain how quarks can coexist inside some hadrons without violating the Pauli exclusion principle. The colour plays the role of the charge for every particle which interacts strongly. Each quark can exist in one of three colour states, *e.g.* red, blue, green or 1, 2, 3. Gluons carry both color and anticolor, *e.g* antired-blue or green-antiblue. It is worth stressing that only colourless objects (colour singlets, like meson composed of red quark and antired antiquark or baryon containing red, blue and green quark) can exist freely in Nature.

An important feature of strong interactions is the so-called *confinement*. With the increase of the distance between two colour objects, the colour field energy increases rapidly. At some point this energy is greater than the rest mass of a quark-antiquark pair, allowing such a pair to be created. In consequence, the colour charge becomes locally equal to zero. This process, often called *hadronisation*, is illustrated in Figure 1.5.

The next QCD peculiar property is the asymptotic freedom, which states that in a very

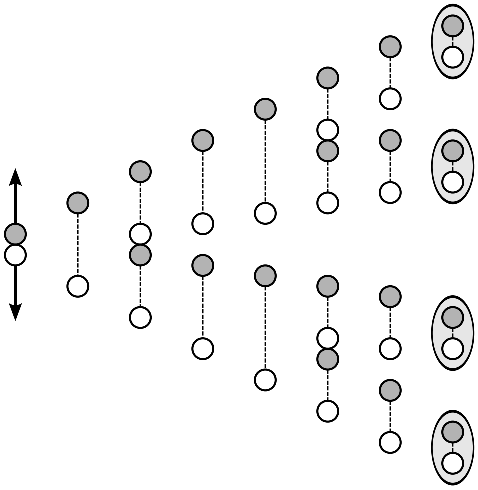

Figure 1.5: Illustration of the hadronisation process. Two quarks with opposite colour charges (white and grey circles) receive some kinetic energy (black arrows). While their distance increases the energy of the colour field (dashed line) increases until a new $q\bar{q}$ pair can be created. The process continues until quarks and anti-quarks combine into colourless particles. Here, only the production of mesons is shown, but in reality baryons are also produced.

high-energy reaction, the interaction between quarks and gluons is relatively weak. In the high-energy regime this feature allows the use of a well known mathematical methods, such as perturbative calculations.

For the majority of problems in High Energy Physics the exact solutions are not known. Instead, in order to calculate the properties (like carried energy or angular distributions) of the produced particles, one has to use approximative methods. In case of QCD the perturbation theory is widely used. This theory leads to an expression for the desired solution in terms of power series in some *small* parameter, named α_s. The leading term in this power series is the solution of the exactly solvable problem, while further terms describe the modification of the solution, due to the changes of the initial state. For example, the approximation of the full solution A looks like:

$$A = A_0 + \alpha_s A_1 + \alpha_s^2 A_2 + \ldots,$$

where α_s is a small parameter, the A_0 term represents the known solution to the exactly solvable initial problem, whereas the $A_1, A_2, \ldots$ represent the high-order terms. In high energy particle physics the QCD equations are usually solved up to leading (α_s) or next-to-leading (α_s^2) order terms.

1.1.3 The Parton Model

Since this thesis is devoted to processes created during proton-proton interactions, it is desirable to discuss the structure of the proton. To describe it, the so-called *Parton Model* [17] is handy and widely used. It states that a hadron (so, in particular, a proton) is composed of a number of point-like constituents, called *partons.* In the Standard Model the role of partons is played by quarks and gluons. Various experiments dedicated to the measurement of the proton inner structure (see *e.g.* [18, 19, 20]) revealed that a proton is not a simple object composed only from three quarks, but has a complicated nature. Deep Inelastic Scattering (DIS) data allowed to measure the so-called *Parton Density Functions* (PDFs) of a proton. These functions represent the probability densities to find a parton carrying a momentum fraction x at a given energy scale Q^2. Such a distribution for $Q^2 = 10$ GeV^2 is plotted as a function of the longitudinal momentum fraction x carried by the parton in Fig. 1.6. This Figure shows that in a wide range of x the proton is mostly composed of gluons. The second-leading contribution is coming from valence (u and d) quarks. Finally, there is an additional contribution from the *sea* composed of non-valence quarks and antiquarks.

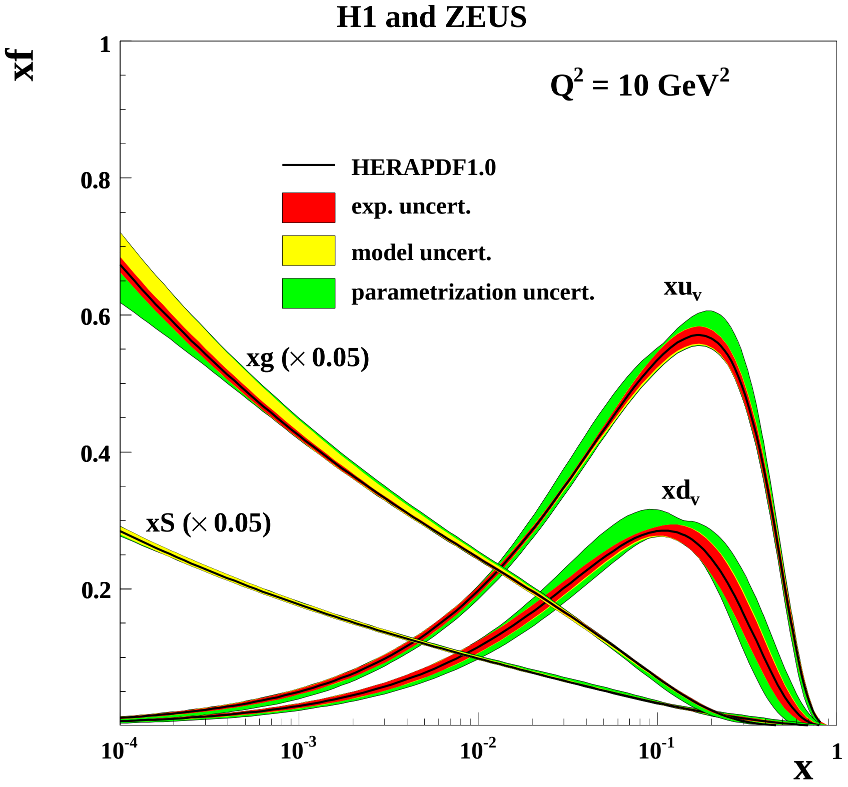

Figure 1.6: Parton Density Function of the proton from combined H1 and ZEUS data plotted as a function of the momentum fraction x of the proton carried by the parton for $Q^2 = 10$ GeV^2. From [21].

1.2 Diffractive Physics

Processes that can occur during proton-proton collisions may be catalogued in various ways. In this thesis a distinction between *diffractive* and *non-diffractive* processes will be used.

Defining diffraction is unfortunately not easy – a single, complete definition does not exist. The two definitions quoted in this Chapter can, however, shed some light on that topic. According to Predazzi [22]: *Every reaction in which no quantum numbers are exchanged between high energy colliding particles is dominated asymptotically by diffraction.*

The interaction in which no quantum numbers are exchanged (so *e.g.* the net colour is equal to zero) can be described in QCD at the lowest order by the exchange of two gluons in the overall colour singlet state. This simple description cannot, however, describe data. Instead, one often speaks about the exchange of a Pomeron, an object defined *e.g.* within the Regge theory [23].

The Regge theory was introduced in order to study the analytic properties of particle scattering. In quantum mechanics the bound states for a spherically symmetric potential fall into families with increasing angular momentum and energy [22]. These bound states appear as poles of the partial wave amplitude with a given integer angular momentum, l. The idea was to continue these amplitudes to complex values of l. For well behaved potentials (like the Yukawa one) the poles lie on a straight line, called the *Regge trajectory.* This trajectory has a form:

$$\alpha_R(t) = \alpha_R(0) + \alpha'_R(0)t,$$

where $\alpha_R(0)$ is called the intercept and $\alpha'_R(0)$ the slope [24]. An example of a Regge trajectory is shown in Figure 1.7. Furthermore, according this theory, the object exchanged in the t channel between two hadrons is not a single particle, but all particles lying on the Regge trajectory. It is worth stressing that all known resonances lie on trajectories with an intercept smaller than 1. This has serious consequences – the total cross section should decrease with increasing collision energy.

The Pomeron[3] was introduced as a Regge trajectory responsible for the observed growth of the cross section with the increase of the collision energy. The experimental fit to the data from which the intercept and the slope of Pomeron were calculated was done by Donnachie and Landshoff [26]. The obtained Pomeron trajectory, with an intercept of $\alpha_R(0) = 1.08$ and a slope $\alpha'_R(0) = 0.25$ GeV^{-2}, is presented in Figure 1.8.

After this introduction, another definition of diffraction, proposed in the book by Donnachie, Dosch, Landshoff and Nachtmann [27] can be quoted: *Events in which a Pomeron is exchanged are often called diffractive events.*

Diffractive processes can be further divided into *soft* and *hard* diffraction. However, one has to remember that this classification is also not exact. Usually, the process is called a *hard* one when the perturbative approach of calculating it is valid (there is an exchange of high-p_T

---

[3] Actually this Pomeron is called a *soft* one. Beside *soft* Pomeron a *hard* Pomeron, which has different intercept and slope than the soft one, exist. The hard Pomeron is needed to explain the experimental discovery at HERA of the steep rise of the gluon distribution as a function of $\sqrt{s}$ [25].

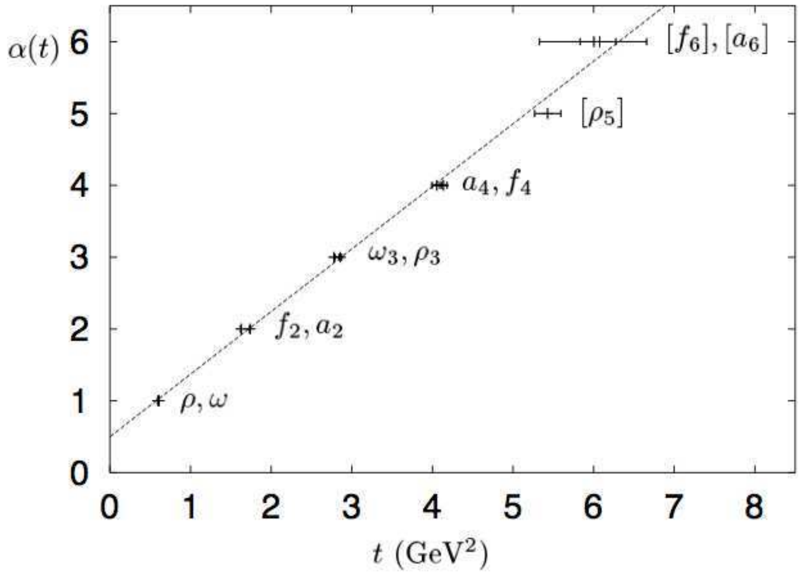

Figure 1.7: Example of Regge trajectory in the mass-spin plane: for values of $t = m^2$ (where m is the mass of a particle in the trajectory) $\alpha(t)$ corresponds to the spin of the particle. From [25].

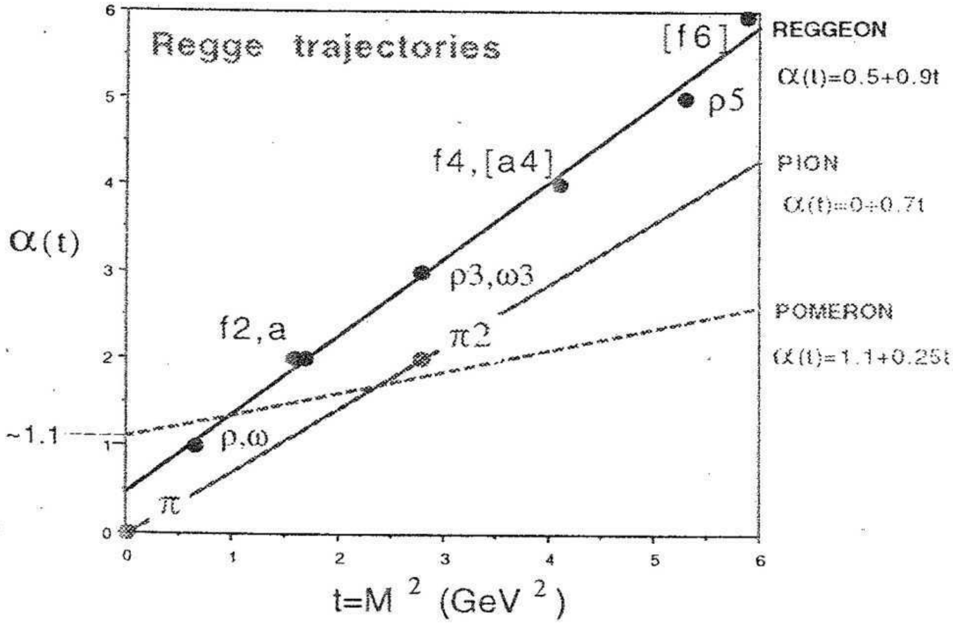

Figure 1.8: Regge trajectories. The vacuum pole, the Pomeron, with an intercept $\alpha(0) \sim 1.1$ is plotted in dashed line. From [28].

object in the event), whereas in the opposite case the process is called *soft* one.

1.2.1 Soft Diffraction

In hadron-hadron collisions a vast majority of events are due to soft interactions. In general, there are five types of soft processes:

- non-diffractive soft scattering,
- elastic scattering,
- Single Diffractive Dissociation (often called Single Diffraction, SD),
- Double Diffractive Dissociation (Double Diffraction, DD),
- Central Diffraction (CD).

The first one is non-diffractive, whereas the later four are of diffractive nature.

Elastic scattering is the simplest process one can imagine – the final state particles are the same as in the initial state, but there is a four-momentum transfer in the t channel:

$$a + b \to a + b.$$

Single Diffraction is the following process:

$$a + b \to a + X,$$

where X is a multi-particle state with the same quantum numbers as particle b. In other words, in Single Diffractive processes, one particle stays intact, whereas the other one dissociates into X.
Double Diffraction is a process in which:

$$a + b \to Y + X,$$

where Y and X are the multi-particle states of the same quantum numbers as particles a and b, respectively. In other words, there is no quantum number exchange between a and b. Schematic diagrams of elastic scattering, Single Diffraction and Double Diffraction are presented in Figure 1.9.

The class of processes:

$$a + b \to a + Z + b,$$

$$a + b \to a + Z + X,$$

$$a + b \to Y + Z + X,$$

is called Central Diffraction. Such events are often called Double Pomeron Exchange, due to the fact that each incoming particle radiates a colour singlet. It is worth noticing that the

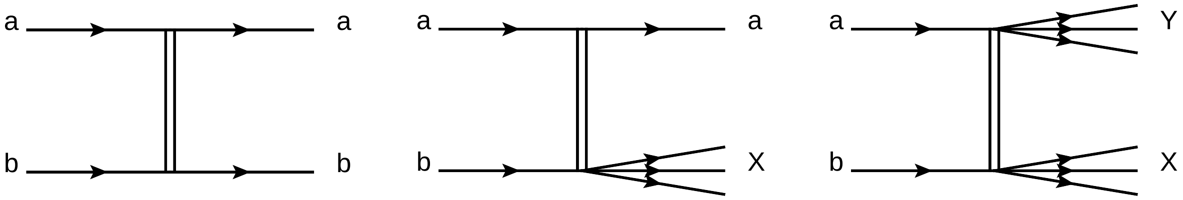

Figure 1.9: Diagrams of soft scattering processes: elastic scattering (**left**), Single Diffraction (**centre**) and Double Diffraction (**right**). The double line represents the Pomeron exchange.

centrally produced system, Z, has always the quantum numbers of the vacuum. The different variants of Central Production are shown in Figure 1.10.

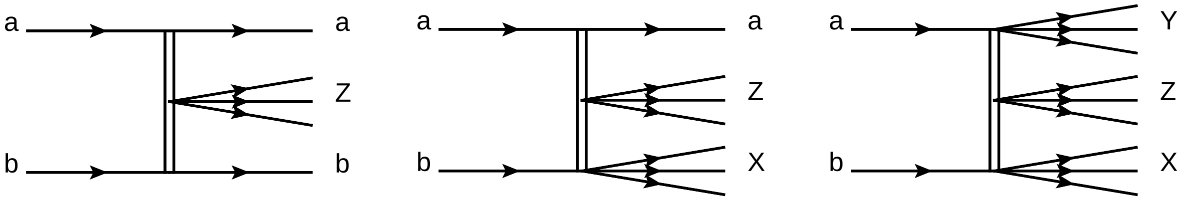

Figure 1.10: Diagrams of Central Diffractive production processes.

1.2.2 Hard Diffraction

The properties, like *e.g.* angular distribution or decay modes, of hard events can be calculated using perturbation theory. The cross section for a hard process can be calculated as a convolution of the Parton Distribution Function with the cross section for parton-parton interaction:

$$\mathrm{d}\sigma = f_p(x_1, Q^2) \cdot f_p(x_2, Q^2) \cdot \mathrm{d}\sigma_{\mathrm{hard}}(x_1, x_2, Q^2),$$

where x_1 and x_2 are the proton momentum fractions carried by the interacting partons, Q is the scale[4] of the process and $f_p(x_1, Q^2)$ and $f_p(x_2, Q^2)$ are the corresponding Parton Distribution Functions.

Similarly as in the case of soft interactions, the hard ones can be classified according to their diffractive and non-diffractive natures. Hard diffraction was proposed for the first time in [29], where the authors suggested the existence of the $p + p \to p + X$ process, where the X system contained two jets (collimated sprays of particles) with high transverse momentum. This process was experimentally measured by the UA8 experiment at the SPS collider at CERN [30, 31].

---

[4] The scale can be thought as the measure of resolution – the larger the Q^2 value is the more closely one can probe the particle structure.

Hard diffractive events can be further divided into subclasses of Single Diffractive (SD) and Double Pomeron Exchange (DPE) processes in which one or both protons stay intact. The diagram of the Non-Diffractive Jet production is shown in Figure 1.11. In this process interacting protons are destroyed and two jets are produced. In the pseudorapidity plane one will see two jets, low-p_T particles produced between them and the proton remnants in forward direction.

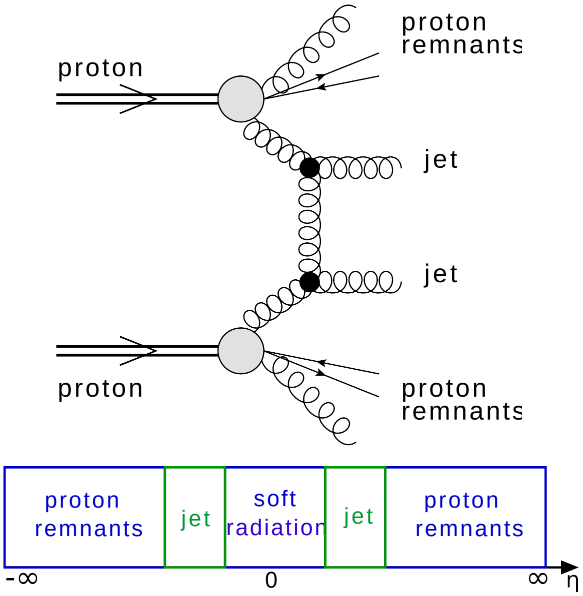

Figure 1.11: Non-Diffractive Jet production: the interacting protons are destroyed and two jets are produced.

The picture is slightly different the Single Diffractive and Double Pomeron Exchange jet production cases. As can be seen from Figure 1.12 one (in case of SD) or both (in case of DPE) protons stay intact, exchange a Pomeron and are scattered at very high pseudorapidities. Due to the colour singlet exchange a gap (region in pseudorapidity devoid of particles) is produced between the intact protons and Pomeron remnants.

There are also two very interesting, special cases of diffractive production. In the first one, there is no proton nor Pomeron remnants in the produced system. In consequence, both protons stay intact and all the energy is used to produce the central system. Such a class of processes is called Exclusive Production. A brief discussion of this class as well as a possibility of measuring the Exclusive Jet Production using the ATLAS detector at the LHC is described in Chapter 5.

In the second case, a color singlet is exchanged in the t channel. The theoretical model for such production is briefly described in the next Section. The measurement of inclusive jet production in which a Pomeron is exchanged in the t channel is described in Chapter 3, whereas the possibility to measure a similar process in Double Pomeron Exchange is discussed in Chapter 4.

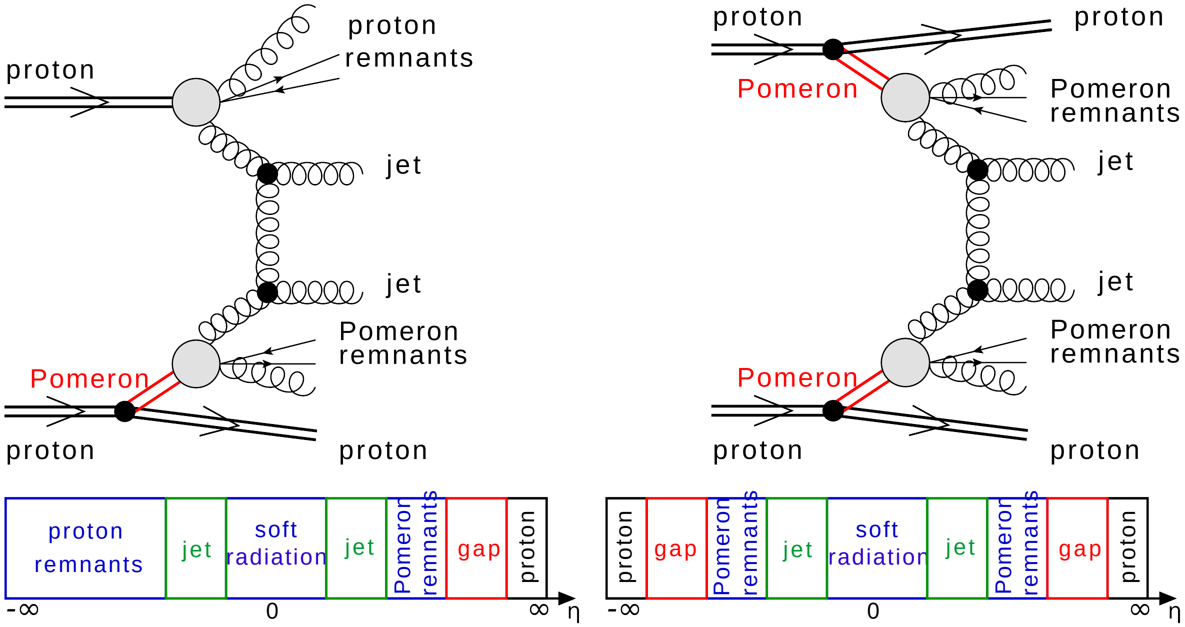

Figure 1.12: **Left:** Single Diffractive Jet production: one interacting proton stays intact, the second one is destroyed and two jets are produced. **Right:** Double Pomeron Exchange jet production: both interacting protons stay intact and two jets are produced.

All hard diffractive processes can be described in terms of the proton *Diffractive Parton Distribution Functions* (DPDFs) [32, 33]. The DPDFs are similar to the PDFs and they are also known from DIS experiments[5]. The Diffractive Parton Distribution Function can be factorised into [34]:

$$f_d(x, Q^2, \xi, t) = \Psi_P(\xi, t) \cdot f_P(\beta, Q^2),$$

where $\Psi_P(\xi, t)$ is the Pomeron flux, $f_P(\beta, \mu^2)$ denotes the Pomeron partonic structure and $\beta = x/\xi$. The DPDFs for $Q^2 = 25$ GeV^2 and $Q^2 = 90$ GeV^2 are plotted as a function of the fractional momentum of the Pomeron carried by the parton (z), which in the lowest order becomes equal to β in Figure 1.13. From these plots one can see that both distributions approach zero for high values of z. One also immediately realise that the gluon contribution dominates for $z < 0.5$.

To be in agreement with data, there is a need (especially in regions of low values of β and high values of ξ) to consider also non-diffractive contributions [32]. This is usually done by adding Reggeons and leads to the following formula:

$$f_d(x, Q^2, \xi, t) = \Psi_P(\xi, t) \cdot f_P(\beta, Q^2) + \Phi_R(\xi, t) \cdot f_R(\beta, Q^2).$$

---

[5] The parton distributions (PDFs) are thought as universal – they are the same for all processes. The QCD theory predicts accurately how the PDFs values change with the scale. Therefore, it is possible to measure them at one scale and predict the results at another one. In case of DPDFs there is the additional suppression due to the survival probability, which cannot be calculated from QCD.

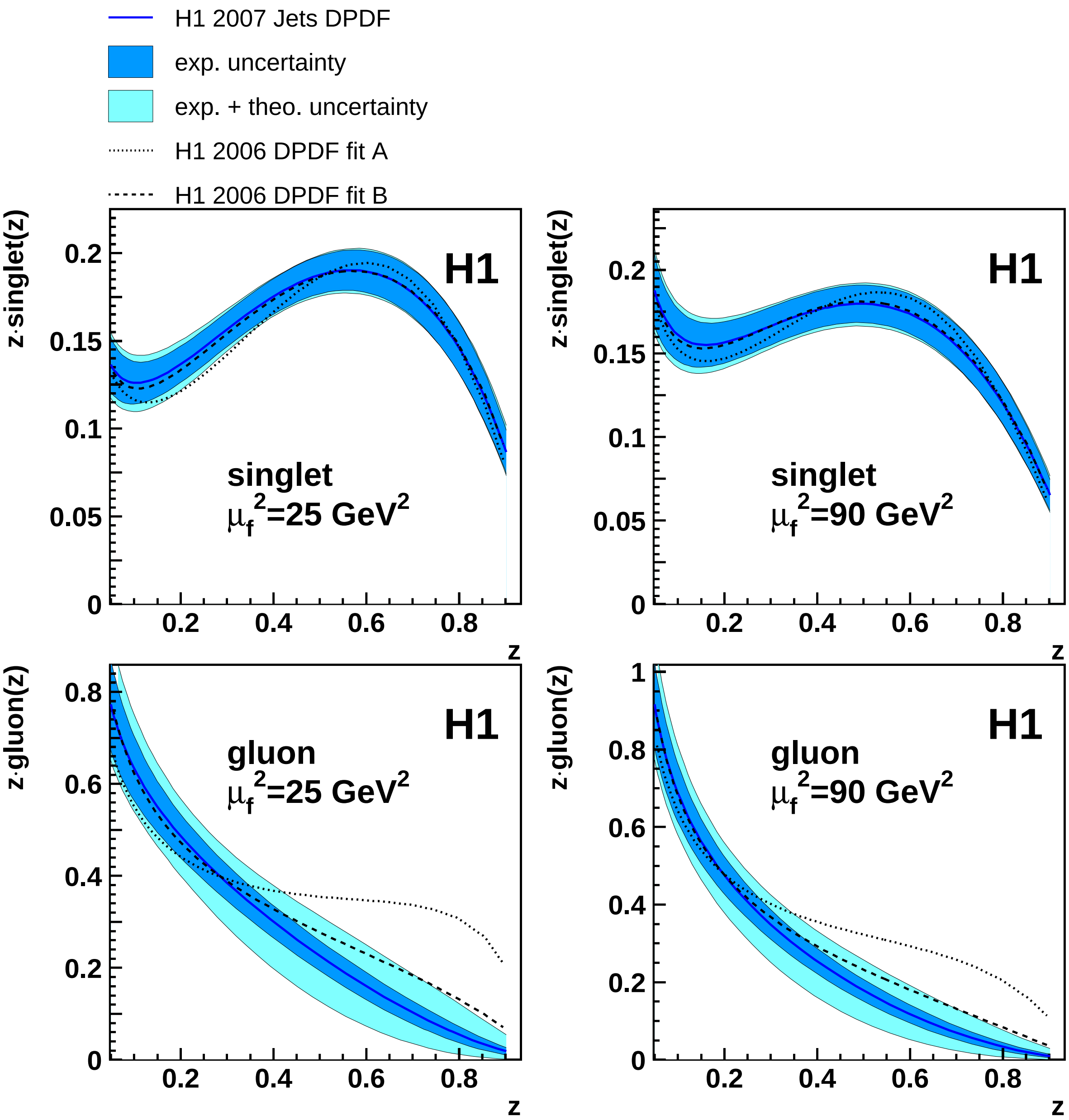

Figure 1.13: Diffractive quark (top) and gluon (bottom) densities for two scales $\mu^2 = 25$ GeV^2 (left) and $\mu^2 = 90$ GeV^2 (right). The solid line indicates the H1 2007 Jets DPDF, surrounded by the experimental uncertainty (dark shaded band) and the experimental and theoretical uncertainties added in quadrature (light shaded band). The dotted and dashed lines show the parton densities corresponding to the H1 2006 fit A and B from [32].

The DPDFs obtained in electron-proton scattering can be used to describe proton-proton or proton-antiproton collisions. The cross section for hard Single Diffractive production can be written as:

$$\mathrm{d}\sigma = S^2 \cdot \Psi(\xi_1, t) \cdot f_P(\beta, Q^2) \cdot f_p(x_2, Q^2) \cdot \mathrm{d}\sigma_{\mathrm{hard}}(x_1, x_2, Q^2),$$

whereas the one corresponding to Double Pomeron Exchange has a form of:

$$\mathrm{d}\sigma = S^2 \cdot \Psi(\xi_1, t) \cdot \Psi(\xi_2, t) \cdot f_P(\beta_1, Q^2) \cdot f_P(\beta_2, Q^2) \cdot \mathrm{d}\sigma_{\mathrm{hard}}(x_1, x_2, Q^2).$$

In the above equations there is an additional factor S. It is called the rapidity gap survival probability and takes into account the fact that an additional soft interactions between the initial or final state particles could destroy the rapidity gap in proton-(anti)proton collisions. This factor was introduced following the analysis of the Tevatron data [35]. It was experimentally discovered that the number of hard diffractive events is smaller by a factor of about 10 than the one expected from the extrapolations of the HERA data. The gap survival probability depends on the centre of mass energy – for the Tevatron ($\sqrt{s} = 1$ TeV) it is about 0.1, whereas for the LHC energies ($\sqrt{s} = 14$ TeV) it is predicted to be of the order of 0.03 [36]. It is worth stressing that soft interactions happen on much longer time scales than the hard ones, therefore it is often assumed that the gap survival probability can be factorised from the hard part.

1.3 Jet-Gap-Jet Production

Jet-Gap-Jet (JGJ) Production is a special case of diffractive proton-proton interactions. In such events both protons are destroyed, but a Pomeron is involved in the process – a colour singlet is exchanged in t channel. Therefore, one can expect a gap in rapidity between the two hard jets. A diagram of JGJ production is shown in Fig. 1.14. The rapidity interval between the two jets is $\Delta\eta_J = \ln(x_1 x_2 s/(p_{T,1} p_{T,2}))$, where $p_{T,1}$ and $p_{T,2}$ are the transverse momenta of the jets and x_1 and x_2 are their longitudinal momentum fraction with respect to the incident hadrons [37]. At parton level the rapidity gap is the same as the rapidity interval between the outgoing partons which initiate the jets. The hadronisation of the partons into jets reduces the size of the rapidity gap to $\Delta\eta_g$. In the pseudorapidity plane one will see two jets and protons remnants spread in forward direction. The space in rapidity between the jets will be devoid of particles.

Although rapidity gaps are expected to occur primarily in colour singlet exchange processes, they can also be observed in colour triplet (quark) or colour octet (gluon) exchanges as a result of fluctuations. An important fact is that the contributions due to colour triplet/octet exchange are expected to decrease sharply with the increasing size of the pseudorapidity gap between the jets. This is due to the larger phase space for hadronisation, which results in an increased average particle multiplicity between the jets. Therefore, when the rapidity distance

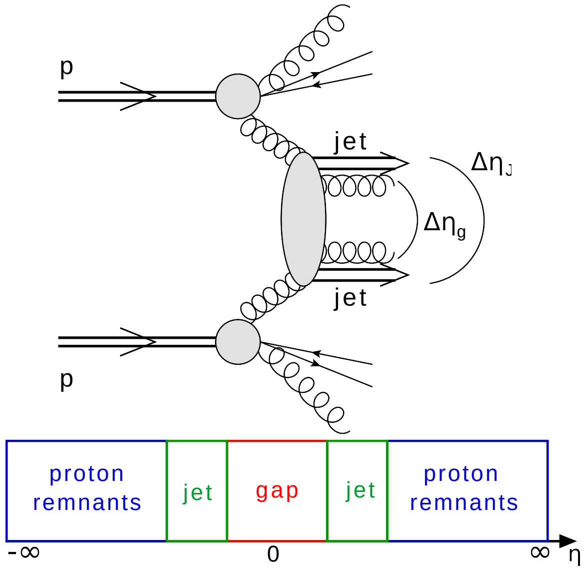

Figure 1.14: Production of two jets surrounding a large rapidity gap in a hadron-hadron collision. The rapidity interval between the jets $\Delta\eta_J$ is bigger than the rapidity gap $\Delta\eta_g$.

between the jets is large, the rapidity gap is mainly due to colour singlet exchange.

There are two main ways of calculating the evolution of parton distribution in strong interaction scattering processes: the Dokshitzer-Gribov-Lipatov-Altarelli-Parisi (DGLAP) [38, 39, 40] and the Balitsky-Fadin-Kuraev-Lipatov (BFKL) [41, 42, 43] evolution equations. The former one provides a good description in a wide range of Q^2 if the momentum fraction carried by a parton, x, is not too small. The latter one is important in the regime in which the values of x are small. It is worth noticing that in usual calculations one uses $\log(1/x)$ rather than x. The sketch showing in which regimes the DGLAP and BFKL frameworks work is presented in Figure 1.15. Usually, the evolution equations are computed for:

- Leading Order (LO), Next-to-Leading Order (NLO) and Next-to-Next-to-Leading Order (NNLO) in α_S for DGLAP,
- Leading Logarithm (LL) and Next-to-Leading Logarithm (NLL) in $\log(1/x)$ for BFKL.

The requirement of the Jet-Gap-Jet production to be dominated by Pomeron exchange implies that the jets are produced at large rapidities – in the forward direction. In this regime the DGLAP evolution equations predict a cross section which is much smaller than the ones observed experimentally at the large rapidity gaps [44]. In such situation one has to use the BFKL framework.

The Jet-Gap-Jet cross section can be written as [45]:

$$\frac{d\sigma^{pp\to XJJY}}{dx_1 dx_2 dp_T^2} = S^2 \cdot f(x_1, p_T^2) \cdot f(x_2, p_T^2) \frac{d\sigma^{gg\to gg}}{dp_T^2}, \tag{1.1}$$

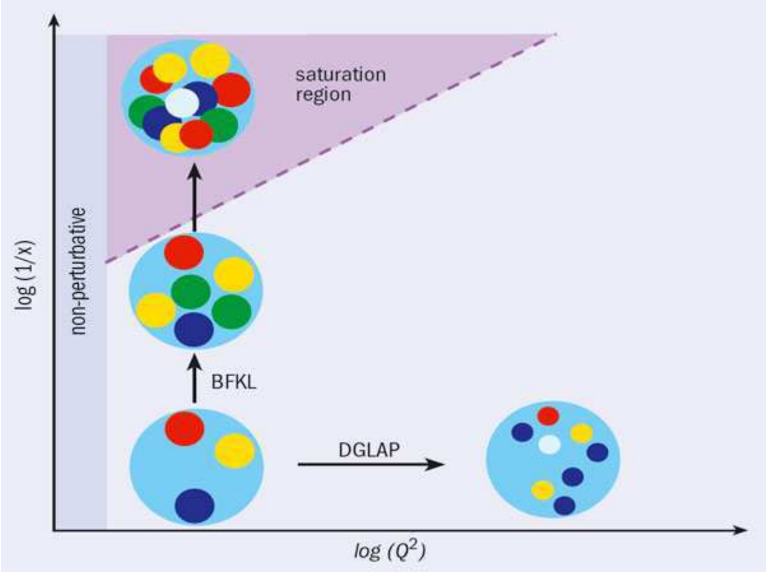

Figure 1.15: As a proton is probed at increasing Q^2, the number of partons rises but their size decreases, as described by the DGLAP evolution equations. By contrast, when the fraction of momentum carried by a parton, x, becomes smaller, the number of partons increases, but their size stays the same; this is where the BFKL evolution applies. Eventually, the region of saturation, in which the partons should start to overlap, is marked.

where S^2 is the gap survival probability, $f(x_1, p_T^2)$ and $f(x_2, p_T^2)$ are the Parton Distribution Functions and $\mathrm{d}\sigma^{gg\to gg}/dp_T^2$ is the jet hard cross-section. The Parton Distribution Functions have the form:

$$f(x,\mu^2) = g(x,\mu^2) + \frac{C_F^2}{N_c^2}(q(x,\mu^2) + \bar{q}(x,\mu^2)) \ ,$$

where g (q, $\bar{q}$) is the gluon (quark, antiquark) distribution function of the incoming hadrons, N_c is the number of colours and C_F is the Casimir operator. The hard cross section in Eq. 1.1 is given by:

$$\frac{d\sigma^{gg\to gg}}{dp_T^2} = \frac{1}{16\pi}\left|A(\Delta\eta, p_T^2)\right|^2 ,$$

where $A(\Delta\eta, p_T^2)$ is the scattering amplitude, which can be written as [45]:

$$A(\Delta\eta, p_T^2) = \frac{16N_c\pi\alpha_S^2(p_T^2)}{C_F p_T^2}\sum_{p=-\infty}^{\infty}\int_{1/2-i\infty}^{1/2+i\infty}\mathrm{d}\gamma\frac{[p^2-(\gamma-1/2)^2]\exp\left\{\bar{\alpha}(p_T^2)\chi_{eff}[2p,\gamma,\bar{\alpha}(p_T^2)]\Delta\eta\right\}}{[(\gamma-1/2)^2-(p-1/2)^2][(\gamma-1/2)^2-(p+1/2)^2]}, \tag{1.2}$$

where the $\chi_{eff}[2p, \gamma, \bar{\alpha}(p_T^2)]$ is the effective BFKL kernel [45], $\alpha(p_T^2) = \pi\bar{\alpha}(p_T^2)/N_C$ is the running coupling constant and p is the conformal spin. The need of summing up all even conformal spins was demonstrated in [46].

In order to compare the theoretical results with data there is a need to implement them in a Monte Carlo program. The Jet-Gap-Jet process is coded *e.g.* in the HERWIG [47] and the HERWIG++ [48] Monte Carlo generators. It is worth stressing that basic versions of these programs contain only the Leading Logarithm terms with conformal spins $p = 0$ (see Eq. 1.2). The details of extending the standard HERWIG routines with the NNL calculations and the sum over all conformal spins are described in [37].

The MC results were compared to the Tevatron data. The D0 Collaboration performed a measurement of the Jet-Gap-Jet event ratio [49], defined as the ratio of the Jet-Gap-Jet cross section to the inclusive jet cross section:

$$\mathrm{R} = \sigma(\text{Jet-Gap-Jet})/\sigma(\text{Jet}).$$

This ratio was measured as a function of the transverse energy of the second-leading jet [6], E_T and the rapidity difference between the two leading jets, $\Delta\eta_J$. In the former case, the data were divided into a low-E_T ($15 < E_T < 25$ GeV) and a high-E_T ($E_T > 30$ GeV) sample. In the analysis the second-leading jet was required to have $E_T > 15$ GeV. In addition, the two leading jets were required to be in the opposite pseudorapidity hemispheres ($\eta_{J,1} \cdot \eta_{J,2} < 0$) and in the forward region ($1.9 < |\eta_{1,2}| < 4.1$). The rapidity gap between the jets ($\Delta\eta_g$) was imposed to be between $\eta = -1$ and $\eta = 1$. These results are shown in Figure 1.16.

Similar studies were performed by the CDF Collaboration [50]. The measurement of the Jet-Gap-Jet event ratio was performed as a function of:

- the average jet transverse momentum, E_T,
- the average transverse momentum of the third jet, $E_T^{(3)}$ (if there is one in the event),
- the rapidity difference between the two leading jets, $\Delta\eta_J$.

One has to note that the cuts on E_T are different than the ones of D0. The rapidity gap definition, $\Delta\eta_g$ remains the same, but the jet energy threshold ($E_T > 20$ GeV) and the jet rapidity range ($1.8 < \eta_{1,2} < 3.5$) definitions are slightly different. The CDF results are shown in Figure 1.17. The theoretically predicted ratios [37] were plotted superimposed over the data. In order to take into account the proper QCD corrections there is a need to multiply the HERWIG results by the ones of NLO JET++ [51]:

$$R = \frac{\sigma(\text{HERWIG BFKL JGJ})}{\sigma(\text{HERWIG JJ})} \cdot \frac{\sigma(\text{LO QCD})}{\sigma(\text{NLO QCD})}.$$

In the above ratio the Jet-Gap-Jet (HERWIG BFKL JGJ) and the Non-Diffractive Jet (HERWIG JJ) cross sections were obtained from the HERWIG MC. The LO QCD (NLO QCD) are the predictions at leading (next-to-leading) order of the cross section for Non-Diffractive Jet production from NLO JET++. The Jet-Gap-Jet cross section was calculated in the LL and NLL approximations. From Fig. 1.17 one can conclude that the NLL calculation is in better agreement than the LL ones, but it is clear that higher statistics is much desirable.

---

[6] Hereafter, the jet with the highest transverse momentum will be referred as the leading jet, whereas the one with second-highest transverse momentum of the second-leading jet.

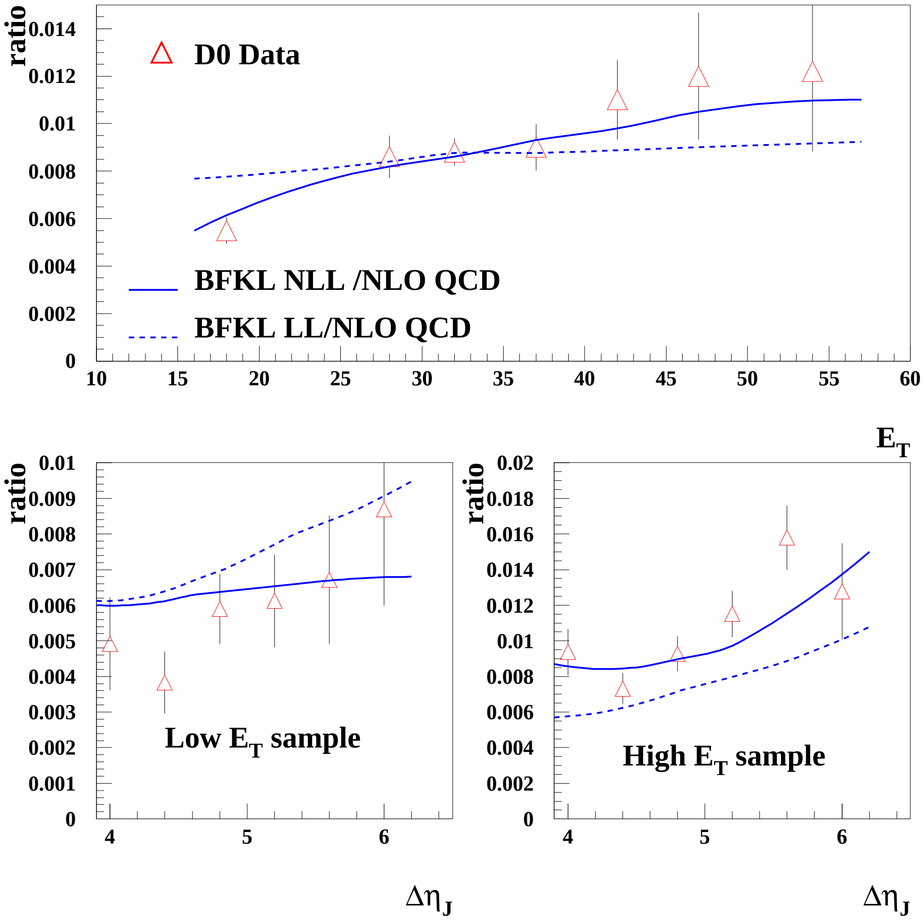

Figure 1.16: Comparisons between the D0 measurement of the Jet-Gap-Jet event ratio with the LL- and NLL-BFKL calculations. Data are presented as a function of the transverse energy of the second-leading, E_T and as a function of the rapidity difference between the two leading jets $\Delta\eta_J$. In the former case data were divided into a low-E_T ($15 < E_T < 25$ GeV) and a high-E_T ($E_T > 30$ GeV) sample. The theoretical ratios taking into account LL and NLL terms are plotted as blue lines.

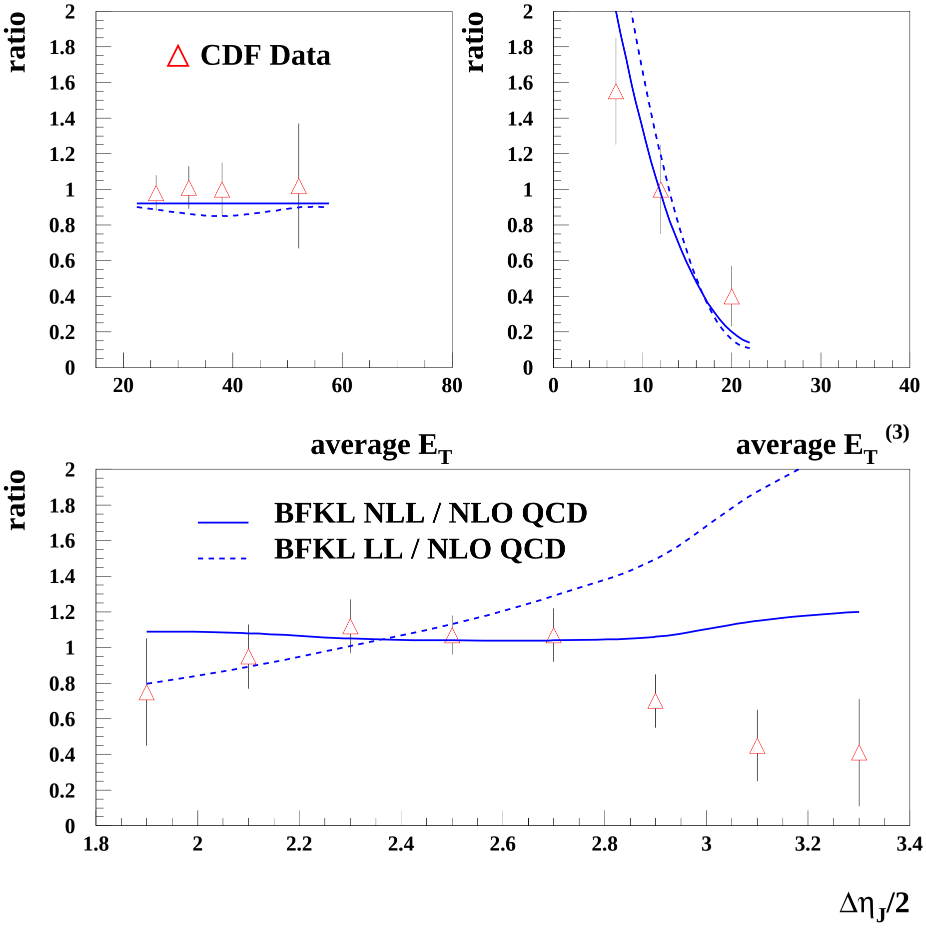

Figure 1.17: Comparisons between the CDF measurement of the Jet-Gap-Jet event ratio with the LL- and NLL-BFKL calculations. Data are presented as a function of the average jet transverse momentum, E_T, the average transverse momentum of the third jet, $E_T^{(3)}$ and the rapidity difference between the two leading jets $\Delta\eta_J$. The theoretical ratios taking into account LL and NLL terms are plotted as blue lines.

The observed differences between the theoretical predictions and the Tevatron data trigger the necessity of providing further tests. The predictions of the Jet-Gap-Jet ratio as a function of the sub-leading jet transverse energy, E_T and the rapidity difference between the two leading jets, $\Delta\eta_J$, for the LHC accelerator are shown in Figure 1.18 and 1.19 [45]. These predictions assume that the two leading jets:

- have $E_T > 20$ GeV,
- are at the opposite pseudorapidity hemispheres ($\eta_{J,1} \cdot \eta_{J,2} < 0$),
- are produced in forward region ($2 < |\eta_{1,2}| < 5$).

The gap survival probability was set to $S = 0.03$ [52]. The results predict that the Jet-Gap-Jet event ratio is about 0.002 and does not vary much with E_T or $\Delta\eta_J$.

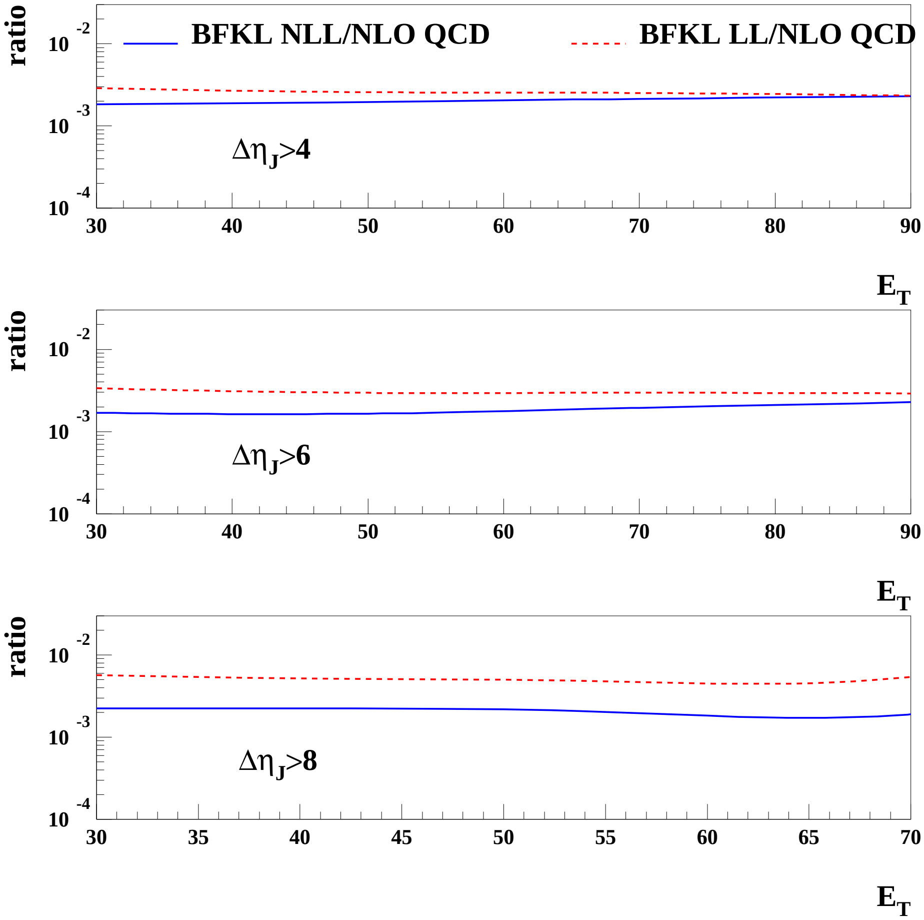

Figure 1.18: Predictions for the ratio of the Jet-Gap-Jet to the inclusive jet cross section at the LHC, as a function of the second-leading jet transverse energy E_T. From [37].

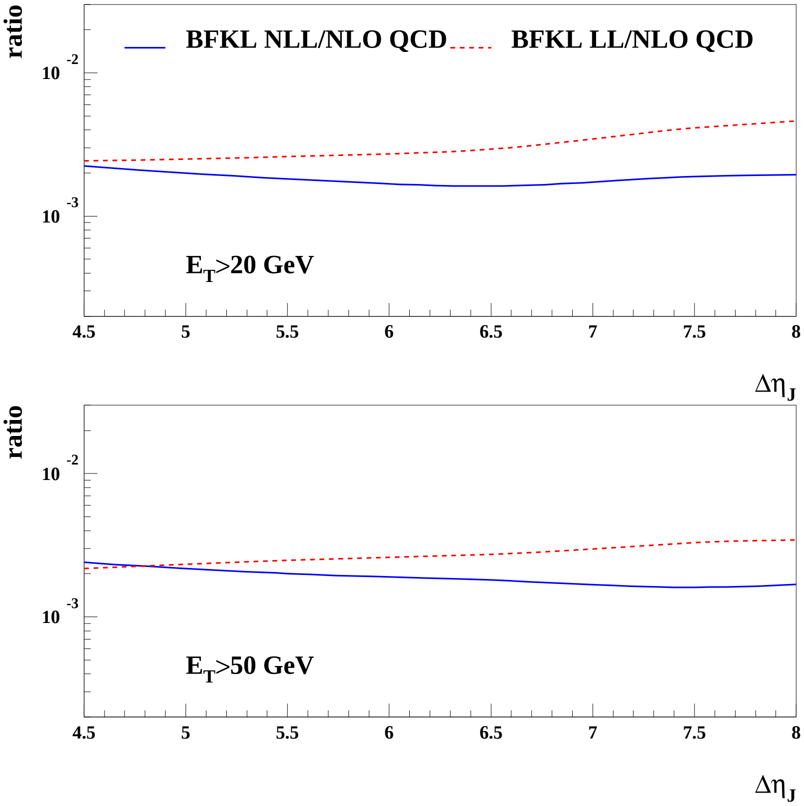

Figure 1.19: Predictions for the ratio of the Jet-Gap-Jet to the inclusive jet cross section at the LHC, as a function of the rapidity difference between the two leading jets $\Delta\eta_J$. From [37].

Chapter 2

Experimental Apparatus

2.1 Large Hadron Collider

The Large Hadron Collider (LHC) [53], built by the European Organization for Nuclear Research (CERN), is the world's largest and highest-energy particle accelerator. It is expected to answer some of the most fundamental questions of physics, allowing humanity to understand the deepest laws of nature.

The LHC is a 27 km long circular particle collider which lies about 100 m underground, in the former Large Electron-Positron (LEP) tunnel. It is a synchrotron designed to collide particle beams of protons with an energy up to 7 TeV and lead nuclei with an energy of 2.76 TeV per nucleon.

The collider consists of two separate rings of beam pipes with eight common sections called Interaction Points (IP) – *cf.* Fig. 2.1. During accelerator work, proton (or lead) beams circulate in opposite directions in each beam pipe. To keep the beams in their circular paths 1232 dipole magnets are used. Additional 392 quadrupole magnets were installed to keep the beams focused. LHC magnets are made of copper-clad niobium-titanium and work at the temperature of 1.9 K ($-271.25\ ^{o}$C). Operating at such a low temperature requires liquid helium cooling, making the LHC the largest cryogenic facility in the world.

Before beams are brought to collisions at nominal energy they pass through several acceleration stages. Each of these stages is important and determine the quality of the beams. The overall scheme of the LHC accelerator facility is presented in Figure 2.2.

Firstly, protons are generated by a duo-plasmatron source and injected (with an initial energy of 100 keV) into LINAC2 [54] – an 80 m long linear accelerator with an extraction energy of 50 MeV. During the acceleration process in the LINAC2 the proton beam is bunched by using the RF cavities. Then protons are injected into the Proton Synchrotron Booster (PSB) [54], a 157 m long circular accelerator capable of accelerating protons up to an energy of 1.4 GeV. Then the particles are injected into the Proton Synchrotron (PS) [55], a 628 m long ring where they are accelerated up to an energy of 26 GeV. All these machines are installed at ground level. At this point the beam is sent in an underground machine, the Super Proton

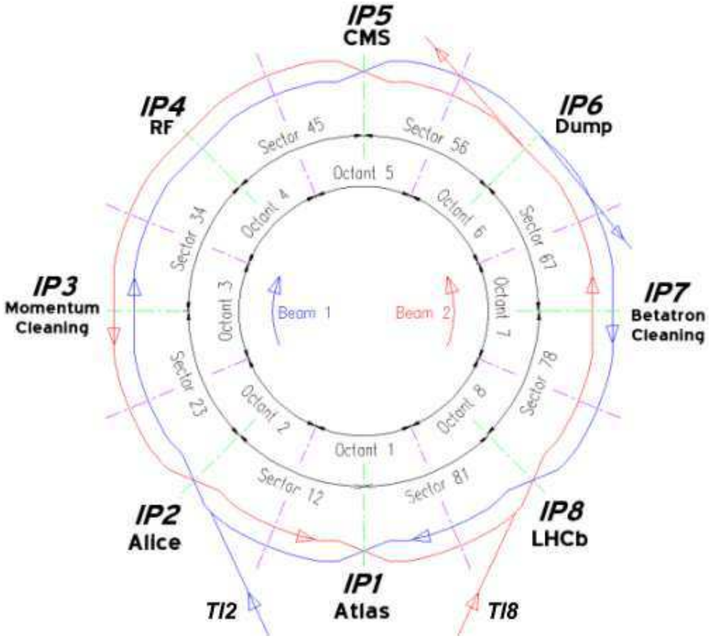

Figure 2.1: Location of the Interaction Points along the LHC ring.

Synchrotron (SPS)[54], which is a 6.9 km long circular accelerator lying 50 m underground. Here, the beam is accelerated to 450 GeV which is the LHC injection energy. The injection of the LHC beams from the SPS is done in Insertion Region 2 (IR2) for beam 1 and IR8 for beam 2. The other insertion regions host: the RF cavities (IR4) which accelerate the beams and keeps them bunched, the beam dump (IR6) used for beam extraction from the LHC and, important for machine protection, cleaning devices dedicated to the removal of particles with large transverse (IR3) or longitudinal (IR7) oscillation amplitude. All mentioned accelerators are connected through transfer lines [56] which allow the particles to travel from one machine to another.
The LHC was also designed to collide heavy ions which first go through the LINAC3 and the Low Energy Ion Ring (LEIR) [54] before being injected to the Proton Synchrotron.

The LHC beams collide in four Interaction Points (IP), where proton-proton collisions are observed by four large experiments:

- ATLAS (A Toroidal LHC Apparatus, located at IP1) [57],
- CMS (Compact Muon Spectrometer, IP5) [58],
- ALICE (A Large Ion Collider Experiment, IP2) [59],
- LHCb (Large Hadron Collider beauty, IP8) [60].

There are also three smaller experiments:

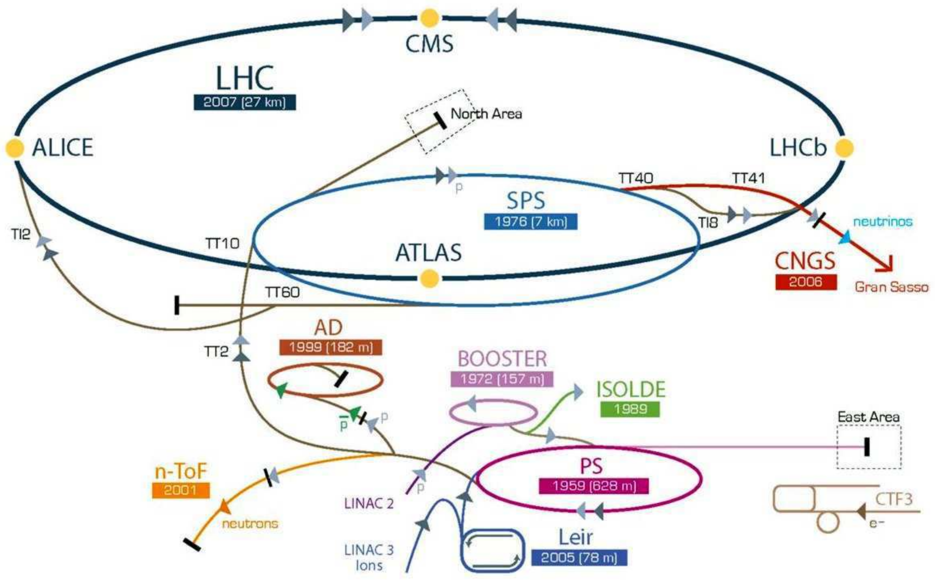

Figure 2.2: CERN accelerator facility.

- LHCf (Large Hadron Collider forward, IP1) [61],
- TOTEM (Total Cross Section, Elastic Scattering and Diffraction Dissociation at the LHC , IP5) [62]
- MoEDAL (The Monopole & Exotics Detector at the LHC, IP8) [63].

ATLAS and CMS are general purpose detectors. ALICE was designed especially for heavy ion collisions and studies the quark-gluon plasma, LHCb is specialized in B-meson physics and devoted to studies of CP violation, TOTEM is a forward detector aiming at proton-proton total cross section measurement and diffractive processes studies, LHCf uses the LHC as a source to study processes relevant for cosmic rays in laboratory conditions and MoEDAL motivation is to provide direct search for the Magnetic Monopole.

2.1.1 LHC Magnets

The LHC collides two proton beams. They circulate in two horizontally displaced beam pipes. The beam pipes join into a common one about 140 m away from the ATLAS, CMS, ALICE and LHCb Interaction Points. The beam performing the clockwise motion (viewed from above the ring) is called $beam1$ and the other one $beam2$. For beam studies a machine is usually described as a sequence of beam elements (magnets, drift spaces) placed along a reference orbit.

The Insertion Regions, where the main LHC experiments are located, have very similar designs. They consist of 13 main quadrupole magnets on both sides of the IP, out of which three on each side (the so-called *triplets*) are situated in the common beamline and are used for final beam focusing. The triplet affects both beams, whereas the other quadrupoles will act on them independently. All these quadrupoles are used to tune and control the optical functions in the Insertion Regions.

Since in the following work only the ATLAS, ALFA (Absolute Luminosity For ATLAS, located around 240 m from the IP1, [64]) and AFP (ATLAS Forward Proton, planned to be installed 210 m from IP 1, [11]) detectors are discussed, only the magnets between IP1 and 240 m are considered.

The LHC magnetic lattice in vicinity of the ATLAS IP is presented in Figure 2.3. The quadrupole magnets are labelled with the letter Q while the dipole ones with D. The final focusing triplet ($Q1 - Q2 - Q3$) is positioned about 40 m away from IP1. The LHC triplet assembly consists in fact of four quadrupole magnets but the central two quadrupoles form one functional entity. In addition, there are three more quadrupoles: Q4, Q5 and Q6, installed at the distances of ∼160 m, ∼190 m and ∼220 m, respectively [54, 65]. Between IP1 and 240 m two dipole magnets were installed: $D1$ at 70 m and $D2$ at 150 m away from the ATLAS IP. They are used for beam separation. Apart from the main dipole and quadrupole magnets there are several correction magnets used to compensate laxities of the former ones.

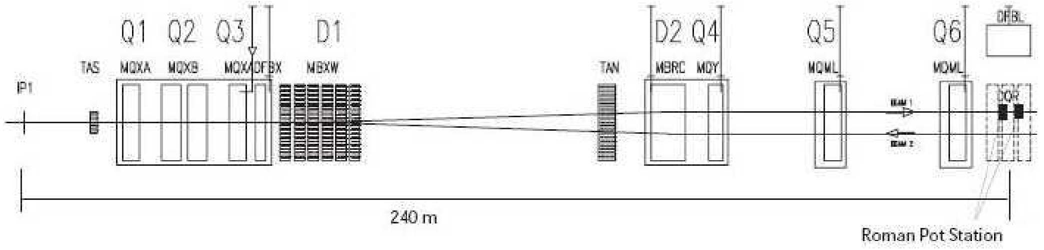

Figure 2.3: LHC magnet structure close to the ATLAS Interaction Point.

Besides magnets there are few more LHC elements installed close to the ATLAS Interaction Point:

- Beam Position Monitors (BPM).
- Target Absorber Neutral (TAN) – absorber for neutral particles leaving the IP, located in front of the D1 dipole magnet on the side facing the ATLAS detector.
- Target Absorber Secondaries (TAS) – absorber for particles which could reach the quadrupole triplet. The first one is located in front of Q1, whereas the second one before the Q3 quadrupole magnet.

2.1.2 LHC Operation

During the operation in years 2010 – 2012 the LHC was running in several different modes. All runs in which the ATLAS detector recorded data can be classified using two parameters:

- centre of mass energy: $\sqrt{s} = 7$ TeV in years 2010 – 2011 and 8 TeV in year 2012,
- betatron function at the IP1: β^*.

In terms of accelerator optics [66], the betatron function β is a measure of the distance from a certain point to the one at which the beam is twice as wide. The lower is the betatron function at the IP (β^*), the smaller is the beam size, thus the larger is the luminosity. During standard data taking the β^* function was changed from 11 m (the so-called *injection optics*, very early data taking – period A in year 2010) to 0.6 m (the so-called *collision optics*, end of the proton-proton running periods in year 2012). The ultimate LHC goal is to lower the betatron function to 0.55 m.

Apart from the betatron function, a very important parameter is the beam emittance, ε, which measures the average spread of particle coordinates in position-momentum phase space. The LHC was designed to obtain $\varepsilon = 3.75\,\mu$m·rad, but due to the outstanding performance this value is about 2 μm·rad in an average run. In this thesis, the former value of the emittance was used in the calculations of the beam properties around ALFA and AFP detectors and the latter one in the case of the calculations considering the beam behaviour at the IP. Such an approach is consistent with the one of the machine group and real experimental conditions. To avoid unwanted parasitic interactions, during which beams interact with each other but not at the Interaction Point, the LHC beams cross at the IP1 with an angle of to 285 μrad in the vertical plane.

From the theory point of view, an important information is how rare processes can be studied at a given experiment. This is directly connected to the rate of events produced in the accelerator. A parameter which describes this rate is called the *luminosity*, L. The number of events of a particular process that can be observed is given by the product of the integrated luminosity, $\int L\ \mathrm{d}t$, and the cross section for the process, σ_{event}. The higher the integrated luminosities are, the rarest processes are accessible.
The luminosity is given by the following equation:

$$L = \frac{N_1\, N_2\, n\, f\, \gamma}{4\, \pi\, \varepsilon\, \beta^*} F,$$

where N_1 and N_2 are the number of protons per bunch in beam 1 and 2, correspondingly, n is the number of bunches per beam, f is the revolution frequency, γ is the beam Lorentz factor, ε is the beam emittance, and F is the geometric luminosity reduction factor due to the crossing angle at the Interaction Point:

$$F = \left(1 + \left(\frac{\theta_c\, \sigma_z^*}{2\, \sigma^*}\right)^2\right)^{-1/2},$$

where θ_c is the crossing angle at the IP, σ_z^* the RMS bunch length, and σ^* the transverse RMS beam size at the IP.
The integrated luminosity delivered by the LHC accelerator to its experiments as a function of time is shown in Figure 2.4.

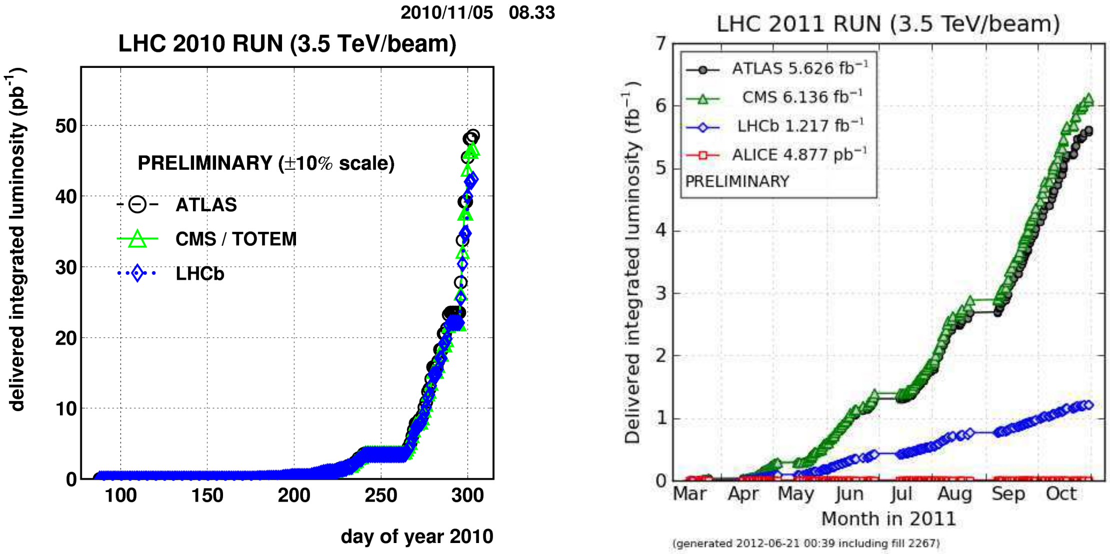

(a) 2010 (b) 2011

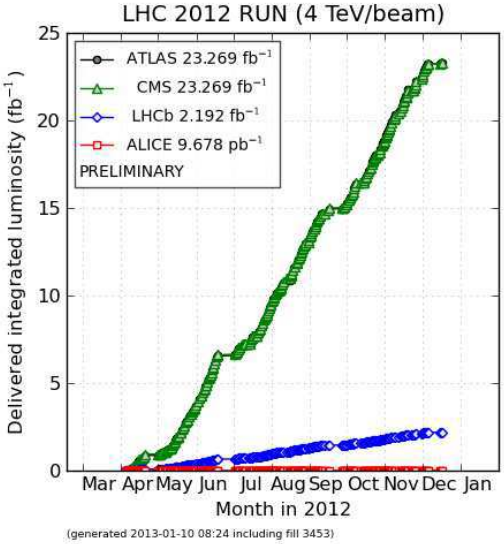

(c) 2012

Figure 2.4: Luminosity delivered by LHC to ATLAS, CMS, ALICE and LHCb experiments in year: a) 2010, b) 2011, c) 2012. The luminosity delivered LHCb experiment is smaller than the one delivered to ATLAS and CMS due to the *luminosity levelling*. ALICE detector collects data mainly during the heavy ions runs.

During the LHC operation few proton-proton runs were dedicated to special data taking, when the ALFA detectors were allowed to be inserted into the LHC beampipe. Such runs were characterized by a large value of the betatron function and therefore are called *high-*β^* runs. So far, apart of few test runs, there were three *high-*β^* runs when the ALFA detectors collected the data:

- $\sqrt{s} = 7$ TeV, $\beta^* = 90$ m,
- $\sqrt{s} = 8$ TeV, $\beta^* = 90$ m,
- $\sqrt{s} = 8$ TeV, $\beta^* = 1000$ m.

It is worth mentioning that the betatron function value foreseen for optimal ALFA data taking is $\beta^* = 2625$ m. Additionally, ALFA could also take data in runs with collision optics (small values of β^*), when the beam intensity was small – it happened during the LHC proton-lead run in the year 2013 when ALFA was used as a proton tagger.
It is worth stressing that the integrated luminosity collected during the ALFA dedicated runs is orders of magnitude smaller than the one gathered during normal LHC operation. The three main factors responsible for this are:

- large value of the betatron function (luminosity increases like $1/\beta^*$),
- smaller number of protons in a bunch (to reduce interactions within the bunch),
- smaller number of bunches (due to the ALFA trigger capabilities).

The high β^* optics requires a special settings of the LHC magnets, as described in [67, 68, 69, 70, 71, 72, 73, 74]. One must remember that the lattice elements used for *beam*1 and *beam*2 are not identical, thus the two beam lines are described by two different optics files. The common feature of all *high-*β^* runs is setting the crossing angle to zero in order to avoid unwanted additional momentum spread.

2.1.3 LHC Beam Size

The beam size can be calculated as:

$$\sigma = \sqrt{\varepsilon \cdot \beta / \gamma}, \tag{2.1}$$

where γ is the Lorentz factor for the beam.

Since the emittance is assumed to be stable and constant in the whole LHC ring during the run, the only parameter defining the beam size is the betatron function value. The beam sizes at the ATLAS Interaction Point for different LHC optics and emittances are listed in Table 2.1. For the designed β^* values the beam at the IP is symmetric in the (x, y) plane.

The knowledge of the betatron function at a given point of LHC ring allows to calculate the beam size. The results for AFP and ALFA detector positions are listed in Tables 2.2 – 2.5.

Table 2.1: LHC beam transverse size at the ATLAS IP for different β^* optics modes for nominal and low emittance.

β^* [m]	crossing angle [μrad]	beam transverse size [mm] low emittance $\varepsilon = 2$ μm·rad	 nominal emittance $\varepsilon = 3.75$ μm·rad
0.55	285	0.017	0.024
90	0.0	0.205	0.281
1000	0.0	0.685	0.938
2625	0.0	1.110	1.520

In the case of the AFP detectors only the parameters for collision optics are given, since there is no plan of using them during *high*-β^* runs. The knowledge of the beam size at the experiment location is important for simulations and data analysis as this factor determines the minimum distance at which detectors are allowed to be inserted. This defines the kinematic regions that are accessible for a given optic settings. The results were obtained using the MAD-X program [75, 76] fed with relevant LHC optic files [66].

Table 2.2: LHC *beam*1 size in x at the AFP and ALFA stations for different β^* optics modes for nominal and low emittance.

β^*	$\sigma^{x,206}_{beam1}$ [mm]		$\sigma^{x,214}_{beam1}$ [mm]		$\sigma^{x,237}_{beam1}$ [mm]		$\sigma^{x,241}_{beam1}$ [mm]	
[m]	$\varepsilon = 2$	$\varepsilon = 3.75$	$\varepsilon = 2$	$\varepsilon = 3.75$	$\varepsilon = 2$	$\varepsilon = 3.75$	$\varepsilon = 2$	$\varepsilon = 3.75$
0.55	0.13	0.18	0.09	0.12	0.10	0.14	0.12	0.17
90	–	–	–	–	0.26	0.35	0.24	0.33
1000	–	–	–	–	0.37	0.50	0.35	0.48
2625	–	–	–	–	0.21	0.29	0.21	0.29

2.1.4 Proton Trajectories

For all studies of diffractive physics in which one or both protons after interaction stay intact and are considered to be tagged in forward detectors, the knowledge of their behaviour inside the LHC aperture is of crucial importance. Therefore, in this Section the proton trajectories from the ATLAS IP to 240 m for various initial conditions are discussed.
In this thesis two coordinate systems are used:

- the ATLAS coordinate system (*cf.* Figure 2.5): right-handed, with the x-axis pointing towards the centre of the LHC ring, and the z-axis along the tunnel.

Table 2.3: LHC *beam*1 size in y at the AFP and ALFA stations for different β^* optics modes for nominal and low emittance.

β^*	$\sigma_{beam1}^{y,206}$ [mm]		$\sigma_{beam1}^{y,214}$ [mm]		$\sigma_{beam1}^{y,237}$ [mm]		$\sigma_{beam1}^{y,241}$ [mm]	
[m]	$\varepsilon = 2$	$\varepsilon = 3.75$	$\varepsilon = 2$	$\varepsilon = 3.75$	$\varepsilon = 2$	$\varepsilon = 3.75$	$\varepsilon = 2$	$\varepsilon = 3.75$
0.55	0.34	0.47	0.31	0.43	0.27	0.37	0.25	0.34
90	–	–	–	–	0.63	0.87	0.60	0.83
1000	–	–	–	–	0.22	0.30	0.22	0.30
2625	–	–	–	–	0.24	0.33	0.23	0.32

Table 2.4: LHC *beam*2 size in x at the AFP and ALFA stations for different β^* optics modes for nominal and low emittance.

β^*	$\sigma_{beam2}^{x,206}$ [mm]		$\sigma_{beam2}^{x,214}$ [mm]		$\sigma_{beam2}^{x,237}$ [mm]		$\sigma_{beam2}^{x,241}$ [mm]	
[m]	$\varepsilon = 2$	$\varepsilon = 3.75$	$\varepsilon = 2$	$\varepsilon = 3.75$	$\varepsilon = 2$	$\varepsilon = 3.75$	$\varepsilon = 2$	$\varepsilon = 3.75$
0.55	0.13	0.18	0.09	0.12	0.10	0.14	0.12	0.17
90	–	–	–	–	0.26	0.35	0.24	0.33
1000	–	–	–	–	0.37	0.50	0.35	0.47
2625	–	–	–	–	0.21	0.28	0.21	0.29

Table 2.5: LHC *beam*2 size in y at the AFP and ALFA stations for different β^* optics modes for nominal and low emittance.

β^*	$\sigma_{beam2}^{y,206}$ [mm]		$\sigma_{beam2}^{y,214}$ [mm]		$\sigma_{beam2}^{y,237}$ [mm]		$\sigma_{beam2}^{y,241}$ [mm]	
[m]	$\varepsilon = 2$	$\varepsilon = 3.75$	$\varepsilon = 2$	$\varepsilon = 3.75$	$\varepsilon = 2$	$\varepsilon = 3.75$	$\varepsilon = 2$	$\varepsilon = 3.75$
0.55	0.34	0.46	0.31	0.42	0.27	0.37	0.25	0.34
90	–	–	–	–	0.63	0.87	0.61	0.83
1000	–	–	–	–	0.22	0.30	0.22	0.30
2625	–	–	–	–	0.24	0.33	0.24	0.33

- the LHC coordinate system: curvilinear, right handed coordinate system (x, y, s). The local s-axis is tangent to the reference orbit at a given point of the beam trajectory. The two other axes are perpendicular to the reference orbit and are labelled x (in the bent plane) and y (perpendicular to the bent plane).

Apart from the Cartesian coordinate system, in ATLAS, the cylindrical coordinates are frequently used. The z axis points again along the beam, $r = \sqrt{x^2 + y^2}$ and $\phi = \tan^{-1}\left(\frac{y}{x}\right)$. The angle of an object with respect to the z axis is denoted θ, but in practice the pseudorapidity variable, $\eta = -\ln\left[\tan^{-1}\left(\frac{y}{x}\right)\right]$, is used more often. The alternative, momentum-based, definition of pseudorapidity is $\eta = \frac{1}{2}\ln\left(\frac{|\mathbf{p}|+p_z}{|\mathbf{p}|-p_z}\right)$, where p_z is the momentum along the beam axis. The region of $-\infty < \eta < 0$ is called the A side whereas the region of $0 < \eta < +\infty$ the C side. Protons circulating in beam 1 travel from A to C side whereas the ones in beam two in the opposite direction (see Figure 2.6).

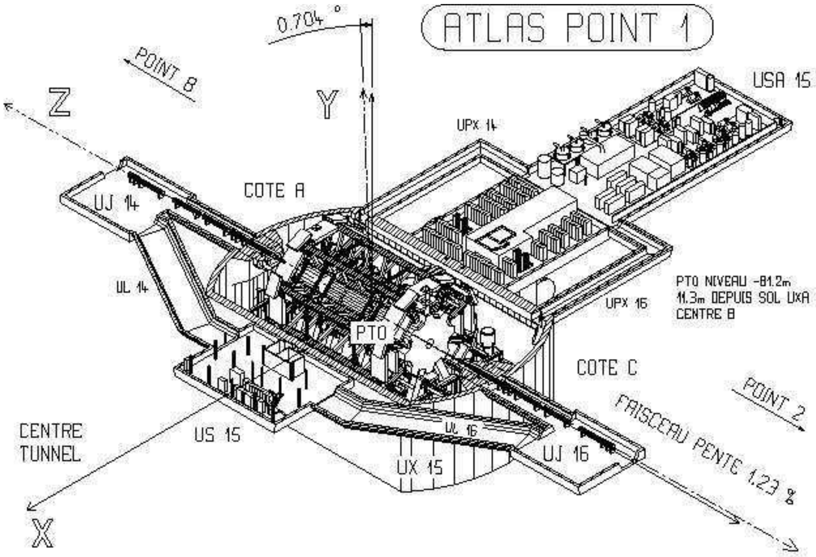

Figure 2.5: The ATLAS coordinate system.

The ALFA experimental set-up consists of four detector stations placed symmetrically with respect to the ATLAS IP at 237.4 m and 241.5 m. The stations on the A side (beam 2) are labelled A7L1 (first station; 237.4 m) and B7L1 (second; 241.5 m), whereas stations on the C side (beam 1) are labelled A7R1 (first station) and B7R1 (second station).

The trajectories in the nominal orbit trajectory reference frame for different proton energies for the $\beta^* = 0.55$ m optics are presented in Figure 2.7. It can be observed that the proton deflection in the x-axis direction (outside the LHC ring) and in the y-axis direction (towards the LHC floor) gets larger with decreasing proton energy *i.e.* with increasing proton relative energy loss defined as

$$\xi = 1 - E_{proton}/E_{beam}. \tag{2.2}$$

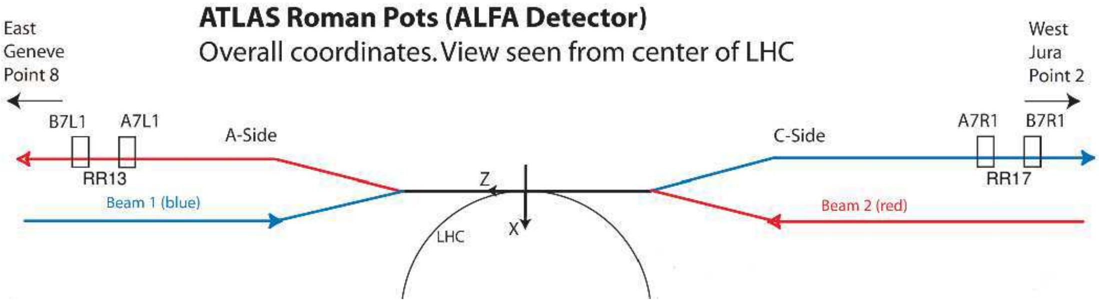

Figure 2.6: The ALFA detectors positions around the ATLAS Interaction Point.

When this deflection is large enough (*cf.* trajectory with $\xi = 0.16$) the proton interact with the LHC structures and is lost. The bent of the proton trajectory around the quadrupole triplet in Fig. 2.7(b) is due to non-zero value of the beam crossing angle.

The trajectories for different proton energies for the *high-*β^* optics are presented in Figure 2.8. These figures show that with increasing energy loss, the proton deflection in the x-axis direction increases. For distances below ~220 m this deflection is outside the LHC ring centre while above $s \approx 220$ m the orbits are bent in the opposite direction. This is different from the collision optics case (*cf.* Fig. 2.7(a)) where the proton trajectories are always bent outside the ring centre in the considered s range. One should also note that, at the distance between 160 m and 200 m, the trajectory reaches a maximum displacement from the nominal orbit and is weakly dependent with β^* value. For $s \approx 220$ m the displacement increases with the increasing value of the betatron function.
Due to the fact that the value of the crossing angle is set to zero in *high-*β^* optics modes, there is no deflection *w.r.t.* the nominal trajectory in the $(y,\ s)$ plane.

The trajectories of protons with nominal energy and different values of the p_x momentum component are plotted in Figures 2.9 and 2.10 for collision and *high-*β^* optic, correspondingly. In all optics modes the trajectories are focused after the AFP detectors location. This is not the case for the ALFA detectors and $\beta^* = 1000$ m optics.
In the case of collision optics the maximum deviation from the nominal orbit is in the Q3 quadrupole. For *high-*β^* optics this maximum is around Q3, Q5 and Q4 for $\beta^* = 90$, $\beta^* = 1000$ and $\beta^* = 2625$ m, respectively. It is worth noticing that the deviation increases with increasing β^*. One has to remember that each LHC element has different, defined size, thus the particles deviated too much from the nominal orbit will be lost in the aperture.

The proton behaviour at the nominal energy and different values of the p_y momentum component is shown in Figures 2.11 and 2.12 for collision and *high-*β^* optics, correspondingly. The maximum deviation in y from the nominal orbit is in Q2 and Q6 for collision and *high-*β^* optics, respectively. It is worth noticing that the presented LHC optics are designed in a way in which an increase of the β^* value causes the increase of the deviation from the nominal

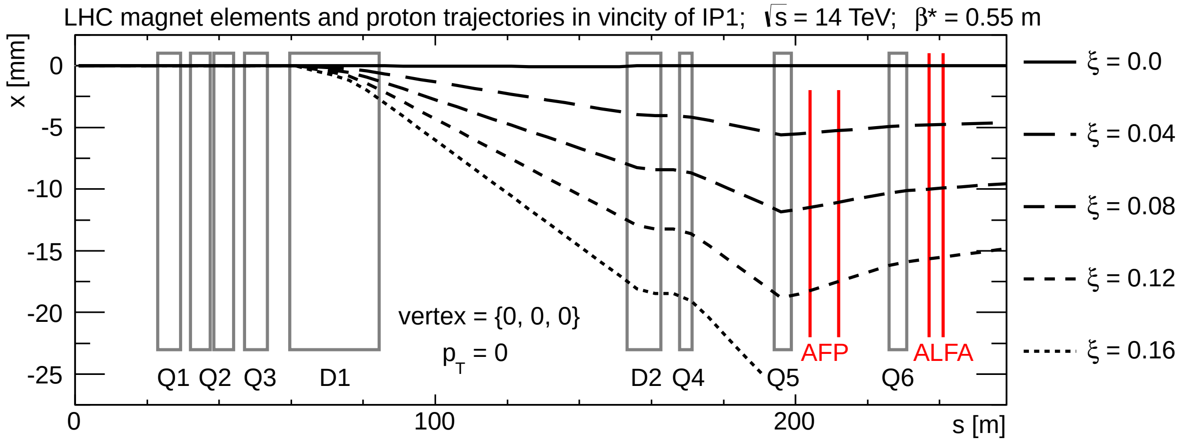

(a) $(x,\ z)$ plane

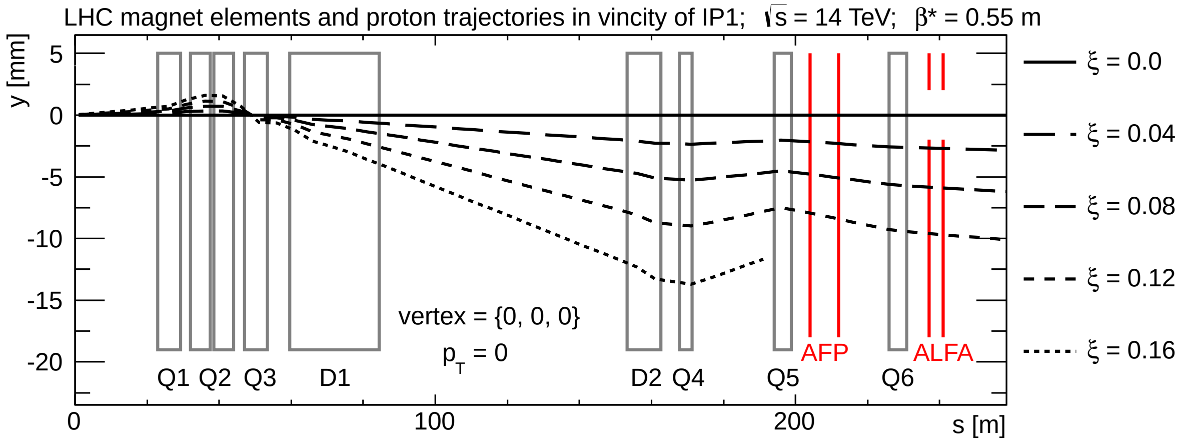

(b) $(y,\ z)$ plane

Figure 2.7: Energy dependence of the proton trajectory for collision ($\beta^* = 0.55$ m) optics at $\sqrt{s} = 14$ TeV. Protons were generated at (0, 0, 0) with transverse momentum $p_T = 0$. The half crossing angle in horizontal plane is equal to 142.5 μrad.

orbit around ALFA detectors location. This in turn implies the possibility of measuring lower p_y momenta which is the key point of ALFA physics programme [64].

From these plots one can conclude that protons scattered elastically can be visible in AFP and ALFA detectors. However, as can be seen from Figs 2.9 and 2.10, for the AFP stations the proton needs to have relatively large x-momentum component of about 2(2, 0.3) GeV for the $\beta^* = 0.55(90,\ 1000)$ m, correspondingly. For the $\beta^* = 2625$ m elastic protons will be visible only in the first AFP station. The situation is different for the ALFA detectors, which have limited acceptance in y. For the collision optics the elastic protons can be tagged once they have $p_y > 1$ GeV. The *high-*β^* optics gives access to lower values of transverse momentum – for the $\beta^* = 90(1000,\ 2625)$ m, a proton can be registered if it has p_y at least[1] of 40(30, 20) MeV.

As can be judged from Figure 2.7, for the collision optics AFP has larger acceptance than ALFA. In case of the *high*-β^* optics the diffractive protons are deflected inside(outside) the LHC ring centre at the AFP(ALFA) detectors position. The details about the ALFA and AFP geometric acceptances are discussed in details in Sections 2.2.6 and 2.2.7, correspondingly.

The behaviour of proton trajectories is a key point for measurements of diffraction with forward proton tagging. It has a direct impact on:

- kinematic region that is accessible for forward detectors (discussed in Section 2.2.6 and 2.2.7),
- energy and momentum reconstruction resolution (presented in Appendix B),
- particle showers creation.

---

[1] One has to remember that actual value is limited also by the distance at which the detector approaches the beam, as is discussed in Section 2.2.6.

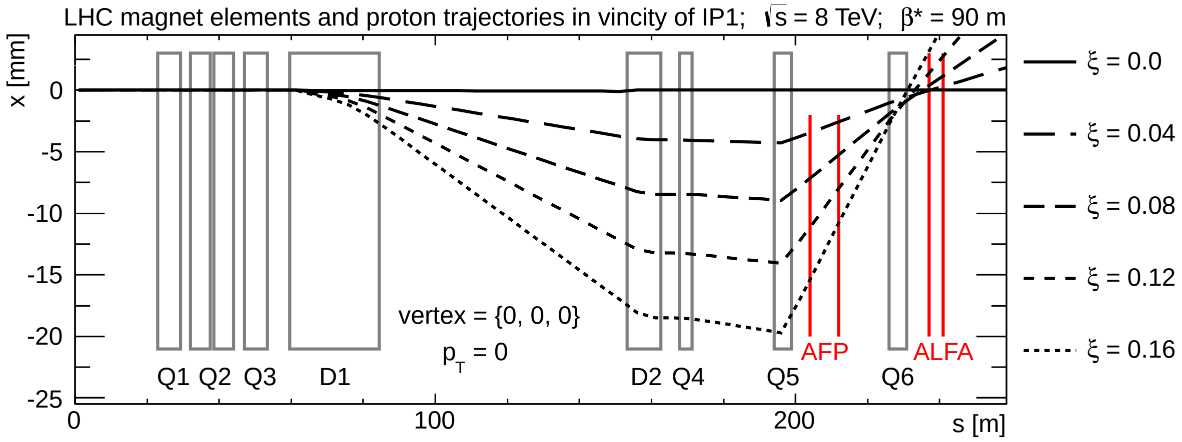

(a) $\beta^* = 90$ m

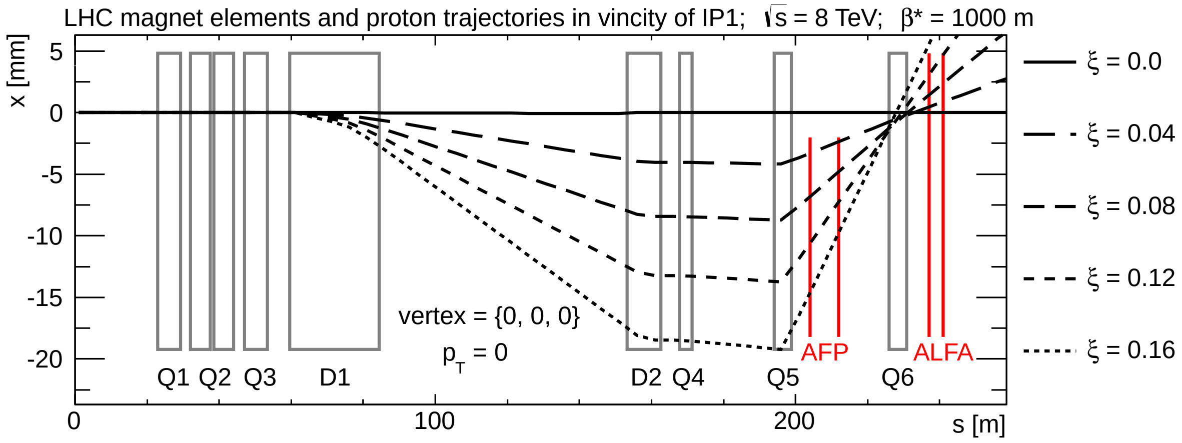

(b) $\beta^* = 1000$ m

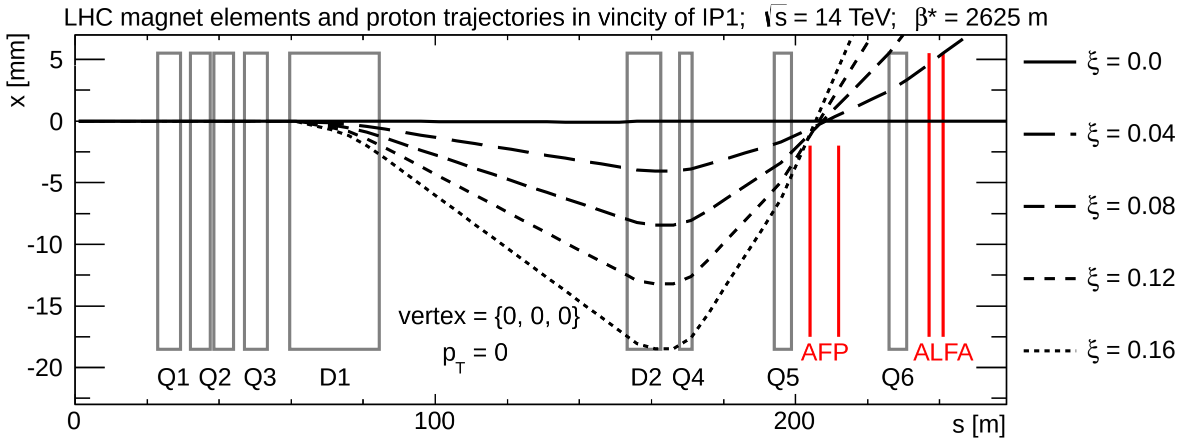

(c) $\beta^* = 2625$ m

Figure 2.8: Energy dependence of the proton trajectory for $\beta^* = 90$ m, 1000 m an 2625 m. Protons were generated at (0, 0, 0) with transverse momentum $p_T = 0$. The crossing angle is set to zero.

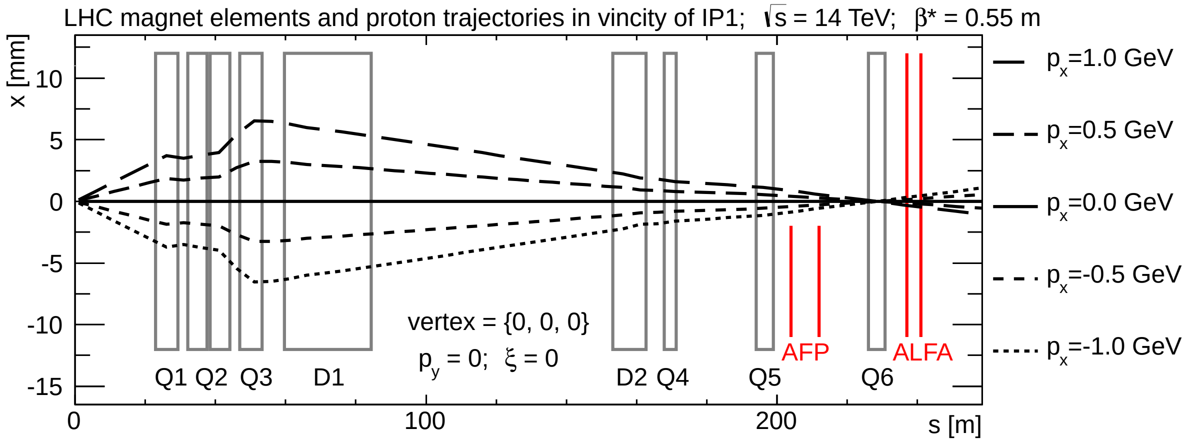

Figure 2.9: Transverse momentum dependence of the proton trajectory for collision optics. Protons were generated at (0, 0, 0) with different p_x momenta. The half crossing angle in horizontal plane is equal to 142.5 μrad.

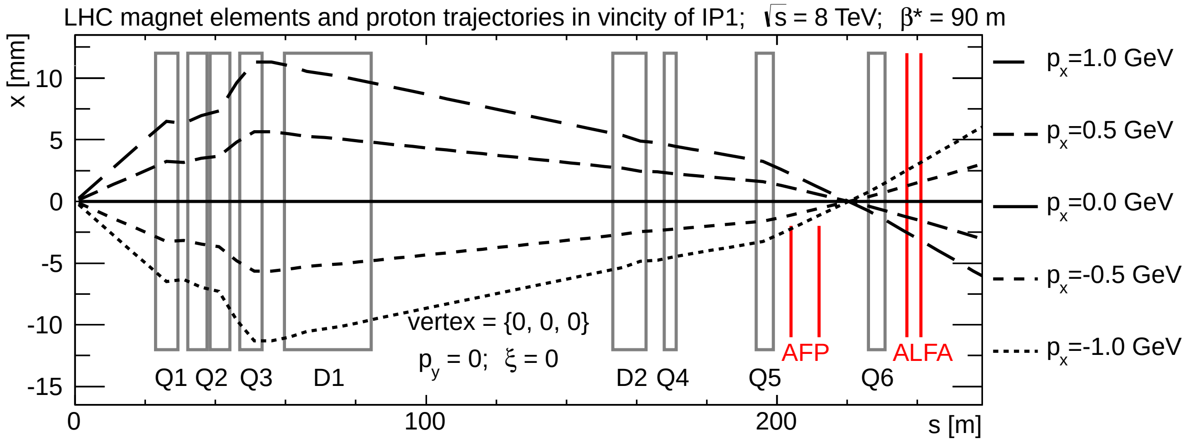

(a) $\beta^* = 90$ m

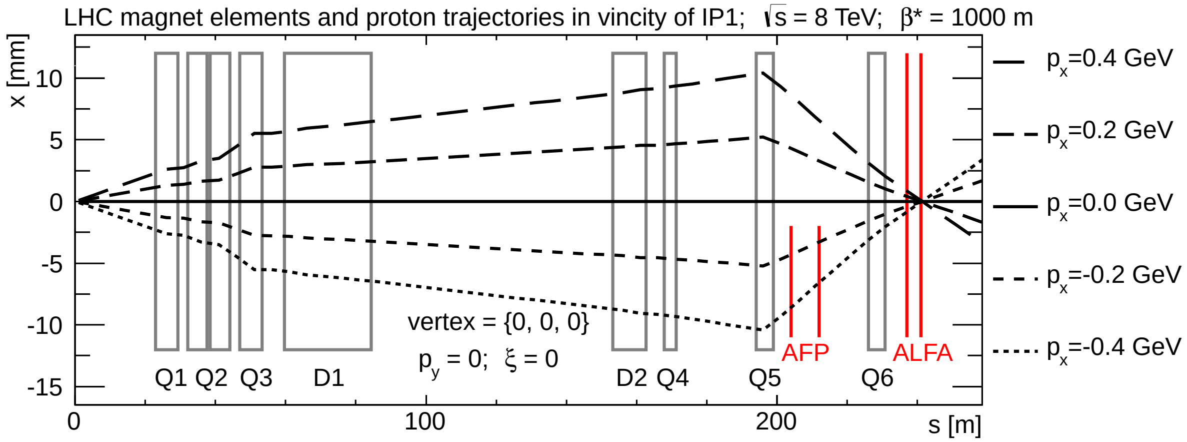

(b) $\beta^* = 1000$ m

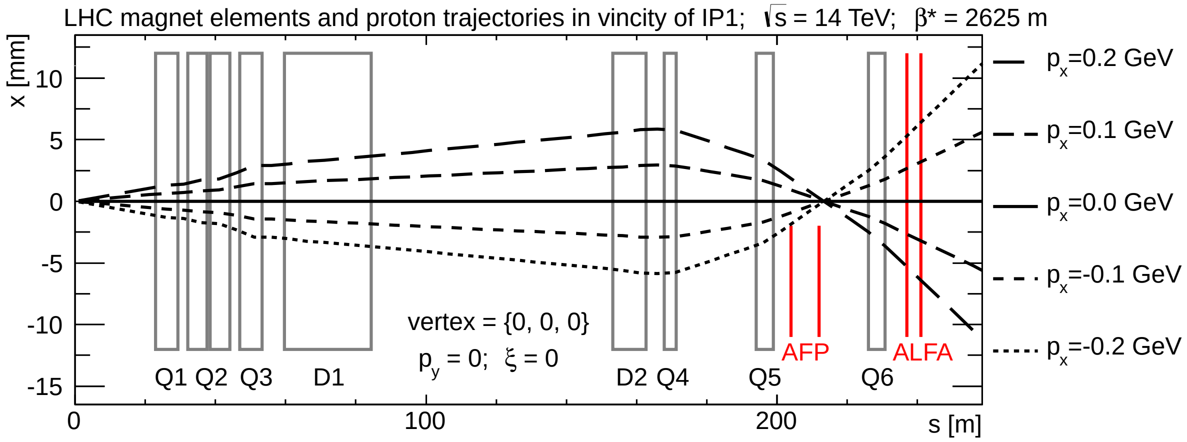

(c) $\beta^* = 2625$ m

Figure 2.10: Transverse momentum dependence of the proton trajectory for $\beta^* = 90$ m, 1000 m an 2625 m. Protons were generated at (0, 0, 0) with different p_x momenta. The crossing angle is set to zero.

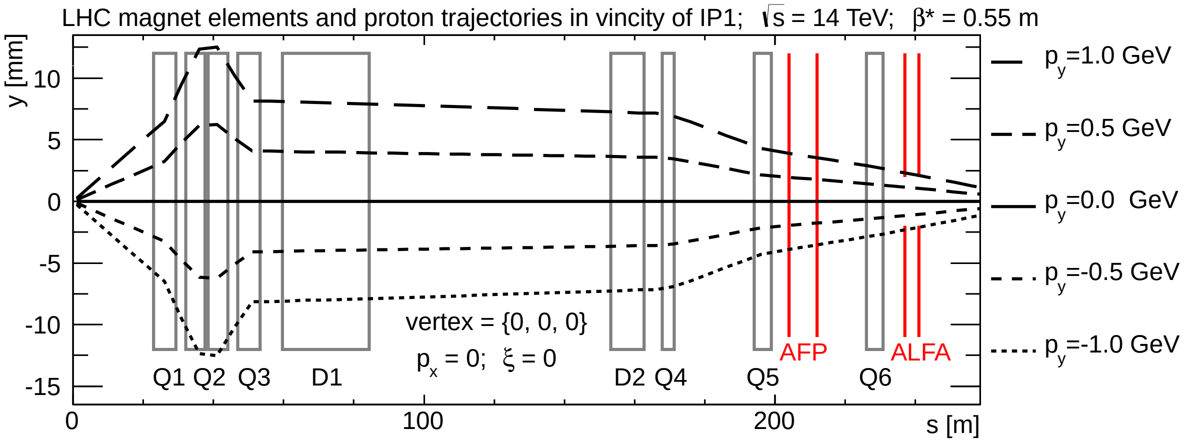

Figure 2.11: Transverse momentum dependence of the proton trajectory for collision optics. Protons were generated at (0, 0, 0) with different p_y momenta. The half crossing angle in horizontal plane is equal to 142.5 μrad.

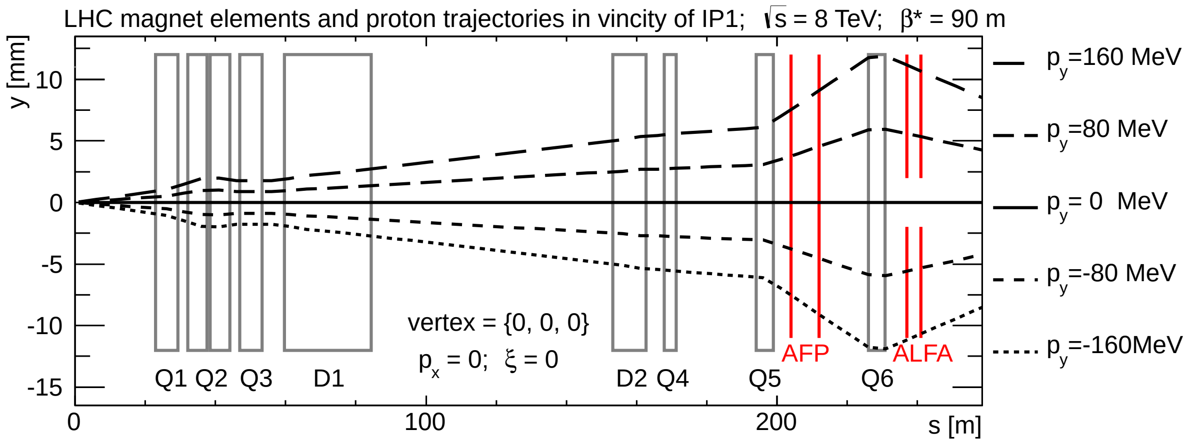

(a) $\beta^* = 90$ m

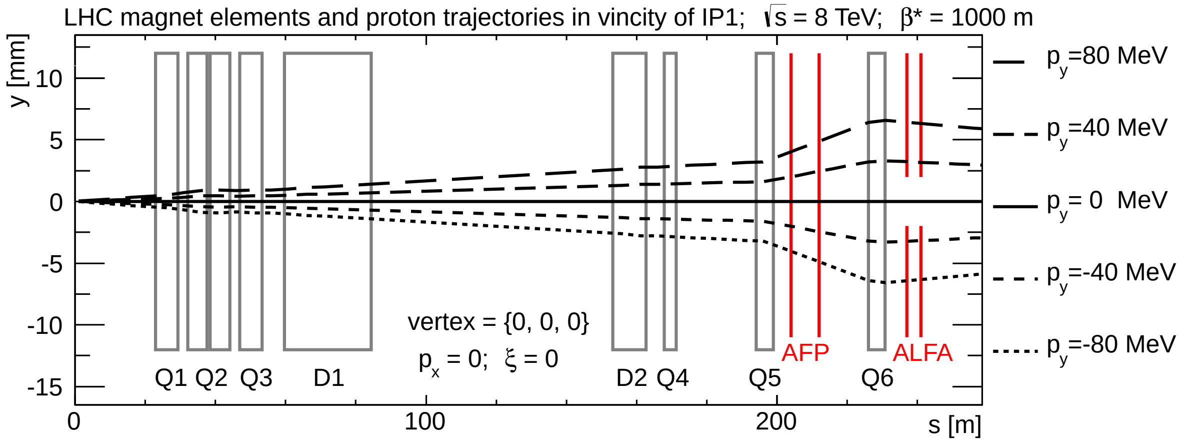

(b) $\beta^* = 1000$ m

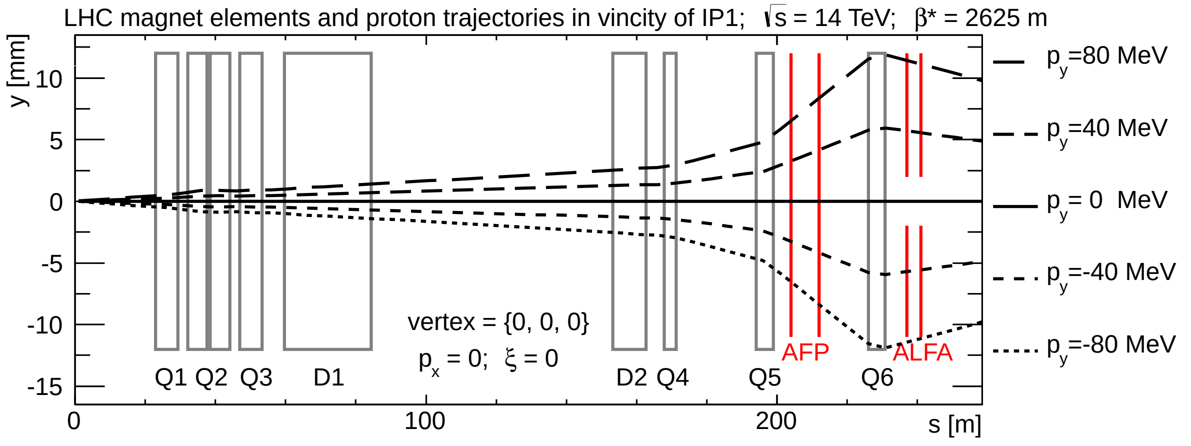

(c) $\beta^* = 2625$ m

Figure 2.12: Transverse momentum dependence of the proton trajectory for $\beta^* = 90$ m, 1000 m an 2625 m. Protons were generated at (0, 0, 0) with different p_y momenta. The crossing angle is set to zero.

2.2 The ATLAS Detector

The Large Hadron Collider was designed to extend the frontiers of particle physics with its high energy and luminosity, thus its detectors had to be fully operational in the environment of high interaction rates, radiation doses, particle multiplicities and energies. In consequence, the performance requirements of the ATLAS detector [57] were defined to face such conditions and to be able to encompass a range of possible Standard Model and new physics signatures that could be produced at the TeV scale. The ATLAS detector has been designed as a general purpose detector with a large acceptance in pseudorapidity, full azimuthal angle coverage, good charged particle momentum resolution and a good electromagnetic calorimetry completed by full-coverage hadronic calorimetry.

To achieve the performance goals, a design consisting of multiple detector sub-systems with cylindrical symmetry around the incoming beams was used (see Figure 2.13). Detectors closest to the Interaction Point are [57]: the Pixel Detector, the Silicon miCrostrip Tracker (SCT) and the Transition Radiation Tracker (TRT), collectively known as the Inner Detector (ID). The entire Inner Detector is immersed in a solenoidal magnetic field to allow precision momentum measurements of the charged particle tracks. The electromagnetic and hadronic calorimeters, placed outside the ATLAS solenoid magnet, perform the energy measurements. Furthest from the Interaction Point, a muon drift chambers perform muon identification and momentum measurements.

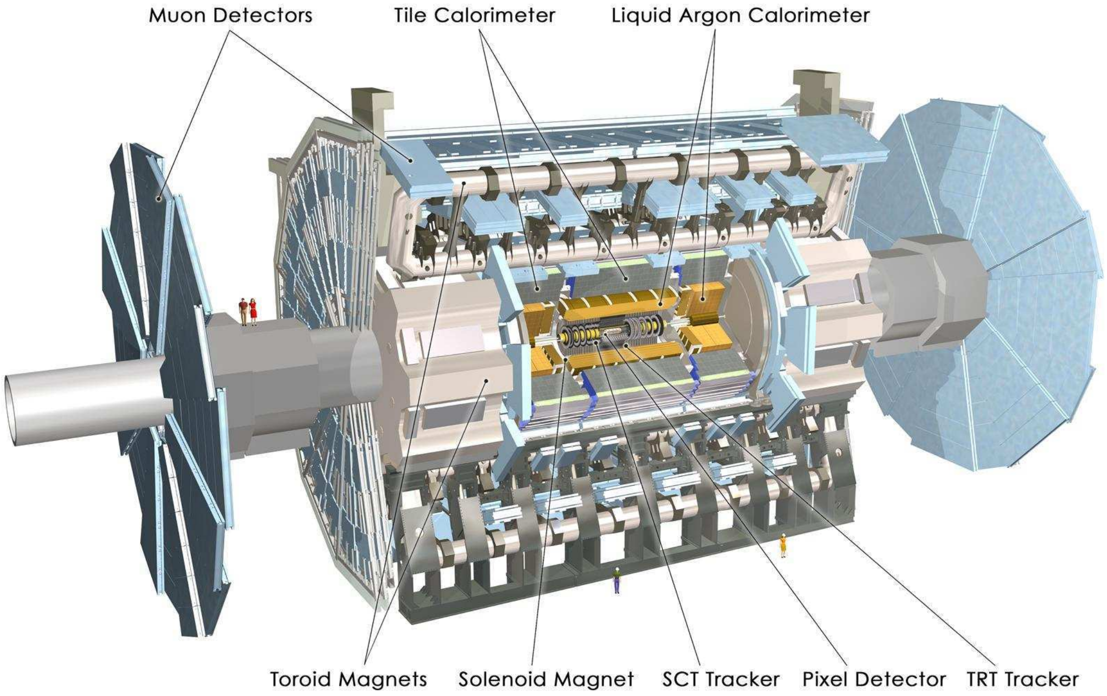

Figure 2.13: General scheme of the ATLAS main detector.

The ATLAS detector has a central, cylindrical part, called *the barrel* surrounding the Interaction Point, and *end-caps* closing it on both sides (*cf.* Fig. 2.15). Such a design provides both excellent measurement capabilities in the central region and a good coverage in the forward one.

2.2.1 Inner Detector

The purpose of the pixel, SCT, and TRT detectors [77, 78, 79] is to provide the charged particle trajectory and momentum reconstruction within a coverage of $|\eta| < 2.5$. All these detectors are composed of sensors that register signals (the so-called *hits*) in response to the passage of a charged particle. Since the whole Inner Detector is inside a 2 T solenoid magnet, the paths of charged particles are bent. The positions of the registered hits are combined to form tracks. At the designed LHC luminosity, the average of 1000 particles will be produced every 25 ns in the central region. Hence, the ID must have sufficient granularity to properly recognise all these tracks. Also, the designed momentum resolution is better than $\Delta p_T/p_T < 30\%$.

The overall layout of the Inner Detector is shown in Figure 2.14. The pixel, SCT, and TRT detectors are designed as concentric cylinders around the beam axis (barrel layers) and as disks perpendicular to the beam at both ends of the barrel (end-cap layers).

The pixel detector is installed closest to the Interaction Point – its innermost layer is ~ 5 cm far away from the beampipe axis. The pixel detector has a total length of 1300 mm and a radius of 150 mm. It is composed of 1744 silicon sensors, with dimensions of $19 \times 63 \times 0.250$ mm^3. Each sensor has 46 080 readout channels and each channel is connected to a pixel size of either 50×400 μm^2 or 50×600 μm^2. This yields about 80 million readout channels in total – an order of magnitude more than in the rest of the ATLAS subsystems. The sensors are placed on three barrel and three end-cap layers, producing typically three pixel position measurements per charged particle track. In practice, a charged particle traversing the sensor will induce some charge in a group of neighbouring pixels forming a *cluster*. Information about the clusters (with an assumption of a perfect knowledge of the pixel sensor positions within the ATLAS geometry) gives a position accuracy of the reconstructed object of $\sim$10 μm in $r - \phi$ plane and 115 μm along z and r in the barrel and end-caps, respectively.

The next-closest to the Interaction Point detector is the SCT. It consists of four barrel layers and nine end-cap layers surrounding the pixel detector, resulting in at least four hits for the charged particle track. Its innermost layer is ~ 25 cm far away from the beams. The SCT barrel has a length of 1500 mm and the radius of 515 mm. The SCT end-caps extend this range to $z \approx \pm 2720$ mm and a radius of $r \approx 560$ mm. There are 15 912 SCT sensors, each of them is $\sim$12.8 cm long and $\sim$285 μm thick. To improve the position resolution, the sensors are stacked back-to-back, with the bottom sensor rotated by 40 mrad with respect to the top one. The SCT detector provides a resolution of 17 μm in $r - \phi$ plane and 580 μm in z and r in the barrel and end-caps, correspondingly.

The TRT is the ID component installed the furthest from the Interaction Point. The TRT sensors are thin drift tubes consisting of cathode metal straws with a diameter of 4 mm, filled

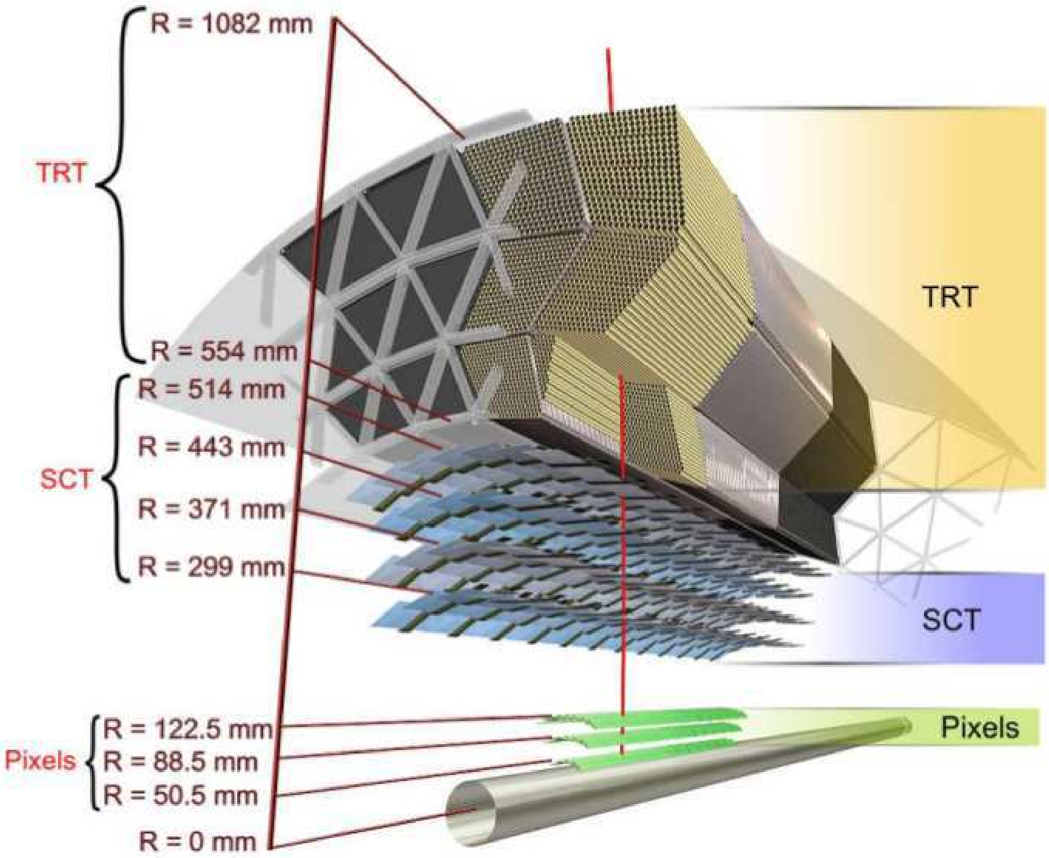

(a) barrel part

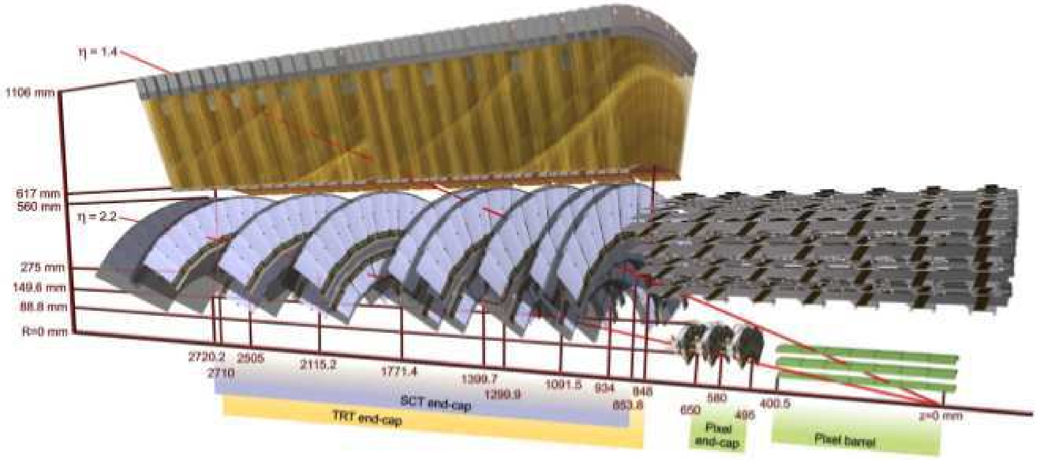

(b) end-cap part

Figure 2.14: General scheme of the a) barrel and the b) end-cap part of the ATLAS Inner Detector.

with a gas mixture of xenon, oxygen, and carbon dioxide, with an anode wire running through the center of the straw. The passage of a charged particle through the gas produces ions and free electrons which, due to the applied electric voltage, travel to the cathode and anode, correspondingly. The comparison of the time that the signals are received at the cathode and the anode gives a drift time measurement. In addition, consecutive layers of straws are separated by foils. Charged particles crossing the foil produce transition radiation, which enhances the signal produced by the particle in the gas. The amount of transition radiation depends on the Lorentz γ factor of a particle and can be used to distinguish electrons from pions, kaons and other heavier particles. The TRT straws are arranged in one barrel cylinder with a length of 1420 mm and a radius of 1060 mm. The two end-cap cylinders extend that reach to $z = \pm 2710$ mm with $r \approx 1000$ mm. There are about 351 000 readout channels in the TRT. To obtain the optimal reconstruction resolution of the particle trajectories the straws lie along the beam direction in the barrel and radially in the end-caps. The maximum drift time is ≈ 48 ns and the detector accuracy is up to 130 μm along the straw radius.

2.2.2 Calorimeters

The ATLAS calorimeters [80, 81] are located around the Inner Detector and the solenoid magnet. The purpose of the calorimeter system is to measure the energy of electrons, photons and hadrons. The calorimeter system consists of electromagnetic (EM) and hadronic (HAD) calorimeters. The EM calorimeters provide a fine measurement of electrons and photons. Since the hadronic calorimeters are designed to capture the full energy of high-momentum jets, their granularity is worse. All ATLAS calorimeters are segmented in both transverse and perpendicular directions to give information about particle position and cascade. The calorimeter system also delivers fast, rough position and energy measurements to serve as trigger signals for photons, electrons, jets, and missing transverse energy. As can be seen from the overall view presented in Figure 2.15, the ATLAS calorimetry system consists of:

- the Liquid Argon (LAr) electromagnetic barrel (EMB),
- the LAr electromagnetic end-cap (EMEC),
- the LAr hadronic end-cap (HEC),
- the LAr forward calorimeter (FCal),
- Tile barrel (central region),
- Tile extended barrel (forward).

The EM calorimeter uses lead as the absorber and liquid argon as the active material. An electron (or positron) travelling through the absorber can interact with it producing photons or charged particles. A photon traversing the absorber interacts with the material via Compton scattering, photo-electric effect or pair production. The produced particles

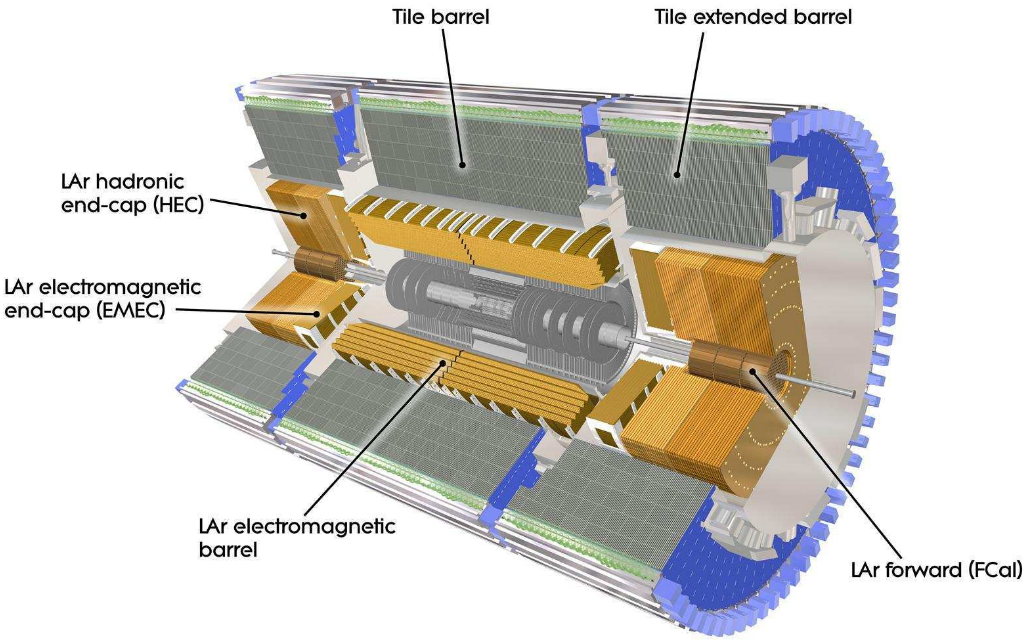

Figure 2.15: General scheme of the ATLAS calorimeters.

ionize the liquid argon. The induced charge is collected by electrodes located in the LAr gap. The position resolution of the EM calorimeter is driven by the readout geometry, consisting of rectangular cells in $\eta - \phi$ space. There are three layers of these cells, segmented along the particles direction of motion. A schematic view of an EM barrel slice is shown in Figure 2.16.

The tile calorimeter is composed of 3 mm thick scintillating tiles laid parallel to the incoming particle direction, interleaved with 14 mm thick iron plates, as shown in Figure 2.17. The LAr hadronic end-cap and the forward calorimeter are made of copper and tungsten absorbers, correspondingly.

The forward calorimeter system provides both electromagnetic and hadronic measurements. It is composed of three modules from which the first one is electromagnetic and the latter ones are hadronic calorimeters. The EM layer is composed of 18 vertical copper plates separated by liquid argon gaps. These plates are punctuated with 12 260 holes containing co-axial copper rods and tubes, aligned along the z axis, that act as electrodes. The hadronic layers consist of two copper end-plates, bridged by copper tubes and filled with liquid argon. The electrode rods are made of tungsten.

In front of the forward calorimeter the Minimum Bias Trigger Scintillator (MBTS) system was installed. These detectors are mainly used to form the trigger signals corresponding to minimum bias events during low-luminosity data taking. They consist of two sets of 16 scintillating counters, covering the pseudorapidity region of $2.09 < |\eta| < 3.84$.

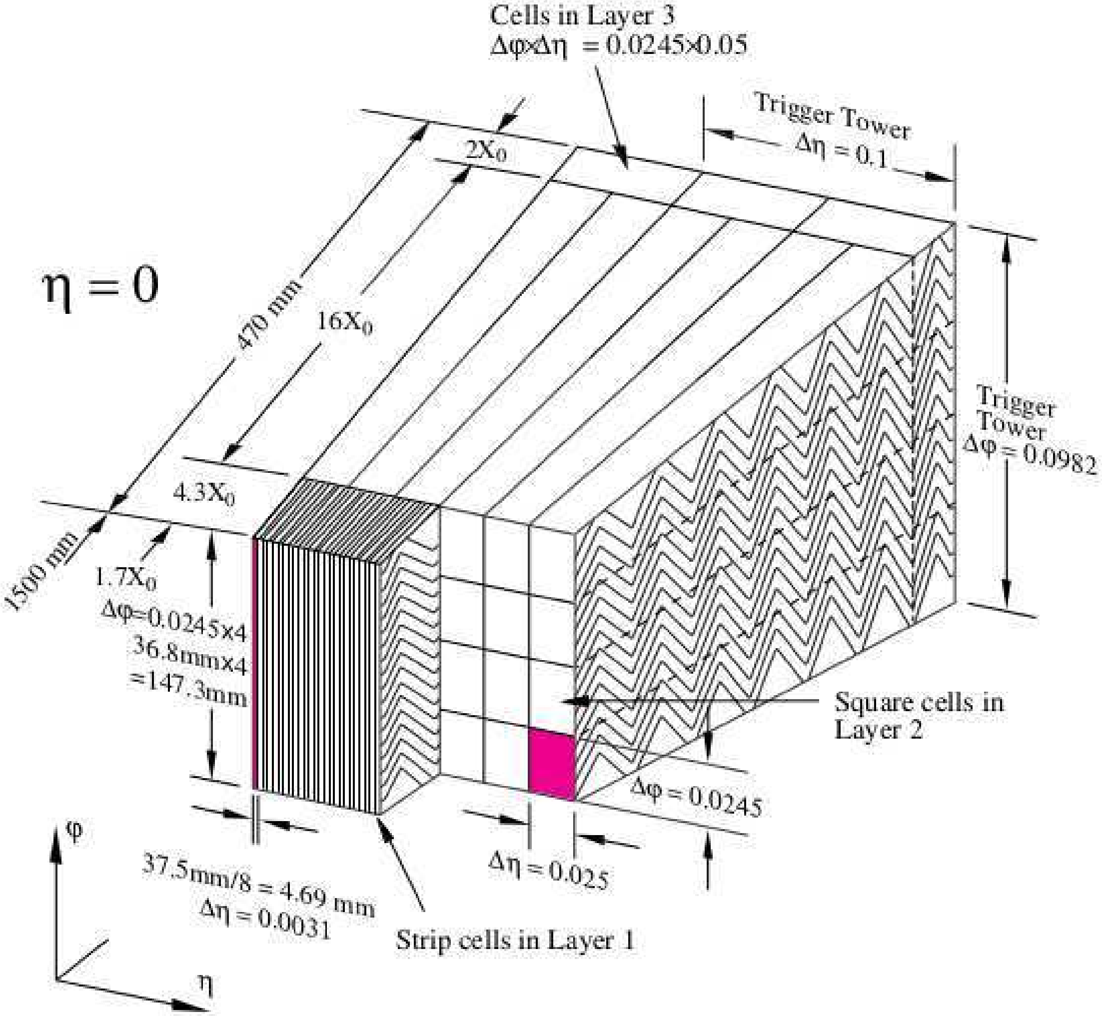

Figure 2.16: Sketch of a barrel module of the calorimeter where the different layers are clearly visible with the ganging of electrodes in ϕ. The granularity in η and ϕ of the cells of each of the three layers and of the trigger towers is also shown. From [57].

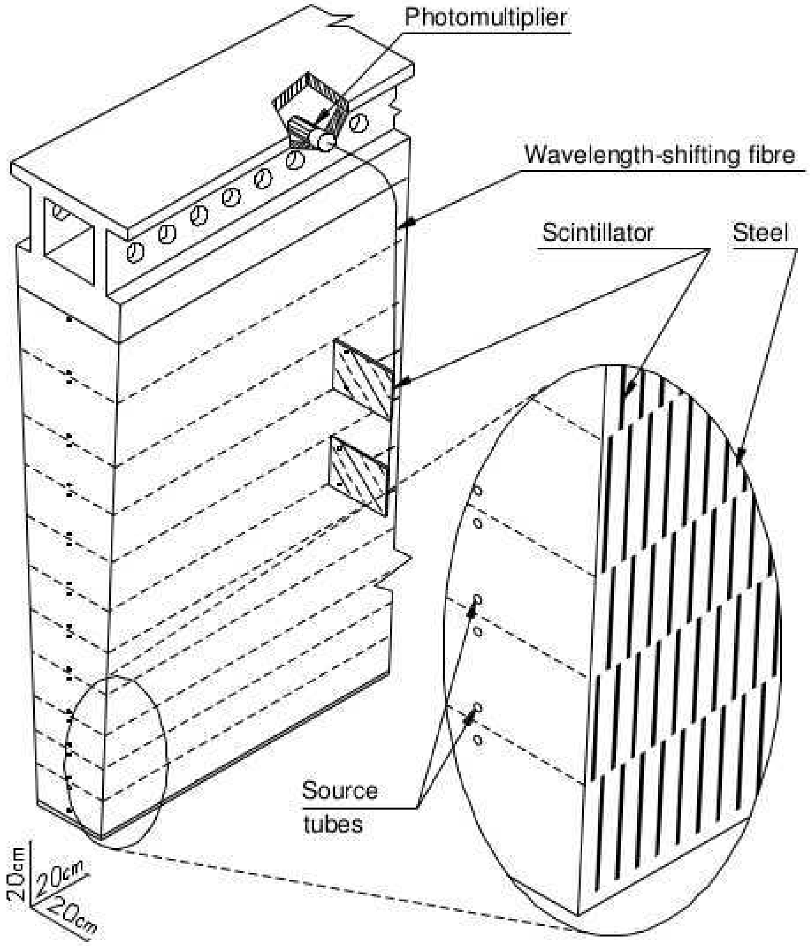

Figure 2.17: Schematic view showing how the mechanical assembly and the optical readout of the tile calorimeter are integrated together. The various components of the optical readout, namely the tiles, the fibres and the photomultipliers, are shown. From [57].

The resolution for electromagnetic and hadronic calorimeters is presented in Figure 2.18 whereas their main parameters are listed in Table 2.6

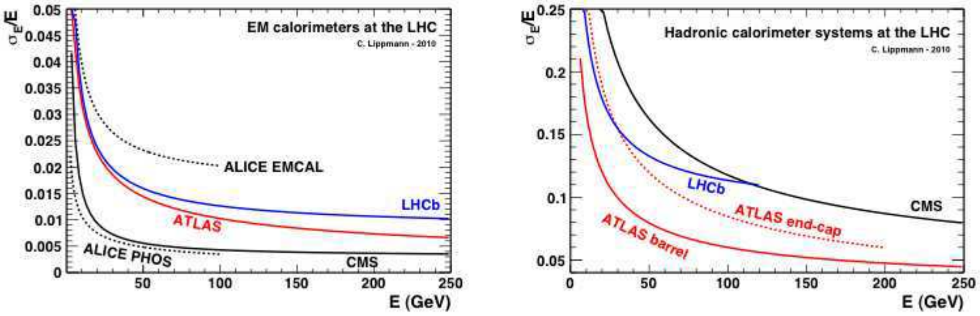

Figure 2.18: Comparison between the ATLAS, CMS, ALICE and electromagnetic (**left**) and hadronic (**right**) calorimeter performances. CMS has better electromagnetic calorimeters than ATLAS while having worse hadronic ones.

2.2.3 Muon System

Muons have much smaller cross section to interact in material than electrons or hadrons, therefore they usually penetrate the calorimeters. The muon system is designed to detect charged particles within $|\eta| < 2.7$ that were not absorbed before. The muon detectors are optimized to provide a momentum measurement with a relative resolution ranging from 3% for muons with transverse momentum of order of GeV to 10% for the ones having p_T of abut 1 TeV.

To provide a momentum measurement a toroidal magnetic field is applied. This field is provided by eight barrel coils toroids and two end-cap with eight coils each. Due to this field, the muon path is deflected in the (r, z) plane. The muon system is the largest of all the ATLAS sub-detectors, covering a radius from ~ 4.5 m to ~ 12.5 m. It consists of four sub-detectors: Monitored Drift Tube chambers (MDT), Cathode Strip Chambers (CSC), Resistive Plate Chambers (RPC) and Thin Gap Chambers (TGC). Its layout is shown in Figure 2.19.

The MDT detector is designed to provide precision momentum measurements. It is built in a technology similar to the one in which the TRT was constructed, with straws filled with Ar/CO$_2$ gas. This detector consists of: three cylindrical shells with radius of 5, 7.5 and 10 m and two disks perpendicular to the beam axis around each end-cap toroids at 7.5 and 21.5 m. The pseudorapidity coverage is $|\eta| < 2.7$.

The main task of the CSC detector is to provide an additional momentum measurement in the pseudorapidity region of $2.0 < |\eta| < 2.7$ in which the rate of particles might be too high to be handled by the MDT sub-system alone. The CSC detector consists of multi-wire proportional chambers constructed from two parallel metal sheets with one plane of parallel

Table 2.6: Main parameters of the ATLAS calorimeter system. From [57].

	Barrel		End-cap	
EM calorimeter				
Number of layers and $\lvert\eta\rvert$ coverage				
Presampler	1	$\lvert\eta\rvert < 1.52$	1	$1.5 < \lvert\eta\rvert < 1.8$
Calorimeter	3	$\lvert\eta\rvert < 1.35$	2	$1.375 < \lvert\eta\rvert < 1.5$
	2	$1.35 < \lvert\eta\rvert < 1.475$	3	$1.5 < \lvert\eta\rvert < 2.5$
			2	$2.5 < \lvert\eta\rvert < 3.2$
Granularity $\Delta\eta \times \Delta\varphi$ versus $\lvert\eta\rvert$				
Presampler	0.025×0.1	$\lvert\eta\rvert < 1.52$	0.025×0.1	$1.5 < \lvert\eta\rvert < 1.8$
Calorimeter 1st layer	$0.025/8 \times 0.1$	$\lvert\eta\rvert < 1.40$	0.050×0.1	$1.375 < \lvert\eta\rvert < 1.425$
	0.025×0.025	$1.40 < \lvert\eta\rvert < 1.475$	0.025×0.1	$1.425 < \lvert\eta\rvert < 1.5$
			$0.025/8 \times 0.1$	$1.5 < \lvert\eta\rvert < 1.8$
			$0.025/6 \times 0.1$	$1.8 < \lvert\eta\rvert < 2.0$
			$0.025/4 \times 0.1$	$2.0 < \lvert\eta\rvert < 2.4$
			0.025×0.1	$2.4 < \lvert\eta\rvert < 2.5$
			0.1×0.1	$2.5 < \lvert\eta\rvert < 3.2$
Calorimeter 2nd layer	0.025×0.025	$\lvert\eta\rvert < 1.40$	0.050×0.025	$1.375 < \lvert\eta\rvert < 1.425$
	0.075×0.025	$1.40 < \lvert\eta\rvert < 1.475$	0.025×0.025	$1.425 < \lvert\eta\rvert < 2.5$
			0.1×0.1	$2.5 < \lvert\eta\rvert < 3.2$
Calorimeter 3rd layer	0.050×0.025	$\lvert\eta\rvert < 1.35$	0.050×0.025	$1.5 < \lvert\eta\rvert < 2.5$
Number of readout channels				
Presampler	7808		1536 (both sides)	
Calorimeter	101760		62208 (both sides)	
LAr hadronic end-cap				
$\lvert\eta\rvert$ coverage			$1.5 < \lvert\eta\rvert < 3.2$	
Number of layers			4	
Granularity $\Delta\eta \times \Delta\varphi$			0.1×0.1	$1.5 < \lvert\eta\rvert < 2.5$
			0.2×0.2	$2.5 < \lvert\eta\rvert < 3.2$
Readout channels			5632 (both sides)	
LAr forward calorimeter				
$\lvert\eta\rvert$ coverage			$3.1 < \lvert\eta\rvert < 4.9$	
Number of layers			3	
Granularity $\Delta x \times \Delta y$ (cm)			FCal1: 3.0×2.6	$3.15 < \lvert\eta\rvert < 4.30$
			FCal1: ~ four times finer	$3.10 < \lvert\eta\rvert < 3.15$, $4.30 < \lvert\eta\rvert < 4.83$
			FCal2: 3.3×4.2	$3.24 < \lvert\eta\rvert < 4.50$
			FCal2: ~ four times finer	$3.20 < \lvert\eta\rvert < 3.24$, $4.50 < \lvert\eta\rvert < 4.81$
			FCal3: 5.4×4.7	$3.32 < \lvert\eta\rvert < 4.60$
			FCal3: ~ four times finer	$3.29 < \lvert\eta\rvert < 3.32$, $4.60 < \lvert\eta\rvert < 4.75$
Readout channels			3524 (both sides)	
Scintillator tile calorimeter				
	Barrel		Extended barrel	
$\lvert\eta\rvert$ coverage	$\lvert\eta\rvert < 1.0$		$0.8 < \lvert\eta\rvert < 1.7$	
Number of layers	3		3	
Granularity $\Delta\eta \times \Delta\varphi$	0.1×0.1		0.1×0.1	
Last layer	0.2×0.1		0.2×0.1	
Readout channels	5760		4092 (both sides)	

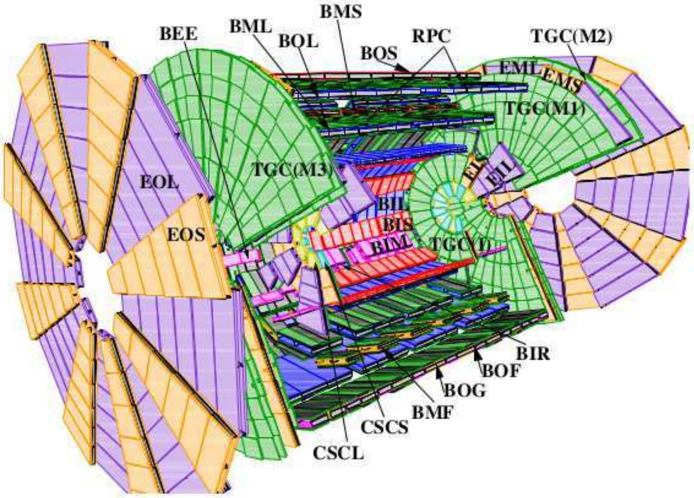

Figure 2.19: Configuration of the muon spectrometer with its four chamber sub-systems: the precision-measurement tracking chambers (MDTs and CSCs) and the trigger chambers (RPCs and TGCs). In the end-cap, the first TGC layer (I) is located in front of the innermost tracking layer; the next three layers stand in front (M1) and behind (M2 and M3) the second MDT wheel. The first letter (B and E) of the MDT naming scheme refers to barrel and end-cap chambers. The second and third letters refer to layer (inner, middle, and outer) and sector (large and small) types, respectively.

wires running in between. The sheets are segmented into cathode strips in such a way that one sheet has strips aligned parallel and the other perpendicular to the direction of the wires. To minimize the multiple scattering effect, the planes are made of a light polyurethane foam with thin copper coats on each surface acting as electrodes. The chambers are filled with Ar/CO_2 gas.

The RPC and TGC detectors are constructed to deliver trigger signal. It uses signal from three cylindrical layers around the beam axis, with two RPC detectors on each, covering the pseudorapidity range of $|\eta| < 1.05$. The RPCs are constructed from two resistive plates separated by 2 mm of ionizing gas.

The goal of the TGC detector is to extend the muon trigger to the rapidity range of $1.05 < |\eta| < 2.4$. It is composed of multi-wire proportional chambers formed by two metal plates, segmented into readout strips, with a plane of parallel metal wires in between.

The main parameters of ATLAS muon detectors are listed in Table 2.7.

2.2.4 Forward Detectors

ATLAS is equipped with several forward detectors that monitor collision conditions, provide instantaneous luminosity estimates and measure particles scattered at large angles. There are three existing forward detectors [57]: LUminosity measurement using Cerenkov Integrating Detector (LUCID), Zero Degree Calorimeter (ZDC) and Absolute Luminosity For ATLAS

Table 2.7: Main parameters of the ATLAS muon system. From [57].

		Chamber resolution (RMS) in			**Measurements/track**		**Number of**	
Type	**Function**	z/R	ϕ	time	barrel	end-cap	chambers	channels
MDT	tracking	35 μm (z)	—	—	20	20	1088 (1150)	339k (354k)
CSC	tracking	40 μm (R)	5 mm	7 ns	—	4	32	30.7k
RPC	trigger	10 mm (z)	10 mm	1.5 ns	6	—	544 (606)	359k (373k)
TGC	trigger	2–6 mm (R)	3–7 mm	4 ns	—	9	3588	318k

(ALFA) [64]. Their locations with respect to the ATLAS IP are shown in Figure 2.20. There is also a plan to install additional proton detectors at 210 and 420 m – the ATLAS Forward Proton (AFP) stations [11]. LUCID and ZDC are briefly described below whereas ALFA and AFP are discussed in details in Sections 2.2.6 and 2.2.7, respectively.

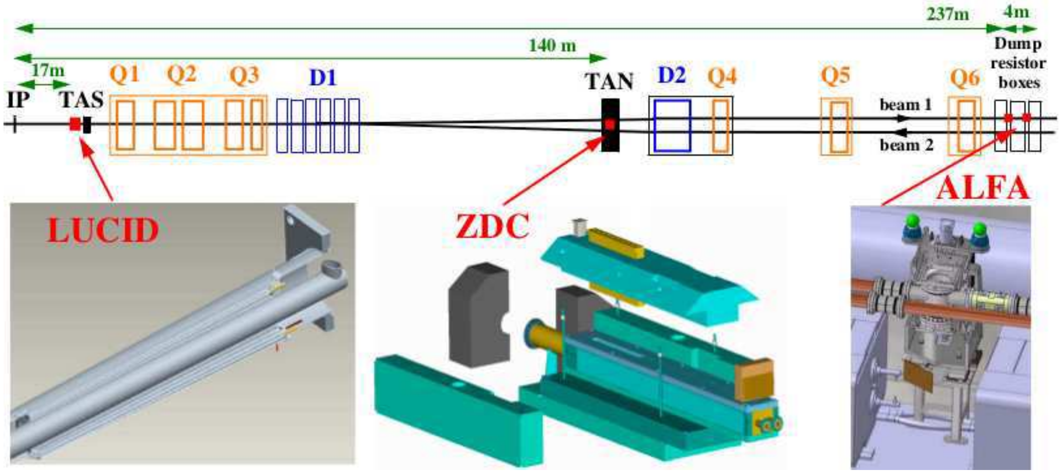

Figure 2.20: Position of the forward detectors along the beam-line around the ATLAS Interaction Point.

The main task of LUCID is to give information about the relative luminosity via the measurement of the inelastic low-p_T proton-proton scattering. This idea is based on the fact that the number of detected particles is proportional to the total number of interactions in a bunch crossing. The LUCID detector is located at $z = \pm 17$ m. It is composed of ten aluminium tubes located on each side of the Interaction Point, surrounding the beampipe and pointing towards it. Each tube is each filled with C_4F_{10} gas.

The two main goals of the ZDC are: detecting neutral particles scattered at very large rapidities and providing a trigger to ATLAS. This detector is located at $z = \pm 140$ m. It is composed of one electromagnetic and two hadronic calorimeter modules. ZDC was dismounted for proton-proton data taking period in the year 2012 and reinstalled for the heavy ion run in the year 2013.

The pseudorapidity range of all ATLAS detector subsystems is plotted in Fig. 2.21.

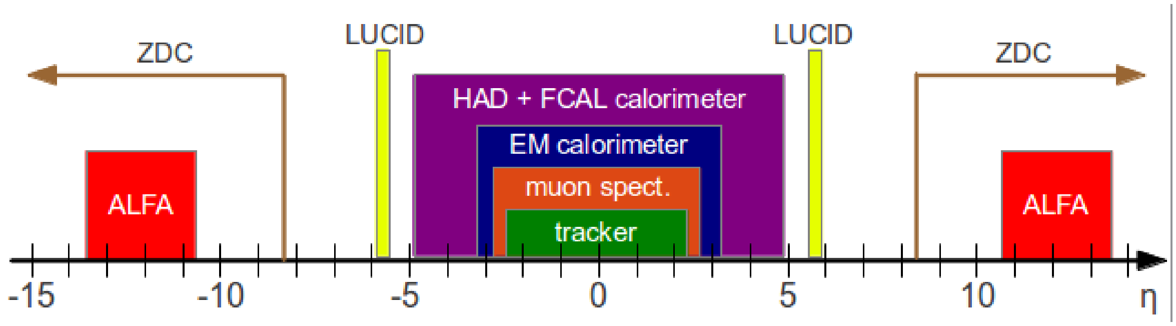

Figure 2.21: Pseudorapidity coverage of ATLAS detectors.

2.2.5 Data Acquisition and Trigger

The foreseen collision rate at the LHC is $\sim$ 40 MHz. With an average ATLAS event size of 2.5 MB, this is far more than what can be stored in the existing resources. Therefore, all major LHC experiments use the trigger system to recognise and save interesting physics events, while rejecting a vast majority of uninteresting ones. The ATLAS trigger is a three stage system:

- a hardware-based Level 1 trigger (L1),
- a software-based Level 2 trigger (L2),
- an event filter (EF).

The goal of the L1 trigger is to reduce the 40 MHz collision rate to 75 kHz by recognising interesting physics events and rejecting others. The L2 trigger is responsible for further reduction to 3.5 kHz and the EF to the rate of few hundred of Hz. The L2 and EF triggers are known collectively as the High-Level Trigger (HLT).

The L1 trigger is designed to accept high-p_T objects like muons, electrons, photons and jets, as well as events with large missing transverse energy (MET) or energy sum. It uses signals from the TGC and RPC detectors for muon triggers and calorimeter information for electron, photon, jet, tau and total energy triggers. Additionally, there are several minimum bias triggers based on signals coming from the MBTS, ZDC, LUCID or ALFA and several zero bias triggers based on random signals.

The Central Trigger Processor (CTP) combines informations from different trigger objects and makes the final trigger decision. This decision includes possible applications of the so-called *prescale*[2], which is an additional rejection factor necessary to reduce the rate of certain high-frequency triggers. The Timing and Trigger Control (TTC) system distributes this decision, along with the 40 MHz clock signal, to the individual sub-detector readouts.

---

[2] Prescale = keep event only every n^{th} event.

While waiting for the L1 decision, the detectors store information in their front-end electronics boards. If an event is accepted, a selected information is moved to the L2 processors while the full one is sent to the Readout Buffers. If an event is rejected by the L1 trigger, the whole information is erased.

The L2 trigger applies additional energy thresholds and multiplicity requirements using the so-called *Regions of Interest* (RoI) around the triggered L1 objects. If the L2 trigger is satisfied, the event information is sent to the EF processing farms, else the contents of the Readout Buffers are discarded.

The EF makes decisions based on fully-reconstructed events including the full information from the Inner Detector. It consists of a processing farm running standard ATLAS event reconstruction and analysis software [82]. Events that are accepted by the EF are moved to the CERN permanent storage. The event information at the EF level is stored at the GRID ([83], a global computer network dedicated to a scientific usage) in the byte-stream format known as the RAW data. These data are grouped according to the trigger streams and typically associated according to common trigger objects. For example, the L1CALO was an early trigger stream that grouped all events that passed any level-1 calorimeter trigger requirement, whereas the JETMET one collects any events that pass jet or missing transverse energy HLT.

At Tier 0 the RAW data are converted to an object-oriented data format using the standard ATLAS reconstruction software – the ATHENA [82] framework. The reconstructed data are stored in several formats (with different levels of detail and sizes) on Tier 1 and Tier 2 computing facilities located all over the world. The most detailed format is called the Events Summary Data (ESD). However, since for many analyses the complete information is not necessary, a more convenient data format – Derived Physic Data (D3PD) – is commonly used. Data are accessible trough the GRID.

2.2.6 The ALFA Detector

The main goal of the ALFA detector is to give information about the absolute luminosity via the measurement of the elastic proton-proton scattering in the Coulomb-nuclei interference region [64]. Since, in this region, the four-momentum transfer is small ($|t| \sim 0.00065$ GeV^2) the protons are scattered at very small angles, typically in a range of few micro radians. This requires, apart of the special LHC optics as discussed in Section 2.1.2, that the detectors have to be installed far away (typically hundreds of meters) from the Interaction Point and as close to the beam as possible. It is worth noticing that, apart from the elastic measurement, ALFA also allows to detect diffractivelly scattered protons.

The measurement of the absolute luminosity is based on the fact that the rate of elastic scattering is related to the total interaction rate through the optical theorem, which states that the total cross section (σ_{tot}) is directly proportional to the imaginary part of the forward elastic scattering amplitude (f_{el}) at zero momentum transfer:

$$\sigma_{tot} = 4\pi \cdot Im\left(f_{el}|_{t=0}\right),$$

where at small angles:

$$-t = (p\theta)^2.$$

The rate of elastic scattering at small t values can be written as:

$$\left.\frac{dN}{dt}\right|_{t=0} = L\pi|f_C + f_N|^2 \approx L\pi\left|-\frac{2\alpha_{EM}}{|t|} + \frac{\sigma_{tot}}{4\pi}(i+\rho)\exp\left(\frac{-b|t|}{2}\right)\right|^2, \tag{2.3}$$

where f_C corresponds to the Coulomb and f_N to the strong (nuclear) interaction amplitude and ρ is defined as:

$$\rho = \left.\frac{Re\ f_{el}}{Im\ f_{el}}\right|_{t\to 0}.$$

One has to note that Equation 2.3 is oversimplified, since *e.g.* the proton form factors were omitted.

To be able to approach the beam as close as possible, the Roman Pot technique [64, 84] was used. The Roman Pot concept is based upon a detector volume (the pot) that is separated from the vacuum of the accelerator by a thin window and connected with bellows which allow the insertion into the beampipe. This idea is illustrated in Figure 2.22. The design assumes that the detectors could be moved as close as 1 mm to the beam in the vertical direction in order to collect data. A schematic view of the ALFA Roman Pot is shown in Figure 2.23.

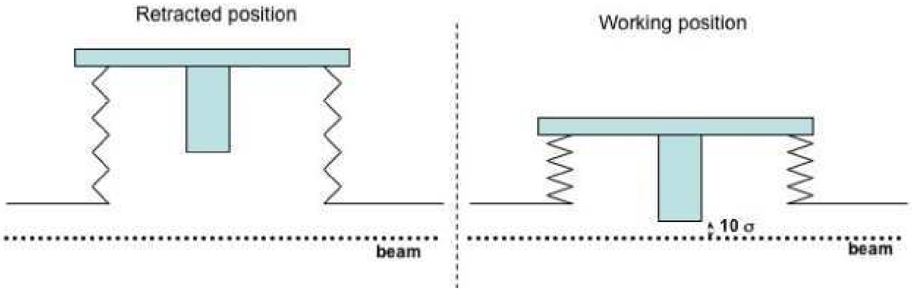

Figure 2.22: Roman Pot concept: on the left the retracted position is shown where the pot is in parking position, whereas on the right – in working position, 10 σ close from the beam centre, where σ is a Gaussian width of the beam.

The ALFA experimental set-up consists of four detector stations placed symmetrically with respect to the ATLAS IP at 237.4 m and 241.5 m. In each station there are two Roman Pot devices. The stations on the A side (beam 2) are labelled A7L1 (first station; 237.4 m) and B7L1 (second; 241.5 m), whereas stations on the C side (beam 1) are labelled A7R1 (first station) and B7R1 (second station). This set-up is illustrated in Figure 2.6.

The main requirements for the ALFA detectors are:

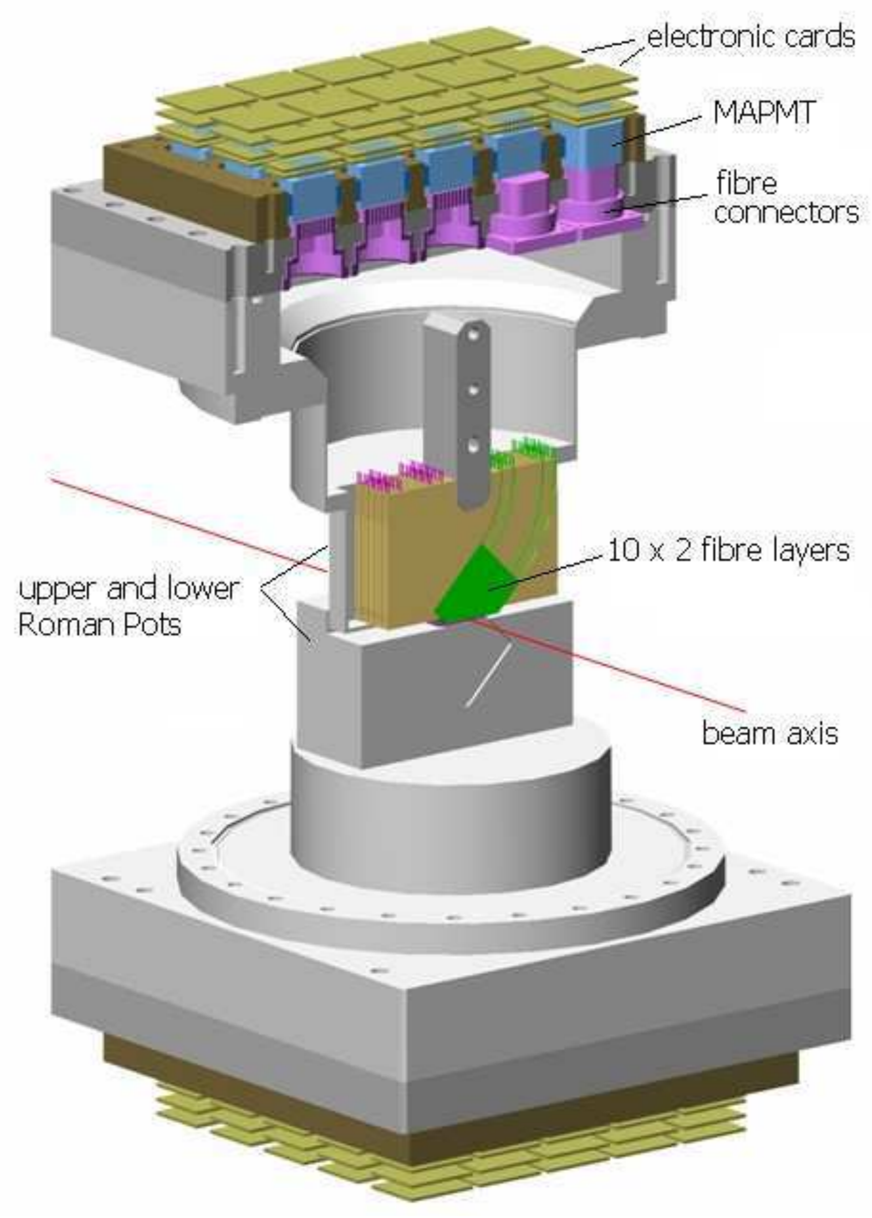

Figure 2.23: Schematic layout of the ALFA detector in the Roman Pot showing the scintillating fibre stack, the fibre connectors, the multi-anode photomultipliers and the front-end boards. The Roman pots approach the beam from above and below.

- a spatial resolution of 30 μm [3],
- no significant inactive edge region, to be as close to the beam as possible,
- minimal sensitivity to the radio-frequency noise from the LHC beams.

The ALFA detectors were built using the scintillating fibre tracker technology. Since the detectors are planned to be used only during the special LHC runs in which the instantaneous luminosity will be low, the applied technology is not radiation-hard.

In order to fulfil the spatial resolution requirements, the detector consists of ten double-sided modules with 64 fibres in each. The modules are arranged in the $U - V$ geometry, as explained in Fig. 2.24. The fibres have a diameter of 0.5 mm, thus the effective area of the detector is about 32×32 mm^2. The modules are staggered in depth by multiples of a tenth of the effective fibre pitch, *i.e.* 70 μm. The fibres are aligned and glued on a precisely machined support structure made of titanium. Before the assembly, the fibres were aluminised to reduce the light losses and optical cross-talk.

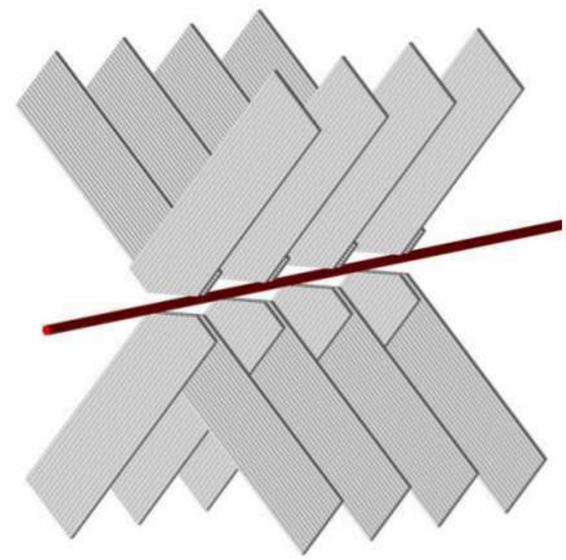

Figure 2.24: Principle of a scintillating fibre detector with 4 planes in $U - V$ geometry. The active area is limited to the overlap region of the fibre layers.

To achieve an accurate alignment of the fibre tracker with respect to the centre of the beam, the Roman Pots are equipped with the Overlap Detectors (OD) – the special interleaved extrusions, yielding a vertical overlap area when in beam position. These extrusions are instrumented with three layers of vertically staggered detectors consisting of 30 horizontally oriented fibres in each layer.

---

[3] This value has to be considerably smaller than the spot size of the beam (130 μm for $\beta^* = 2625$ m) at the detector location.

The detectors are instrumented with two optically separated trigger scintillator tiles providing a fast L1 trigger signal. In addition, single trigger tiles are used in each of the overlap extrusions.

Geometric Acceptance

For all measurements which are possible to be done using the ALFA detectors, it is important to understand the dependence of the scattered proton trajectory position in the detector on its energy and momentum. This is illustrated in Figure 2.25 for various β^* settings. This figure shows the positions of elastically and diffractively scattered protons with various transverse momenta in the detector plane at the detector locations. The detector shape is shown in solid lines. For the collision optics (Fig. 2.25 a) one can observe the following:

- the elastically scattered protons ($\xi = 0$) with small transverse momentum do not reach the detector active area,
- diffractively scattered protons ($\xi \neq 0$) have negative value of x, *i.e.* they fly outside the LHC ring,
- negative values of y are due to the non-zero beam crossing angle at the IP.

This picture changes with increasing β^* (see Fig. 2.25 b – d). In the case of elastically scattered protons, more and more particles with small transverse momentum values reach the detector as β^* increases. A change of a picture is also seen for the protons scattered diffractivelly:

- proton trajectories are bent towards the LHC ring centre and observed at positive x values,
- the centres of the ellipses have $y = 0$ (due to the fact that the beam crossing angle is equal to zero),
- for high β^* optics the impact of the p_y-momentum component at the IP on the proton position at the detector plane is much larger than that due to p_x.

For all considered optics settings the higher the proton relative energy loss is, the higher is its deflection in the ring plane.

The energy and the transverse momentum ranges of the protons that can be registered by the ALFA detectors are central to physics analysis. They depend on the geometrical acceptance of the whole system. Obviously, not all scattered protons can be measured in ALFA. A proton can be too close to the beam to be detected or it can hit the LHC element (a collimator, the beam pipe, a magnet) upstream the ALFA station. The geometric acceptance is defined as the ratio of the number of protons of a given relative energy loss (ξ) and transverse momentum (p_T) that reached the ALFA station to the total number of the scattered protons

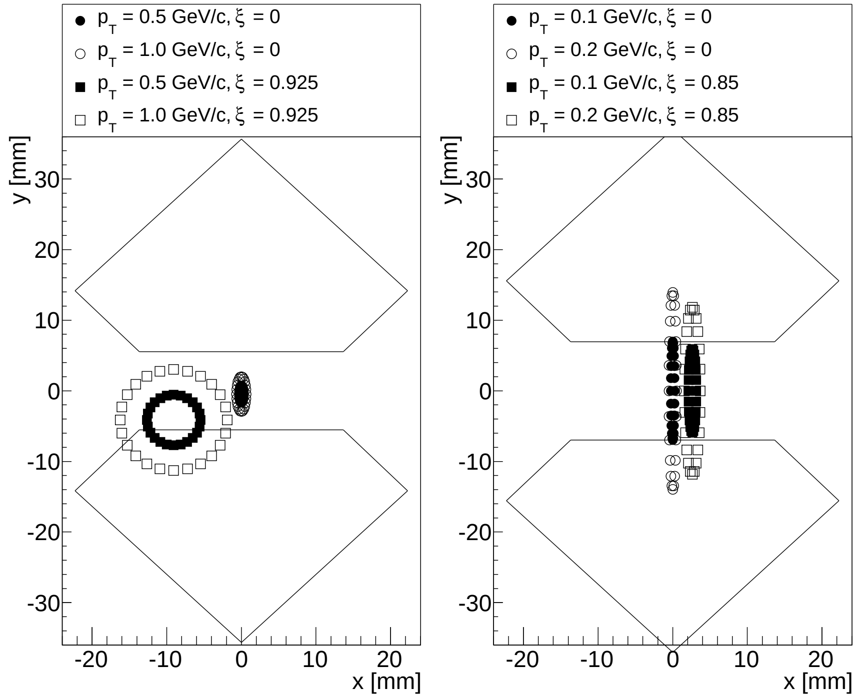

(a) $\beta^* = 0.55$ m

(b) $\beta^* = 90$ m

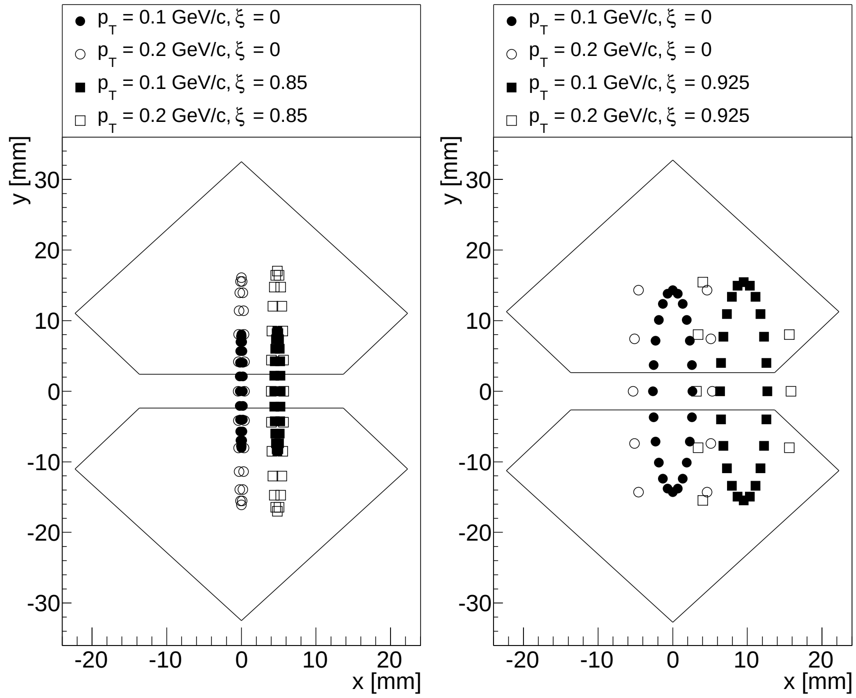

(c) $\beta^* = 1000$ m

(d) $\beta^* = 2625$ m

Figure 2.25: Proton positions with different relative energy loss (ξ) and transverse momentum (p_T) at the first ALFA station for the different LHC high β^* optics settings. The solid lines mark the ALFA detector active area.

having ξ and p_T. In the calculations, the beam properties at the IP, the beam chamber geometry and the LHC lattice magnetic properties were taken into account. Such calculations result the LHC filtering ability of the scattered protons at a given optics conditions. The outcome for different LHC optics is shown in Figure 2.26. One can see that the scattered protons reaching the ALFA stations can have quite large energy loss whereas, except for the $\beta^* = 0.55$ m case, their transverse momentum is not high.

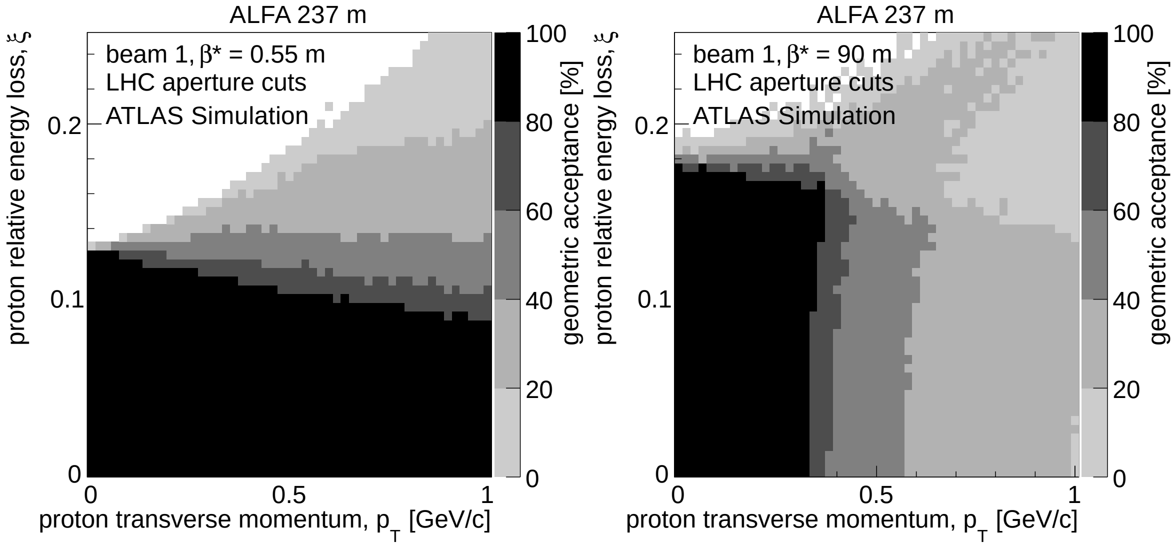

(a) $\beta^* = 0.55$ m (b) $\beta^* = 90$ m

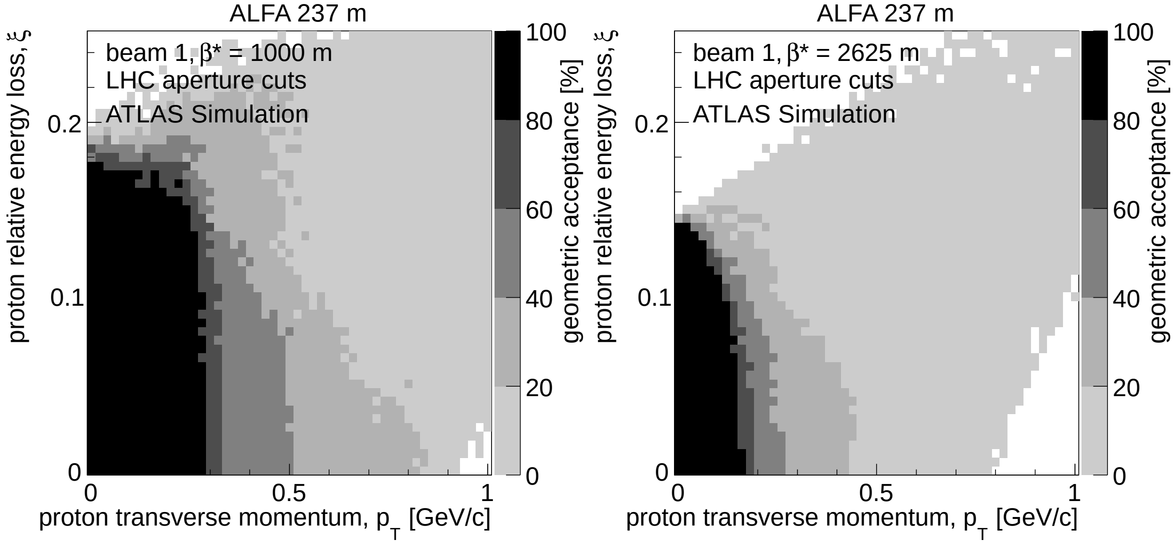

(c) $\beta^* = 1000$ m (d) $\beta^* = 2625$ m

Figure 2.26: LHC filtering ability as a function of the proton relative energy loss (ξ) and its transverse momentum (p_T) for different LHC optics settings. The beam properties at the IP and the beam chamber geometry were taken into account (see text).

An additional requirement that a proton is registered in the detector leads to the detector geometrical acceptance. It has to be stressed that it very strongly depends on the distance between the beam centre and the detector edge as was studied in *eg.* [1]. This distance is directly connected with the beam size at the detector location (see Tables 2.2 – 2.5). Since the ALFA detectors approach the beam from the top and the bottom, only the y component is meaningful. The geometric acceptance for different β^* optics is presented in Figure 2.27. The distance from the beam centre was set to 15 σ in the case of collision optics and to 8 σ for the *high*-β^* ones, where σ is the Gaussian width of the beam.

For collision optics, the region of high acceptance (above 80%) is limited by $p_T < 0.1$ GeV and $0.11 < \xi < 0.13$. This shows that in the runs using such machine tune the elastic events practically cannot be observed. However, the diffractively scattered protons can be registered if the energy loss is large enough. It is worth mentioning that in this configuration protons with transverse momentum $p_T = 0$ can be measured.

In the case of *high*-β^* optics, the protons scattered elastically are well within the detector geometrical acceptance. One should also note that the limit on the minimum value of the proton p_T is decreasing with β^* increasing. In other words, the higher the β^* is, the smaller t values are reachable, as shown in Figure 2.28.

Energy and Momentum Reconstruction Resolution

In the vast majority of physics analyses using the ALFA detectors the important variables are the proton energy and transverse momentum after interaction. These values can be obtained using several different methods. In this thesis the parametrisation and unfolding procedure, described in details in Appendix B, is used.

Below, the precision of the momentum and energy reconstruction that can be obtained for different LHC optics is studied. As for the input, a sample of single diffractive dissociation events, generated with PYTHIA 8 MC generator [85], was used. The vertex was Gaussian smeared in the (x, y, z) coordinates to reflect the beam size at the IP. The width of the Gaussian distribution was taken accordingly to the width of the beam for a given optics settings – see Table 2.1. The final state forward protons were transported to the ALFA stations using the FPTRACKER [86, 87] program. Their positions at the ALFA detector station were smeared in order to take into account the detectors spatial resolution of 30 μm in x and y. In addition, the multiple scattering effect of 0.6 μrad was taken into account [4].

The multiple scattering effect reflects the fact that a charged particle traversing a medium is deflected by many small-angle scatters. The Coulomb scattering distribution is well described by the Molière theory [88, 89]. The angular spread at which particle is scattered can be calculated using the following formula [90]:

$$\theta_0 = \frac{13.6\ \text{MeV}}{\beta c p} z \sqrt{x/X_0}\left[1 + 0.038 \ln(x/X_0)\right], \tag{2.4}$$

---

[4] This value corresponds to the scattering on 2×300 μm of stainless steel plus 20 layers of scintillating fibres and one trigger scintillator.

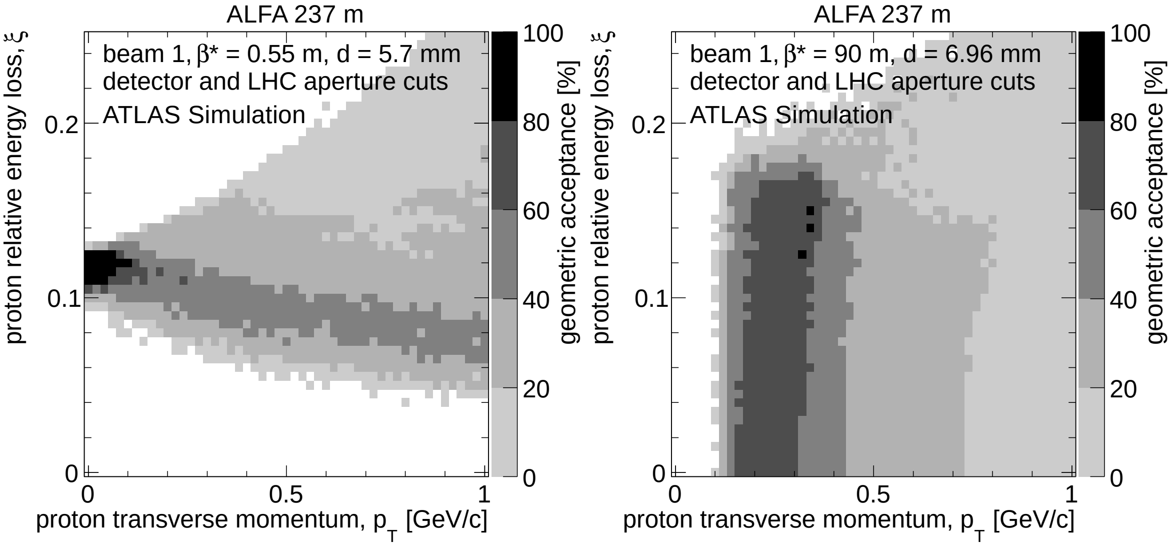

(a) $\beta^* = 0.55$ m (b) $\beta^* = 90$ m

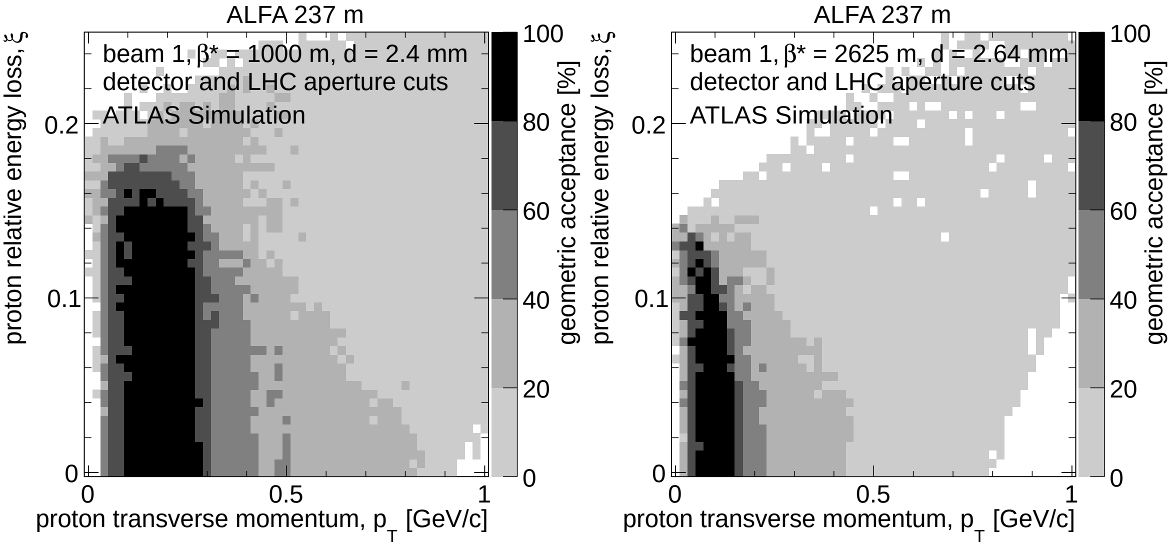

(c) $\beta^* = 1000$ m (d) $\beta^* = 2625$ m

Figure 2.27: Geometrical acceptance of the ALFA detector as a function of the proton relative energy loss (ξ) and its transverse momentum (p_T) for different LHC optics settings. The beam properties at the IP, the beam chamber and the detector geometries, the distance between the detector edge and the beam centre were taken into account (see text). This distance was set to 15σ for collision optics and to 8σ for *high-*β^* ones ($\varepsilon = 3.75$ μm·rad was assumed).

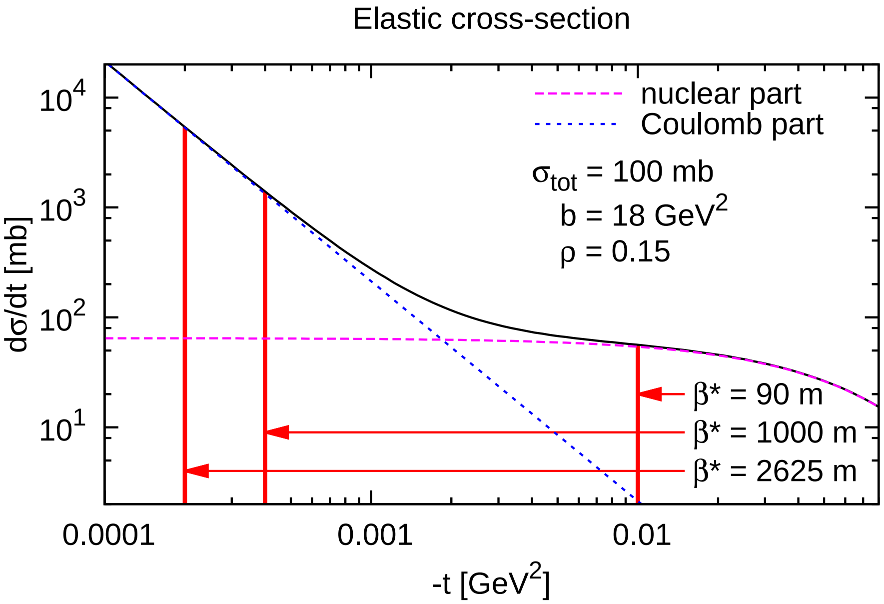

Figure 2.28: Elastic cross section as a function of t. The expected t values reachable for a given β^* are plotted.

where p, βc and z are the momentum, velocity and charge number of incident particles, and x/X_0 is the thickness of the scattering medium in the radiation length units. The radiation length is defined as a path at which a particle loses $1/e$ of its energy.

Each effect mentioned above influences the reconstructed variables. Their individual contributions as well as the overall effect on the energy and momentum reconstruction are shown in Figure 2.29 and 2.30 for ξ and t, respectively.

In the case of collision optics ($\beta^* = 0.55$ m), the dominating uncertainty in the energy reconstruction (Fig. 2.29 a) comes from the detector spatial resolution. The multiple scattering effect and the lack of knowledge about the interaction vertex position are negligible. The reconstruction resolution increases linearly from 15 GeV for $\xi = 0.04$ to 30 GeV for $\xi = 0.14$. The lower limit on ξ of 0.04 comes from the detector geometric acceptance. For $\beta^* = 90$ m (Fig. 2.29 b) the overall reconstruction resolution is almost evenly due to the vertex smearing effect and the detector spatial resolution uncertainty. Contrary to the collision optics, the reconstruction resolution decreases with the increase of the proton relative energy loss – for $\xi = 0$ it is about 40 GeV whereas for $\xi = 0.14$ it is of about 20 GeV. In the case of $\beta^* = 1000$ m (Fig. 2.29 c) the main contribution comes from the lack of knowledge about the vertex. The reconstruction resolution distribution is roughly flat and about 55 GeV. Such a flat distribution is also present in the case of $\beta^* = 2625$ m (Fig. 2.29 d). However, here the lack of knowledge about the vertex and detector resolution contributes equally to the overall uncertainty of 70 GeV.

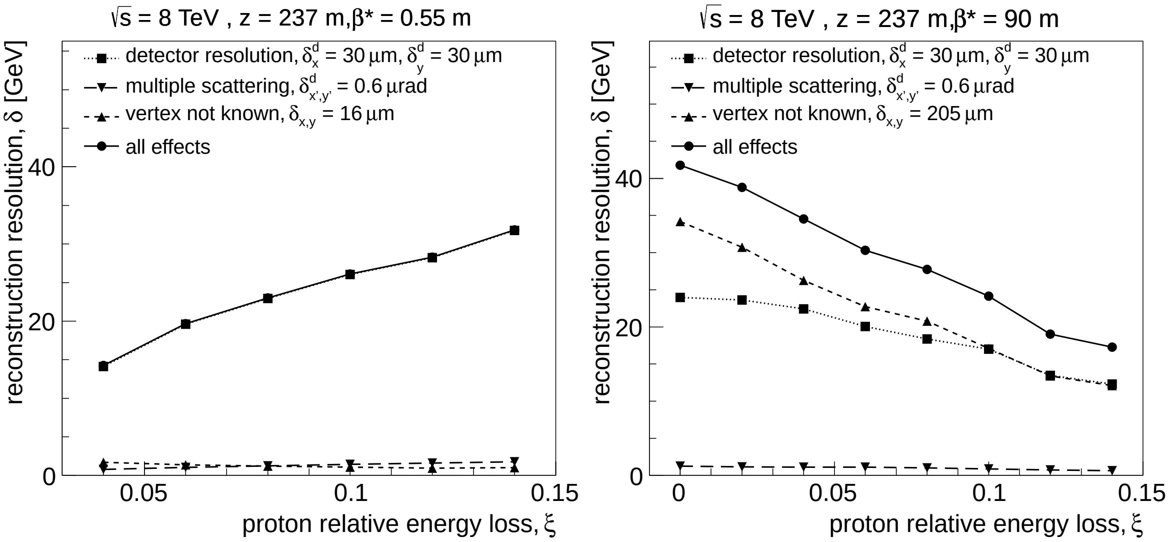

(a) $\beta^* = 0.55$ m (b) $\beta^* = 90$ m

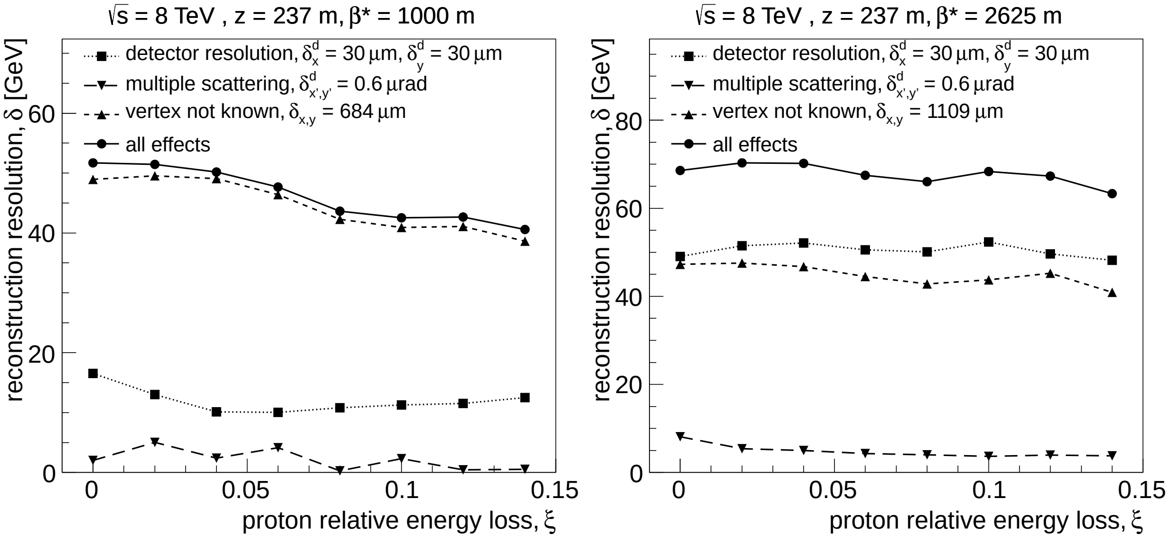

(c) $\beta^* = 1000$ m (d) $\beta^* = 2625$ m

Figure 2.29: Proton energy reconstruction resolution. The various experimental effects were taken into account: the ALFA detector spatial resolution, the lack of information about the vertex coordinates and the multiple scattering effect (see text).

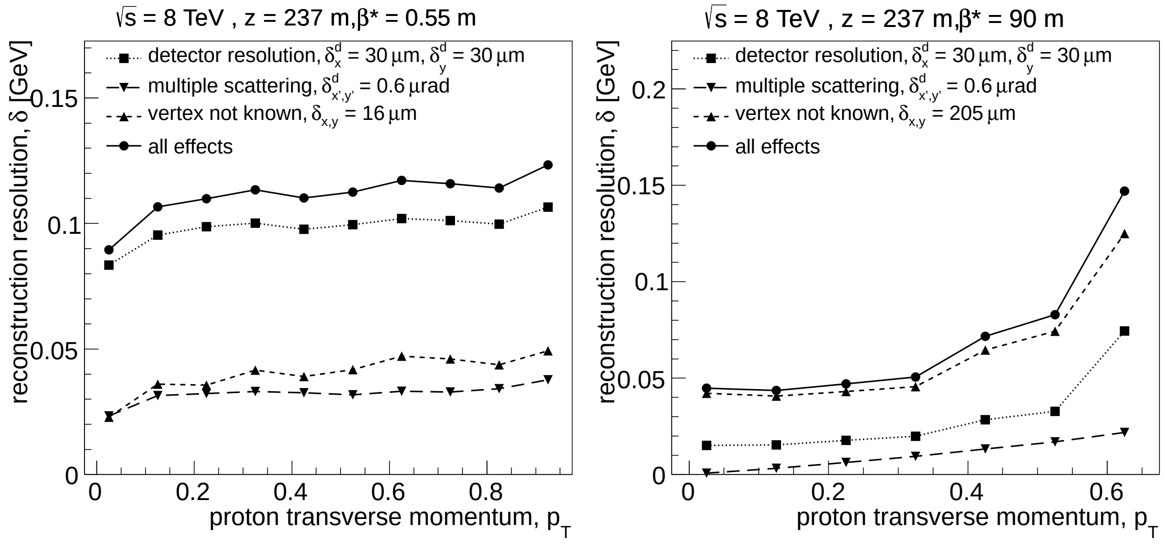

(a) $\beta^* = 0.55$ m (b) $\beta^* = 90$ m

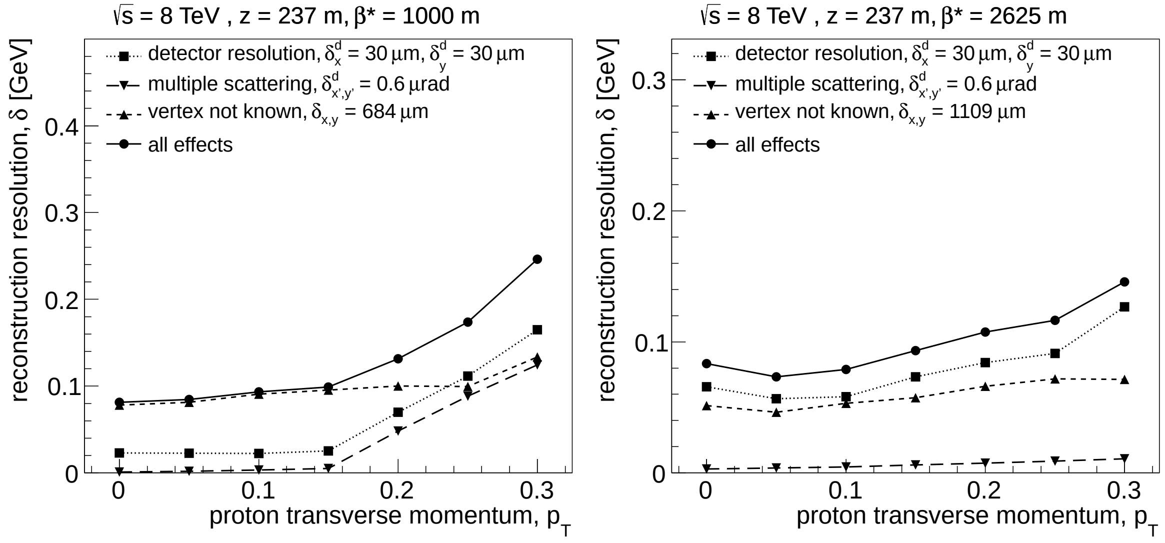

(c) $\beta^* = 1000$ m (d) $\beta^* = 2625$ m

Figure 2.30: Proton transverse momentum reconstruction resolution. The various experimental effects were taken into account: the ALFA detector spatial resolution, the lack of information about the vertex coordinates and the multiple scattering effect (see text).

The proton transverse momentum is reconstructed with a precision of about 0.1 GeV for $\beta^* = 0.55$ m (Fig. 2.30 a). The main uncertainty comes from the detector spatial resolution. For the $\beta^* = 90$ m optics (Fig. 2.30 b) the reconstruction resolution is about 0.05 GeV for the $p_T < 0.3$ GeV. It starts to grow to 0.15 for p_T of 0.6 GeV. The main uncertainty comes from the lack of knowledge about the vertex. In the case of $\beta^* = 1000$ m (Fig. 2.30c) the overall reconstruction resolution is about 0.1 GeV for the region of $p_T < 0.15$ GeV and it grows to 0.25 for p_T of 0.3 GeV. For $\beta^* = 2625$ m (Fig. 2.30 d) the lack of knowledge about the vertex and detector resolution contribute equally to the overall uncertainty. In this case, the reconstruction resolution is about 0.1 GeV for all particles within the detector acceptance.

In conclusion, the collision optics offers better opportunities to reconstruct diffractively scattered proton energy than the *high-β^** ones, whereas the transverse momentum reconstruction is comparable for all optics. Naturally one has to remember that this could be different when the p_x and p_y components are treated separately as was shown in [1]. In the case of $\beta^* = 0.55$ m, the main contribution to the uncertainty comes from the detector spatial resolution, whereas the lack of knowledge about the vertex plays a minor role. The situation is opposite for *high-β^** optics. For all optics the multiple scattering effect is the least important factor.

2.2.7 The AFP Detector

Due to the design of the ALFA detector, it is impossible to use it during the standard LHC runs, when the beam intensity is large. Therefore, the ATLAS Forward Proton (AFP) detector is proposed to be installed during ATLAS Upgrade Phase 0 and I at 210 m far from the ATLAS Interaction Point [11]. A prime interest on physics is focused on Central Exclusive Production (CEP), $pp \rightarrow p+X+p$, in which the central system X may be, for example, a pair of W or Z bosons or jets. The second class of processes include Double Pomeron Exchange, *i.e.* processes in which apart from two intact protons and a hard central system, Pomeron remnants are produced. An idea of the measurement with help of the AFP detectors is plotted in Figure 2.31.

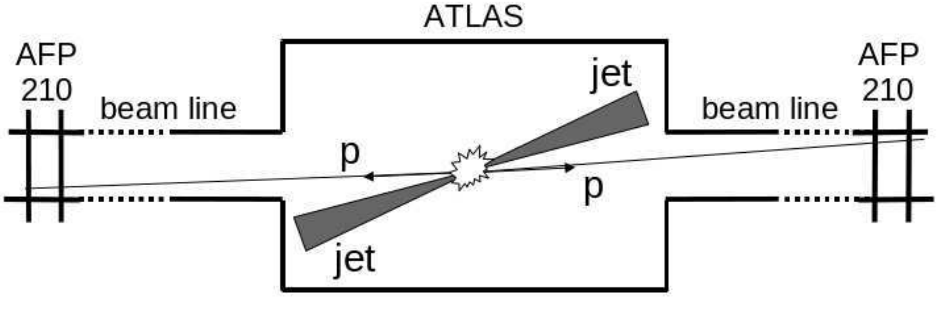

Figure 2.31: Schematic view of the possible measurement using the AFP detectors: jets are measured in the ATLAS detector whereas forward protons are tagged in the AFP stations.

Since the final design of the AFP detector is not fully decided yet, the idea assuming the usage of the so-called *Hamburg beam-pipes* [91] is presented in this thesis. The second considered option is to use the Roman Pot technology. The Hamburg beam-pipe solution is based on the idea of a detector integrated with the beam pipe that is separated from the vacuum of the accelerator by a thin window and is connected with bellows to the LHC beam pipe, thus can be moved close to the beam. The goal is to move the detectors as close as 1 mm to the beam in the horizontal direction. A schematic view of the AFP Hamburg beam pipes is shown in Figure 2.32. There will be four Hamburg beam-pipes placed symmetrically with respect to the ATLAS IP at 204 m and 212 m. Stations located closer to the IP1 will contain the position detectors, whereas the further ones the position and timing devices, as schemed in Figure 2.33.

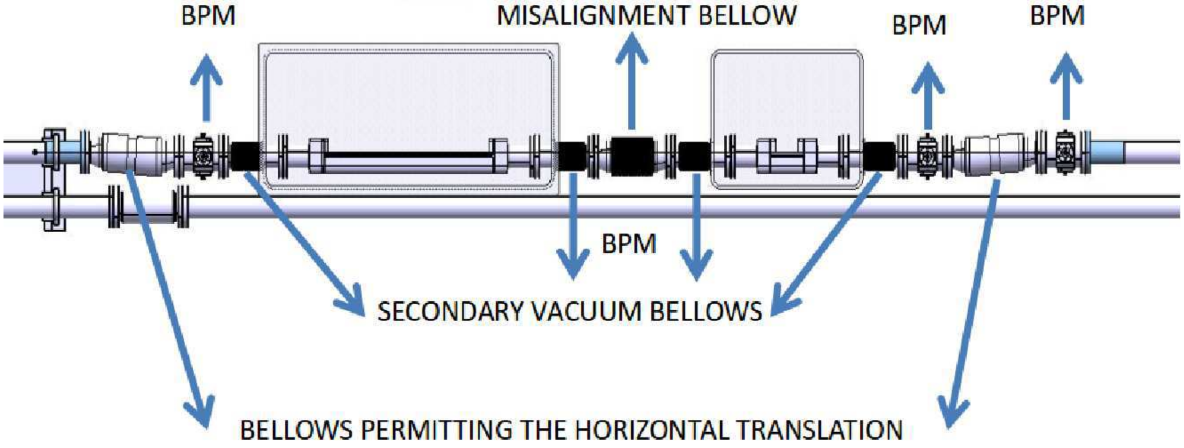

Figure 2.32: A schematic view of AFP infrastructure: two Hamburg beam-pipes connected with bellows to the LHC beam-pipe. The positions of the additionsl Beam Position Monitors are marked.

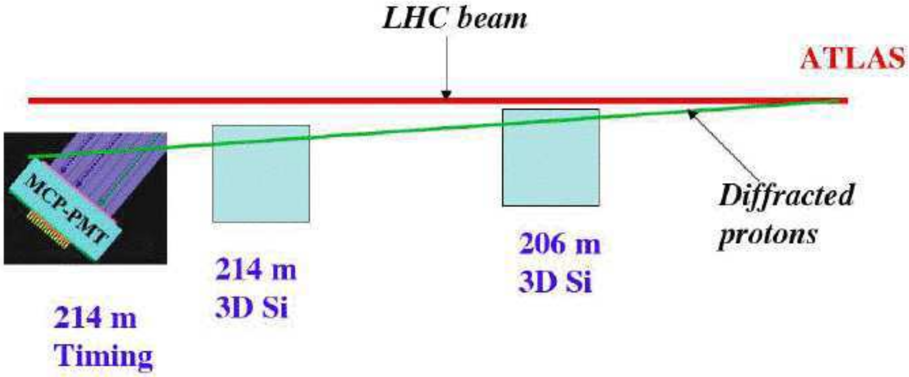

Figure 2.33: A schematic view of AFP: position and timing detectors.

The purpose of the AFP tracking system is to measure points along the trajectory of protons that were deflected at the Interaction Point as a result of interaction. The detector is described in detail in *e.g.* [11], whereas here only the main requirements are highlighted:

- a spatial resolution of about 10 μm in the horizontal direction[5],
- a spatial resolution of about 30 μm in the vertical direction,
- radiation hardness,
- no significant inactive edge region, in order to measure protons as close to the beam as possible.

The proposed solution fulfilling these requirements is a pixel detector consisting of six layers of silicon 3D pixel sensors [92]. A pixel layer will cover an area of about 20×20 mm^2 with a pixel size of 50×250 μm^2.

The purpose of the AFP timing system is to reduce background due to the multiple proton-proton interactions in the same bunch crossing (*pile-up*). Much of this background can be removed by matching the hard vertex measured by the central detector and the one reconstructed on a basis of Time-of-Flight difference from the AFP stations (see 5.1.1 for more detailed discussion). The main requirements on the AFP timing detectors are:

- a timing resolution of about 10 ps or better, which translates to vertex reconstruction resolution of about 3 mm,
- acceptance that fully covers the tracking detectors,
- nearly 100% efficiency,
- radiation hardness (at least 200 kGy per year).

The QUARTIC detector was shown to be a solution[6] which fulfils these requirements [93, 94]. It consists of quartz bars oriented at the Cerenkov angle with respect to the beam trajectory. A proton traversing a bar emits Cerenkov photons, which are then detected in a MCP-PMT detector as shown in Figure 2.34. Since the measurement in one bar provides a resolution of about 30 ps [95], the required 10 ps resolution is obtained with eight quartz bars, arranged one after another. An important issue is that there is a high probability that a proton traversing this detector will interact and create a shower. Therefore, the position measurement in AFP must be performed before the timing one.

The AFP project considers also the possibility of installing the position and timing detectors at 420 meters (the so-called AFP420 project). These detectors would be sensitive to smaller energy losses of protons and, hence, smaller masses produced centrally. However, since the hypothetical installation of such detectors is not considered before the LHC 2017 shutdown, they will not be discussed in this thesis.

---

[5] This value has to be considerably smaller than the spot size of the beam at the detector location.

[6] The other solution is to use 3D diamond detectors with SAMPIC readout chip developed in Saclay.

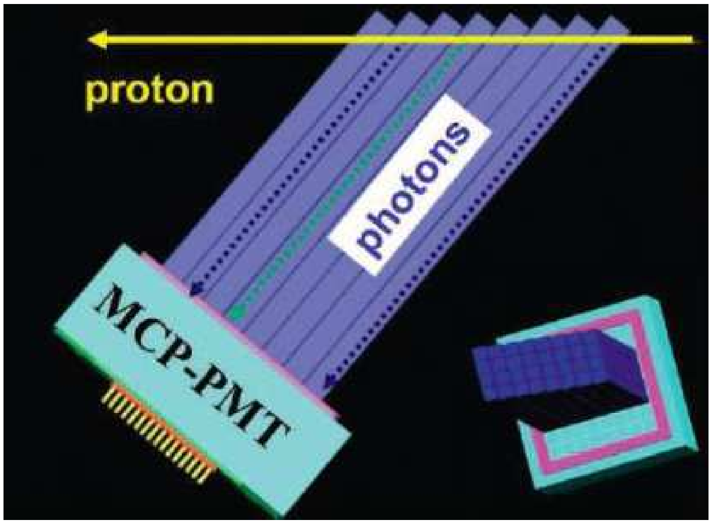

Figure 2.34: Schematic view of the QUARTIC detector.

Proton Interactions with AFP Detector

The design of the AFP detector is not finalised yet – there are still some technological issues that have to be addressed. One of them is the construction of the *thin window* and *floor* (see Figure 2.35). The thin window is an area of the Hamburg beam-pipe (a Roman Pot) behind which silicon detectors will be installed. The floor is an area between the beam centre and the edge of the position detector. Two effects connected to the amount of the material in the thin window and floor impact the physics measurements: multiple scattering and the probability to create the particle shower.

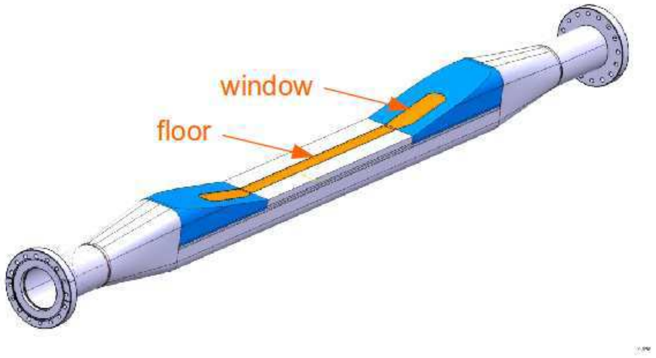

Figure 2.35: Scheme of Hamburg beam-pipe: thni window and floor.

The spread of the multiple scattering angle as a function of the amount of dead material is plotted in Fig. 2.36. The multiple scattering effect is important only for the thin window case, since the proton hitting the floor will not be the measured in silicon detectors.

The probability that a particle will interact with a medium at a certain distance is given by the equation:

$$P(x) = \int_A^B \frac{1}{\lambda_T} \exp\left(-\frac{x}{\lambda_T}\right) \, \mathrm{d}x,$$

where λ_T is the nuclear collision length which for the stainless steel is $\lambda_T^{ss} \sim 17$ mm [90].

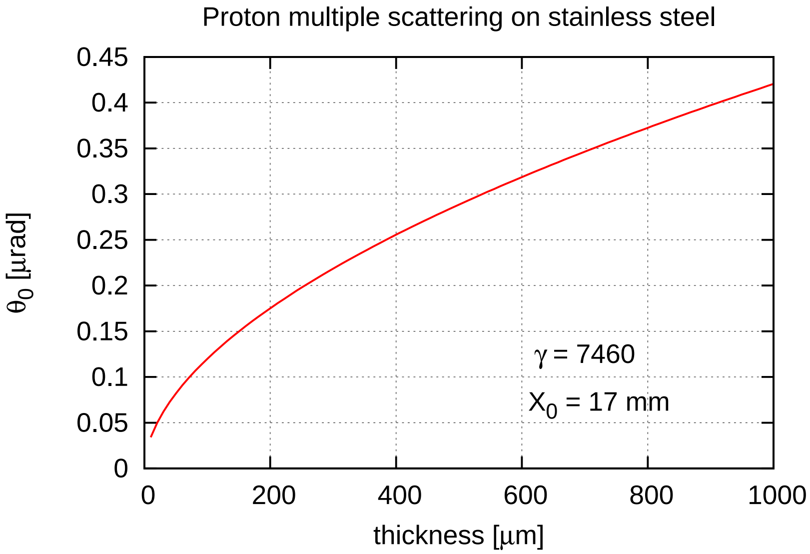

Figure 2.36: Spread of the multiple scattering angle, θ_0 as a function of amount of stainless steel thickness. The radiation length is $\sim$ 106 mm [90].

The probability of interacting with the AFP window and floor is presented in Figure 2.37 a) and b), respectively. In the case of the thin window this effect is small, of the order of permils. For the floor, the multiple scattering effect is more complicated since protons can cross this volume at different angles as illustrated in Figure 2.38. The probability that a proton with a given trajectory will cross the AFP floor is shown in Figure 2.39. In a vast majority of cases the protons will not hit the AFP floor (event types 1 and 2). In other cases, the proton approaches the floor with positive values of the x-slope (getting closer to the beam; event types 4, 6, 9) rather than with negative values (getting further from the beam; event types 3, 5, 8). This behaviour is expected from the LHC optics (see Figs 2.7, 2.9 and 2.11). The domination of events of type 6 and lack of events of type 7 is caused by the fact that the x-slopes are very small – the proton trajectories are almost parallel to the beam.

This behaviour is also visible in Fig. 2.40 where the proton trajectories for various distances from the beam (a) and floor thickness (b) are plotted. From these figures one can conclude that the mean path is equal to the overall length of the AFP floor. Therefore, by combining the probability of interaction for a given length (Fig. 2.37 b) with the probability that a proton will hit the AFP floor, one will obtain the probability of having a shower. The latter probability is shown in Figure 2.41 as a function of different floor thickness and various distances from the beam for the mean pile-up $<\mu>= 0$ and $<\mu>= 50$. From these figures one can conclude that in the case of no pile-up the probability that proton will create the shower is negligible (below 1 permil) for all considered floor thickness and distances from the beam. In the high pile-up environment the probability approaches 0.01 for the distances smaller than 1 mm and floor thickness of 0.5 mm. This value is still not critical for the measurements, but should be avoided if possible.

The LHC Collimators

The LHC runs in which the ALFA detectors are included are performed for special beam configuration. In such conditions, the collimators are set to be opened enough not to interfere with the measurements. In the nominal collision runs such situation is impossible since the LHC magnets could quench or even be destroyed due to the high intensity. Unfortunately, the designed values of 15 σ at which collimators should be closed impact the AFP acceptance, as illustrated in Figures 2.42 and 2.43. The 15 σ distance is equal to 7.89 mm in case of TCL4 and 4.36 mm in the case of TCL5.

To make the measurements possible, the AFP Group proposed [11] to install an additional TCL6 collimator in front of the $Q6$ magnet as illustrated in Figure 2.44. This new collimating scheme assumes that the positions of TCL4 and TCL5 will be at 30 σ (15.77 mm) and 50 σ (14.53 mm) from the beam, respectively. In addition, the TCL6 new collimator is positioned at 40 σ from the beam. This solution allows to keep a good acceptance (as will be shown in the next Section) for diffracted protons and was admitted as a possible alternative to the present scheme by the LHC Vaccuum group [11].

Geometric Acceptance and Energy and Momentum Reconstruction Resolution

The dependence of the scattered proton trajectory position in the detector on its energy and momentum is shown in Figure 2.45. It was calculated assuming the new proposed collimation scheme. Similarly as in the ALFA case (Sect. 2.2.6), this figure shows the positions of elastically and diffractively scattered protons in the detector plane at the detector locations. The detector shape is marked with the grey area.

The geometrical acceptance of the AFP detector as a function of the proton relative energy loss (ξ) and its transverse momentum (p_T) is presented in Figure 2.46. Note that the region with the acceptance higher than 80% is much larger than the corresponding one for the ALFA case (*cf.* Figure 2.27 a). This is mainly due to the fact that the ALFA detectors are inserted vertically (from the top and the bottom), whereas the AFP ones horizontally (from the outside of the LHC ring). The geometrical acceptance translates to the mass acceptance, which is plotted in Figure 2.47.

The beam sizes at the AFP station are given in Tables 2.2 – 2.5. Since the AFP detectors are approaching the beam in the horizontal plane, only the values of the x component are meaningful.

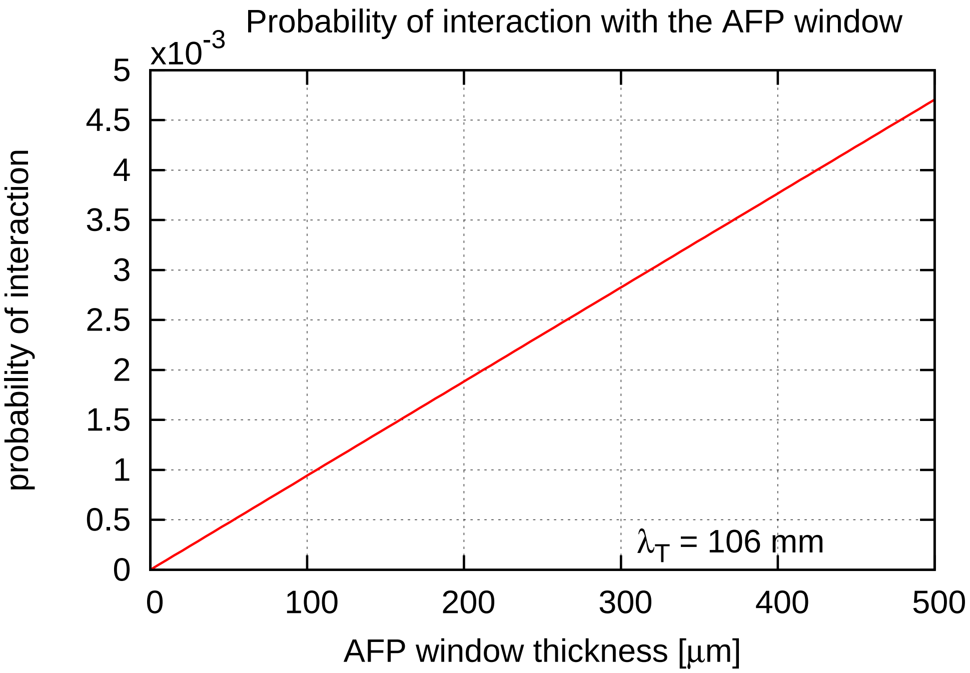

(a) AFP window

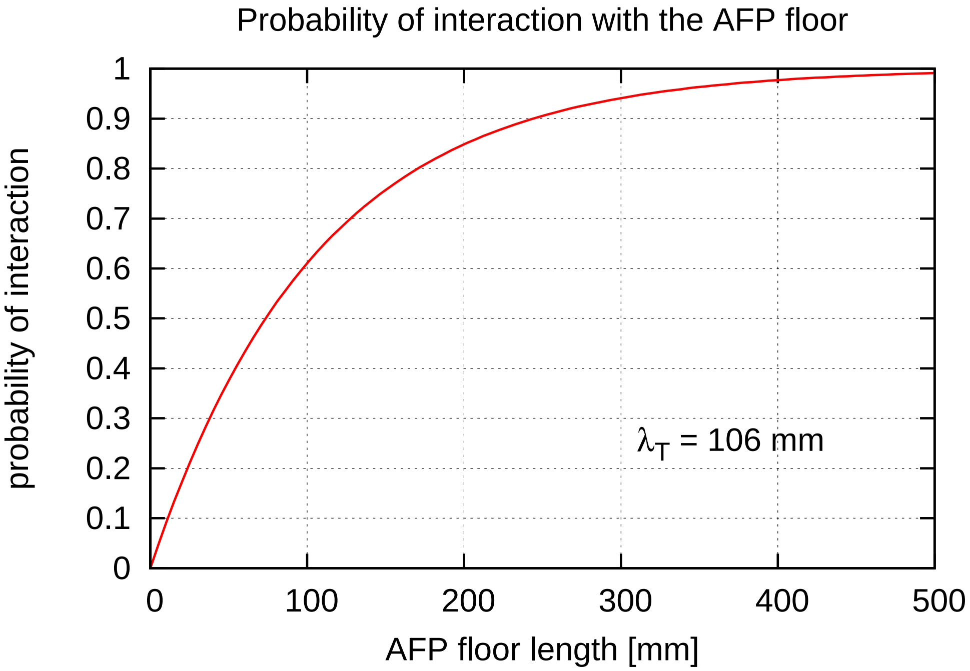

(b) AFP floor

Figure 2.37: Probability of interacting with the AFP window (a) and floor (b) as a function of its length. The proton Lorentz factor is equal to $\gamma = 7460$ which corresponds to a beam energy of 7 TeV. The nuclear collision length is ~ 17 mm [90].

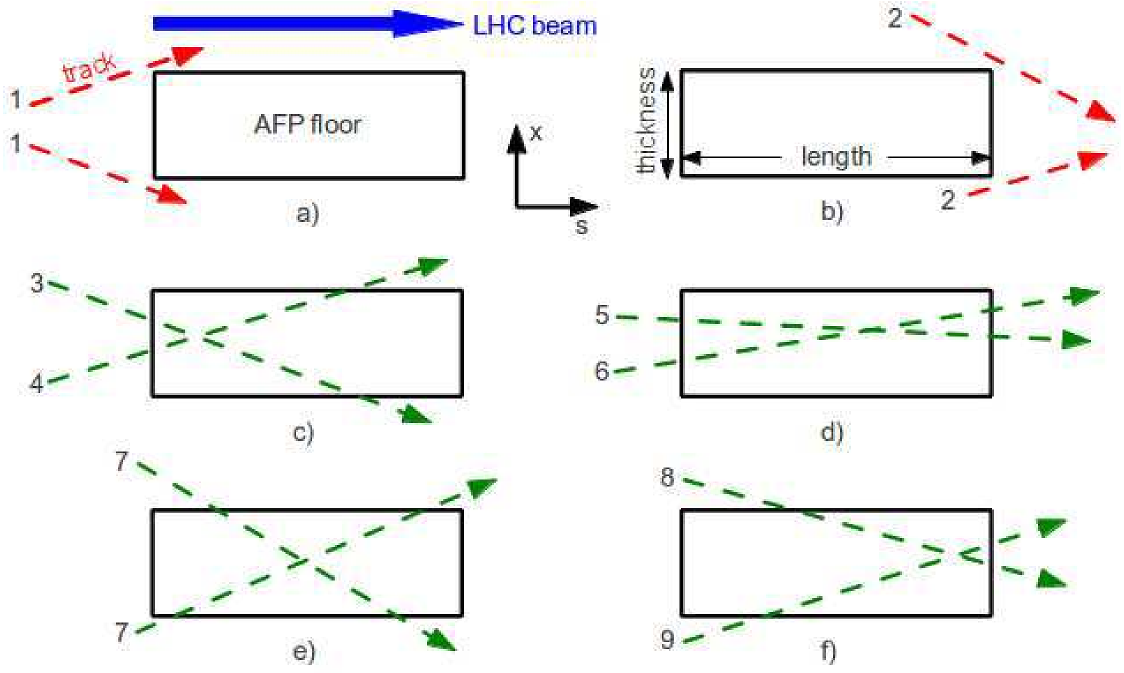

Figure 2.38: Various proton trajectories in the vicinity of the AFP floor. Situations (a) and (b) illustrate the case in which the proton does not hit the AFP floor.

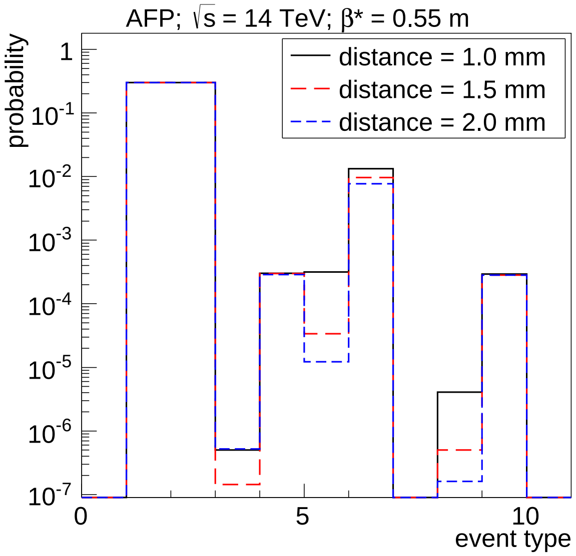

Figure 2.39: Probability that a proton will have a given trajectory. The definitions of the different event types are marked as numbers in Fig. 2.38. In the vast majority of cases the diffractive protons will not hit the AFP floor (event types 1 and 2). In other cases, the proton approaches with positive values of the x-slope (getting closer to the beam; event types 4, 6, 9) rather than with negative values (getting further from the beam; event types 3, 5, 8).

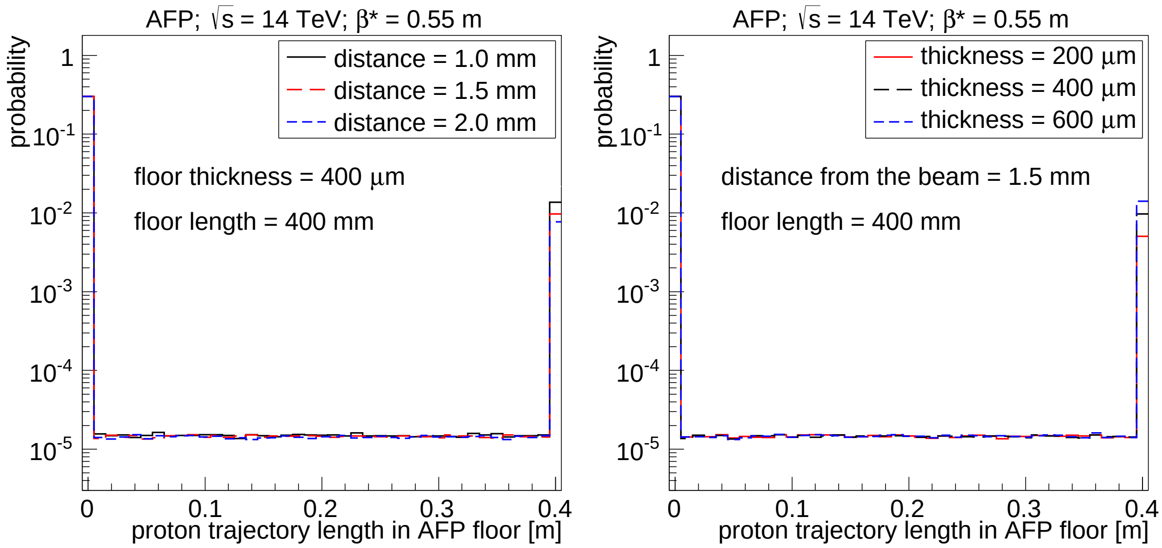

(a) distance (b) thickness

Figure 2.40: Proton trajectories for various distances from the beam (a) and floor thickness (b). If proton hits the AFP floor than its mean path is in almost 99% of cases equal to the floor length.

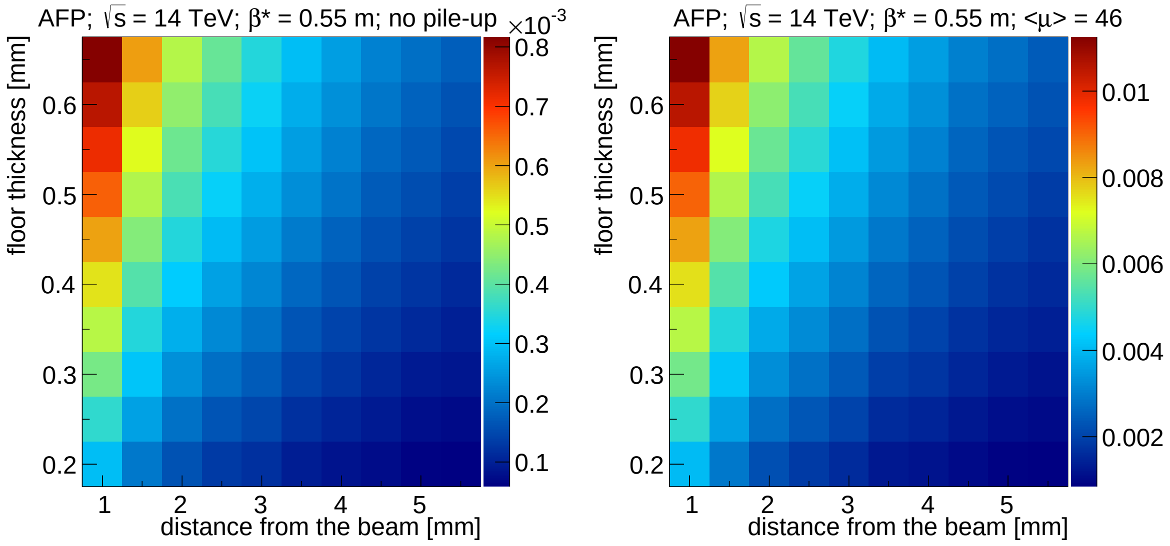

(a) (b)

Figure 2.41: Probability that a proton survive and hits the AFP floor when: (a) there is no pile-up, (b) the mean pile up is equal 46. In the case of no pile-up the probability that proton will create the shower is negligible (below 1 permil) for all considered floor thickness and distances from the beam. In the high pile-up environment the probability approaches 0.01 for the distances smaller than 1 mm and floor thickness of 0.5 mm. This value is still not critical for the measurements, but should be avoided if possible.

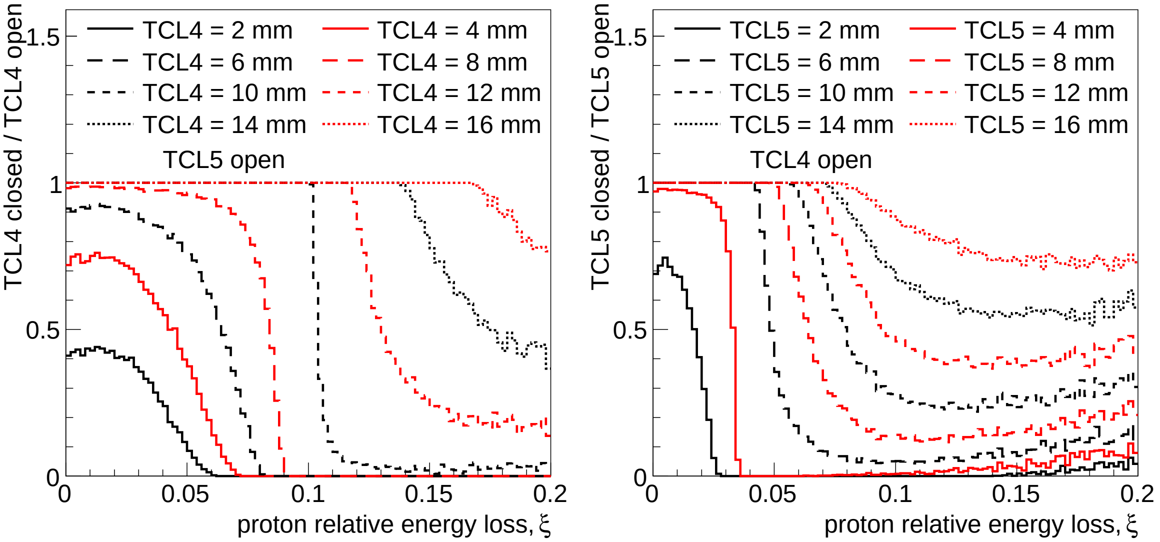

(a) different positions of TCL4 (b) different positions of TCL5

Figure 2.42: Ratio of the number of events that could be detected with the AFP detector a given collimator is closed to the number of events when it is wide open as a function of the relative energy loss. The default distance of 15 σ is equal to 7.89 mm in case of TCL4 and 4.36 mm in the case of TCL5. In consequence, the AFP geometric acceptance is much smaller than the one with open collimators.

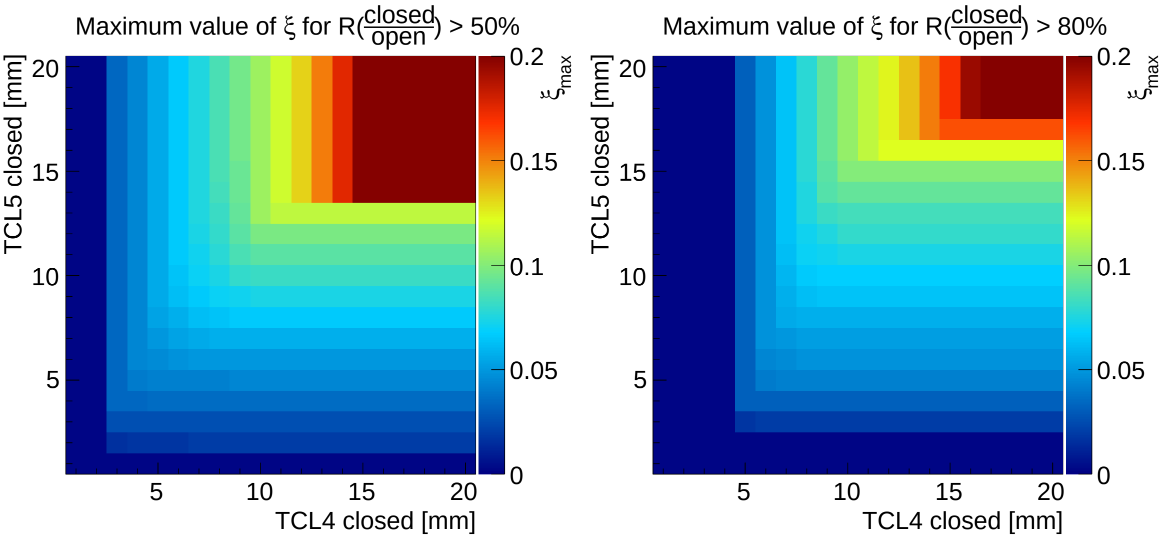

(a) $R\left(\frac{\text{closed}}{\text{open}}\right) > 50\%$ (b) $R\left(\frac{\text{closed}}{\text{open}}\right) > 80\%$

Figure 2.43: Maximum value of the proton energy loss that could be registered in AFP with a probability of a) 50% b) 80% for different TCL4 and TCL5 settings. The value ξ_{max}, at which the AFP geometric acceptance is not affected is for TCL4 and TCL5 closed at 15 mm from the beam.

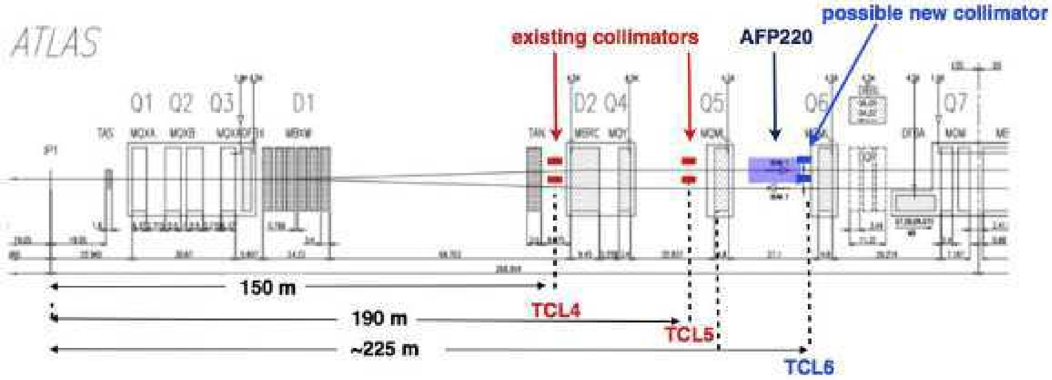

Figure 2.44: Layout of the straight section on the right side of ATLAS: positions of the existing and planned collimators.

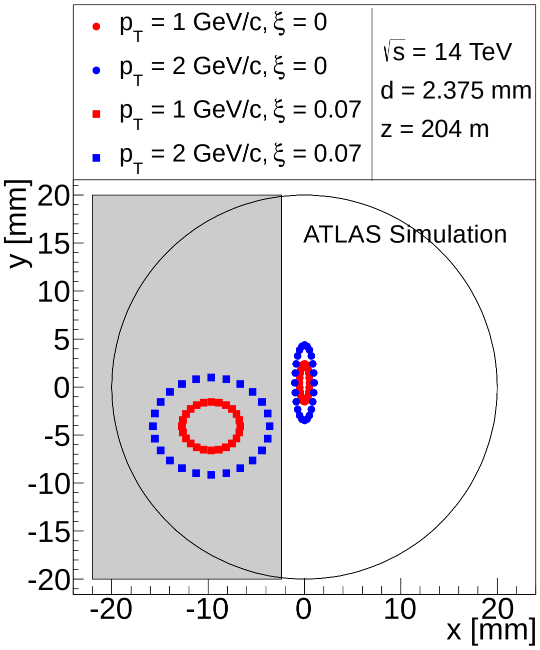

Figure 2.45: Positions of protons with different relative energy loss (ξ) and transverse momentum (p_T) at the first AFP station for the LHC collision optics. The grey area show the AFP detector active area.

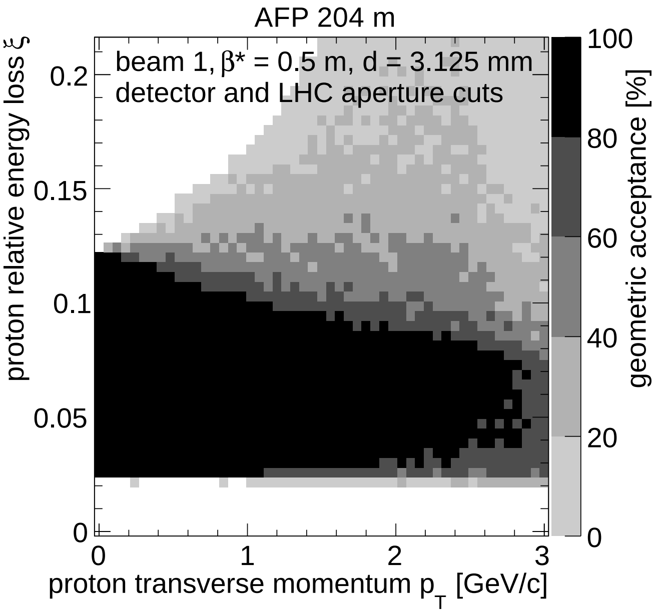

Figure 2.46: Geometrical acceptance of the AFP detector as a function of the proton relative energy loss (ξ) and its transverse momentum (p_T) for the LHC collision optics. The factors taken into account are: the beam properties at the IP, the beam chamber and the detector geometries, the distance between the detector edge and the beam centre. This distance was set to 15σ.

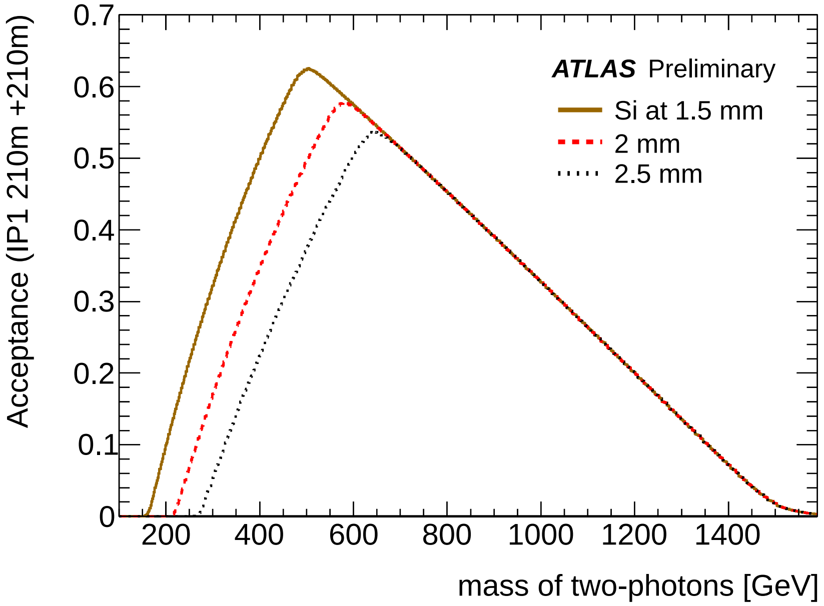

Figure 2.47: Geometrical acceptance due to a limited coverage of the forward detectors in ξ and t in terms of mass of two-photon exclusive production.

The reconstruction precision of the proton energy for the LHC collision optics and the AFP detector case is presented in Figure 2.48. The main uncertainty comes from the detector resolution of 10 μm in x and 30 μm in y. The lack of knowledge about the vertex and the multiple scattering effect are much smaller, except for the low values of ξ where the lack of knowledge about the vertex is a dominant factor. The reconstruction resolution grows from 5 GeV for $\xi = 0.04$ to 10 GeV for $\xi = 0.14$. These values for a given optics practically do not depend on the beam energy. The reconstruction precision of proton momentum is presented in Figure 2.49. Here all uncertainties contribute equally. The reconstruction resolution is about 0.1 GeV for $p_T < 1$.

In conclusion, in order to not be limited by the LHC collimators, AFP should use a new collimation scheme. In these settings, the TCL4 and TCL5 collimators should be at least 15 mm far away from the beam. This allows to reach an acceptance greater than 80% in a region of ξ between 0.014 and 0.14 and for a transverse momentum, $p_T < 3$ GeV. This translates into an acceptance in central mass between 300 and 1200 GeV. The energy reconstruction resolution grows from 5 GeV for $\xi = 0.04$ to 10 GeV for $\xi = 0.14$, whereas the momentum reconstruction resolution is flat and of about 0.1 GeV. These values are much smaller than *e.g.* uncertainties of the jet energies coming from the ATLAS main detector.

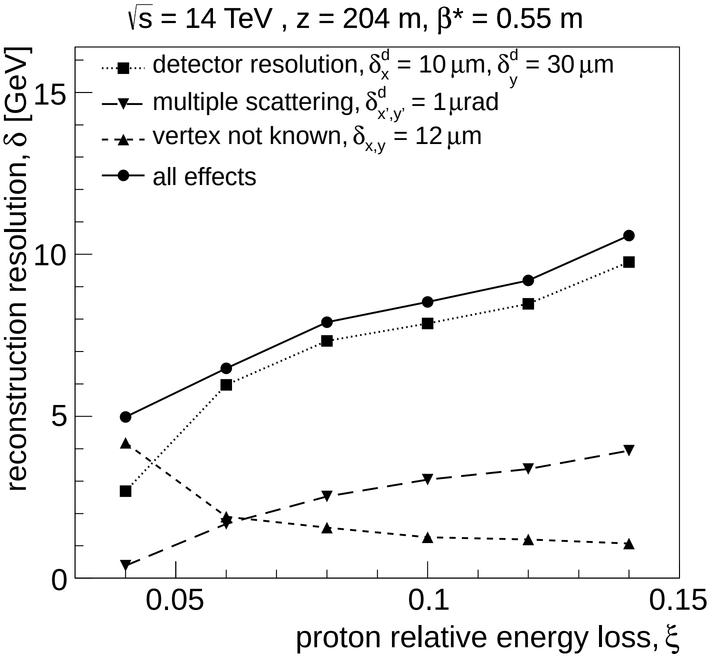

Figure 2.48: Proton energy reconstruction resolution. The experimental effects taken into account are: the AFP detector spatial resolution, the lack of information about the vertex coordinates and the multiple scattering effect.

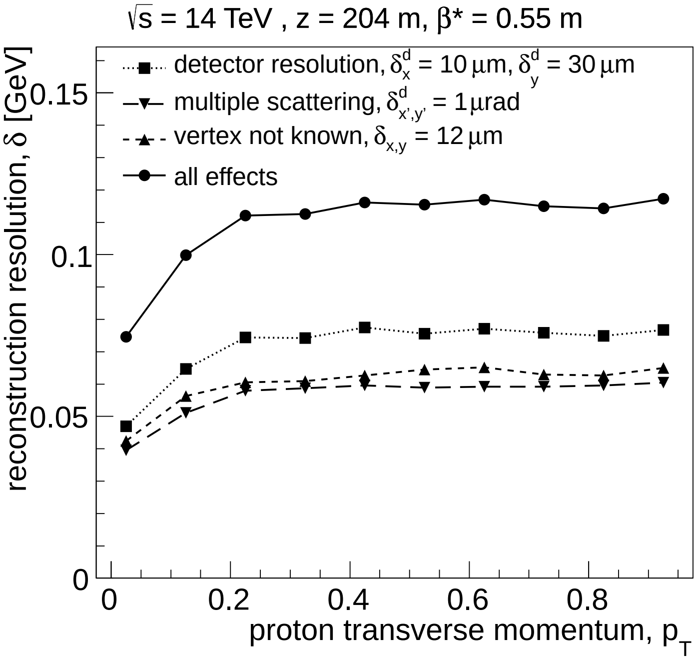

Figure 2.49: Proton transverse momentum reconstruction resolution. The experimental effects taken into account are: the AFP detector spatial resolution, the lack of information about the vertex coordinates and the multiple scattering effect.

Chapter 3

Jet-Gap-Jet Measurement

During proton-proton collisions at the LHC, events in which a pair of jets is produced are very common. Among them the most probable one is a situation in which both protons are destroyed and the jet system is produced in the central pseudorapidity region. The leading diagram for such a production is presented in Figure 1.11. In the pseudorapidity plane such an event will look like the one shown in Figure 1.11 (bottom) – apart of the two produced jets there are proton remnants (moving in the forward direction) and some soft activity between the jets. An example of such an event is drawn in the pseudorapidity-azimuthal angle (η, ϕ) plane in Figure 3.1. In this event, generated by the PYTHIA 6 Monte Carlo, the jets are produced at $\eta_{J,1} \sim -2$ and $\eta_{J,2} \sim 1.5$. In addition, there is some soft production spread quasi-uniformly in the central region. The size of the circles reflects the transverse momentum of the produced particles.

As it was discussed in Section 1.3, the colour triplet or octet exchanges are not depleting all possibilities. The object exchanged in the t channel can be also a colour singlet. The leading diagram for such a production is presented in Figure 3.2. The signature of this process is different from the two previously mentioned ones as the colour singlet induces that there is no soft energy production between the jets – a *gap* is created. When both jets are produced at relatively high rapidities ($|\eta_J| > 1.5$), such event should look like the one presented in Figure 3.3.

The cross section for such production is much smaller than the one for Non-Diffractive jets mainly because of two reasons:

- requirement of the colour singlet exchange,
- gap survival probability.

As it was shown in Section 1.3, at the LHC energies, the cross section for JGJ production is about three orders of magnitude smaller than that for Non-Diffractive (ND) Jet production. Having in mind that a gap can also appear in the ND events due to fluctuations, one has to consider cases in which the gap is large in order to select the Jet-Gap-Jet events. The distributions of the half-gap size for ND and JGJ jet productions are plotted in Figure 3.4.

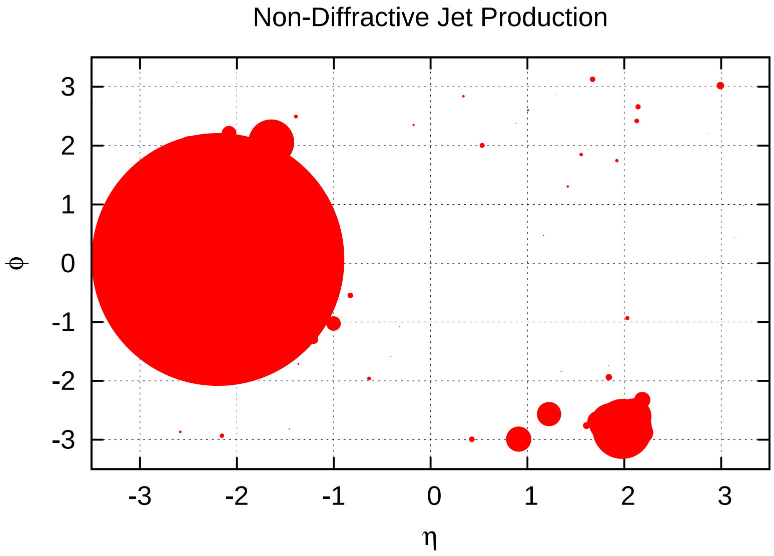

Figure 3.1: Non-Diffractive Jet production as produced by the the Pythia 6 MC. Two jets are produced in the forward region ($|\eta| \sim 2$) and low p_T particles appear between them. The size of the point is proportional to the particle transverse momentum.

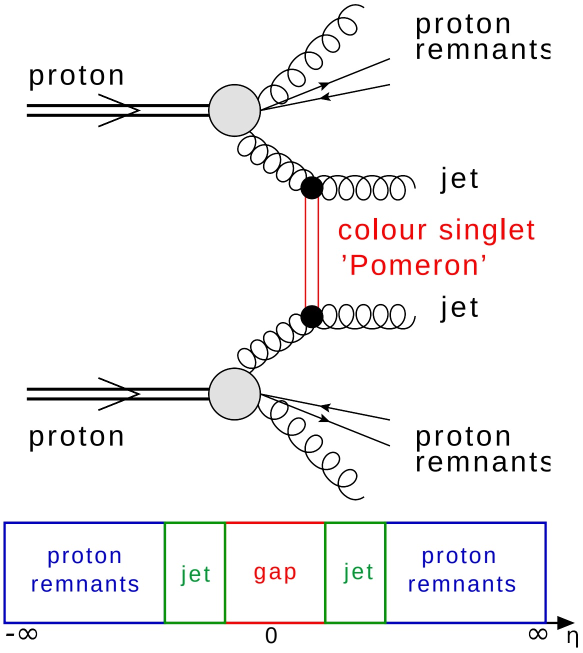

Figure 3.2: Jet-Gap-Jet production: the interacting protons are destroyed and two jets are produced. Since the object exchanged in the t-channel is a colour singlet, there are no soft exchanges between the jets.

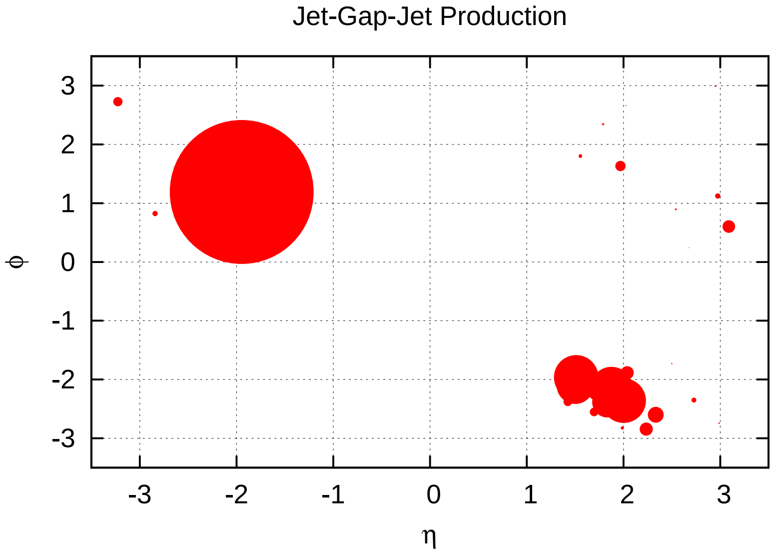

Figure 3.3: Jet-Gap-Jet production as produced by FPMC. Two jets are produced in the forward regions ($|\eta| \sim 2$) and there is a gap in rapidity between them. The size of the point is proportional to the particle transverse momentum.

In case of Non-Diffractive events (black line), the cross section falls steeply with increasing of the gap size whereas JGJ (red line) show much larger gaps. From this plot one can conclude that events with half-gaps higher than 0.4 are mainly due to the colour singlet exchange.

Requiring such large gaps induces that the distance in rapidity between jets should also be large. Due to hadronisation effects the centre of the jets should be at least few tenths units of rapidity further than the defined gap border. In consequence, there are three classes of events:

1. both jets are produced in forward direction in the same pseudorapidity hemisphere,
2. one jet is central, whereas the other one is forward,
3. both jets are produced in forward directions, but belong to opposite hemispheres.

These possibilities are illustrated in Fig. 3.5. Clearly, the largest differences in pseudorapidity between jets (for which the BFKL effects are enhanced [45]) can appear in the third class. Another advantage is that the gap is produced in the central region, which provides good tracking possibilities and has the lowest calorimeter noise. This definition was also used in the measurements performed at the Tevatron [49, 50]. Taking all these into account, the third class is studied in this work.

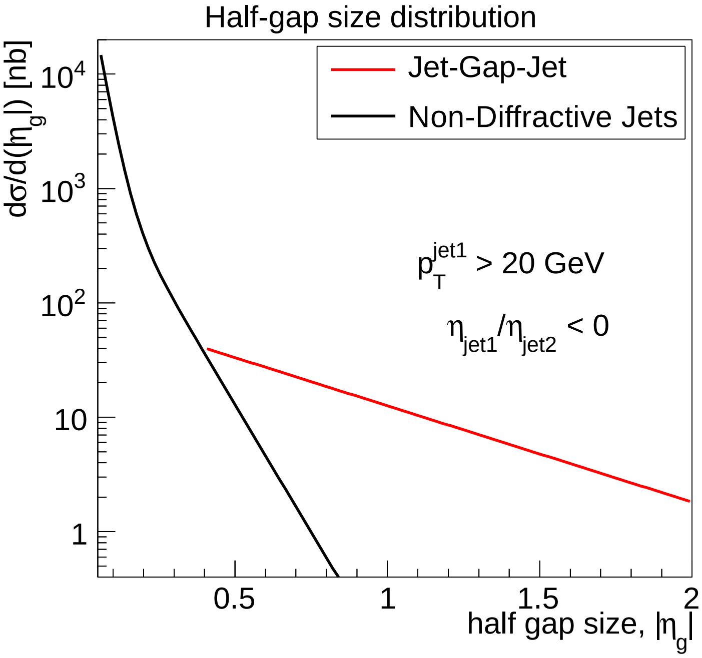

Figure 3.4: The half-gap size distribution for Non-Diffractive jets and Jet-Gap-Jet events. For half-gaps larger than 0.4, events are mainly due to colour singlet exchange.

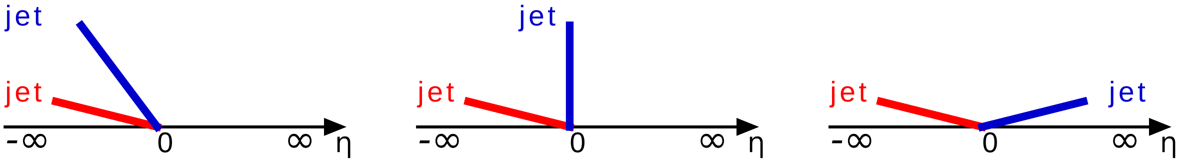

Figure 3.5: Three classes of Jet-Gap-Jet events: both jets are produced in the forward direction in the same pseudorapidity hemisphere (**left**), one jet is central, whereas the other one is forward (**center**) and both jets are produced in the forward direction but are in opposite hemispheres (**right**).

3.1 Data

The high pile-up environment which was present in most of LHC runs made the observation of the Jet-Gap-Jet events very hard. It is due to the fact that particles originating from pile-up events are produced in all regions of the $(\eta - \phi)$ plane. This situation is sketched in Figure 3.6 – the gap created in a JGJ event is populated by particles coming from pile-up. The tracker enables the recognition of the origin of tracks and rejects the ones which do not come from the jet vertex. Unfortunately, such an identification is not possible using the calorimeter method. Taking this into account, in the presented work, only the first periods of 2010 data are considered since they show the lowest pile-up value[1]. For these data the mean pile-up value, $<\mu>$, is not significantly greater than 1. Informations about used datasets are listed in Table 3.1.

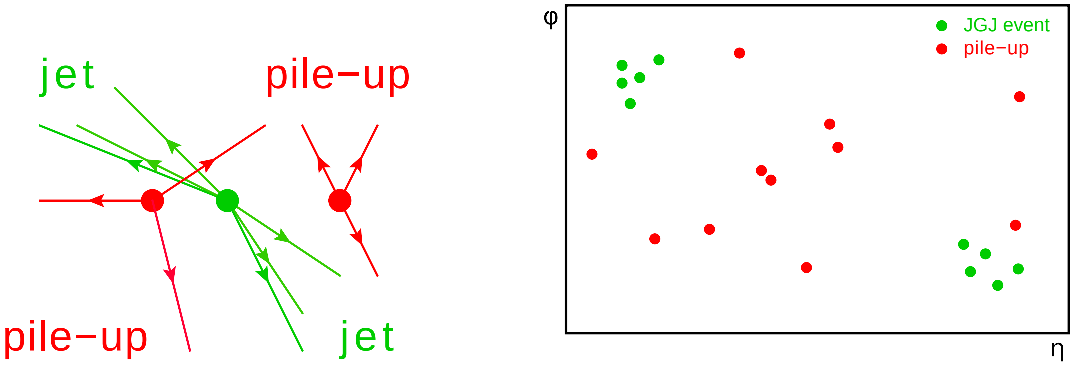

Figure 3.6: Sketch of Jet-Gap-Jet event in which a gap is populated with pile-up particles.

Table 3.1: Properties of ATLAS data for periods A-D in year 2010.

period	run range	β^* [m]	$<\mu>$	luminosity [nb^{-1}]
A	152166-153200	10	0.01	0.4
B	153565-155160	2	0.1	9
C	155228-156682	2	0.1	9.5
D	158045-159224	3.5	1	320

---

[1] This measurement is also possible at $\sqrt{s} = 8$ TeV using the proton-proton low pile-up runs taken in the year 2013. It can be also probably extended to the runs with slightly higher pile-up, since the gap recognition based on the track method gives an opportunity to reject tracks not originating from the hard vertex. This requires dedicated studies and is not discussed further in this thesis.

3.2 Trigger

The ATLAS trigger menu contains about 500 trigger configurations. The main objects identified by the ATLAS triggers and their corresponding labels are listed in Table 3.2. The naming convention is as the following: if object passed muon trigger on $L1$ it will be labelled as $L1\_MU$, whereas after passing the HLT it will be tagged as $L2\_mu$.

Table 3.2: The main objects identified by the trigger system and their description in the ATLAS trigger.

Object	$L1$	$L2$ & EF
electron	EM	e
photon	EM	g
muon	MU	mu
jet	J	j
b-jet	–	b
forward jet	FJ	fj
tau	TAU	tau
Missing E_T	XE	xe
Sum E_T	TE	te
total jet energy	JE	je
Minimum Bias Scintilators	MBTS	mbts

The ATLAS triggers can be classified as:

- single object triggers that are used for final states with at least one characteristic object, *e.g.* a single muon trigger with a nominal 6 GeV threshold is referred as $mu6$,
- multiple object triggers that used for final states with two or more characteristic objects[2] of the same type, *e.g.* di-muon triggers for selecting $J/\psi \rightarrow \mu\mu$ decays is defined as $2mu6$,
- combined triggers that are used for final states with two or more characteristic objects of different types, *e.g.* a 13 GeV muon plus 20 GeV missing transverse energy trigger for selecting $W \rightarrow \mu n$ decays would be denoted $mu13\_xe20$.
- topological triggers used for final states that require selections based on information from two or more Regions of Interest (RoI)[3].

---

[2] Triggers requiring a multiplicity of two or more are indicated in the trigger menu by prepending the multiplicity to the trigger name.

[3] RoI is a geometrical region of the ATLAS detector. A simple RoI description is via: (ϕ_{min}, ϕ_{max}), (η_{min}, η_{max}).

When referring to a particular trigger, the level ($L1$, $L2$ or EF) appears as a prefix.

The triggers are grouped into the so-called *trigger streams*. The signal selection in the analysis is based on any trigger from the calorimeter stream (L1CALO). This stream contains events passing single (inclusive) or JETETSUM triggers signatures: $L1\_J$, $L1\_FJ$, $L1\_XE$, $L1\_TE$, $L1\_EM$, $L1\_MU$, $L1\_TAU$. The technical details as well as the reconstruction algorithms are described elsewhere [96, 97, 98], whereas here only the main aspects are presented.

The central and forward jet triggers select data independently, using several thresholds for the jet transverse energy, E_T, each of which requires the presence of a jet with sufficient E_T at the electromagnetic scale. There are eight thresholds for the central jets (having $|\eta| < 3.2$): $L1\_J5$, $L1\_J10$, $L1\_J15$, $L1\_J30$, $L1\_J55$, $L1\_J75$, $L1\_J95$, $L1\_J115$ and seven threshold for the forward jets ($3.2 < |\eta| < 4.9$): $L1\_FJ5$, $L1\_FJ10$, $L1\_FJ15$, $L1\_FJ30$, $L1\_FJ55$, $L1\_FJ95$, $L1\_FJ95$. The number after J (or FJ) means the energy threshold in GeV. If jet passes the threshold N but fails the threshold $N + 1$, its E_T lies in the range $E_T(N) < E_T^{jet} \leq E_T(N+1)$. For the considered data the lowest unprescaled jet triggers were: $L1\_J15$ and $L1\_FJ15$.

The efficiency of each trigger jet is determined using the so-called *bootstrap* procedure in which the efficiency is measured with respect to a trigger which is fully efficient at a considered region. In the case of the lowest threshold jet trigger, the efficiency is determined using the Minimum Bias Trigger Scintillators (MBTS). The MBTS was shown to be nearly 100% efficient in selecting events with jets having the transverse momentum greater than 20 GeV [98], but it was prescaled (up to 123) in periods C and D and, therefore, not used in this analysis.

As an example, the efficiency for an anti-k_T jet with $R = 0.4$ to satisfy the $L1$ trigger as a function of the jet p_T for $|y| < 2.8$ is shown in Figure 3.7. From this figure one can conclude that this trigger is fully efficient for jets having a p_T greater than 50 GeV.

In summary, the events used in the presented analysis were required to be registered by any trigger from the calorimeter stream. This includes all events passing single or JETETSUM triggers signatures: $L1\_J$, $L1\_FJ$, $L1\_XE$, $L1\_TE$, $L1\_EM$, $L1\_MU$, $L1\_TAU$. For the further studies, especially for the measurement of the Jet-Gap-Jet cross section, it will be desirable to consider only events for which jet triggers ($L1\_J$ and $L1\_FJ$) are fully efficient.

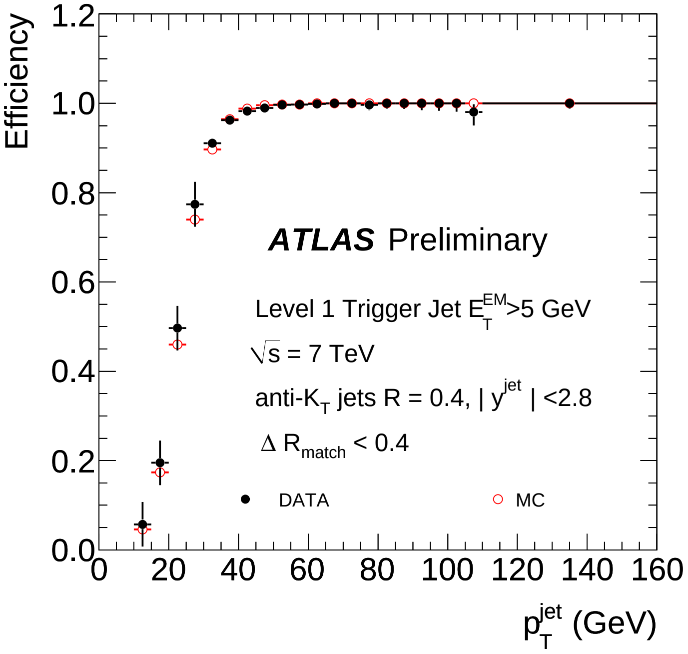

Figure 3.7: $L1\_J5$ trigger efficiency as a function of the jet p_T for $|y| < 2.8$. Jets were reconstructed using the anti-k_T algorithm with $R = 0.4$.

3.3 Jets

Jets were reconstructed using the anti-k_T jet algorithm [99] with a distance parameter of $R = 0.4$. The input to the algorithm were clusters formed using calorimeter cells energies as explained in [100].

For each reconstructed jet the data quality requirements were applied. In this analysis jets marked as BAD or UGLY were rejected. A jet is marked as BAD if one of the following criteria is fulfilled:

- $f_{EM} > 0.95$ and $|f_{quality}| > 0.8$, where f_{EM} is the fraction of the jet energy in the electromagnetic (EM) calorimeter and $f_{quality}$ is the fraction of the jet energy from the calorimeter cells with a shape that is significantly different from the reference one. This criteria identify the miss-reconstructed jets according to the coherent noise in the EM calorimeter,

- $f_{HEC} > 0.8$ and $n_{90} \geq 5$, where f_{HEC} is the fraction of the jet energy in the LAr Hadronic EndCap (HEC) and n_{90} is the minimum number of energy-ordered cells that accounts for at least 90% of the jet energy,

- $f_{HEC} > 0.5$ and $|f_{quality}| > 0.5$. The jets that satisfied this requirement or the previous one could cause a sporadic noise bursts in the HEC,

- the timing of the jet with respect to the event time, $|t_{jet}| > 25$ ns. This requirement eliminates the jets reconstructed from the out-of-time energy depositions in the calorimeter,
- $f_{EM} < 0.05$ requirement limits the impact from cosmic rays,
- $f_{max} > 0.99$ and $|\eta| < 2$, where f_{max} is the maximum energy fraction in one calorimeter layer,

An UGLY jet is defined according to the following criteria:

- the energy fraction in the Tile calorimeter *gap* region is greater than 0.5,
- the energy fraction in cells that receive a correction is greater than 0.5.

The UGLY jets correspond to the real energy depositions which are not accurately measured in the calorimeter.

3.4 Gap Definition

In a real experiment one cannot perfectly reconstruct a gap. Despite the fact that some particles like neutrinos are undetectable in the ATLAS detector, also reconstruction inefficiencies should be considered. These effects will cause larger gaps that in reality. On the other hand, one has to remember that the detector noise can fake signal and, in consequence, make the gap smaller than it should be.

In the following work two methods of gap reconstruction were studied. The first one is based on reconstructed tracks and the second one on the calorimeter activity.

3.4.1 Track Reconstruction

The ATLAS software offers several track reconstruction algorithms. In practice, they can be grouped in two classes:

- tuned to reconstruct tracks of particles with a transverse momentum of at least 500 MeV,
- designed for reconstructing particles with transverse momentum greater than 100 MeV.

The first class is often referred as the *standard* tracking and is commonly present in all main ATLAS D3PDs. The latter one, known as *low-p_T tracking*, is switched on only for a special requests, as the calculations are much more time-consuming (especially at higher pile-up values). In the considered datasets (periods A – D from year 2010) and Monte Carlo samples both reconstruction methods are switched on.

The lower limit on the transverse momentum of the reconstructed tracks comes from the quality requirements. In order to be reconstructed, a particle must be registered in several layers of the Inner Detector. Due to the ATLAS magnetic field, the particles with transverse momentum lower than about 200 MeV are often not passing the quality cuts. These criteria are described in details elsewhere ([101, 102]), whereas here only the main conclusions are presented. In order to be classified as a *good*, the track should minimally have the following properties:

- number of hits in Pixel detector should be greater or equal to 1,
- number of hits in the SCT detector should be greater or equal to:
  - 2 for tracks with $p_T > 100$ MeV,
  - 4 for tracks with $p_T > 200$ MeV,
  - 6 for tracks with $p_T > 300$ MeV.

The reconstruction efficiency as a function of the particle transverse momentum is shown in Figure 3.8. One can conclude that ATLAS starts to detect particles when the track has a transverse momentum greater than 100 MeV. However, the reconstruction efficiency for such low-p_T tracks is only about 10%. The efficiency grows with increasing transverse momentum and is about 75% for $p_T \sim 500$ MeV.

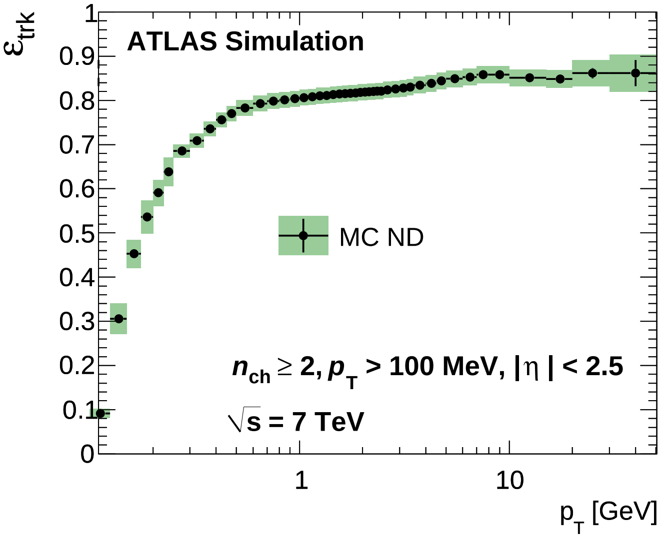

Figure 3.8: Track reconstruction efficiency as a function of p_T.

In order to define a gap based on tracks in the central region, one can consider three classes of events according to the reconstruction efficiency:

1. all reconstructed tracks with *good* quality flag,
2. tracks with $p_T > 200$ MeV, as having the $\sim 50\%$ chance to be reconstructed,
3. tracks with $p_T > 500$ MeV, as present in standard ATLAS D3PDs.

Matching to Monte Carlo

In order to check how adequate the reconstructed track reflects the location of the generated particle, it is desirable to construct a variable that can quantify that value. In this analysis the R_{trk} is defined as the variable describing the distance in the $(\eta - \phi)$ plane between the reconstructed tracks to the closest charged generated particle. In other words it is a circle in the $(\eta - \phi)$ plane with centre at the position of the reconstructed track and radius of $r = \sqrt{(\eta_{track} - \eta_{MC})^2 + (\phi_{track} - \phi_{MC})^2}$, where $\eta_{track}(\phi_{track})$ and $\eta_{MC}(\phi_{MC})$ are the pseudorapidity (azimuthal angle) coordinates of the reconstructed tracks and the generated charged particle, respectively. The scheme how to define R_{trk} is presented in Figure 3.9. An example of how this algorithm works is shown in Fig. 3.10:

1. for each reconstructed track (A, B, C), the MC charged particle (1, 2, 3) which is closest to the track is assigned,
2. from all pairs (A1, B1, C2) the one with the smallest distance (A1) is chosen and removed from further iterations,
3. for each reconstructed track (B, C), the MC charged particle (2, 3) which is closest to the track is assigned,
4. from all pairs (B2, C2) the one with the smallest distance (C2) is chosen and removed from further iterations,
5. for each reconstructed track (B), the MC charged particle (3) which is closest to the track is assigned.

One has to remember that such a definition implies that for one track exactly one particle is assigned.

This procedure was applied for the signal (JGJ) and background (ND) Monte Carlo samples. The considered tracks were requested to be reconstructed in the central region $(|\eta < 1.5|)$ in which the gap is expected to be produced (*c.f* Fig. 3.5). The Monte Carlo particles were required to have pseudorapidities $|\eta < 2.5|$. The results are shown in Figure 3.11. In the majority of cases ($> 95\%$), the tracks are perfectly matched to the generated particles – the distance in the $(\eta - \phi)$ plane is smaller than 0.05. A slightly higher tail in the Jet-Gap-Jet distribution is due to the fact that in these events there are no particles produced over a large regions of η. Therefore, if a fake track appears centrally, it will have a large R_{trk} value.

3.4.2 Gap computed using Reconstructed Tracks

The correlations between the half-gap size using the ATLAS reconstructed tracks and the one using generated charged particles are shown in Figure 3.12 (left). The correlations were done for three requirements:

- all reconstructed tracks with *good* quality flag (top),

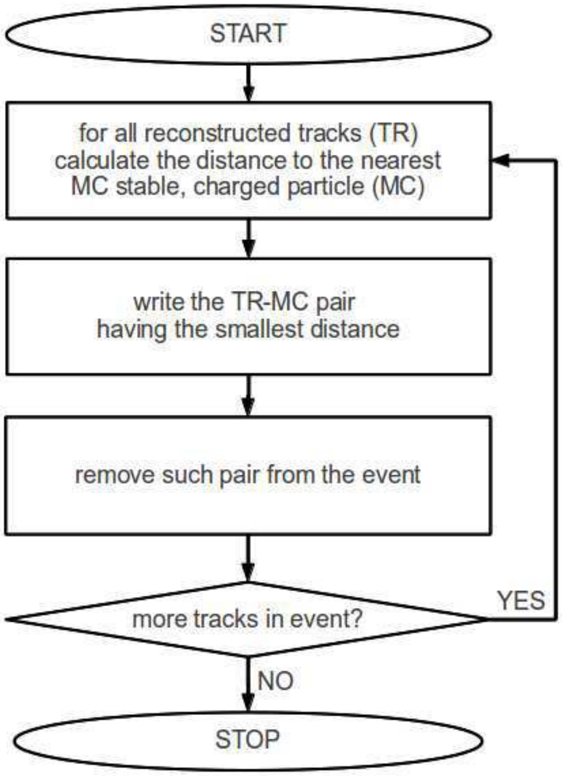

Figure 3.9: Algorithm defining the closest distance from the reconstructed object to the generated particle.

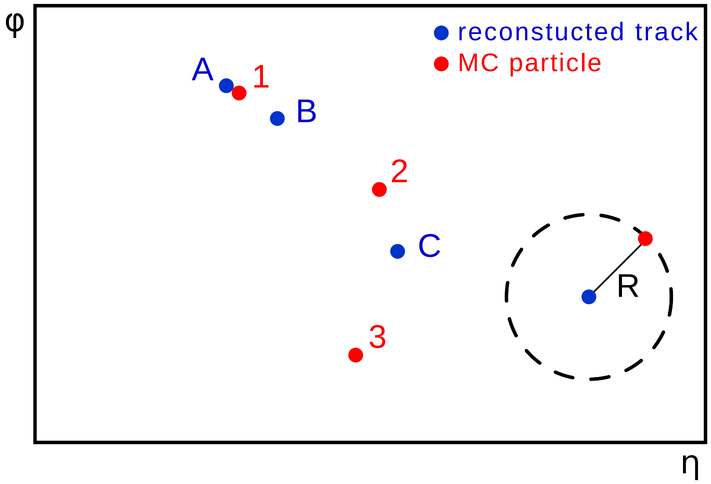

Figure 3.10: Illustration how the reconstructed tracks are matched to the closest MC particle.

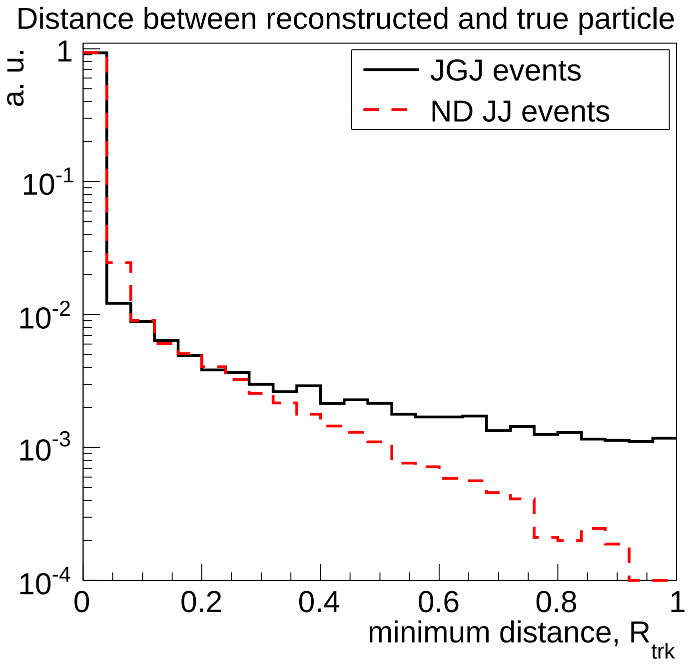

Figure 3.11: Smallest distance between the reconstructed track and the MC charged particle.

- tracks with $p_T > 200$ MeV (middle),
- tracks with $p_T > 500$ MeV (bottom).

The points on the diagonal represent perfectly reconstructed gaps. Due to the reconstruction inefficiency, in some cases the reconstructed gap is larger than the true one. A few events for which the reconstructed gap is smaller are due to the fake tracks.

In order to quantify the effects of inefficiency and fake rate, the difference, $gap(MC\ charged) - gap(reco)$, is shown in Figure 3.12 (right). These plots were prepared for both background (the Non-Diffractive Jet Production; dashed red line) and signal (the Jet-Gap-Jet Production; solid black line). Like for the correlation plots, these differences are plotted for all good reconstructed tracks (top), tracks with $p_T > 200$ MeV (middle) and with $p_T > 500$ MeV (bottom). From these figures one can see that in $\sim 95\%$ of cases the difference between the charged true particles and the reconstructed tracks is smaller than 0.1 unit of pseudorapidity. In $\sim 5\%$ of cases, due to inefficiencies, the reconstructed gap is larger than the true one calculated using charged particles. The fake tracks are marginal and cause a larger gaps for JGJ events in less than 0.5% of cases for all track definitions.

Increasing the track p_T threshold has a minor influence for the JGJ signal – in all cases the gap is properly reconstructed in $\sim 95\%$ of events. This is slightly different for background. Setting the track threshold at 200(500) MeV decreases the gap reconstruction efficiency to $\sim 90\%(\sim 80\%)$.

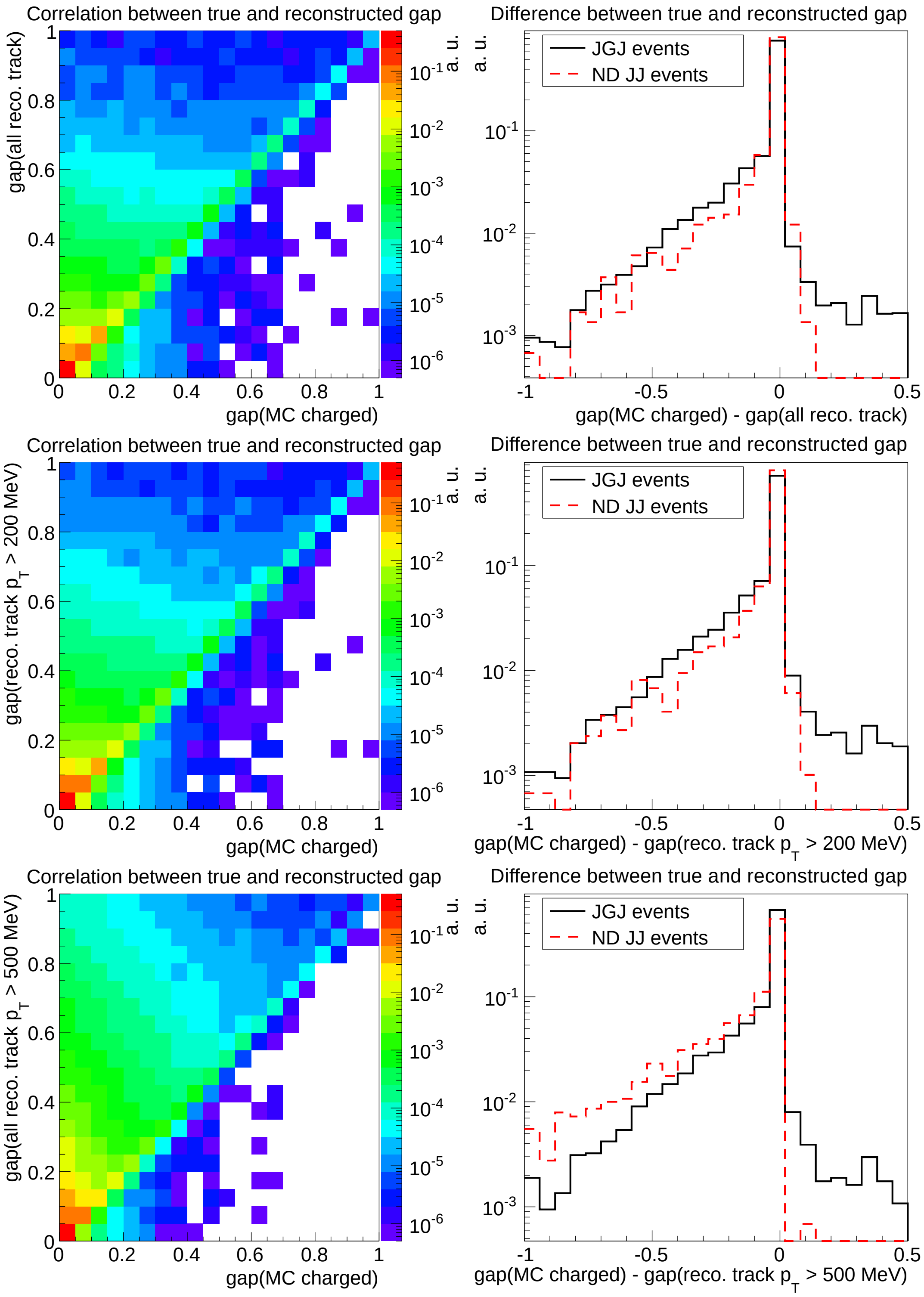

Figure 3.12: **Left:** correlations between the half-gap size obtained using the reconstructed tracks and the charged particles. **Right:** the difference between the generated charged particles and the reconstructed tracks for background (the Non-Diffractive Jet Production; dashed red line) and signal (the Jet-Gap-Jet Production; solid black line). Three track definitions are considered: all good reconstructed tracks (top), tracks with $p_T > 200$ MeV (middle) and with $p_T > 500$ MeV (bottom).

In order to judge how well the gap can be reconstructed taking into account all produced particles, the correlations between the half-gap size obtained from the reconstructed tracks and the one using generated particles are shown in Figure 3.13 (left). The difference, $gap(MC) - gap(reco)$, is shown in Figure 3.12 (right). These figures are plotted for all good reconstructed tracks (top), tracks with $p_T > 200$ MeV (middle) and ones with $p_T > 500$ MeV (bottom). For all good reconstructed tracks the difference between the half-gap using true particles and reconstructed tracks is smaller than 0.1 unit of pseudorapidity in $\sim 65\%$ of cases. Requiring higher p_T threshold worsens the results.

3.4.3 Clusters

The procedure described in Section 3.4.1 can also be applied to the calorimeter clusters. In this case one should study a variable sensitive to the accuracy of matching the reconstructed cluster to the Monte Carlo particle, R_{cl}. Due to the ATLAS magnetic field not all particles reach the calorimeter. In order to be detected, such a particle should either: carry a neutral charge or be charged and have a transverse momentum of at least of $p_T \sim 2$ GeV [4].

The results are shown in Figure 3.14. The distance in the pseudorapidity-azimuthal angle plane is larger than 0.05 in more than 80% of cases. This means that many of these calorimeter clusters originate from the noise. A high fraction of fakes makes the gap reconstruction difficult and is a reason why this method cannot be used easily in presented analysis.

It is also worth mentioning that in the standard ATLAS datasets one has only basic informations about the reconstructed clusters. However, for dedicated analyses, a Monte Carlo samples containing extended information about calorimeter cells, like the cluster size, shape, energy deposited in electromagnetic and hadronic, *etc.*, were produced. In addition, this sample contained information about the cell significance – the variable describing the amount of energy deposited in a given cell divided by its electromagnetic noise.

Having these additional informations in hands, one can study them considering two classes of events. In the first one, reconstructed clusters are close to the generated particle ($R_{cl} < 0.05$) and in the second one they are far away ($R_{cl} > 0.5$). The conclusion from these studies is that there is no clear cut that can separate these two classes.

3.4.4 Conclusions

The charged particles are properly reconstructed in more than 95% of cases (*cf.* Fig. 3.11). In $\sim 95\%$ of events the gap from charged tracks is not larger than by 0.1 unit of rapidity than the one from generated charged particles (see Fig. 3.12). The probability of reconstructing a gap not smaller than the generated one is shown in Figure 3.15. The solid red line represents the probability that the reconstructed gap is not larger than by 0.2 pseudorapidity units than the generated one (*e.g.* if the generated gap is equal to 0.8, than in 90% of cases the reconstructed

---

[4] This value comes from the relation $p = 0.3 \cdot B \cdot r$, where p is the particle momentum in GeV, B the magnetic field in T and r the trajectory radius in m.

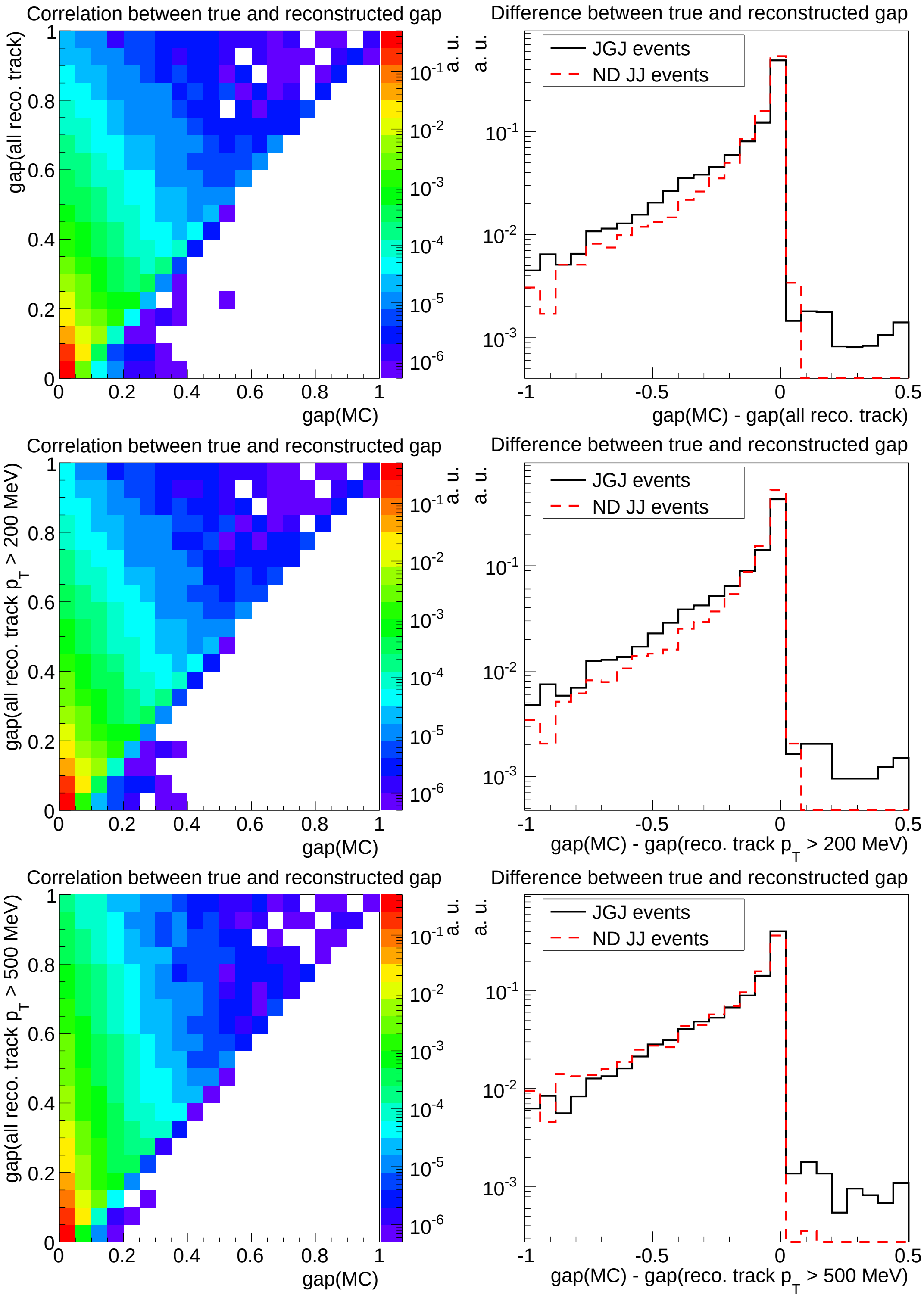

Figure 3.13: **Left:** correlations between the half-gap size obtained using the reconstructed tracks and all generated particles. **Right:** the difference between the generated particles and the reconstructed tracks for background (the Non-Diffractive Jet Production; dashed red line) and signal (the Jet-Gap-Jet Production; solid black line). Three track definitions are considered: all good reconstructed tracks (top), tracks with $p_T > 200$ MeV (middle) and with $p_T > 500$ MeV (bottom).

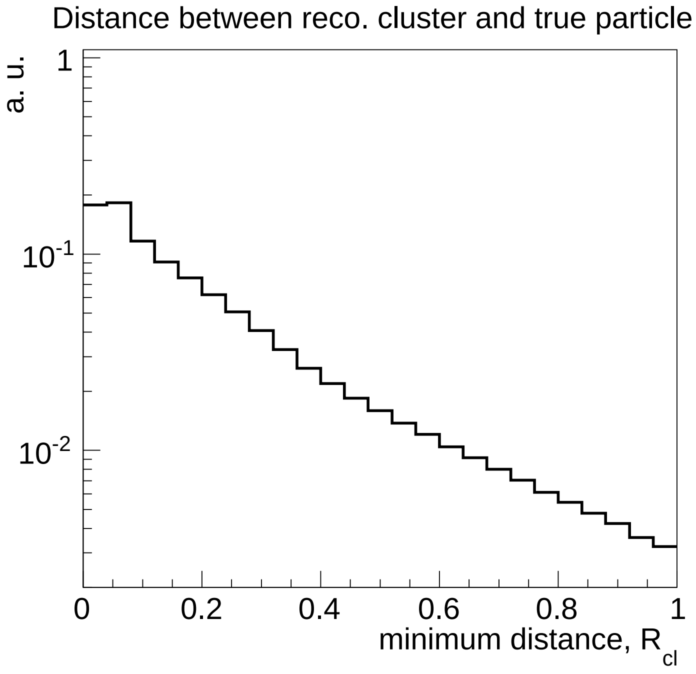

Figure 3.14: Smallest distance between the reconstructed calorimeter cluster and the MC particle.

gap will be not smaller than 0.6). The dashed green (dotted blue) line shows the probability that the reconstructed gap is not larger than by 0.1(0) than the generated one. The decrease of these probabilities as a function of the half-gap size is due to the larger phase space in which fake tracks or neutral particles can be created.

The gap reconstruction method based on the calorimeter activity suffers from the calorimeter noise. In $\sim 80\%$ of events the calorimeter clusters are further away than the MC particles by more than 0.1 in $(\eta - \phi)$ plane (see Fig. 3.14). The possible improvement of the calorimeter method, in which one considers datasets with additional informations about calorimeter cells, does not improve much the overall results. In consequence, the cluster method is not used in this analysis.

In conclusion, one has to use the gap reconstruction method based on all good reconstructed tracks. The half-gap size distributions for the Jet-Gap-Jet (red lines) and Non-Diffractive Jet (black lines) samples are shown in Figure 3.16. In this figure, normalised to the cross-section, the true half-gap size (dotted lines), the one using charged particles (dashed lines) and the one using all reconstructed tracks (solid lines) are plotted. For gaps from the reconstructed tracks, the number of events originating from JGJ production is equal to the one from ND production for a half-gap size of about 0.8. For a larger half-gap sizes, the JGJ production dominates over the ND contribution. This is better visible in Figure 3.17, where

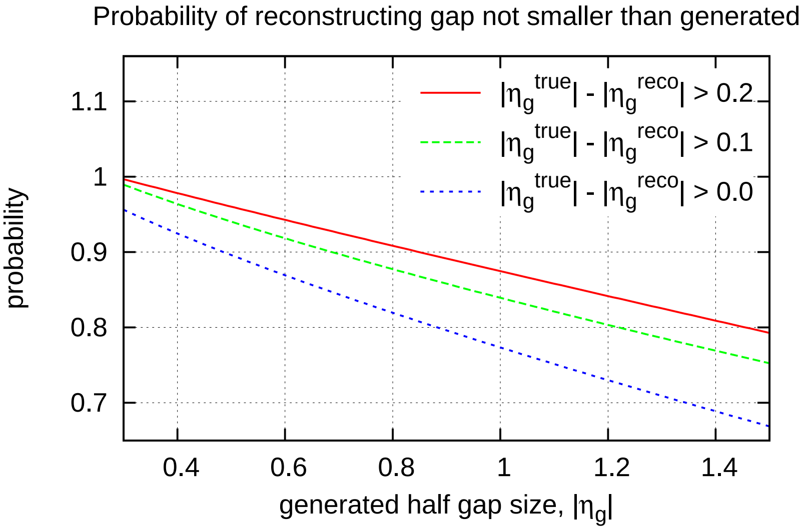

Figure 3.15: Probability of reconstructiong a half-gap not smaller than generated one. The solid red (dashed green, dotted blue) line represents the probability that the reconstructed gap is not larger than by 0.2(0.1, 0) pseudorapidity units than the generated one.

the purity of the sample as a function of the half-gap size is plotted. The purity is defined as:

$$purity = \frac{\sigma(JGJ)}{\sigma(JGJ) + \sigma(ND)},$$

where the $\sigma(JGJ)$ and $\sigma(ND)$ are the cross sections for Jet-Gap-Jet and Non-Diffractive Jet, correspondingly. The purity is greater than 0.9 for half-gap sizes larger than 1.2.

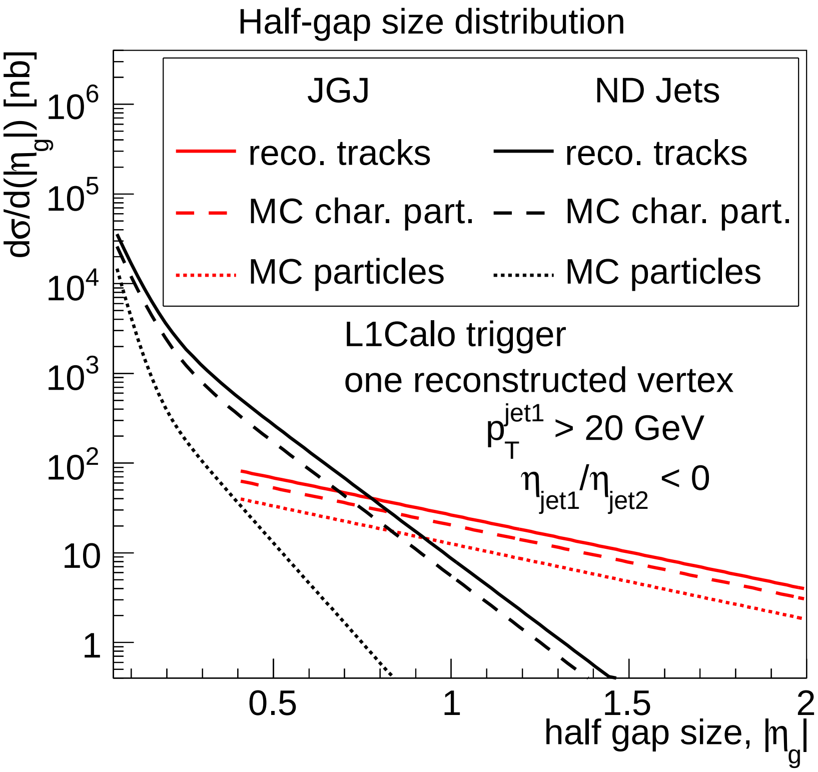

Figure 3.16: Half-gap size distribution for Non-Diffractive jets (black lines) and Jet-Gap-Jet events (red lines). The true half-gap size is plotted as dotted lines, the half-gap using charged particles as dashed lines and the one using all reconstructed tracks as solid lines.

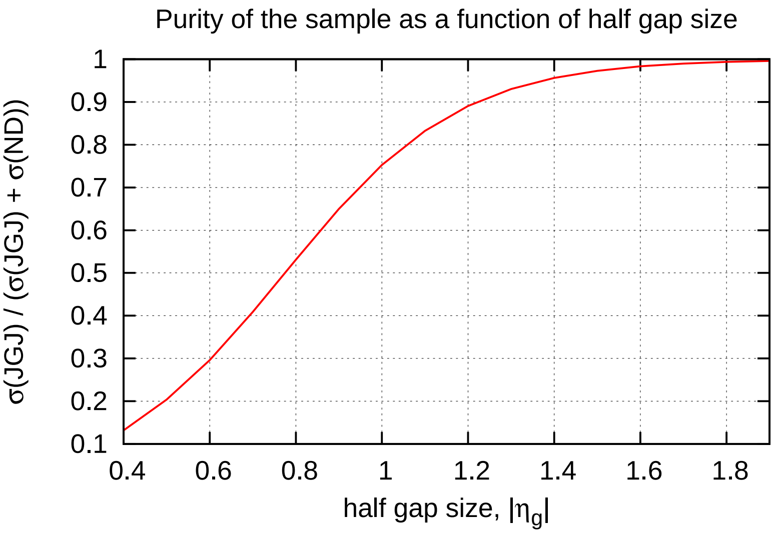

Figure 3.17: Purity of the sample, defined as a ratio of JGJ events to all events with a given gap, as a function of the half gap size. For half-gap sizes larger than 1.2 the purity is greater than 0.9.

3.5 Data – Monte Carlo Comparison

The amount of data collected by the ATLAS detector in periods A – D is equal to $\int L\ \mathrm{dt} = 339\ \mathrm{nb}^{-1}$. In the presented analysis the following requirements were taken into account:

- L1Calo trigger (see Section 3.2),
- exactly one reconstructed interaction vertex, in order to not consider events with pile-up,
- the transverse momentum of the leading jet, $p_T > 20$ GeV,
- two leading jets on the opposite pseudorapidity hemispheres,
- $|\eta_{jet1}| > 1$ and $|\eta_{jet2}| > 1$, to preselect events with larger gaps.

The comparison between the Non-Diffractive samples to the data collected by the ATLAS detector as a function of the leading jet transverse momentum, p_T^{jet1}, and difference in azimuthal angle between the two leading jets, $|\phi_{jet1} - \phi_{jet2}|$, is presented in Figure 3.18. In addition, in these plots the ratio between MC and data is shown. From these figures one can see that the Monte Carlo is in a fair agreement with data – the shapes of distributions are very similar. The average ratio is slightly bigger than 1. This is due to the NLO corrections, as discussed *e.g.* in [103].

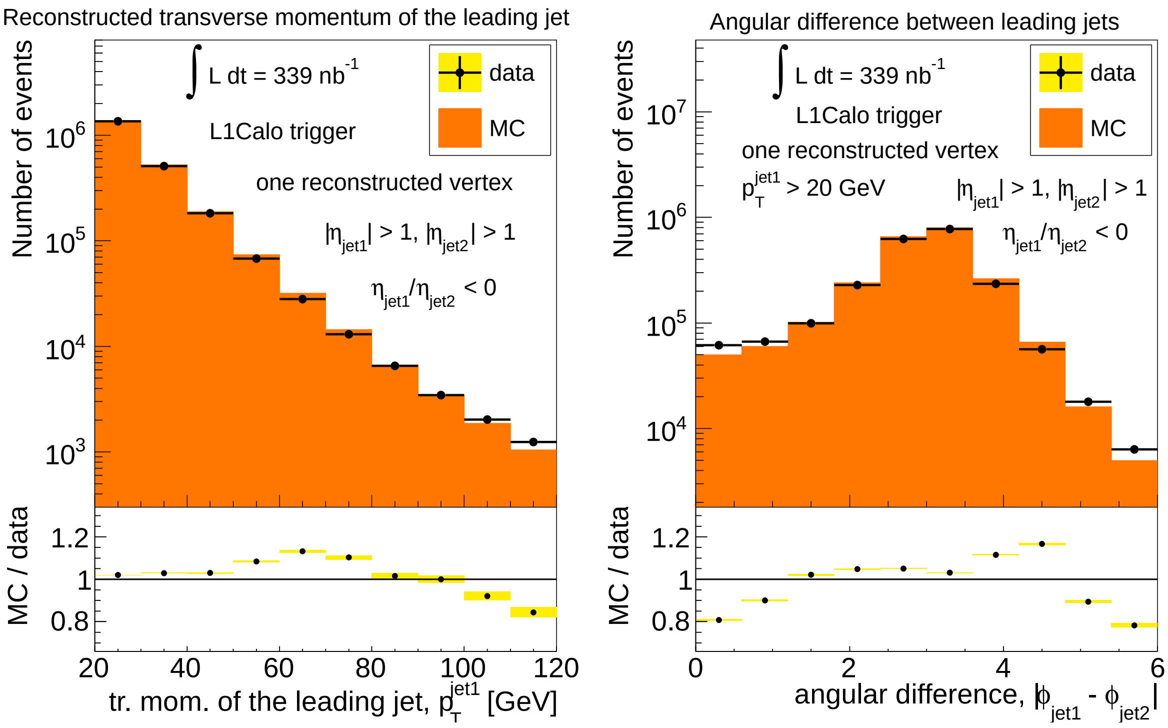

Figure 3.18: **Left:** distribution of the leading jet transverse momentum, p_T^{jet1}, for the PYTHIA 6 MC (orange area) and the ATLAS data (black points). **Right:** distribution of the difference in azimuthal angle between the two leading jets, $|\phi_{jet1} - \phi_{jet2}|$, for the PYTHIA 6 MC (orange area) and the ATLAS data (black points). For both plots the MC/data ratio is also plotted. The yellow areas reflect the statistical uncertainty.

3.6 Jet-Gap-Jet Measurement

In this section the events must fulfil the requirements listed in Section 3.5. In order to reconstruct the gap, the track method was used.

The distribution of the half-gap size is shown in Figure 3.19. The ATLAS data are plotted as black points, whereas the Non-Diffractive Jet (generated by Pythia 6) and Jet-Gap-Jet (FPMC, LL approximation) Monte Carlo are drawn as orange and blue areas, respectively. The Non-Diffractive component dominates for small gaps, as expected. For larger gaps this distribution falls steeply and data are not properly described without a contribution from the JGJ sample. Considering the combined ND and JGJ contributions, one can compare the Monte Carlo predictions and the data. Such a ratio, plotted in Fig. 3.19 (bottom), confirms that data with a large gap cannot be described with Non-Diffractive events only and a clear signal of Jet-Gap-Jet events is seen. The difference between MC and data is less than 20%.

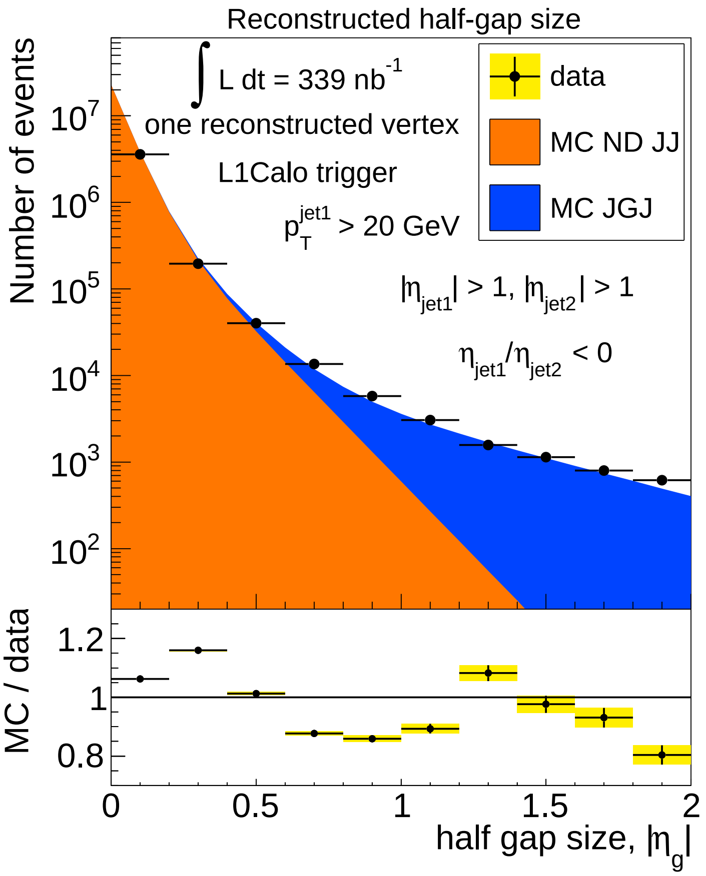

Figure 3.19: Distribution of the half-gap size reconstructed using track method. ATLAS data are plotted as black points, Non-Diffractive Jet and Jet-Gap-Jet Monte Carlo are drawn as orange and blue areas, respectively. The (MC JGJ + MC ND)/data ratio is plotted at the bottom. The yellow areas reflect the statistical uncertainty.

3.6.1 Event Displays

In order to visualise the events with large gaps, a few event displays were made. In all of them a gap reconstructed using the track method was required to be greater than $|\eta_g| > 1$. The jets were required to be on the opposite pseudorapidity hemispheres and the transverse momentum of the leading jet was set to be greater than 20 GeV.

On the figures, the Inner Detector is coloured in black, the electromagnetic calorimeter in green, the hadronic calorimeter in red and the muon chambers in blue. The jets are marked as thick dark blue brackets and the tracks are cyan lines. The track was plotted if the following requirements were fulfilled:

- distance from the primary vertex, $|d_0| < 1.5$ mm and $|z_0| < 10$ cm,
- number of hits in the pixel detector, $n_{pix} \geq 1$,
- number of hits in the SCT detector, $n_{pix} \geq 4$.

The calorimeter cell is marked yellow if the energy deposit is greater than:

- 500 MeV in LAr Layer 0 (presampler),
- 60 MeV in LAr Layer 1,
- 155 MeV in LAr Layer 2,
- 125 MeV in LAr Layer 3,
- 250 MeV in Tile,
- 2.5 GeV in HEC,
- 2.0 GeV in FCAL.

These thresholds reflect the level of the electromagnetic noise in a given calorimeter subsystem (*cf.* Figure 5.24).

The visualisation of event number 7536537 from a run 152409 is presented in Figure 3.20, whereas the distribution of energy deposit in the pseudorapidity-azimuthal angle plane is shown in Figure 3.21. One can see two jets of energy 53 GeV (at $\eta \sim -2.5$) and 54 GeV (at $\eta \sim 1.5$). Another event (number 2509915 from a run 152878) is displayed in Figure 3.22. The corresponding energy deposits are shown in Figure 3.23. In these plots, the two jets of energy 22 GeV (at $\eta \sim -3$) and 25 GeV (at $\eta \sim 2$) are visible.

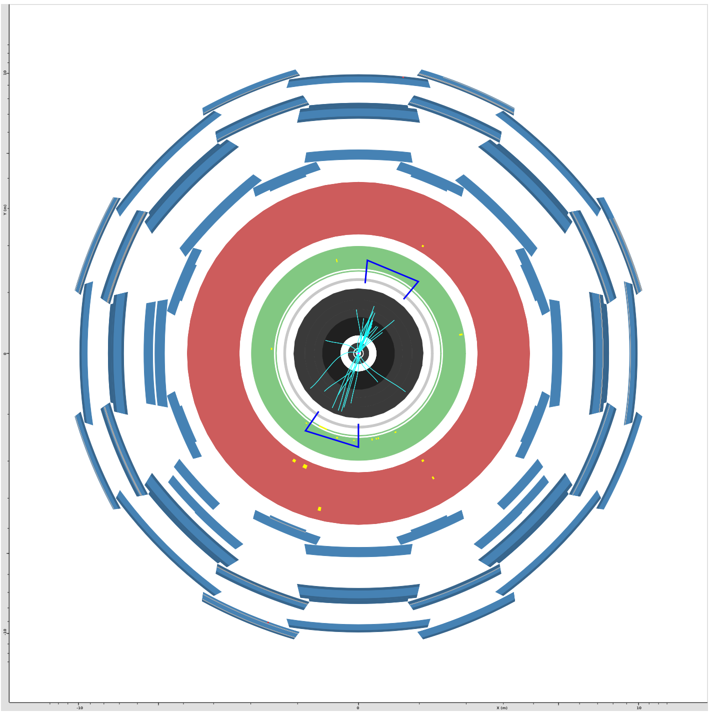

(a) front view

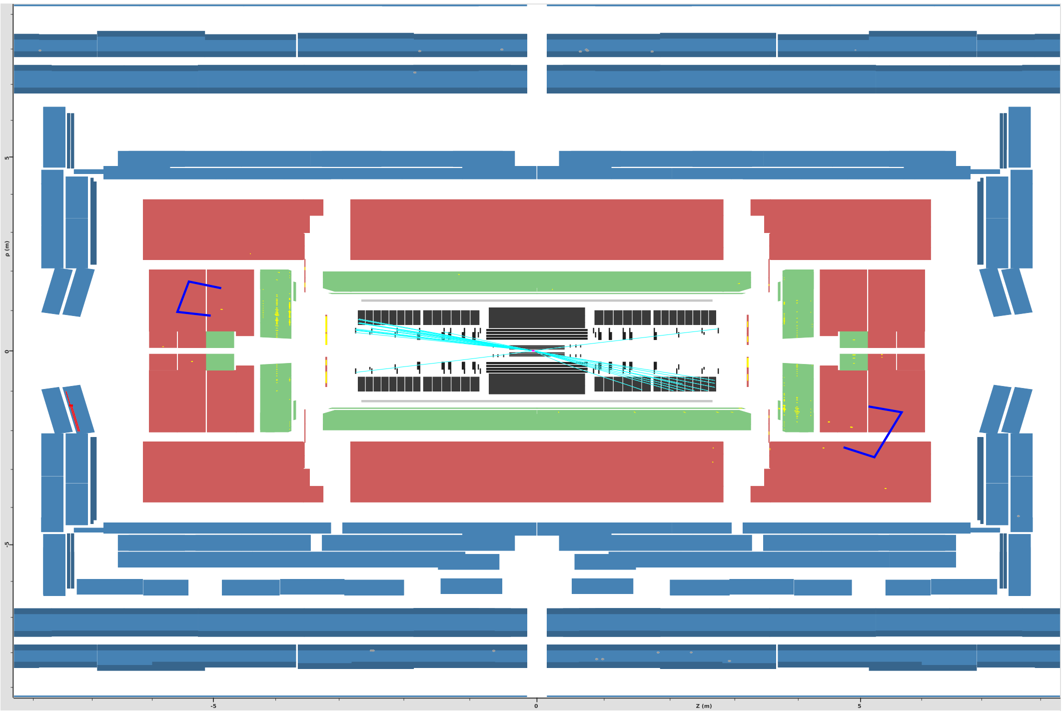

(b) side view

Figure 3.20: Display of run 1524090, event 7536537. The two leading jets have (p_T, η) of (53 TeV, -2.5) and (54 TeV, 1.5), respectively. The half-gap in rapidity using track method is greater than 1.

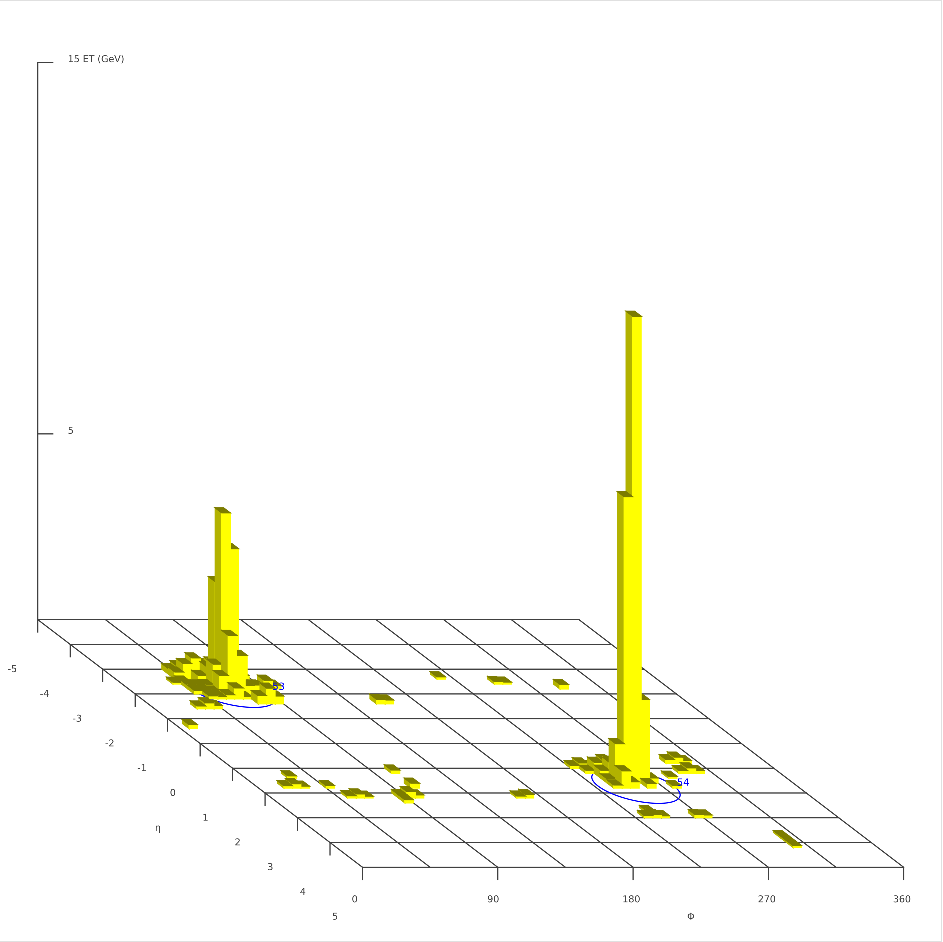

Figure 3.21: Run 1524090, event 7536537 – distribution of energy deposit in the pseudorapidity-azimuthal angle plane. The two leading jets have (p_T, η) of (53 TeV, -2.5) and (54 TeV, 1.5), respectively.

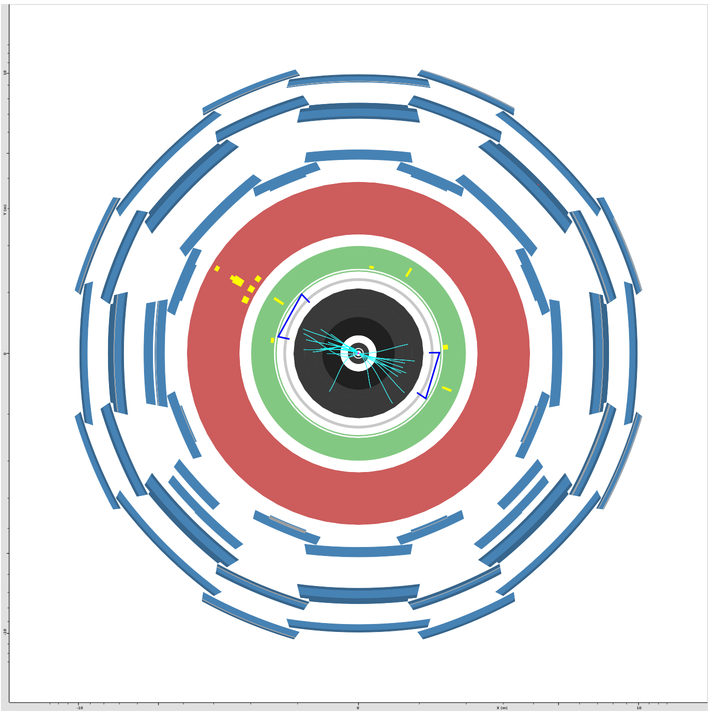

(a) front view

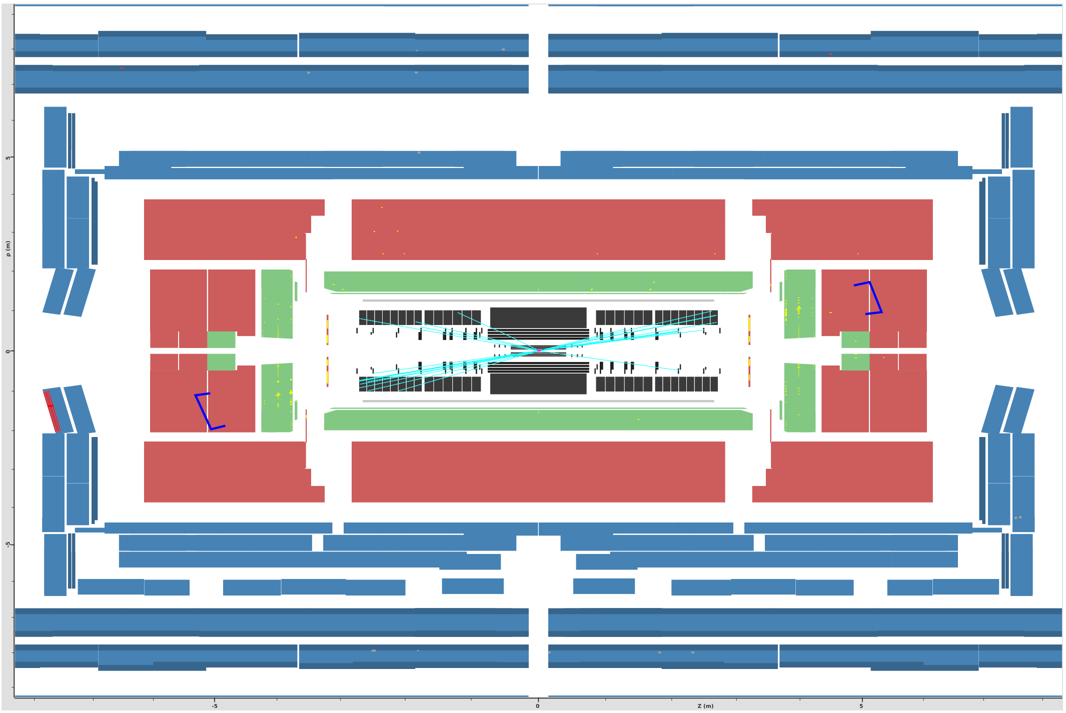

(b) side view

Figure 3.22: Display of run 152878, event 2509915. The two leading jets have (p_T, η) of (22 TeV, -3) and (25 TeV, 2), respectively. The half-gap in rapidity using track method is greater than 1.

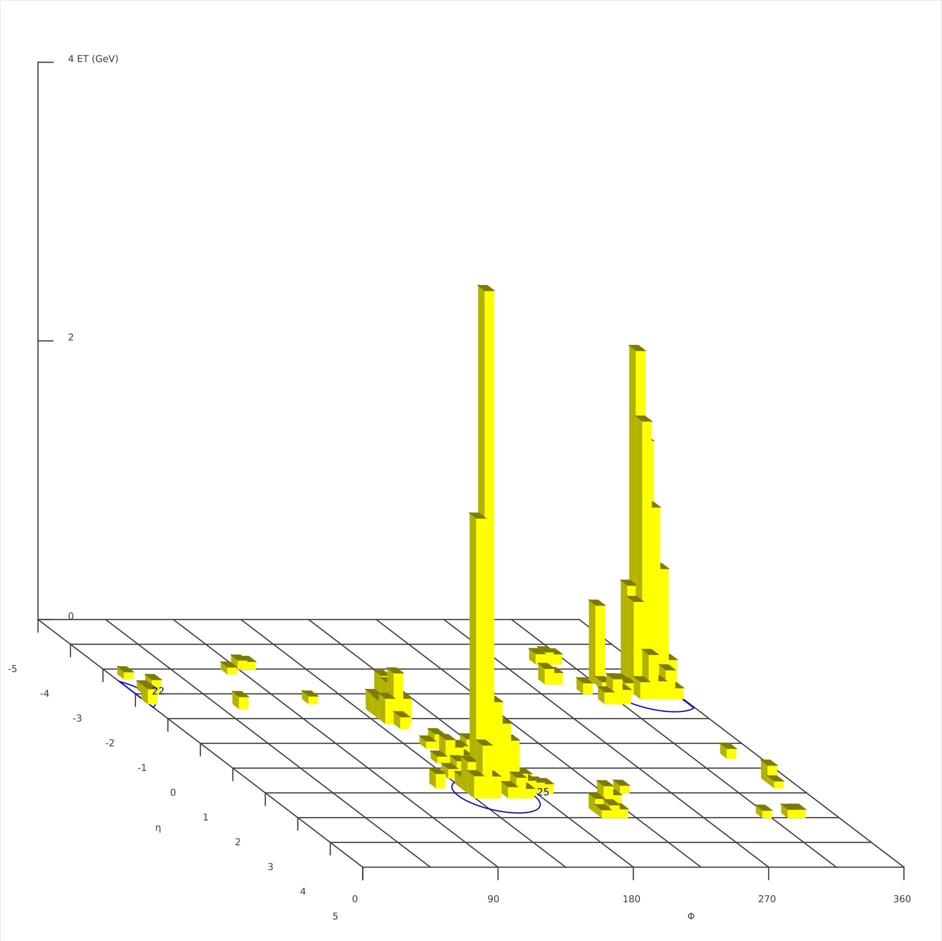

Figure 3.23: Run 152878, event 2509915 – distribution of energy deposit in the pseudorapidity-azimuthal angle plane. The two leading jets have (p_T, η) of (22 TeV, -3) and (25 TeV, 2), respectively.

3.7 Summary

The gap reconstruction method based on tracks allows the observation of the Jet-Gap-Jet events at the LHC, with the amount of data collected by the ATLAS detector in periods A – D equal to $\int L\ \mathrm{dt} = 339\ \mathrm{nb}^{-1}$. In the presented analysis the following requirements were taken into account: L1Calo trigger, one reconstructed vertex, the transverse momentum of the leading jet $p_T > 20$ GeV, two leading jets on the opposite pseudorapidity hemispheres, $|\eta_{jet1}| > 1$ and $|\eta_{jet2}| > 1$. After this selection, the Monte Carlo distributions are in a fair agreement with data.

The distribution of the gap size cannot be properly described without a contribution coming from Jet-Gap-Jet events. The Non-Diffractive sample alone predicts orders of magnitude less events that are observed in data. The ratio of combined ND and JGJ contribution to the data leads to differences not larger than 20%.

Clearly, the next step following the observation of the Jet-Gap-Jet events at the LHC, is the unfolding to the parton level. In order to do this a further, very detailed studies of the ATLAS calorimeters will be needed in order to take into account neutral particles. Having this information in hand one can measure the Jet-Gap-Jet cross section.

Chapter 4

Double Pomeron Exchange Jet-Gap-Jet Production

The measurement presented in the previous Chapter can also be performed for the Double Pomeron Exchange (DPE) Process. Compared to the original Jet-Gap-Jet measurement, the DPE process has certain advantages. For example, the observable:

$$R = \frac{\sigma(DPE\ JGJ)}{\sigma(DPE\ Jets)},$$

is much larger than the corresponding one in JGJ process. This is due to the fact that in the former process the gap survival probability factor applies to both DPE Jet-Gap-Jet and DPE Jet events, while in the latter case it applies only to the JGJ events.

In DPE JGJ events a colour singlet is exchanged between both protons and in the t-channel between the jets. In consequence, the signature, as shown in Figure 4.1, is:

- both protons stay intact and are scattered in forward regions,
- a gap in rapidity is present between the jets.

In this generator-level analysis, a gap is defined as a rapidity interval devoid of particles with transverse momentum greater than 200 MeV. The jets were reconstructed using a *cone* algorithm with R = 0.7. The differences between the used (cone) and standard ATLAS (anti-k_T) algorithms are not important at this stage of analysis.

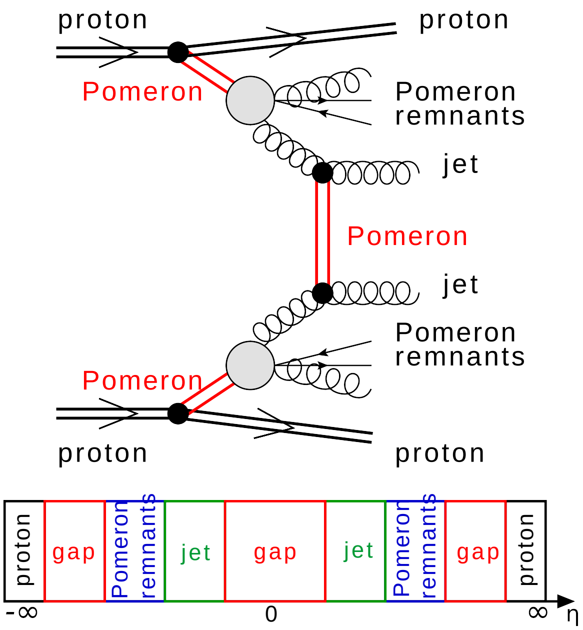

Figure 4.1: Double Pomeron Exchange Jet-Gap-Jet production: both interacting protons stay intact and two jets are produced. In both cases the object exchanged in the t channel is colour singlet and there is a gap in rapidity between the two jets.

4.1 Monte Carlo Generator

To simulate DPE events the FPMC program [104] was used. This event generator is designed to simulate central particle production with one or two intact protons and a hard scale present in the event. In the original version of this program only LL calculations were implemented without summing over non-conformal spins (see Section 1.3). Therefore, in order to perform such a sum in the LL and NLL approximations, the modifications computed in [45] were embedded[1]. In practice, the function responsible for the calculation of the elementary parton-parton scatterings was modified. The 2-to-2 leading-order matrix elements originally used in the case of central dijet production, are replaced by 2-to-2 parton-level processes in the BFKL framework. This modification accounts for the t channel exchange of a colour singlet gluon ladder with a large momentum transfer, and therefore for the presence of a rapidity gap in between the final-state jets.

In practice, the function which implements the matrix element squared for elementary parton-parton scattering was modified. Formula 1.2, which gives the BFKL $d\sigma/dp_T^2$ cross section was too complicated to be implemented directly in FPMC. In addition, it would take too much computing time to generate a reasonable number of events [4]. To avoid this issue, the parametrisation $d\sigma/dp_T^2$ as a function of the parton p_T and $\Delta\eta$ between both partons at

---

[1] This modified function is named HWHSNM in FPMC and HERWIG

generator level was used. Denoting $z(p_T^2) = \bar{\alpha}(p_T^2)\Delta\eta/2$, the parametrization is:

$$\begin{aligned}\frac{d\sigma}{dp_T^2} &= \frac{\alpha_S^4(p_T^2)}{4\pi p_T^4} \times [a + bp_T + c\sqrt{p_T} + (d + ep_T + f\sqrt{p_T}) \times \\ &\quad z + (g + hp_T) \times z^2 + (i + j\sqrt{p_T}) \times z^3 + \exp(k + lz)].\end{aligned} \tag{4.1}$$

This formula is purely phenomenological, not motivated by theory, and was introduced to obtain a very good χ^2 value while fitting Eq. 4.1 to the full expression of $d\sigma/dp_T^2$. The fit was performed with 12 free parameters $a - l$, and 2330 points were used for parton p_T ranging from 10 to 120 GeV. Formula 4.1 was implemented into FPMC with the values of $a - l$ listed in Table 4.1.

Table 4.1: Parameters values used the parametrisation function implemented in FPMC.

parameter	value	parameter	value	parameter	value
a	47.4	e	-0.298	i	10.39
b	0.0072	f	-3.112	j	1.38
c	1.57	g	120.	k	5.98
d	-121.5	h	0.557	l	-17.2

4.2 Experimental Environment

A crucial element of the DPE jet-gap-jet measurement is the possibility to tag the protons with forward detectors. In the presented analysis ATLAS is the central detector and the presence of the AFP is assumed. The overall view of the experimental setup is shown in Figure 2.31.

The produced jets will be measured in the central detector. To fulfil the ATLAS detector trigger, the leading jet is requested to have a transverse momentum greater than 40 GeV. This, rather low, value is realistic for the low pile-up LHC runs required to perform this measurement (due to the gap reconstruction). For the jet reconstruction issues, the transverse momentum of the second leading jet is required to be greater than 20 GeV. In this analysis the two leading jets are required to be in the opposite pseudo-rapidity hemispheres and the rapidity gap is required to be symmetric around zero, *i.e.* from $-|\eta_g|$ to $|\eta_g|$ with $|\eta_g| = \Delta\eta_g/2$.

4.2.1 Forward Protons

Since there are several LHC magnets between IP1 and the AFP detectors, the proton trajectory depends not only on the scattering angle but also on the proton energy. Obviously, as was discussed in Section 2.2.7, not all forward protons can be measured in the AFP detectors. Such protons can be either too close to the beam to be detected or can hit one of the LHC elements (a collimator, the beam pipe) before they reach the AFP detector. This is illustrated in Fig. 2.46, where the geometric acceptance of the AFP detector is shown. As can be observed, the region of high (> 80%) acceptance is approximately limited by $0.012 < \xi < 0.14$ and $p_T < 4$ GeV, where ξ is the relative energy loss and p_T is the proton transverse momentum (see Section 2.2.7).

Since both protons need to be tagged in the AFP stations, not all events can be recorded. In fact, the visible cross section depends on the distance between the AFP active detector edge and the beam centre (it will be varied during the runs according to the beam conditions). This dependence is presented in Fig. 4.2. For the rest of the analysis a distance of 3.5 mm is assumed, which results in a visible cross section of about 1 nb (for a leading jet $p_T > 40$ GeV). This distance, corresponding to 15σ from the beam and 0.5 mm of detector dead material, is assumed to be a probable value[2] for the AFP.

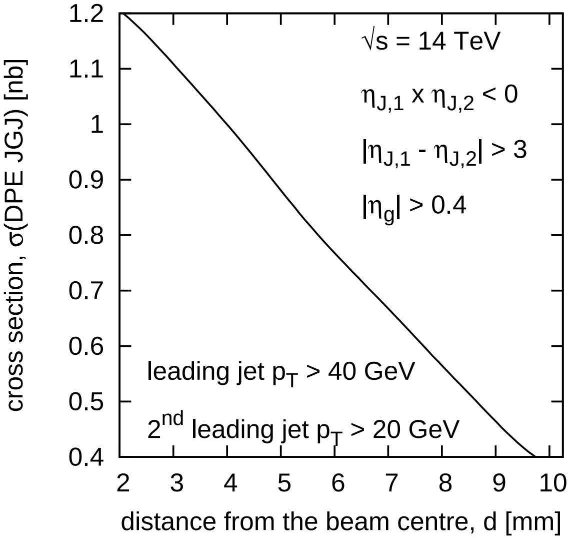

Figure 4.2: Visible cross-section as a function of the distance between the detector and the beam centre (for a leading jet with $p_T > 40$ GeV). A distance of 3.5 mm would mean 15 σ from the beam and 0.5 mm of the detector dead material.

4.2.2 Background Suppression

The main background to the DPE Jet-Gap-Jet production will be DPE inclusive jet production. Indeed, in such processes, a gap between the jets can appear due to fluctuations, but this background is significantly reduced by requiring large enough gap sizes (*cf.* Fig. 4.3 (left)). The DPE background is plotted as a continuous or dashed line whereas the DPE JGJ signal is plotted as a grey area. The probability of having a gap due to a fluctuation falls rapidly

---

[2] This value was calculated taking into account the designed LHC emittance of 3.75 mum·rad. For the emittance of 2 mum·rad the corresponding distance is 2.5 mm, as discussed in Section 2.1.3.

with the increase of the gap size. For example, if $|\eta_g| > 0.5$ the background will mimic the signal in less than 5% of cases.

Obviously, the bigger the gap size is, the larger is the DPE Jet-Gap-Jet contribution. However, the cross-section falls steeply. The jet transverse momentum distribution for three different gap sizes ($|\eta_g| > 0.6, 1.0, 1.4$) is presented in Fig. 4.3 (right). Assuming both protons being tagged in AFP, a good balance between the signal to background ratio and the visible cross-section is found for a gap between $-1 < \eta_g < 1$.

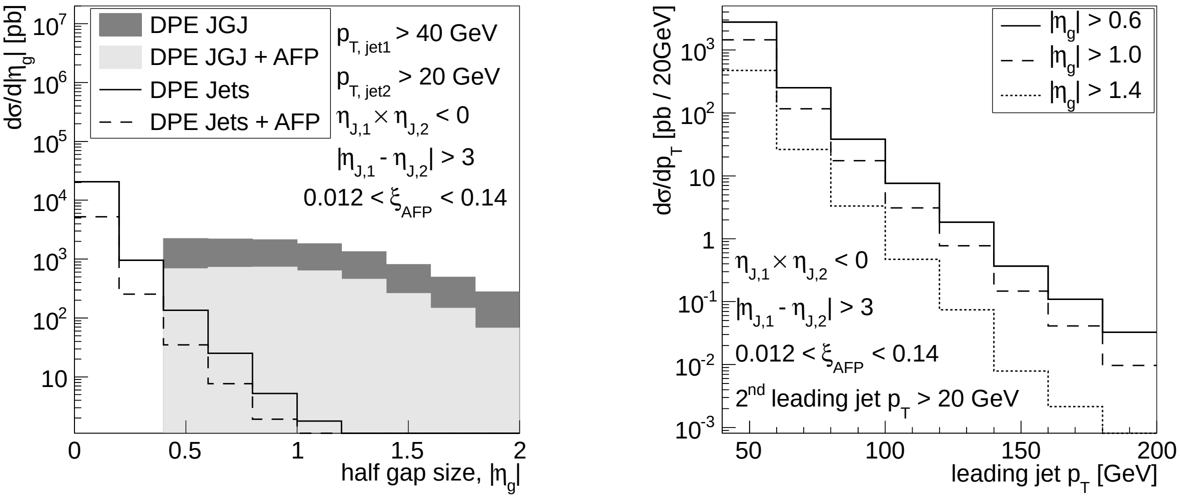

Figure 4.3: **Left**: gap size distribution for DPE jets and DPE jet-gap-jet events with and without the AFP tag requirement. For large enough gaps $\Delta\eta_g > 0.5$, the gap-between-jets events are not dominated by fluctuations in di-jets events. **Right**: jet transverse momentum distribution for different gap sizes.

4.3 Test of the BFKL Model at the LHC

The DPE Jet-Gap-Jet event ratio is plotted in Fig. 4.4 as a function of the transverse momenta of the leading jet and as a function of the pseudorapidity difference between the two jets with the highest transverse momentum, $\Delta\eta_J$. To verify the statistical power of this measurement, the statistical errors corresponding to 300 pb^{-1} of integrated luminosity were plotted. The predicted ratio slightly decreases as a function of the leading jet p_T from 0.3 ($40 < p_T < 60$ GeV) to 0.2 ($180 < p_T < 200$ GeV). Due to the AFP acceptance, it has a parabolic shape – see Fig. 4.4 (right).

To take into account the NLO QCD effects, absent in the FPMC program, the obtained DPE cross section was corrected by the ratio $\sigma(DPE\ LO)/\sigma(DPE\ NLO)$, obtained with the NLO Jet++ program [51]. This program, providing perturbative parton-level cross-sections was adapted for the diffractive applications as described in [105]. In addition, for di-jet production in proton-proton collisions, this program was independently validated by comparison with the NLO calculated by FRIXIONE [106]. Also, a cross-check of the implementation of the resolved Pomeron model into NLO JET++, the diffractive dijet cross sections have been successfully compared to the predictions of the Monte Carlo generator RAPGAP [107]. For the calculations, the Diffractive Parton Distribution Functions from the H1 2006 Fit B were used [108].

As far as the gap fraction $\sigma(DPE\ JGJ)/\sigma(DPE\ Jets)$ is concerned, there is no need to consider an additional large suppression factor for DPE Jet-Gap-Jet production on top of the 0.03 of DPE inclusive jet production [3]. Therefore, in the predictions of Fig. 4.4, all the rapidity gap survival probability should cancel.

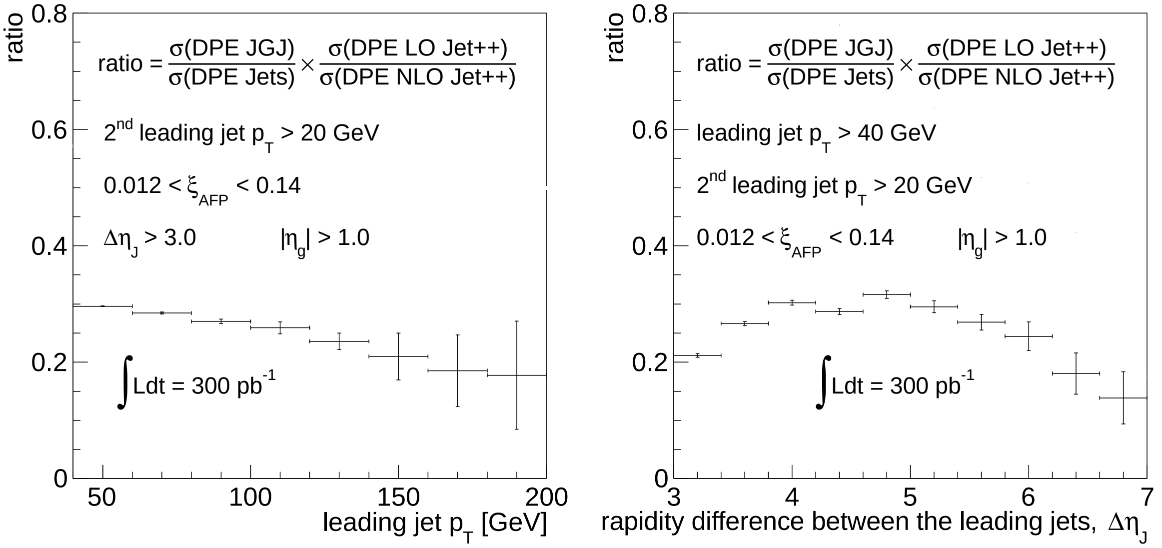

Figure 4.4: Predictions for the DPE jet-gap-jet to DPE jet cross section ratio at the LHC, as a function of the leading jet transverse momentum p_T (**left**), and of the rapidity difference between the two leading jets $\Delta\eta_J$ (**right**). For both plots, we assumed an integrated luminosity of 300 pb^{-1}.

4.4 Conclusions

The measurement of the ratio of JGJ to Non-Diffractive Jet Production can be performed for Double Pomeron Exchange (DPE) Process using protons tagged in AFP. The most important advantage is that the gap survival probability factor applies to both DPE Jet-Gap-Jet and DPE Jet events making this ratio bigger than in processes without forward protons.

The process of DPE JGJ production was embedded in the FPMC generator. For a gap defined as no particles with transverse momentum above 200 MeV, the background will mimic the signal in less than 5% of cases for $|\eta_g| > 0.5$. The $\sigma(DPE\ JGJ)/\sigma(DPE\ Jets)$ ratio is

---

[3] One should not expect this additional suppression factor to be large, due to the fact that the 2-to-2 hard scattering takes place on much shorter time scale compared to the soft interactions filling the rapidity gaps.

predicted to be about 0.25. Finally, the amount 300 pb^{-1} of integrated luminosity was shown to be sufficient to perform this measurement.

Chapter 5

Exclusive Production with Forward Detectors

The Central Exclusive Production (CEP) is a special class among diffractive processes. In these events both protons stay intact and all energy available due to the colourless exchange is used to produce the central system. In the LHC environment this means that in order to assure the exclusivity of the process, both protons scattered at small angles have to tagged in the forward detectors. As a consequence, the properties of the central system can be precisely matched to the properties of the intact protons. As it will be shown, this allows for an accurate mass reconstruction as well as introduces very powerful experimental constraints to reduce the background.

In this Chapter a possibility of measuring two interesting exclusive processes will be discussed. The first one, Central Exclusive Jet production, is a hard diffractive process, whereas the second one, Exclusive $\pi^+\pi^-$ production, is a soft one.

5.1 Central Exclusive Jet Production

The Feynman diagram describing the Central Exclusive Jet production process is shown in Figure 5.1. At the leading order the colourless exchange is represented by an exchange of two gluons. In theoretical models (like the one developed by Khoze-Martin-Ryskin, KMR [109, 110, 111, 112]) it is assumed that one gluon is hard, whereas the other one is soft. The role of the soft gluon is to provide the colour screening in order to keep the net colour exchange between protons equal to zero. The exclusivity of the event is assured via the Sudakov form factor [113], which prohibits an additional radiation of gluons in higher orders of perturbative QCD. Unfortunately, this constraint reduces significantly the cross section.

In this thesis the KMR model, embedded in the FPMC program [104], was used to simulate the exclusive signal events. The cross section predicted at the LHC energy of $\sqrt{s}$ = 14 TeV is about 0.5 nb for a leading jet with a transverse momentum greater than 150 GeV. Such a relatively small cross section implies that the collected luminosity needs to be

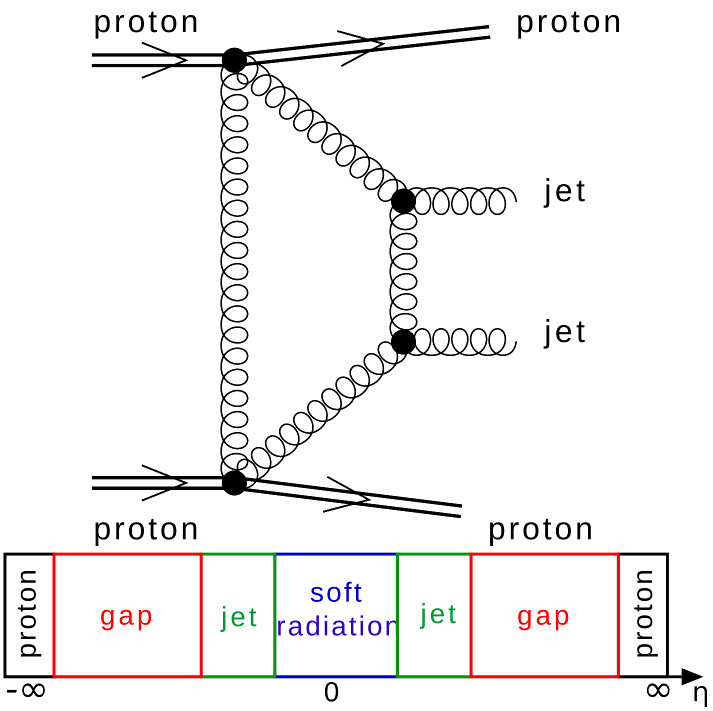

Figure 5.1: Exclusive Jet Production: both interacting protons stay intact and two jets are produced. There are no Pomeron nor proton remnants in the produced system.

large – at least of the order of inverse femtobarns. This cause a need to use all data that can be collected by the ATLAS experiment. In consequence, this process has to be measured in the high values of pile-up. In the following analysis two scenarios were considered: $<\mu>= 23$ and $<\mu>= 46$. These pile-up conditions are foreseen for the normal LHC runs, after the 2013-2014 LHC technical stop. The integrated luminosity that is assumed to be collected during these runs is about 40 fb^{-1} and 300 fb^{-1} for $<\mu>= 23$ and $<\mu>= 46$, respectively.

Operating in the high pile-up environment introduces new types of backgrounds. The signal, two hard central jets and two intact protons, might be mimicked by hard Non-Diffractive or Single Diffractive jets overlaid with intact protons coming from minimum bias events. This situation is illustrated in Figure 5.2. One has to remember that the cross sections for Non-Diffractive or Single Diffractive Jet Production are orders of magnitude higher than those of the exclusive signal (see Fig. 5.3). The third important background contribution comes from Double Pomeron Exchange Jet Production, since its cross section is about two orders of magnitude larger than the exclusive production (*cf.* Fig. 5.3).

5.1.1 Forward Protons

In soft events an outgoing proton can be produced in two different ways:

- the initial proton can stay intact, in the case of Pomeron exchange,

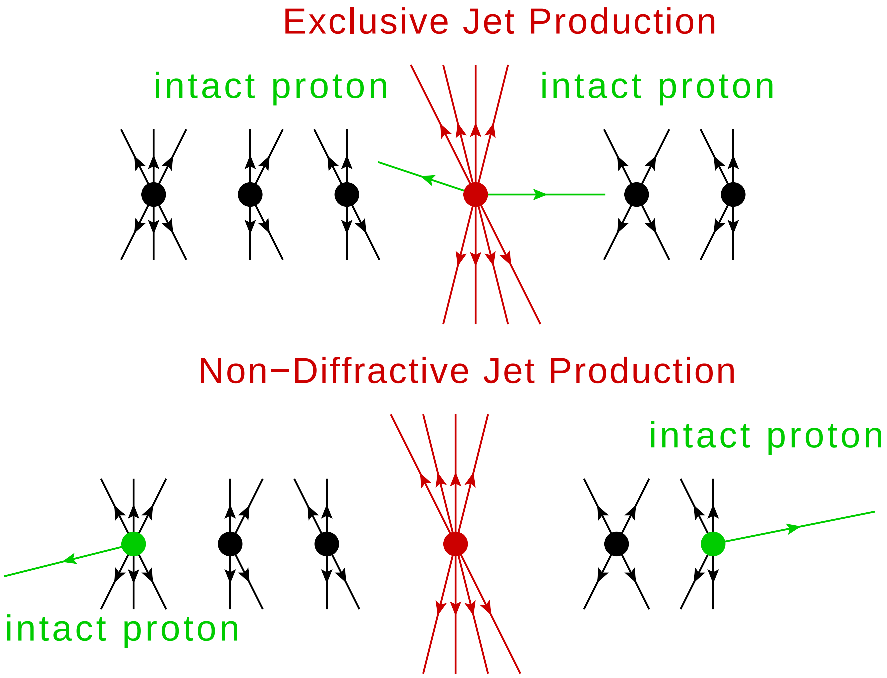

Figure 5.2: **Top**: signal – the Exclusive Jet Production – two hard central jets and two intact protons. **Bottom**: background – the Non-Diffractive Jet Production with two intact protons originating from pile-up.

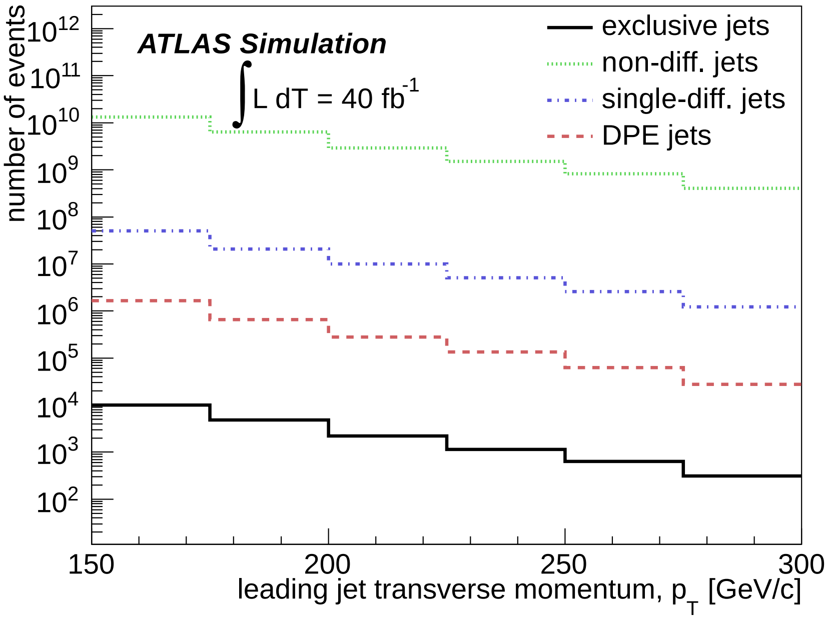

Figure 5.3: Leading jet transverse momentum distribution (p_T) for an integrated luminosity of 40 fb^{-1} and a pile-up $\mu = 23$ before the signal selection.

- the hadronisation process can produce protons in the final state.

The first mechanism is dominant in Single Diffractive and Central Diffractive processes. With the latter one, protons with small relative energy loss can appear in Double Diffractive and Non-Diffractive Processes as well as in the dissociated part of SD events as a result of fragmentation. The differences in the cross section predicted by different MC generators are quite large. The regions of $\xi > 0.1$ were never studied experimentally and, thus, the proton probability to remain intact is taken from extrapolations. In the analysis presented below, the predictions of the Pythia8 Monte Carlo were used, as the output of this generator was shown to be in fair agreement with ATLAS data – see *e.g.* [114].

The distribution of the relative energy losses of: protons, neutrons, antiprotons and antineutrons generated for Single Diffractive, Double Diffractive and Non-Diffractive Production is shown in Figure 5.4. From these plots few interesting observations can be made:

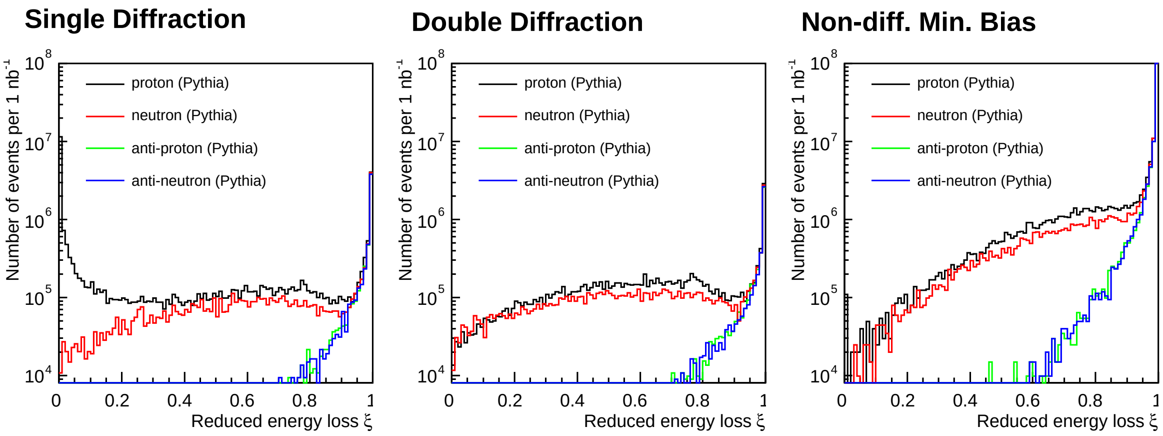

Figure 5.4: Distribution of relative energy losses of protons, neutrons, antiprotons and antineutrons generated for Single Diffraction (**left**), Double Diffraction (**middle**) and Non-Diffractive Production (**right**). Events were generated using the Pythia8 MC.

- the amount of protons, neutrons, antiprotons and antineutrons is very similar for $\xi > 0.95$,
- the amount of protons and neutrons are comparable in the case of DD and ND processes for all ξ values. For Single Diffraction they are comparable for $\xi > 0.3$,
- in the case of Single Diffraction many protons have a small relative energy loss. Moreover, their fraction is orders of magnitude larger than that of neutrons in the same region.

From these points one can conclude that protons produced in Single Diffractive Processes are mainly due to:

- Pomeron exchange for region of $\xi < 0.1$ (which lies mostly in the AFP acceptance),

- hadronisation in region of $\xi > 0.3$.

For Double Diffraction and Non-Diffractive production the protons with small energy loss come from hadronisation.

Obviously, not all produced protons will reach the AFP detector. The limiting factor is the detector geometric acceptance (see Fig. 2.46). It causes that the visible cross section for events with intact protons within the AFP acceptance is smaller than the total one. This is illustrated in Table 5.1, in which the cross section of having an event with one proton in the AFP station is presented. As can be seen, soft protons tagged in the AFP stations originate mainly from Single Diffractive Production, whereas Double Diffractive and Non-Diffractive Processes contribute only in $\sim 25\%$ of cases.

Table 5.1: Cross section and probability of having an event with a proton in the AFP detector for Single Diffractive, Double Diffractive and Non-Diffractive processes.

Process	σ [mb]	σ_{AFP} [mb]	$\sigma_{AFP}/\sigma_{tot}$
Single Diffraction	12.9	2.0	2%
Double Diffraction	8.9	0.4	0.4%
Non-Diffractive Production	57.5	0.2	0.2%

The probability of having a double tag in the event depends on the pile-up value. Its distribution is shown in Figure 5.5. As can be seen, the probability of having double tagged events (solid black line) is about $2 \cdot 10^{-4}$ for $\mu = 1$ and grows rapidly to about 0.1 for $\mu = 25$. At higher pile-up the increase is much slower and for $\mu = 50$ the probability is about 0.4.

The AFP timing detectors can significantly reduce the background originating from pile-up. The idea is as following:

1. measure the time of flight for each proton registered in the AFP station,
2. calculate the difference between the times of flight, $c \cdot (t_A - t_C)/2$, where c is the speed of light, for every proton tagged on side A with every proton detected on side C,
3. compare this difference with the hard vertex reconstructed by the central detector $|c \cdot (t_A - t_C)/2 - z_{hard}| < \varepsilon$, where ε is the uncertainty due to the reconstruction resolution of both the timing detectors and the hard vertex.

The rejection power of this constraint is demonstrated in Figure 5.5. For timing resolution of $\sigma_t = 20$ ps (blue solid line) the pile-up reduction is about one order of magnitude higher w.r.t. the requirement of a double tag. Improving this resolution to $\sigma_t = 10$ ps (red solid line) results in a further gain of a factor of 2.

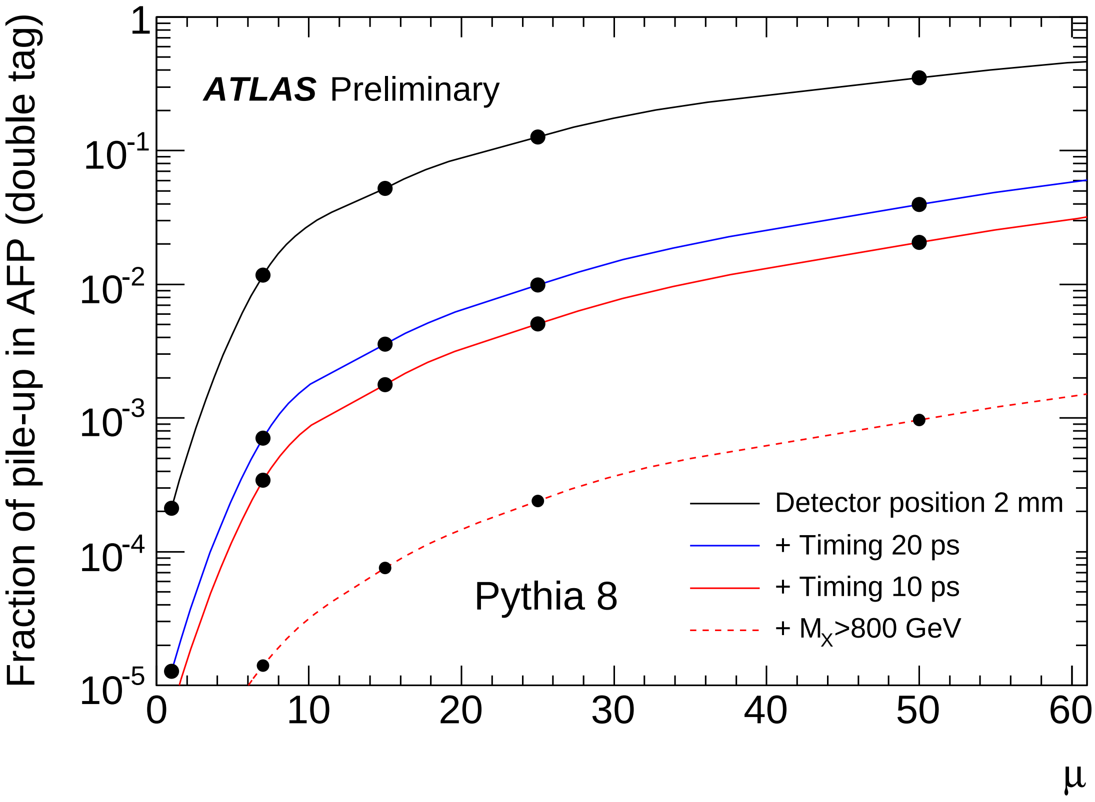

Figure 5.5: Fraction of events that passed the successive experimental selection criteria as a function of the average pile-up multiplicity, $<\mu>$. The experimental cuts are: AFP double tag with an active detector area 2 mm from the beam centre (solid black line), time compatibility with timing detectors providing a resolution of 20 and 10 ps (solid blue and red line, respectively), missing mass $M_X > 800$ GeV (dashed red line). Events were generated using the PYTHIA8 MC.

5.1.2 Monte Carlo Samples

To generate the Non-Diffractive Jets the PYTHIA8 [85] generator was used. Since in PYTHIA hard processes with intact protons, like Single Diffractive or Double Pomeron Exchange Jet Production, are not implemented, the HERWIG++ [48] was employed. To generate the Central Exclusive Jet event sample the FPMC [104] generator was used. All events were reconstructed using the ATLAS reconstruction procedure [115], in order to simulate the detector response. This procedure was slightly modified in order to include forward protons. The FPTRACKER [87] program was used to calculate the proton transport trough the LHC structures between the ATLAS IP and the AFP detectors. In order to reconstruct the proton energy and momentum from its trajectory position measurements in the AFP stations, the parametrisation and unfolding procedure, described in Appendix B and Section 2.2.7, was used.

A full list of the Monte Carlo samples is given in Table 5.2. All datasets were reconstructed for two values of $<\mu>= 23$ and $<\mu>= 46$. The Single Diffractive jet (SD JJ) samples were divided into two classes: $\mathrm{SD}^+(\mathrm{SD}^-)$ in which the diffractive proton is scattered into $beam1(beam2)$.

Table 5.2: List of signal and background Monte Carlo samples. All events were reconstructed assuming a pile-up of $<\mu>= 23$ and $<\mu>= 46$. the Single Diffractive jet samples were divided into two classes: in SD^+ samples diffractive proton is scattered into $beam1$ whereas in SD^- it is going into $beam2$.

Process	generator	p_T of the leading jet	number of events
ND JJ	PYTHIA8	140 – 280 GeV	100 000
		280 – 560 GeV	100 000
SD^- JJ	HERWIG++	140 – 280 GeV	25 000
		280 – 560 GeV	25 000
SD^+ JJ	HERWIG++	140 – 280 GeV	25 000
		280 – 560 GeV	25 000
DPE JJ	HERWIG++	140 – 280 GeV	50 000
		280 – 560 GeV	25 000
CEP JJ	FPMC	140 – 280 GeV	50 000
		280 – 560 GeV	25 000

At this stage, a few remarks need to be done about the produced samples. Firstly, it was needed to switch on special routines responsible for storing informations about the outgoing protons. In the case of pile-up such step was not possible – information about particles with $|\eta| > 6$ was not stored. Therefore, it was needed to add information about forward protons to the produced data samples. It was done in the following way:

1. minimum-bias samples (containing ND, SD and DD processes) were generated using Pythia8,
2. every forward proton was transported to the AFP station position. If it reached the detector then its spatial coordinates and four-momentum were stored,
3. the proton energy and momentum were unfolded taking into account effects like the interaction vertex smearing, the detector spatial resolution and the multiple scattering (*cf.* Section 2.2.7).

These informations were stored in the so-called *Proton Pile-up Database*. In the next step, for each reconstructed pile-up vertex in Non-Diffractive (ND JJ), Single Diffractive (SD JJ), Double Pomeron Exchange (DPE JJ) and Central Exclusive (CEP JJ) jet sample one proton from Proton Pile-up Database was added.

After this procedure all samples contained events in which there was a hard process and at least one proton in each AFP station. These samples were used to obtain the timing cut (see Section 5.1.4). In the next step, the SD JJ and ND JJ samples were reprocessed in a way that every event was passing the timing cut – the vertex reconstructed from the time of flight of protons from the Proton Pile-up Database was required to mimic the hard vertex. It is worth to stress that such an approach was needed due to the fact that requesting statistically equal, but not weighted samples, containing fully simulated events, is beyond the reasonable computing capacities.

5.1.3 Trigger

The need to operate at high luminosities causes that the installed ALFA detectors (see Section 2.2.6) cannot be used as proton taggers since they are not radiation hard. Another reason is that they are not equipped with the timing detectors which are, as will be shown in this Chapter, crucial for background reduction. In consequence, the measurement of the Exclusive Jet Production process can be done only with the proposed AFP stations (*cf.* Section 2.2.7) as the forward detectors. The AFP acceptance (see Fig. 2.46) limits the number of the exclusive events that can be tagged. The restriction on the minimal proton relative energy loss sets the limit on the smallest possible mass of the central system. The exclusivity ensures that:

$$M_X = \sqrt{s \cdot \xi_1 \cdot \xi_2},$$

where M_X is the mass of the central system and $\xi_{1,2}$ is the proton relative energy loss (see Eq. 2.2). Since for the AFP the minimal value of the proton relative energy loss is $\xi^{min} = \xi_1^{min} = \xi_2^{min} \approx 0.015$, the produced central mass is approximately limited to $M_X > 200$ GeV.

The lower limit of 150 GeV on the leading jet transverse momentum causes that there is no need to construct a dedicated trigger for this measurement. The standard ATLAS L1_J75 trigger should be unprescaled (as it was during the proton-proton data taking at the end of the year 2012, when the pile-up was about 30). In addition, as can be seen from Figure 5.6, the efficiency of this trigger is above 95% for jets with $p_T > 150$ GeV.

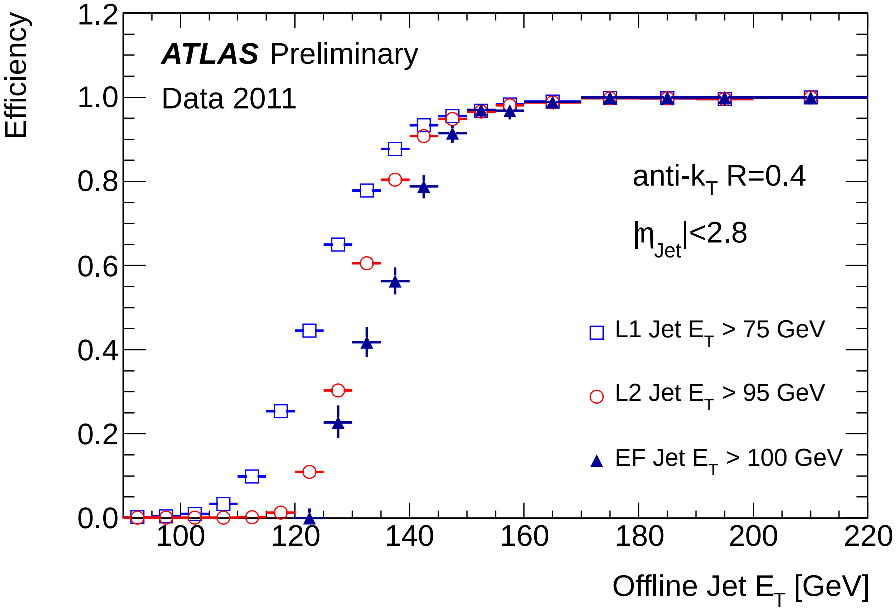

Figure 5.6: Efficiency for anti-k_t jets with $R = 0.4$ that satisfy Level 1 ($L1$), Level 2 ($L2$), and the Event Filter (EF) inclusive jet trigger for a single $L1 \rightarrow L2 \rightarrow EF$ trigger chain. Different thresholds are applied at each level of the trigger to increase the rejection of events while keeping an acceptance for events for high-p_T jets. From [97].

5.1.4 Signal Selection

Figure 5.3 clearly shows that the exclusive signal is orders of magnitude smaller than the backgrounds. Therefore, there is a need to introduce the stringent requirements concerning the data, in order to enhance the signal. First, there is a need to set the requirements for the jet quality. In this analysis both leading jets were requested not to be reconstructed as BAD nor UGLY (for the definitions, see Section 3.3).

Timing Cut

As it was mentioned before, the AFP stations are planned to be equipped with timing detectors. In the high pile-up environment it can happen that there will be more than one proton in the AFP station. If that is the case, all possible combinations between the A and C sides need to be taken into account. The reconstructed vertex (vertices) is compared with the hard vertex z position reconstructed by the ATLAS main detector, z_{hard}. The interaction vertex reconstruction resolution is typically of the order of hundreds of microns for the ATLAS main detector[1]. The AFP timing reconstruction resolution was assumed to be $\sigma_t = 10$ ps and $\sigma_t = 5$ ps for $<\mu>= 23$ and $<\mu>= 46$, correspondingly. The value of 5 ps was assumed for the measurements done after the possible upgrade of the AFP detectors during the Second LHC Long Shutdown (LS2).

The difference between the vertex z position reconstructed by the ATLAS main detector and the one reconstructed from the AFP time measurement, Δz, is shown in Figure 5.7 for exclusive signal and backgrounds. It is worth stressing that in the case where several combinations due to multiple protons in the AFP are possible, the one with the smallest Δz value was chosen. The exclusive signal is plotted as a solid black line, whereas the backgrounds are a dotted green (Non-Diffractive Jet Production), dashed-dotted blue (Single Diffractive Jet Production) and dashed red (Double Pomeron Exchange Jet Production) lines. This convention will be held for all plots in this Section.

From Figure 5.7 one can see that the Δz distribution is much broader in the cases of ND JJ and SD JJ than in the case of CEP JJ production. This is due to the fact that in the case of exclusive signal the protons originate from the same hard vertex, whereas in the other two cases they are associated to the different pile-up vertices. The tail represents the situation when (at least) one *hard* proton is lost in the beampipe and replaced by the one originating from the pile-up.

The vertical dashed lines show the value of the applied cut, $|\Delta z| < 3.5$ mm. This value was optimised taking into account the best ratio between the number of signal and the square root of the number of background events. Such a procedure was applied to optimise all cuts in this analysis.

Rapidity Fraction

Another requirement to enhance the signal-to-background ratio is related to the rapidity fraction. The rapidity of the proton system is defined as $y_X = 0.5 \cdot \ln\left(\frac{\xi_1}{\xi_2}\right)$, where ξ_1 and ξ_2 denote the relative energy loss of the protons tagged in the AFP station located on the ATLAS C and A side, respectively. The difference between the rapidity of the jet system (y_{jj}) and the rapidity of the proton system, $\Delta y = y_{jj} - y_X$, is plotted in Figure 5.8.

In the case of exclusive events there is a strong correlation between these two rapidities. The width of the distribution is due to the uncertainties coming from the jet reconstruction and the energy unfolding of the forward proton. In the case of DPE, SD and ND jet production the y_{jj} and y_X variables are not correlated. In DPE processes this is due to the presence of Pomeron remnants in the event. In the SD/ND case the correlation between the rapidity of the central jet system and the one reconstructed from the pile-up protons is purely accidental. The optimal value of the cut was found to be $|\Delta y| < 0.075$.

---

[1] The interaction vertex reconstruction resolution depends slightly on the value of pile-up, as studied in [116].

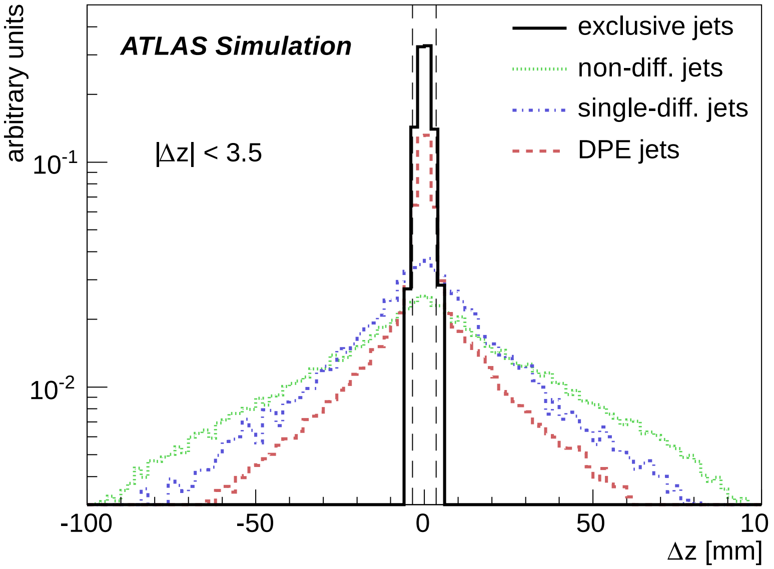

Figure 5.7: Difference between the vertex z-coordinate as reconstructed by the ATLAS main detector and the one reconstructed from the AFP time measurement. The AFP time resolution of 10 ps was assumed for background rejection. The dashed line represents the value of the applied cut at 3.5 mm.

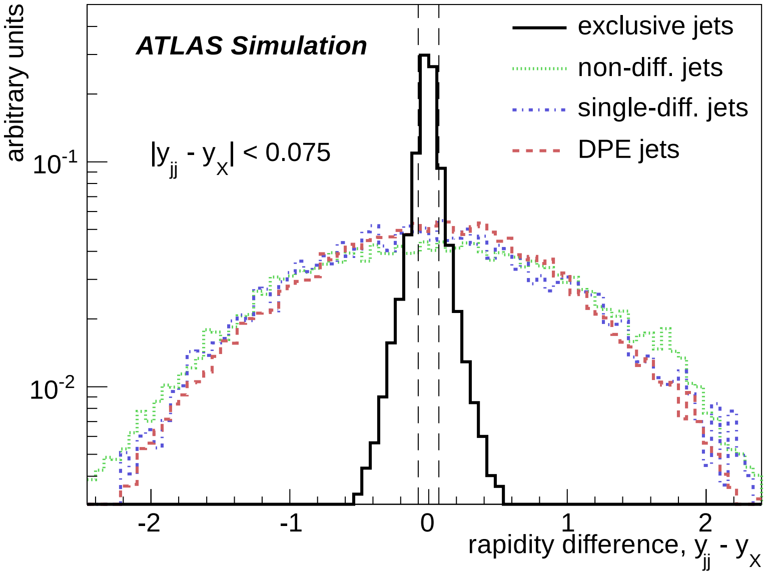

Figure 5.8: Difference, $y_{jj} - y_X$, of the rapidity of the jet system (y_{jj}) and the rapidity of the proton system $y_X = 0.5 \cdot \ln\left(\frac{\xi_1}{\xi_2}\right)$, where ξ_1 and ξ_2 are the relative energy losses of the protons tagged in the AFP C and A stations. The dashed line represents the value of the applied cut of 0.075.

Mass Fraction

The distribution of the jet mass fraction, defined as the ratio of the mass of the two leading jets produced in the event to the total diffractive mass, $R_{jj} = M_{jj}/M_X$, is shown in Figure 5.9.

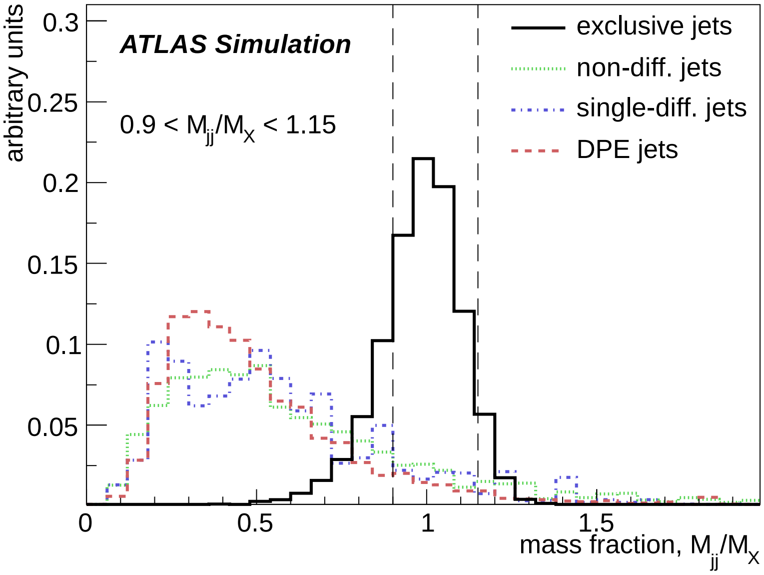

Figure 5.9: Ratio of the jet system mass to the missing mass $M_X = \sqrt{s \cdot \xi_1 \cdot \xi_2}$, where ξ_1 and ξ_2 are the relative energy losses of the protons tagged in the AFP C and A stations. The dashed line represents the value of the applied cut of $0.9 < M_{JJ}/M_X < 1.15$.

In exclusive events the produced mass is related to the system of the two leading jets. The deviation to the values different than 1 are due to the possibility of having third (forth, ...) jet in the event or due to the detector imperfection and resolution.

Jets produced in DPE processes have in most cases a mass fraction much smaller than 1. This is due to the fact that in such events a large fraction of the central mass is carried away by Pomeron remnants. The events with the values of R_{jj} of about 1 and higher are due to pile-up. In the case of SD and ND production it is worth remembering that the pile-up protons are required to be inside the AFP acceptance. This causes that the missing mass is $M_X \; > 200$ GeV. For this discriminant the optimal value of the cut was found to be $0.9 < R_{jj} < 1.15$. This cut was performed after the rapidity fraction one.

Number of Track Outside Jet System

As was mentioned before, in case of the exclusive processes,the majority of particles belong to the jet system. In consequence, it is expected that the radiation in other regions is small. In the high pile-up environment the only way to study this effect is by looking at the tracks reconstructed in the Inner Detector.

In order to choose the tracks originating from the hard vertex there is a need to introduce the quality cuts. The tracks were labelled *good* if all the following requirements were fulfilled:

- if a hit in B-layer was expected than the number of hits in B-layer has to be greater than zero; the B-layer is the layer of pixel detector located closest to the Interaction Point, used for B-jet recognition,
- number of hits in the Pixel detector, $n_{pix} > 0$,
- number of hits in the SCT detector, $n_{SCT} > 3$,
- total number of hits in the Pixel the SCT detectors, $n_{pix} + n_{SCT} > 5$.

A small change of this definition w.r.t. the Jet-Gap-Jet analysis is due to different pile-up conditions considered. The origin (hard or pile-up vertex) of the good tracks was defined by the following matching criteria:

- $|d_0|/\sigma(d_0) < 3$ [2], where d_0 is the smallest distance in the (x, y) plane between the reconstructed track and the hard vertex and $\sigma(d_0)$ is the measurement uncertainty,
- $|z_0 \cdot \sin\theta|/\sigma(z_0 \cdot \sin\theta) < 3$, where $z_0 \cdot \sin\theta$ is the smallest distance in z between the reconstructed track and the hard vertex and $\sigma(z_0 \cdot \sin\theta)$ is the measurement uncertainty.

In order to investigate the difference between signal and backgrounds, the (η, ϕ) plane was split into the three areas:

1. region outside the jet system in η,
2. region outside the jet system in ϕ,
3. region inside the jet system,

where the size of a jet is defined as three times its reconstructed width[3]. This division is illustrated in Figure 5.10.

In the case of the exclusive signal the number of tracks outside the jet system is expected to be low, due to the absence of proton and Pomeron remnants. The distribution of the number of tracks originating from the hard vertex and belonging to region 1, n_1, is plotted in Figure 5.11 (left). The number of tracks in region 2, n_2, is shown in Figure 5.11 (right). The optimal cuts were found to be $n_1 < 5$ and $n_2 < 2$.

---

[2] This value was checked to significantly reduce the contribution from tracks not related to the vertex.

[3] Jet width is a dimensionless quantity related to the jet mass, defined as $W = \frac{\sum_i \Delta R^i p_T^i}{\sum_i p_T^i}$, where $\Delta R^i = \sqrt{(\Delta\phi_i)^2 + (\Delta\eta_i)^2}$ is the radial distance between the jet axis and the i^{th} jet constituent and p_T^i is the constituent transverse momentum with respect to the beam axis [117]. The area of $W = 3$ around jet contains more than 99% of produced particles.

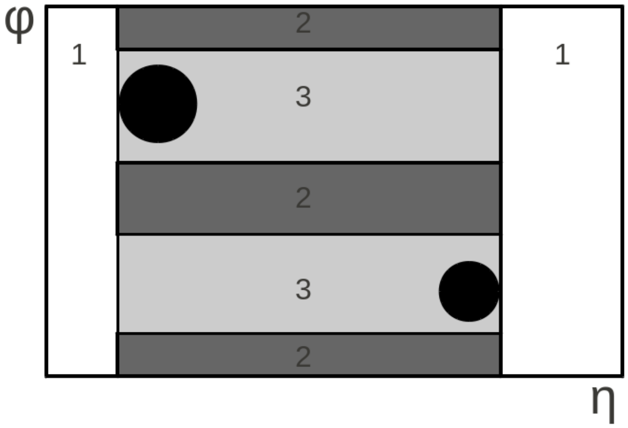

Figure 5.10: Schematic of tracks cut: region 1 corresponds to tracks outside the jet system in η, region 2 corresponds to tracks perpendicular in ϕ to the leading jet and region 3 to the one inside the jet system.

Signal Selection – Summary

The values of all cuts described above are summarised in the following list:

- two good quality leading jets with a transverse momentum of the leading jet $p_T > 150$ GeV,
- at least one proton tagged in each of the AFP stations,
- the distance between the hard interaction vertex reconstructed by ATLAS and from the one obtained from the AFP time measurement $|\Delta z| < 3.5$ mm, assuming 10 ps AFP timing resolution,
- azimuthal angle between the two leading jets $2.9 < \Delta\phi < 3.3$,
- difference of rapidity of the jet system and rapidity of the proton system $-0.075 < y_{jj} - y_X < 0.075$,
- ratio between the mass of the jet system and the missing mass $0.9 < \frac{M_{jj}}{M_X} < 1.15$,
- missing mass $M_X < 550$ GeV^2,
- mass fraction[4] $0.9 < R_j < 1.3$,
- number of tracks (*cf.* Fig. 5.10):
  - outside of the jet system (in η, region 1) < 5,

---

[4] The R_j is defined as $R_j = \frac{2E_T(\cosh\eta^*)}{M_X}$, where the E_T is the transverse energy and $\eta^* = \eta - y_{jj}$, where η is the pseudorapidity of the leading jet. This discriminant was proposed in [111] as the one that reduces the effects of final state radiation. It is strongly correlated with the Δy and R_{jj}.

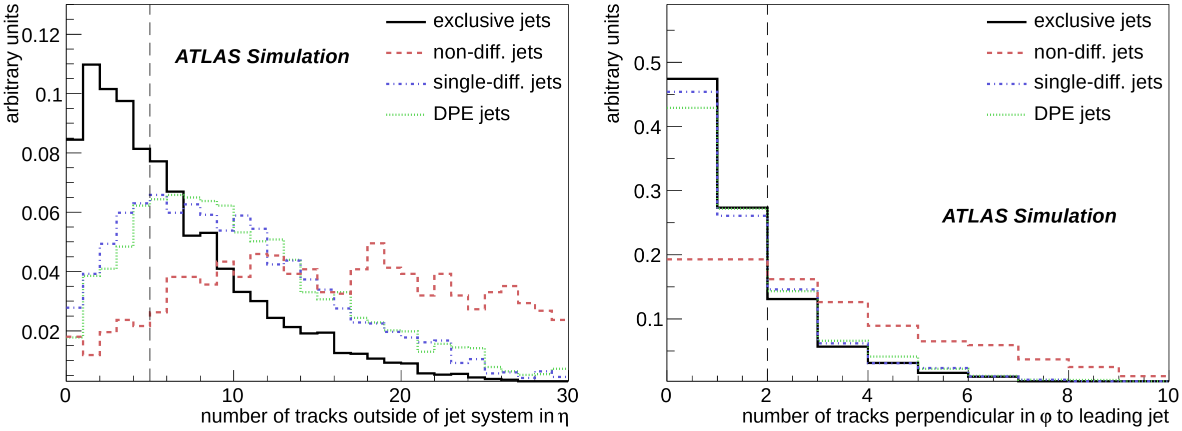

Figure 5.11: Number of tracks (fitted to the hard vertex) outside the jet system in η (**left**) and number of tracks perpendicular to the leading jet in ϕ (**right**) for signal and background events at a pile-up $\mu = 23$. The dashed line represents the value of the applied cut – $n_1 < 5$ and $n_2 < 2$.

  - perpendicular to the leading jet (in ϕ, region 2) < 3.

The evolution of the visible cross section after the cut sequence for a pile-up of $<\mu>= 23$ for signal and background is listed in Table 5.3 whereas the ratio of exclusive signal to background is shown in Table 5.4. The evolution of the number of events as a function of the cut sequence for a pile-up $<\mu>= 23$ and integrated luminosity of $L = 40$ fb^{-1} is also graphically presented in Figure 5.12. The initial signal to background ratio is about $7.60 \cdot 10^{-7}$ ($2.17 \cdot 10^{-4}$, $1.23 \cdot 10^{-2}$) for Non-Diffractive (Single Diffractive, DPE) case. After all applied cuts the signal to background ratio is about 5/9. It is worth stressing that the Non-Diffractive background was reduced by six orders of magnitude.

The analysis was repeated for the pile-up of 46 and an integrated luminosity of 300 fb^{-1}. The values of the cuts listed above were rechecked and found not to be different for the higher pile-up environment. The only exception was the Δz cut. For the AFP timing resolution of $\sigma_t = 5$ ps, the optimal range of this requirement was found to be $|\Delta z| < 2.5$ mm.

The evolution of the number of events as a function of the cut sequence for the pile-up $<\mu>= 46$ is graphically presented in Figure 5.13. After all applied cuts the signal to background ratio was about 1/13. This ratio is significantly lower than that in case of $<\mu>= 23$, mainly due to the fact that for higher pile-up the probability of having at least one proton in every AFP stations is larger.

At this point two remarks need to be done. Firstly, the beam induced background at 14 TeV is not perfectly known – if it is much higher than expected, the measurement will be difficult. Secondly, during the time the analysis was done, the vertex reconstruction algorithms were not tuned for a such high pile-up environment. Their retuning may lead to more accurate results.

Table 5.3: Signal and background cross sections in fb for a pile-up $<\mu>= 23$ after applied cuts. The background contains Double Pomeron Exchange (DPE), Single Diffractive (SD) and Non-diffractive (ND) Jets. Time resolution of 10 ps was assumed for background rejection.

Cut	$\sigma(EX)$ [fb]	$\sigma(DPE)$ [fb]	$\sigma(SD)$ [fb]	$\sigma(ND)$ [fb]
$p_T > 150$ GeV	492	$4.00 \cdot 10^4$	$2.26 \cdot 10^6$	$6.45 \cdot 10^8$
AFP	306	$2.50 \cdot 10^4$	$2.29 \cdot 10^5$	$5.86 \cdot 10^7$
$\lvert\Delta z\rvert < 3.5$ mm	209	$1.04 \cdot 10^4$	$2.78 \cdot 10^4$	$4.58 \cdot 10^6$
$2.9 < \Delta\phi < 3.3$	150	$6.51 \cdot 10^3$	$1.56 \cdot 10^4$	$2.07 \cdot 10^6$
$\lvert y_{jj} - y_X\rvert < 0.075$	92.6	399	879	$1.07 \cdot 10^5$
$0.9 < \frac{M_{jj}}{M_X} < 1.15$	65.2	24.3	62.6	$7.90 \cdot 10^3$
$M_X < 550$ GeV^2	58.7	15.1	27.5	$3.47 \cdot 10^3$
$0.9 < R_j < 1.3$	58.6	14.6	25.4	$2.84 \cdot 10^3$
tracks	24.7	2.16	4.37	38.2

Table 5.4: Signal to background ratio for a pile-up $<\mu>= 23$ after applied cuts. The background contains Double Pomeron Exchange (DPE), Single Diffractive (SD) and Non-diffractive (ND) Jets. Time resolution of 10 ps was assumed for background rejection.

Cut	$\sigma(EX)/\sigma(DPE)$	$\sigma(EX)/\sigma(SD)$	$\sigma(EX)/\sigma(ND)$
$p_T > 150$ GeV	$1.23 \cdot 10^{-2}$	$2.17 \cdot 10^{-4}$	$7.60 \cdot 10^{-7}$
AFP	$1.24 \cdot 10^{-2}$	$2.14 \cdot 10^{-3}$	$8.36 \cdot 10^{-6}$
$\lvert\Delta z\rvert < 3.5$ mm	$2.01 \cdot 10^{-2}$	$7.51 \cdot 10^{-3}$	$4.55 \cdot 10^{-5}$
$2.9 < \Delta\phi < 3.3$	$2.30 \cdot 10^{-2}$	$9.62 \cdot 10^{-3}$	$7.24 \cdot 10^{-5}$
$\lvert y_{jj} - y_X\rvert < 0.075$	$2.32 \cdot 10^{-1}$	$1.05 \cdot 10^{-2}$	$8.65 \cdot 10^{-4}$
$0.9 < \frac{M_{jj}}{M_X} < 1.15$	2.69	1.04	$8.25 \cdot 10^{-3}$
$M_X < 550$ GeV^2	3.90	2.14	$1.70 \cdot 10^{-2}$
$0.9 < R_j < 1.3$	4.01	2.31	$2.07 \cdot 10^{-2}$
tracks	11.40	5.65	0.65

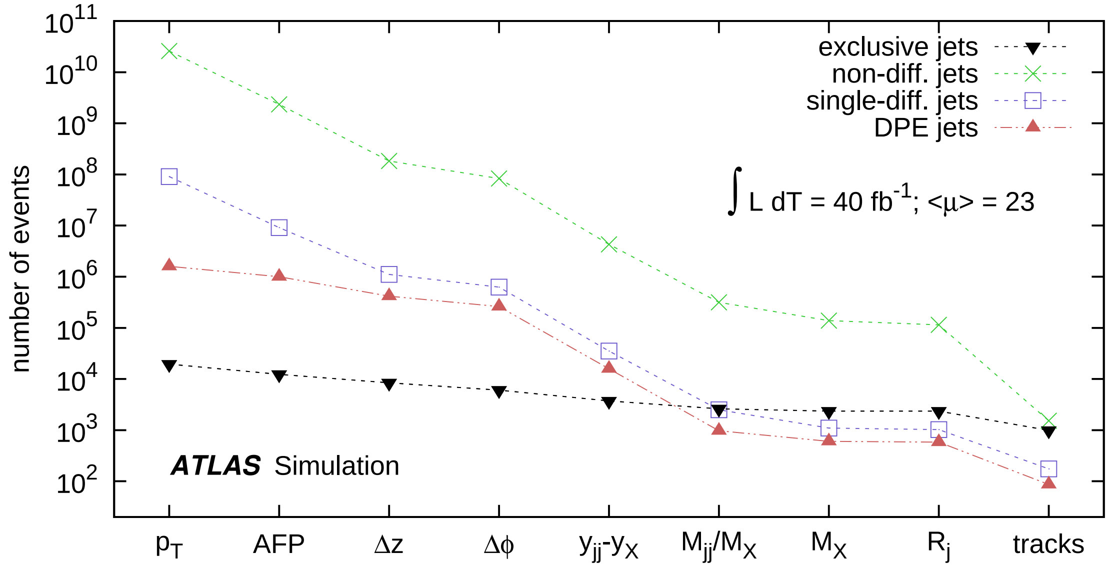

Figure 5.12: Number of events accepted after a given cut for signal (Exclusive Jet Production) and background (Double Pomeron Exchange (DPE), Single Diffractive (SD) and Non-diffractive (ND) Jet Production) for an integrated luminosity of 40 fb^{-1} at a pile-up $<\mu>= 23$ as a function of the applied consecutive cuts. The AFP timing resolution of 10 ps was assumed.

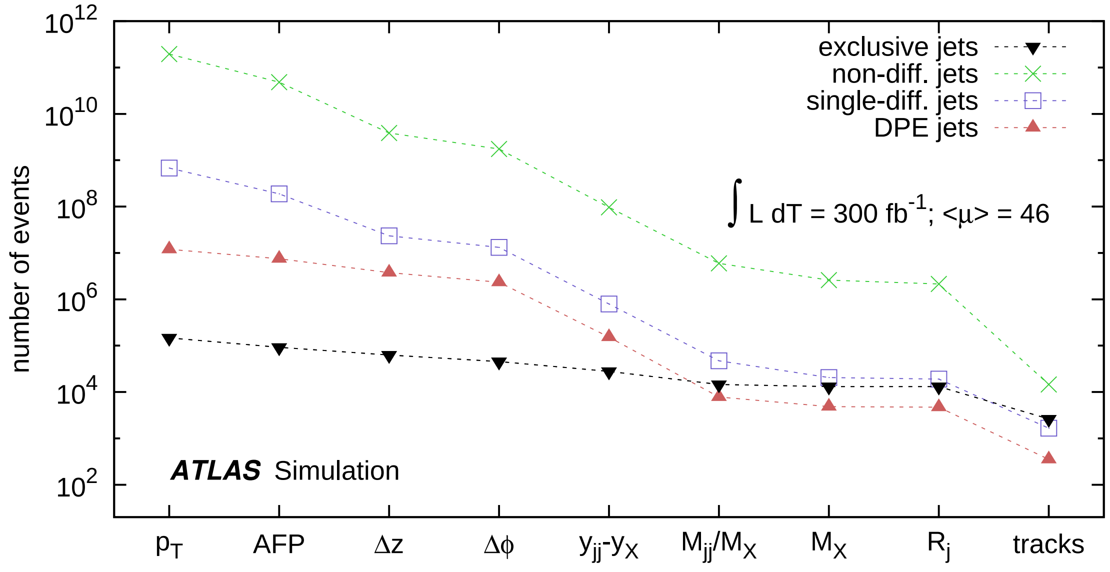

Figure 5.13: Number of events accepted after a given cut for signal (Exclusive Jet Production) and background (Double Pomeron Exchange (DPE), Single Diffractive (SD) and Non-diffractive (ND) Jet Production) for an integrated luminosity of 300 fb^{-1} at a pile-up $<\mu>= 46$ as a function of the applied consecutive cuts. The AFP timing resolution of 5 ps was assumed.

5.1.5 Results

The number of events as a function of the leading jet transverse momentum above a given threshold and the mass of the jet system after the selection for a pile-up of $< \mu >= 23$ and $< \mu >= 46$ is presented in Figure 5.14 and 5.15, respectively.

In these plots the exclusive signal is represented by a yellow area. The total number of events is marked as black points. The inner error bars show the statistical uncertainties (σ_{stat}), whereas the outer represents statistical and systematic errors added in quadrature $\sigma_{tot} = \sqrt{\sigma_{sys}^2 + \sigma_{stat}^2}$. The systematic uncertainty was calculated taking the Jet Energy Scale uncertainty (JES) and the Jet Energy Resolution (JER) into account. The JES was set to 3%, whereas the JER was considered as 4%. These values were assumed on a basis of [118] and [119]. The dashed line represents the theoretical model uncertainty – the best constraints from the Tevatron data [120, 121]. For each bin the statistical significance (S) was calculated.

In the case of $< \mu >= 23$ a statistical significance up to 18.9 σ_{stat} was obtained. For $< \mu >= 46$ and for the integrated luminosity of $L = 300$ fb^{-1} the statistical significance is still at the level of 18 σ_{stat} but the background is larger. From these results one can conclude that the constraints on the theoretical models of the exclusive production obtained from this measurement could be one order of magnitude better than the ones from Tevatron [120, 121].

5.1.6 Summary

The cross section for the Central Exclusive Jet Production is about 0.5 nb for $\sqrt{s} = 14$ TeV and a transverse momentum of the leading jet $p_T > 150$ GeV. Therefore, in order to have enough statistics, there exist a need to collect data during the nominal LHC operation – in the large pile-up environment. This condition introduces new backgrounds – the exclusive signal will be mimicked by Non-Diffractive and Single Diffractive jets with forward protons coming from soft processes. The analysis presented above was performed for two different experimental conditions:

- integrated luminosity $L = 40$ fb^{-1} and pile-up $\mu = 23$,
- integrated luminosity $L = 300$ fb^{-1} and pile-up $\mu = 46$.

The initial signal to background ratio is about 10^{-7}. Therefore, in order to make the measurement possible, there was a need to introduce effective cuts. Among them the ones with the greatest discriminating power were:

- at least one proton tagged in each of the AFP stations,
- the distance between the hard interaction vertex reconstructed by ATLAS and from the one obtained from the AFP time measurement,
- difference of rapidity of the jet system and rapidity of the proton system,
- ratio of the jet system mass to the missing mass,

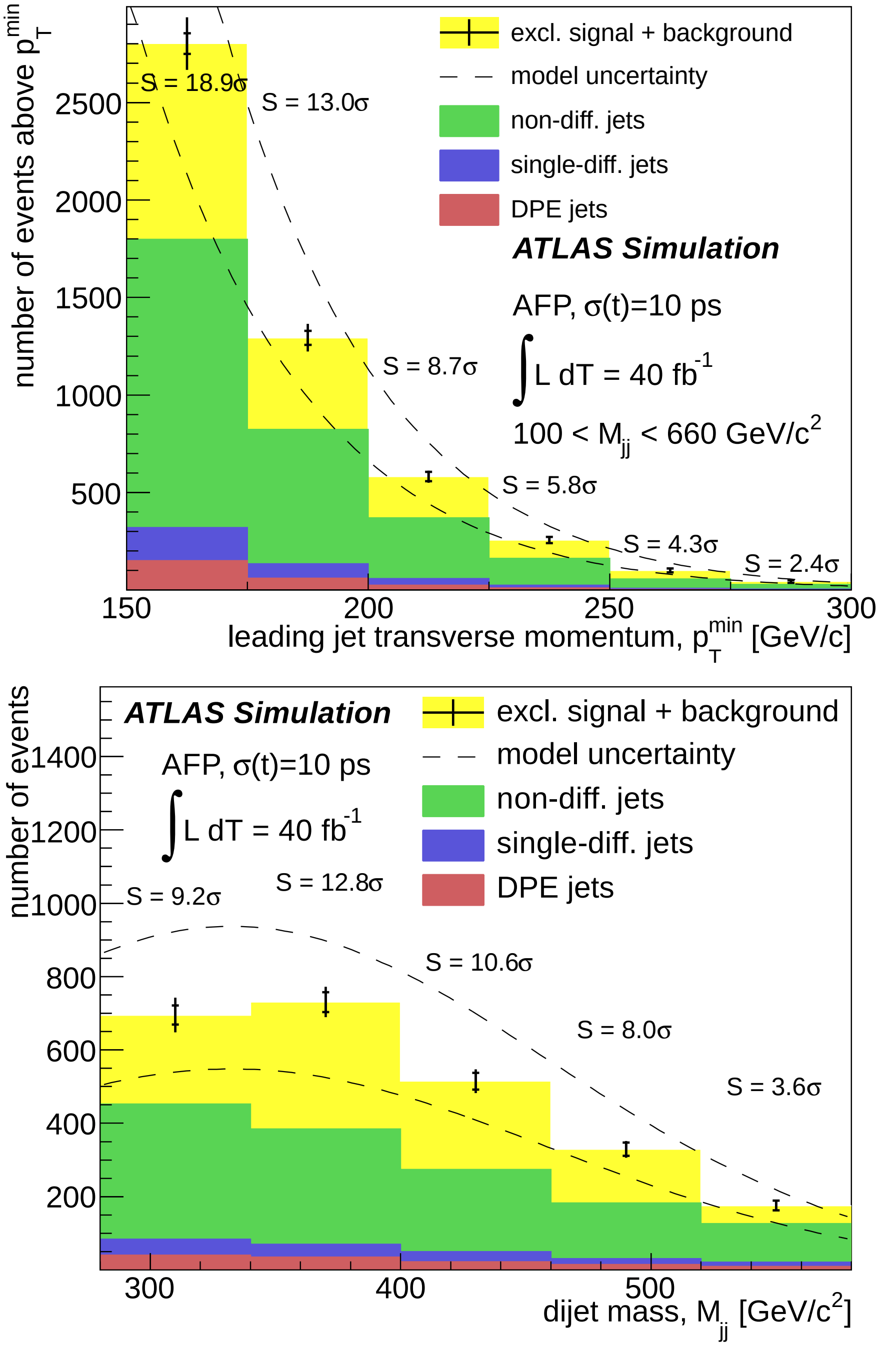

Figure 5.14: Leading jet transverse momentum distribution above a given threshold (p_T^{min}, **top**) and mass of the jet system distribution (M_{jj}, **bottom**) for signal and background events for an integrated luminosity $L = 40$ fb^{-1} at a pile-up $< \mu >= 23$. The error bars show the statistical and systematic uncertainties. The background consists of the production of Double Pomeron Exchange (DPE), Single Diffractive (SD) and Non-diffractive (ND) Jets. The dashed line represents the theoretical model uncertainty – the best constraints from the Tevatron data. For each bin the significance (S) is presented.

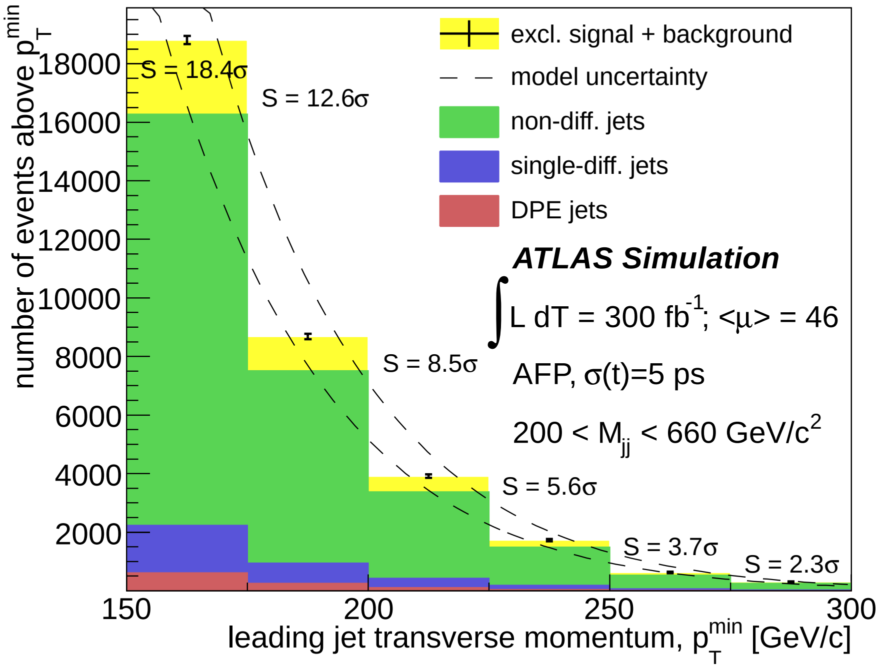

Figure 5.15: Leading jet transverse momentum distribution above a given threshold (p_T^{min}) for signal and background events for an integrated luminosity $L = 300$ fb^{-1} at a pile-up $<\mu>= 46$. The error bars show the statistical and systematic uncertainties. The background consists of Double Pomeron Exchange (DPE), Single Diffractive (SD) and Non-diffractive (ND) Jets. The dashed line represents the theoretical model uncertainty – the best constraints from the Tevatron data. For each bin the significance (S) is presented.

- number of tracks outside of the jet system in η and in ϕ.

After selection, the signal to background ratio was about 5/9 (1/13) for $<\mu>= 23$ (46). In both cases the statistical significance up to about 18 σ_{stat} was obtained, but for $<\mu>= 46$ the purity of the sample is smaller. The collected data should deliver ten times better constraints on the theoretical models than the most recent ones.

5.2 Exclusive $\pi^+\pi^-$ Production

In recent years a lot of theoretical studies were done in order to describe the soft exclusive production (see *i.a.* [122, 123, 124]). One has to remember that recent High Energy Physics experiments (*e.g.* ATLAS) are designed to measure hard processes, in which the transverse momentum of the produced particles is high – typically greater than few GeV. This tune causes that the soft, low p_T particles are at the edge of the detector acceptance as well as its reconstruction capabilities. For example, ATLAS reconstructs tracks with a transverse momentum not smaller than 100 MeV. However, the reconstruction efficiency for such low-p_T tracks is only about 10%. The efficiency grows with the transverse momentum and is about 75% for $p_T \sim 500$ MeV (see Fig. 3.8). In consequence, despite having much larger cross sections than the hard processes, soft events are often not even registered.

The $\pi^+\pi^-$ exclusive pair production was found to be measurable in these *unfriendly* conditions [2]. The measurement of the cross section at LHC energies is very interesting from the theory point of view [122]. Moreover, this reaction is a natural background for the exclusive production of resonances decaying into the $\pi^+\pi^-$ channel, such as: $f_2(1270)$, glueballs or charmonia (*e.g.* $\chi_c(0)$). It is worth mentioning that the measurements at high energies were performed at the CERN ISR for $\sqrt{s} = 62$ GeV [125, 126] and $\sqrt{s} = 63$ GeV [127] and CDF for $\sqrt{s} = 1.96$ TeV [128].

5.2.1 Production Mechanism

The formalism used to calculate the $pp \to p\pi^+\pi^-p$ process is explained in detail elsewhere [122, 124] and here only the main aspects are discussed. The dominant mechanism at high energies is sketched in Fig. 5.16. The p_a and p_b are the four-momenta of the incoming protons, whereas p_1, p_2 and p_3, p_4 are the four-momenta of the outgoing proton and pion, respectively. The π^* is an additional virtual pion necessary to produce a pion pair.

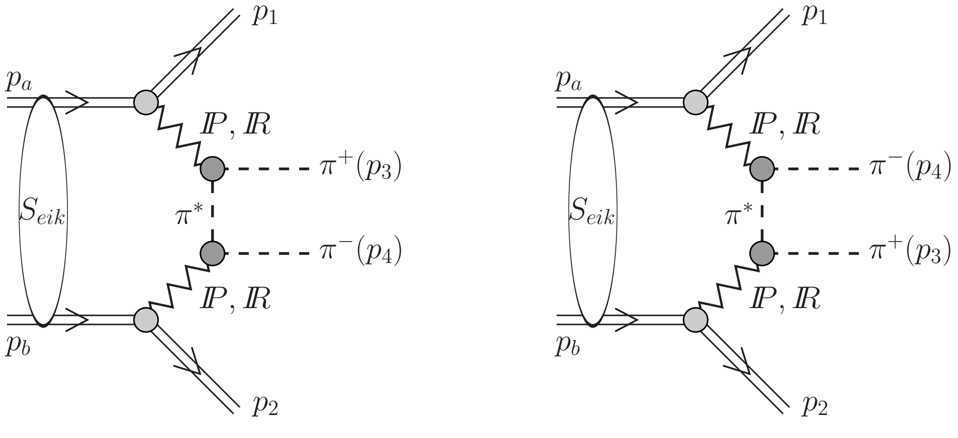

Figure 5.16: Double-diffractive mechanism of exclusive $\pi^+\pi^-$ production.

Since it is necessary to include the possibility of having additional interactions between the protons (represented in Figure 5.16 by the blob, denoted with S_{eik}), the full amplitude has to be written as a sum of the bare and rescattering amplitudes:

$$\mathcal{M}^{full} = \mathcal{M}^{bare} + \mathcal{M}^{rescatt},$$

where the bare amplitude is given by:

$$\begin{aligned} \mathcal{M}^{bare} &= M_{13}(s_{13}, t_1) F_\pi(t_a) \frac{1}{t_a - m_\pi^2} F_\pi(t_a) M_{24}(s_{24}, t_2) \\ &+ M_{14}(s_{14}, t_1) F_\pi(t_b) \frac{1}{t_b - m_\pi^2} F_\pi(t_b) M_{23}(s_{23}, t_2). \end{aligned}$$

M_{ik} denotes the coupling between the protons ($i = 1$ and $i = 2$) and the pions ($k = 3$ and $k = 4$) and $1/(t - m_\pi^2)$ is the pion propagator. The form factors, $F_\pi(t)$, are responsible for corrections for the off-shellness of the exchanged virtual pions [122]. These corrections can be parametrised as [2]:

$$F_\pi(t) = \exp\left(\frac{t - m_\pi^2}{\Lambda_{off}^2}\right),$$

where the parameter $\Lambda_{off} = 2$ GeV was obtained from a fit to experimental data [126].

The energy dependence of the πp elastic amplitudes is parametrised in terms of Regge theory by Pomeron and Reggeon exchanges. The values of the coupling constants and the Regge trajectory parameters were taken from the Donnachie-Landshoff analysis of the total and elastic cross sections for πN scattering [26]. The slope parameters of the elastic πp scattering were taken as:

$$B(s) = B_i + 2\alpha_i' \ln\left(\frac{s}{s_0}\right),$$

where $B_{I\!P} = 5.5$ GeV^{-2}, $\alpha'_{I\!P} = 0.25$ GeV^{-2} and $B_{I\!R} = 4$ GeV^{-2}, $\alpha'_{I\!R} = 0.93$ GeV^{-2}, for Pomeron and Reggeon exchanges, respectively. The value of s_0 is set to 1 GeV^2.

Due to the fact that the Donnachie-Landshoff parametrisation is not applicable in the low mass region, there was a need to introduce the proper corrections. The ones proposed in [122] allow a smooth behaviour of M_{ik} for πp subsystem masses below ~ 2 GeV.

The absorptive corrections to the bare amplitude can be written as:

$$\mathcal{M}^{rescat} = \mathrm{i} \int \frac{d^2\mathbf{k}_t}{2(2\pi)^2} \frac{A_{pp}(s, k_t^2)}{s} \mathcal{M}^{bare}(\mathbf{p}_{a,t}^* - \mathbf{p}_{1,t}, \mathbf{p}_{b,t}^* - \mathbf{p}_{2,t}),$$

where $\mathbf{p}_a^* = \mathbf{p}_a - \mathbf{k}_t$, $\mathbf{p}_b^* = \mathbf{p}_b + \mathbf{k}_t$ and $\mathbf{k}_t$ are the transverse momentum exchanged in the blob. The amplitude for the elastic proton-proton scattering was parametrised as:

$$A_{pp}(s, k_t^2) = A_0(s) \exp(-Bk_t^2/2)$$

The real part of A_0 is assumed to be negligible at high energies, whereas the imaginary part is given by the optical theorem:

$$ImA_0(s, t = 0) = s \cdot \sigma_{tot}(s).$$

In order to calculate the rescattering amplitude, the Donnachie-Landshoff parametrisation of the total and elastic pp or $p\bar{p}$ cross sections was used. The value of $B_{I\!P}^{pp}$ was set to 9 GeV^{-2}.

The cross section was obtained by integrating over the four-body phase space, which was performed numerically. In the following analysis a weighted Monte Carlo generator based on this model has been developed and used. It predicts a cross section of 230 μb for $\sqrt{s} = 7$ TeV.

5.2.2 Predictions for the ATLAS Experiment

The final state of the $pp \to p\pi^+\pi^-p$ consists of four particles – two protons and two pions. In order to tag all final state particles there is a need to have a central detector (to measure the pions) and very forward ones (to tag the protons). In this analysis ATLAS is assumed to be the central detector whereas the ALFA stations play the role of the proton taggers. The concept of the measurement is shown in Figure 5.17.

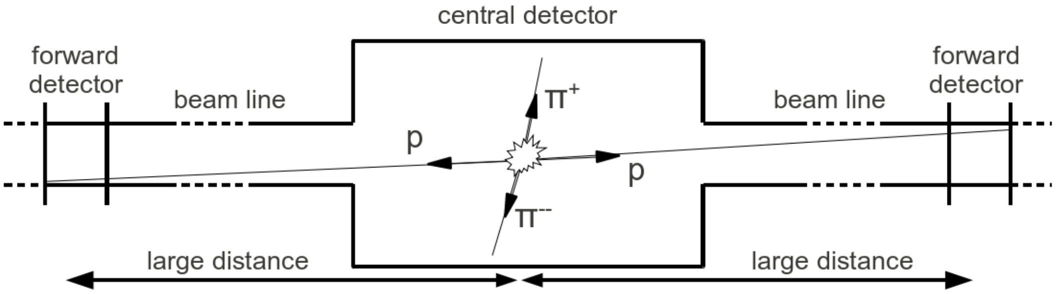

Figure 5.17: Scheme of the measurement concept – the pions are registered in the central detectors and the protons in the very forward detectors.

The phenomenological results were obtained under the following conditions:

- centre of mass energy, $\sqrt{s} = 7$ TeV,
- betatron function, $\beta^* = 90$ m,
- integrated luminosity, $L = 100\ \mu\text{b}^{-1}$,
- the distance between the ALFA detector and the beam centre, $d = 4$ mm,

which corresponds to the conditions under which ALFA collected data in 2011 (*cf.* Section 2.1.2).

Trigger

The only objects in this process that have a chance to be produced inside the acceptance of the main ATLAS detector are pions. Since this process is a soft one, they are expected to carry relatively low transverse momentum. In consequence, triggers based on the ATLAS main detectors cannot be used.

In order to register the Exclusive $\pi^+\pi^-$ production one has to use triggers based on hits in the ALFA detectors. During the *high-*β^* runs, in order to collect the elastic data, the dedicated ALFA triggers were added to the ATLAS trigger menu. Among them, the following four are very useful in the case of Exclusive Pion production:

- ALFA *symmetric* triggers:
  - signal in at least one upper ALFA detector on the side A and signal in at least one lower ALFA detector on the side C,
  - signal in at least one upper ALFA detector on the side C and signal in at least one lower ALFA detector on the side A,
- ALFA *asymmetric* triggers:
  - signal in at least one upper ALFA detector on the side A and signal in at least one upper ALFA detector on the side C,
  - signal in at least one lower ALFA detector on the side A and signal in at least one lower ALFA detector on the side C,

The scheme of the ALFA triggers is shown in Figure 5.18.

Forward Protons

The exclusivity requirement of both protons to be tagged in the ALFA detectors reduces the visible cross section, σ_{vis}. This is due to the limited acceptance of the detectors (*cf.* Section 2.2.6). The limiting parameter is the distance between the edge of the ALFA detector and the beam centre as it is illustrated in Fig. 5.19. For the presented analysis a distance of 4 mm is assumed, which corresponds to a visible cross section of 75 μb.

Since the proton relative energy loss is rather small (because of the value of the mass of the produced $\pi^+\pi^-$ system), the key variable is the proton transverse momentum, p_T, is plotted in Figure 5.20. In this figure, the dashed line represents the requirement of both protons to be tagged. This reduces the cross section by a factor of about 2. The peak of the distribution (plotted as solid line) is located in the region of high detector acceptance (see Fig. 2.27b).

Pion Pair

In this analysis the produced pions are assumed to be measured in the central detector. To ensure that the pions are detectable one has to address two items:

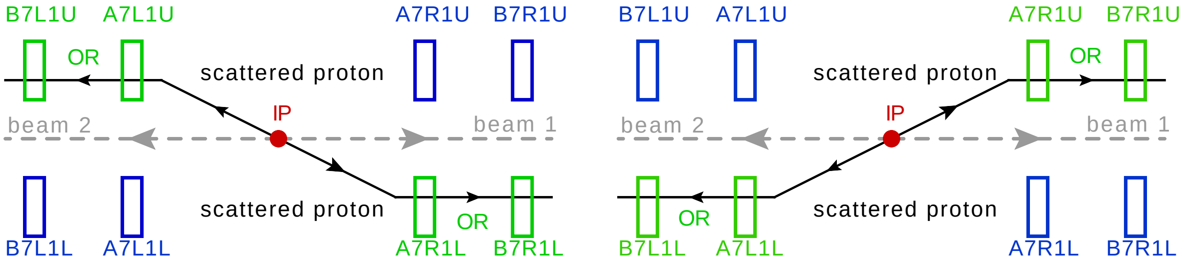

(a) (B7L1U OR A7L1U) AND (A7R1L OR B7R1L) (b) (B7L1L OR A7L1L) AND (A7R1U OR B7R1U)

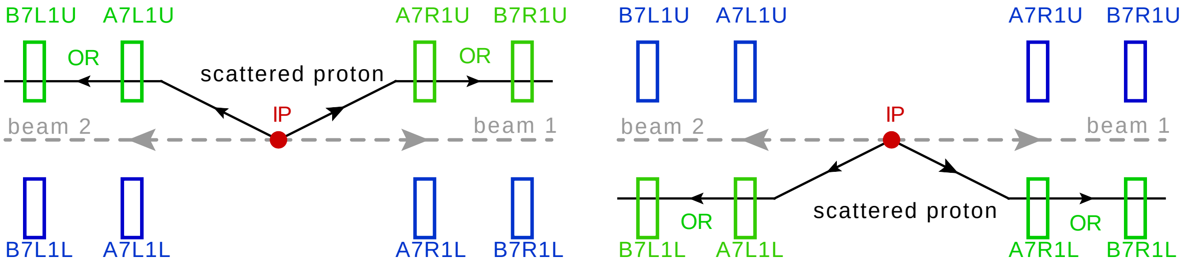

(c) (B7L1U OR A7L1U) AND (A7L1U OR B7L1U) (d) (B7L1L OR A7L1L) AND (A7L1L OR B7L1L)

Figure 5.18: Scheme of the ALFA triggers useful for the Exclusive $\pi^+\pi^-$ analysis.

- region(s) in which the pions are produced,
- distributions of the pion energy and transverse momentum.

The answer to the first item is shown in Figure 5.21 (left), where the pion pseudorapidity distribution is presented. As can be seen, the production is peaked around pseudorapidities of about 6. In consequence, a large fraction of the events cannot be detected in the ATLAS detector, due to its geometrical acceptance. Fortunately, there is a strong correlation between the pseudorapidities of the produced pions, as shown in Figure 5.21 (right). This causes that if one pion is inside the detector acceptance, it is very likely that the other one will also be detected. In consequence, the remaining visible cross section is still large enough to make the measurement possible.

Accordingly to their pseudorapidities, the produced pions can be detected in the ATLAS tracking detector ($|\eta| < 2.5$) or in the ATLAS calorimetry system ($|\eta| < 4.9$). From the experimental point of view these are two different measurements, as the tracker enables the particle momentum and charge determination, whereas the calorimeter is sensitive only to its energy. In the central region the measurement is possible using both detector systems. One has to remember that, in this case, the tracker is favoured as it provides particle charge identification. In addition, particles with transverse momentum below 1400 MeV cannot reach the calorimeter due to the detector magnetic field. Since the correlation between the pseudorapidities of both pions were found to be large, the analysis was performed independently for the tracking detector and the forward calorimetry system.

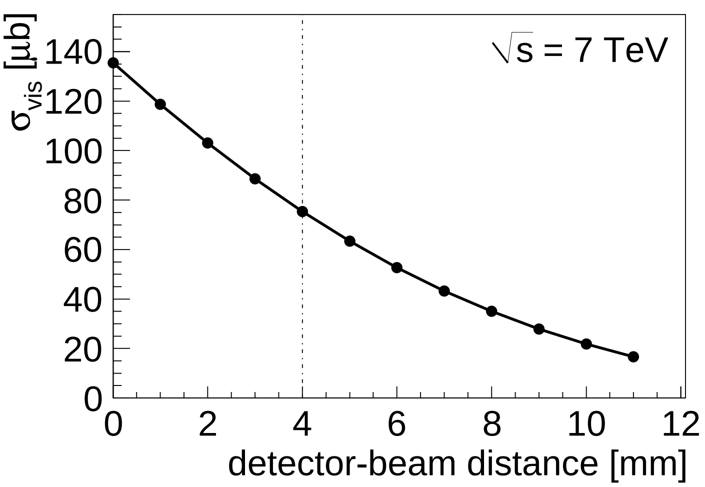

Figure 5.19: Cross section for $pp \to p\pi^+\pi^- p$ with both protons tagged by the ALFA detectors as a function of the distance between the detectors edge and the beam centre. This distance was assumed to be identical for all ALFA stations.

In the following analysis the low-p_T tracking (which allows the reconstruction of tracks down to a p_T of 100 MeV, [101, 102]) was assumed. Since process will be measured during the *high-*β^* LHC runs with low beam intensity, one can expect that the reconstruction efficiency will be higher due to the simplicity of the events containing only two tracks.

The pion transverse momentum distribution with (dashed lines) and without (solid lines) the requirement that forward protons are tagged in the ALFA detectors is shown in Figure 5.22. The shaded area marks the region where the measurement is possible taking into account the limitations on the pion minimal transverse momentum. The requirement of both protons being tagged in the ALFA detectors reduces the visible cross section value by a factor of about 3.

The impact of the minimal transverse momentum that can be reconstructed on the visible cross section is shown in Figure 5.22 (right). The visible cross section is about 12 μb for $p_T > 100$ MeV and drops to 3 μb for $p_T > 500$ MeV. This plot clearly shows that the low-p_T tracking plays a crucial role in this analysis.

The pion energy distribution with (dashed lines) and without (solid lines) the requirement that forward protons are tagged in the ALFA detectors is shown in Figure 5.23. This measurement might be influenced by the calorimeter noise. This effect can be quite high, especially in the forward calorimeter region as shown in Figure 5.24. In order to be well above the noise, one needs to select particles of correspondingly higher energies. In this analysis the pion energy was required to be $E > 4$ GeV, which gives the visible cross section value of about 9 μb.

The sum of the visible cross sections from the tracker ($|\eta| < 2.5$) and the calorimetric ($2.5 < |\eta| < 4.9$) measurements results in the total visible cross section of about 21 μb. For 100 μb^{-1} of integrated luminosity this means the sample size of about 2000 events. This should

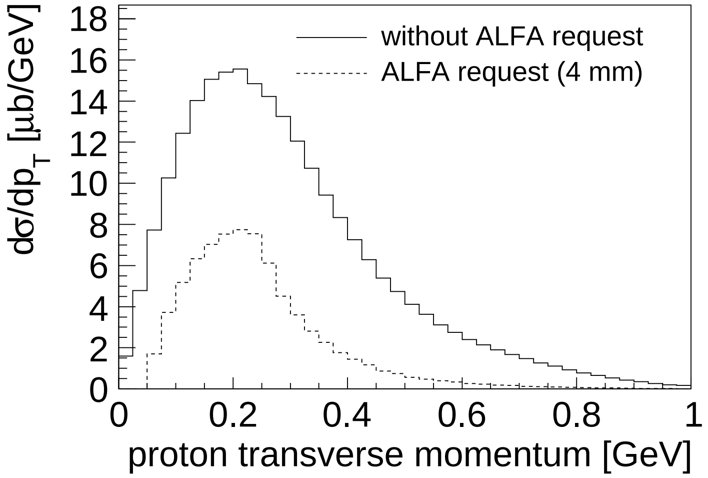

Figure 5.20: Proton transverse momentum distribution; the dotted line gives the distribution for the events with both protons tagged by ALFA detectors positioned at 4 mm.

be sufficient not only to measure the cross section, but also to study various distributions from which the most important ones is the pion system invariant mass distribution. The predictions are shown in Figure 5.25. The data contain a sub-sample of the pion pairs that fulfil $|\eta_{3,4}| < 2.5$.

5.2.3 Summary

It has been demonstrated that events due to the exclusive pion pair production process can be measured with the ATLAS detector and the ALFA stations used as the forward proton taggers. For $\sqrt{s} = 7$ TeV and $\beta^* = 90$ m, the collected data sample should be enough to measure the cross section and various distributions, especially the invariant mass of the produced pion system.

As can be concluded from Fig. 2.27, the change of the betatron function should have a minimal impact on the detector geometric acceptance in the phase space region in which the protons are scattered. In consequence, this process should be measurable in the LHC runs, in which the ALFA detectors collected data.

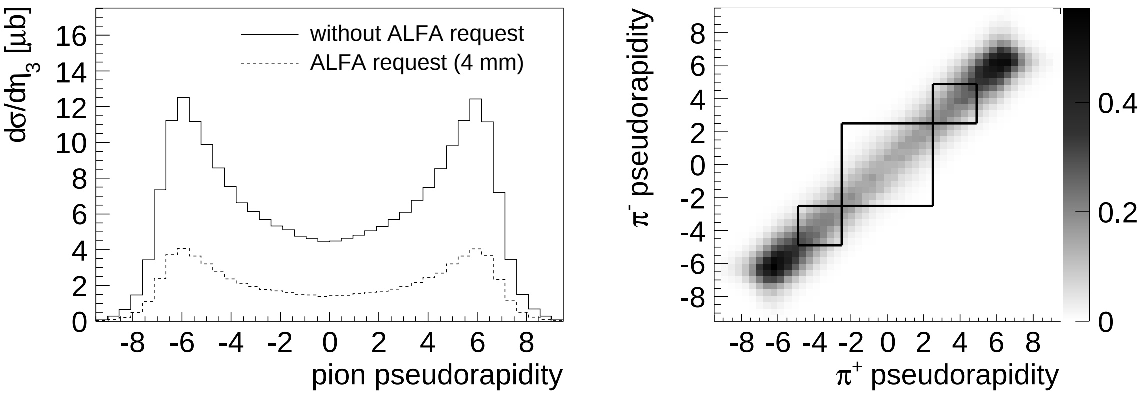

Figure 5.21: **Left**: total cross section as a function of pion pseudorapidity. **Right**: correlation between the pseudorapidies of the black frames represent regions of tracker and forward calorimeters.

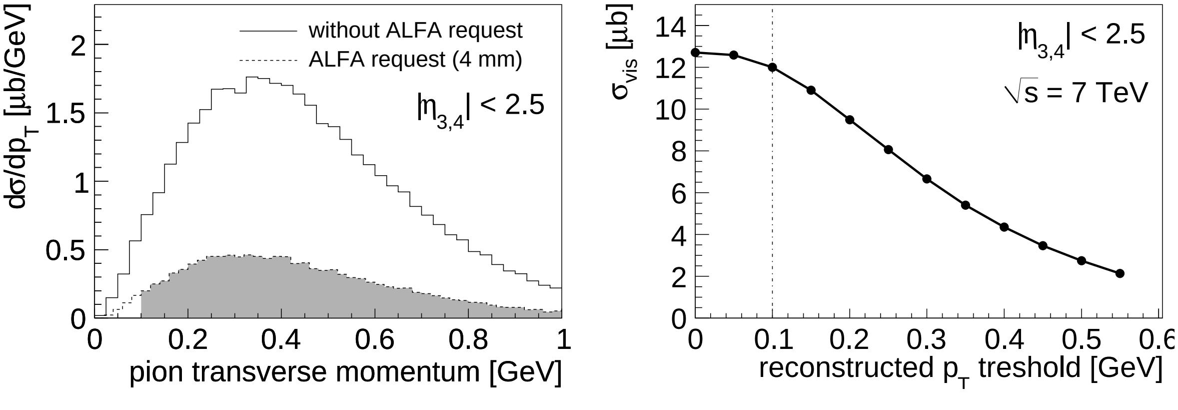

Figure 5.22: **Left**: pion transverse momentum distribution in the tracking detector. **Right**: cross section for $|\eta| < 2.5$ as a function of p_T threshold. The grey area and the dash-dotted line indicates the lower limit of the region accessible by ATLAS.

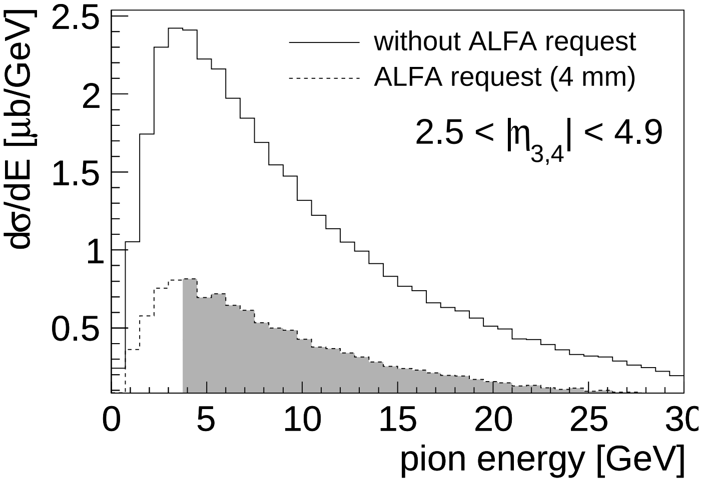

Figure 5.23: Pion energy distribution in the calorimeter. The grey area and the dash-dotted line indicates the lower boundary of the region accessible by ATLAS.

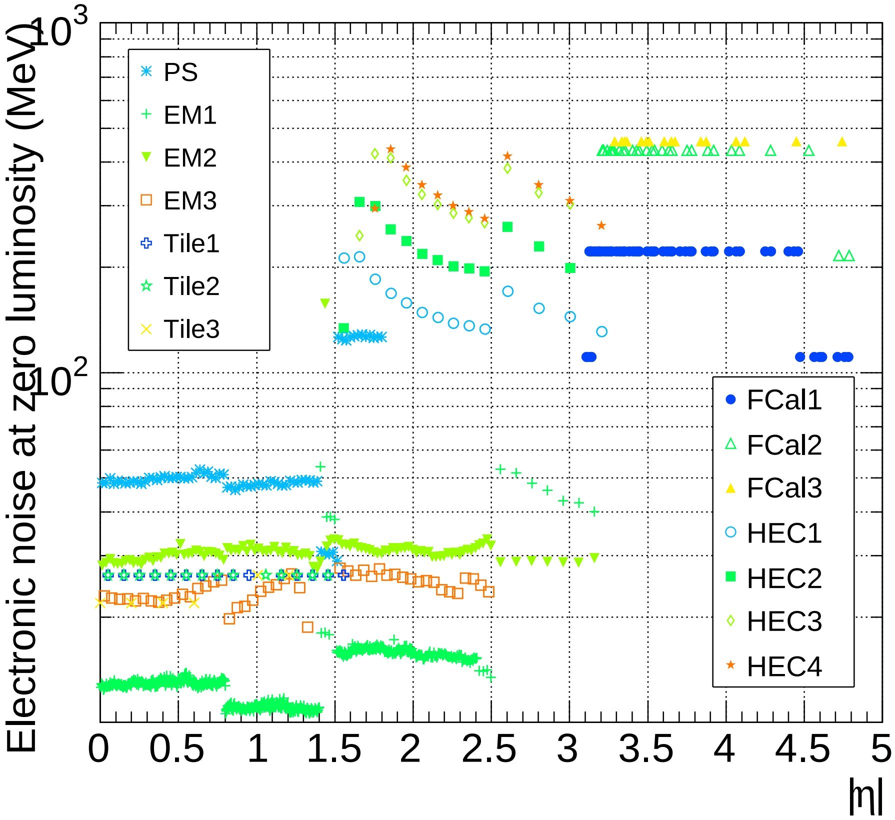

Figure 5.24: Expected electronic noise in individual cells of the various sampling layers of the calorimeters as a function of $|\eta|$. From [57].

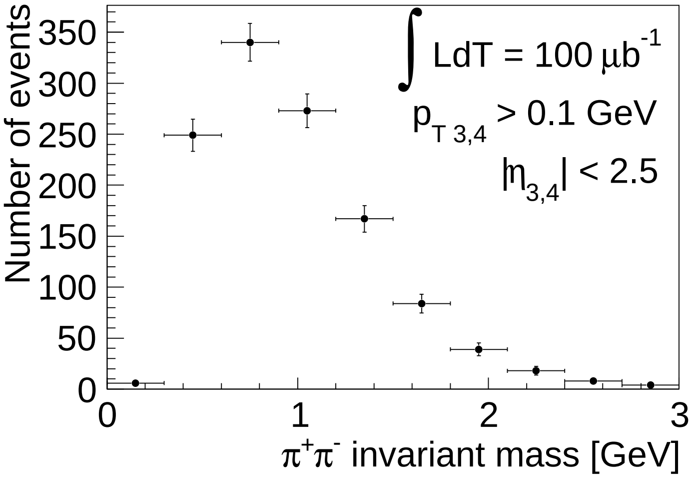

Figure 5.25: Possible measurement of the $\pi^+\pi^-$ invariant mass distribution for 100 $\mu\mathrm{b}^{-1}$ of the integrated luminosity (only the statistical errors are plotted).

Chapter 6

Summary

The presented thesis has been devoted to studies of diffractive processes with the ATLAS detector at the LHC. A gap reconstruction method based on the reconstructed tracks has been shown to work well in case of the ATLAS detector, whereas the one based on signals from the calorimeter suffers considerably from the noise. Using low-p_T tracking algorithms and requiring exactly one reconstructed vertex, the transverse momentum of the leading jet greater than 20 GeV and two leading jets belonging to the opposite pseudorapidity hemispheres, the amount of data collected by the ATLAS corresponding to the integrated luminosity of $\int L$ dt = 339 nb^{-1} was sufficient to observe a clear signal from the JGJ events. Starting from the half-gap size of 0.8 the data cannot be properly described using only the Non-Diffractive Jet sample. However, an admixture of the contribution from the Jet-Gap-Jet events as generated with the FPMC generator, makes the difference between data and Monte Carlo smaller and brings it to the ratio of 20% in the whole range of studied half-gap sizes.

As all other processes studied in this thesis require the measurement of both intact protons, a detailed studies of protons behaviour in the LHC structures (both collimators and magnets) has been performed. The proton trajectories for various LHC optics as well as the geometrical acceptance of the ALFA and AFP detectors have been studied. Finally, the energy and momentum reconstruction resolutions for ALFA and AFP stations and relevant LHC optics have been calculated.

Furthermore, it has been demonstrated that the measurement of the Jet-Gap-Jet events can be also performed for the Double Pomeron Exchange (DPE) Process. Compared to the original JGJ measurement, the DPE process has certain advantages. For example, the ratio between the DPE JGJ and DPE Jet events is much larger than the corresponding one in JGJ process. The process of DPE JGJ production was embedded in the FPMC generator. For a gap defined as a region devoid of particles with the transverse momentum above 200 MeV, the background has been shown to mimic the signal in less than 5% of cases for $|\eta_g| > 0.5$. This measurement has been shown to provide a significant test of the BFKL theory, once the 300 pb^{-1} of integrated luminosity is collected.

Finally, the two Central Exclusive Production processes have been discussed: the Central

Exclusive Jet and the Exclusive $\pi^+\pi^-$ productions. Since the cross section for the Central Exclusive Jet Production is relatively small (0.5 nb for $\sqrt{s} = 14$ TeV and a transverse momentum of the leading jet $p_T > 150$ GeV), there is a need to collect data during the nominal LHC operation, in the large pile-up environment. The analysis has been performed for two different experimental conditions: integrated luminosity of 40(300) fb^{-1} and pile-up of 23(46). After the postulated data selection, the signal to background ratio has been found to be of about 5/9 (1/13) for $<\mu>= 23$ (46). In both cases the statistical significance up to about 18 σ_{stat} has been obtained, but for $<\mu>= 46$ the purity of the sample is smaller. The collected data should deliver ten times better constraints on the theoretical models than the most recent ones.

It has been also demonstrated that the Central Exclusive Pion Pair production process can be measured with the ATLAS detector and the ALFA stations. The produced pions can be detected in the ATLAS tracking detector ($|\eta| < 2.5$) or in the ATLAS calorimetry system ($|\eta| < 4.9$). The sum of the visible cross sections from the tracker and the calorimetric measurements results in the total visible cross section of about 21 μb. For 100 μb^{-1} of integrated luminosity this means the sample size of about 2000 events. Such sample should be sufficient to measure the cross section and to study properties of various distributions, especially the invariant mass of the produced pion system.

The diffractive physics programme using the forward detectors as proton taggers has gain a lot of interest during last years. Clearly, results of the studies presented in this thesis convinced a part of the ATLAS community about importance of the diffractive physics and delivered new, interesting arguments to built and install ATLAS Forward Proton detectors.

Appendices

Appendix A

Transport Programs

The ALFA and AFP experiments are intended to measure protons scattered at very small angles. To reach this angular region, these detectors have to be placed far away from the ATLAS Interaction Point and in the immediate vicinity of the beams. Since there are several LHC magnets between the IP and forward detectors, the proton trajectory is not a straight line. To calculate it, several tools were created. They range from exact solutions of the equations of motion in the magnetic field in the small deviations approximation, FPTrack [86], FPTracker [87] or Hector [129], to the matrix description of the motion including the edge effects, MAD-X [75, 76]. There is also a possibility to make a full simulation of a particle motion through the accelerator magnetic lattice, including all physical processes, using a special tool, like Geant4 [130].

MAD-X is a program used to design and simulate particle beam behaviour within an accelerator. It takes into account not only the magnetic structure but also the geometry of the beam chamber. It enables the use of the thick lens magnet approximation in the calculations [66]. This can be achieved with the Polymorphic Tracking Code (PTC) module [76]. This code allows also the backward propagation and recirculation of particles. The MAD-X, widely used by the LHC beam division, is relatively slow and not particularly handy for ATLAS forward experiments.

FPTrack is a stand-alone code written in C. It is designed as a fast tracking tool for the forward physics detectors. This program uses exact solutions of the equations of particle motion in the magnetic field in the small deviations approximation. It is worth noticing that only the drift spaces, the dipole and the quadrupole magnets are considered in the calculations. Its C++ version was created and implemented within the ATHENA framework [82] as a package named FPTracker.

The FPTrack program is much faster than MAD-X. There is, however, a question of its accuracy. The answer, based on [7], is presented below.

A.1 Proton Transport

In this Section, the calculations were performed for *beam*1 and *beam*2 with both MAD-X PTC and FPTracker and the following factors were taken into account:

– the beam properties at the ATLAS IP,

– the magnet settings,

– the beam pipe geometry.

In the following, only results concerning *beam*1 are presented, since the ones obtained for *beam*2 are similar. The presented results are for the $\beta^* = 2625$ m optics and $\sqrt{s} = 14$ TeV. The applicability to other LHC settings is discussed at the end of the Appendix.

A.1.1 Influence of the Interaction Vertex Position

To study the influence of the interaction vertex position on the scattered proton trajectory the vertex position was generated at -0.6, -0.4, 0.0, 0.4, 0.6 mm. This range reflects the geometric properties of the interaction vertex distribution (*cf.* Table 2.1). The vertex displacement was performed in the transverse plane for the x- and y-coordinate separately. The protons were generated with the zero transverse momentum and the longitudinal coordinate of the interaction vertex, z, was set to zero.

The results of the calculations, for two different proton energies, are presented in Figures A.1(a), A.1(b) and A.2(a), A.2(b) – for the x and y-position of the trajectory, respectively. The differences in positions given by the MAD-X PTC and FPTracker, $\Delta x = x_{MADX} - x_{FPTracker}$ and $\Delta y = y_{MADX} - y_{FPTracker}$, are presented on Figs A.1(c), A.1(d) and A.2(c), A.2(d), for the x and y-position of the trajectory, correspondingly.

The Δx difference at 240 m increases with decreasing proton energy. Between the D1 (80 m) and D2 (160 m) dipole magnets the proton trajectories calculated by FPTracker are bent more than the ones calculated by MAD-X. At the Q4 (170 m), Q5 (200 m) and Q6 (230 m) quadrupoles the situation is opposite – the MAD-X is bending more. It is worth stressing that overall difference is at the level of tenths of nanometers – three orders of magnitude smaller than the ALFA or AFP detectors spatial resolution.

The Δy difference at 240 m does not practically depend on the proton energy. Up to the D1 dipole magnet, there is no difference between the MAD-X and FPTracker results. Beyond this point, the Δy increases with increasing z value. Also, the further the proton vertex is from the IP = (0, 0, 0), the bigger is Δy. Similarly as for the Δx, this difference is much smaller than the ALFA or AFP detectors spatial resolution and, hence, will not impact the measurements.

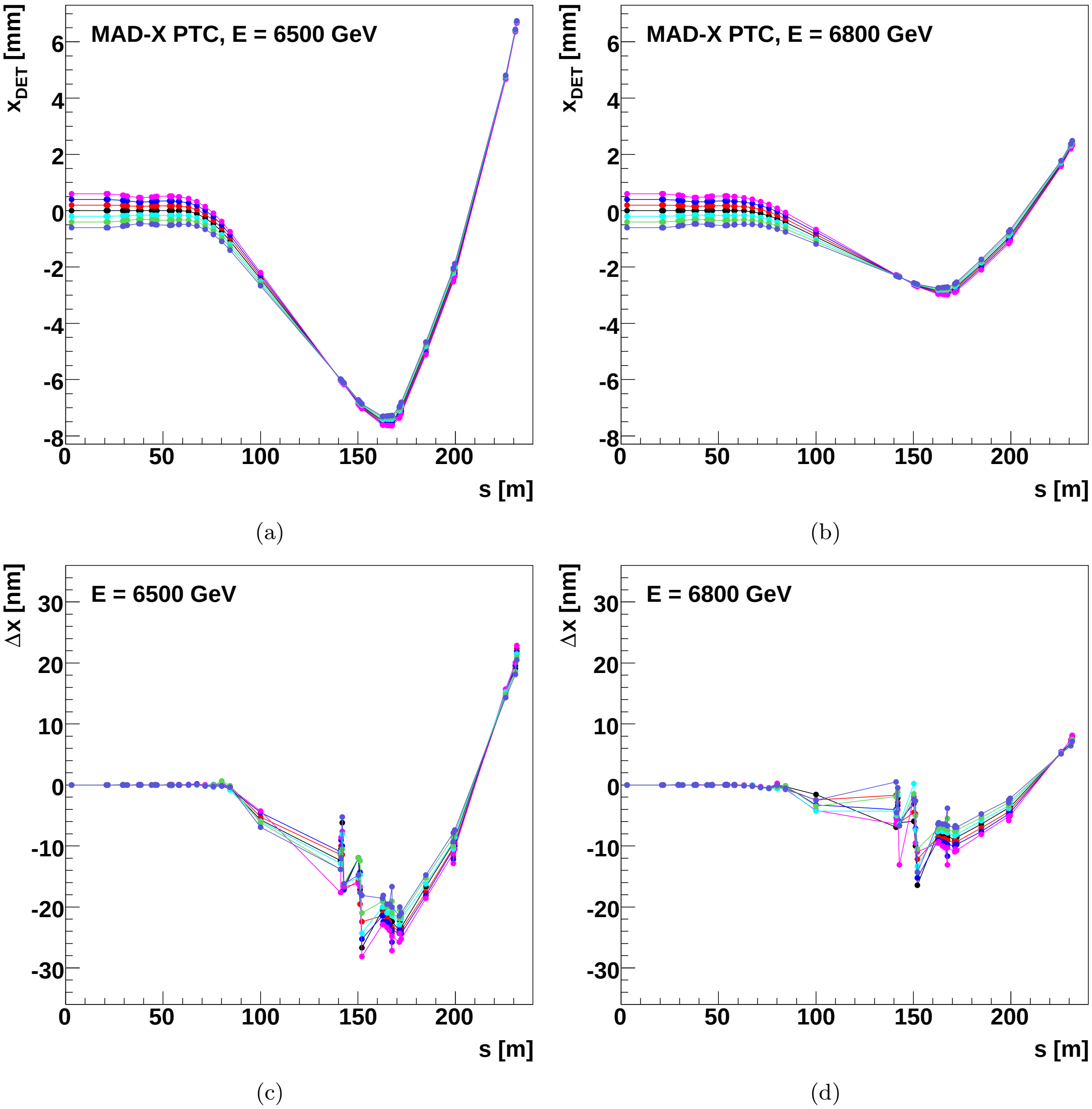

(a)

(b)

(c)

(d)

Figure A.1: **Top**: proton trajectory, as calculated by MAD-X PTC, for *beam*1 for different energies. **Bottom**: difference $\Delta x = x_{MADX} - x_{FPTracker}$ in transport between the MAD-X PTC and the FPTracker programs. The x vertex coordinate was generated at -0.6, -0.4, $\ldots$, 0.6 mm, whereas y and z coordinates and the transverse momentum of a proton were set to 0. Differences are much smaller than the ALFA or AFP detector spatial resolution.

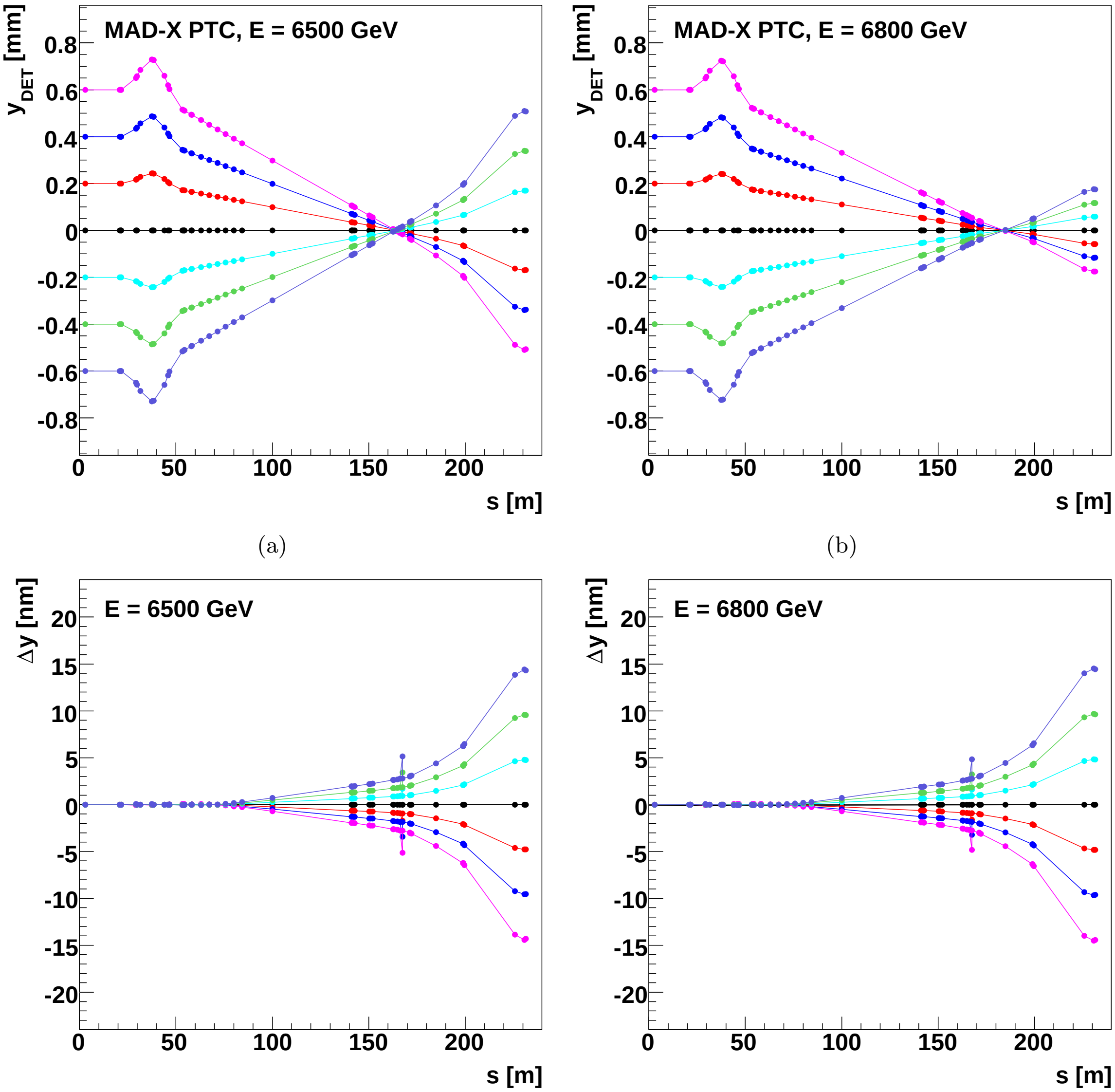

(a) (b)

(c) (d)

Figure A.2: **Top**: proton trajectory, as calculated by MAD-X PTC, for *beam*1 for different energies. **Bottom**: difference $\Delta y = y_{MADX} - y_{FPTracker}$ in transport between the MAD-X PTC and the FPTracker programs. The y vertex coordinate was generated at -0.6, -0.4, $\ldots$, 0.6 mm, whereas x and z coordinates and the transverse momentum of a proton were set to 0. Differences are much smaller than the ALFA or AFP detector spatial resolution.

A.1.2 Influence of the Proton Transverse Momentum

The influence of the scattered proton transverse momentum, p_T, was studied for protons generated at the IP = (0,0,0) with the transverse momentum components ranging between -0.3 and 0.3 GeV in both, x- and y-directions.

The results of the calculations, for two different proton energies, are presented in Figures A.3(a), A.3(b) and A.4(a), A.4(b) – for the x and y-position of the trajectory, correspondingly. The differences, $\Delta x = x_{MADX} - x_{FPTracker}$ and $\Delta y = y_{MADX} - y_{FPTracker}$, of positions given by MAD-X PTC and FPTRACKER are presented on Figures A.3(c), A.3(d) and A.4(c), A.4(d), for the x and y-position of the trajectory, respectively.

The differences in the orbit trajectory positions observed in Figs A.3 and A.4 are similar to the ones observed in Section A.1.1. The Δx remains at the level of tenths of nanometers. The Δy is of order of 0.1 μm, which is still much smaller than the detector resolution. These results show that the differences between MAD-X PTC and FPTRACKER codes are marginal and will not impact measurements.

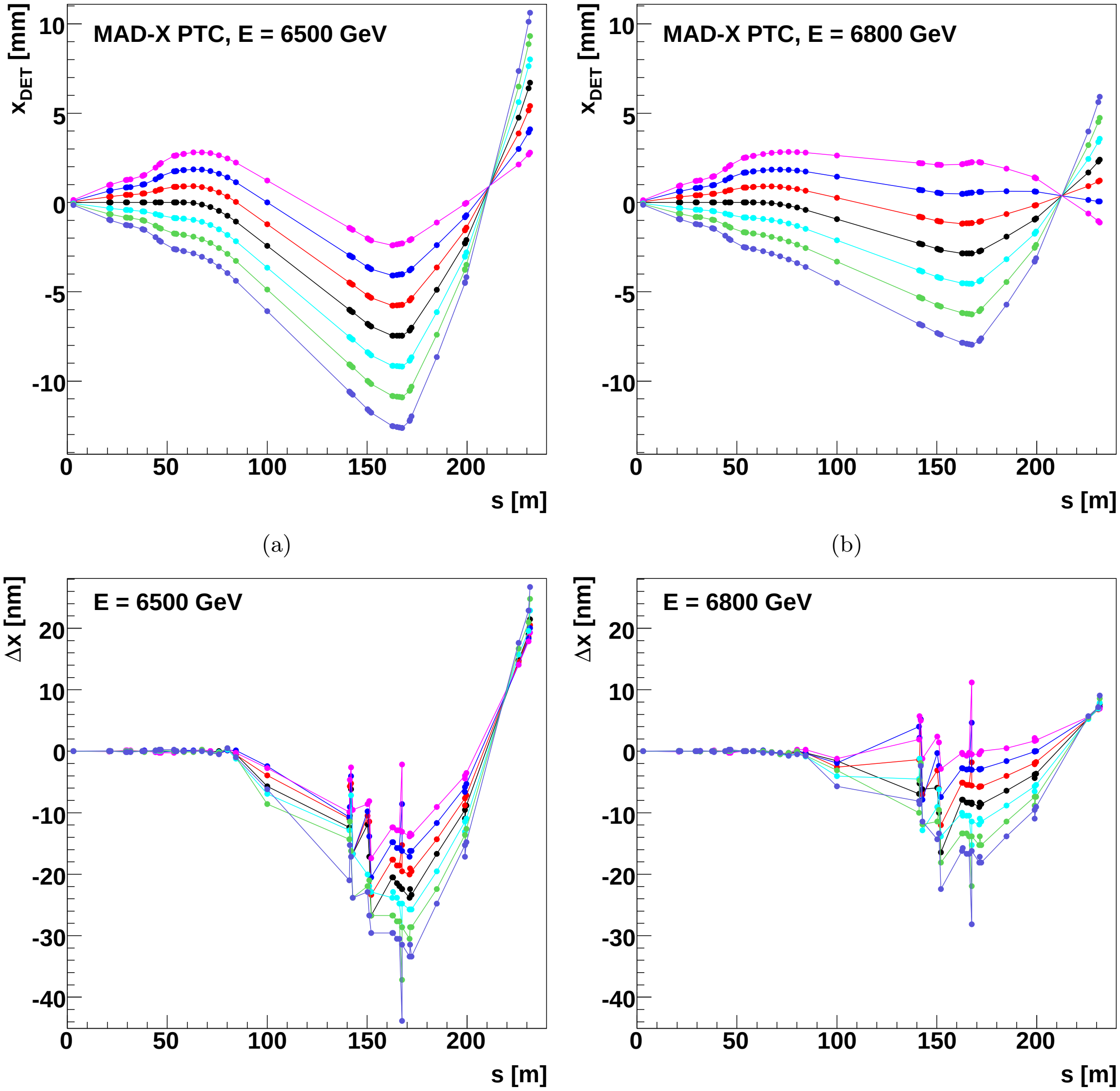

(a) (b)

(c) (d)

Figure A.3: **Top**: proton trajectory, as calculated by MAD-X PTC, for *beam*1 for different energies. **Bottom**: difference $\Delta x = x_{MADX} - x_{FPTracker}$ in transport between the MAD-X PTC and the FPTRACKER programs. The generated p_x momentum was ranging between -0.3 and 0.3 GeV, whereas the IP vertex coordinates and the p_y momentum were set to 0. Differences are much smaller than the ALFA or AFP detector spatial resolution.

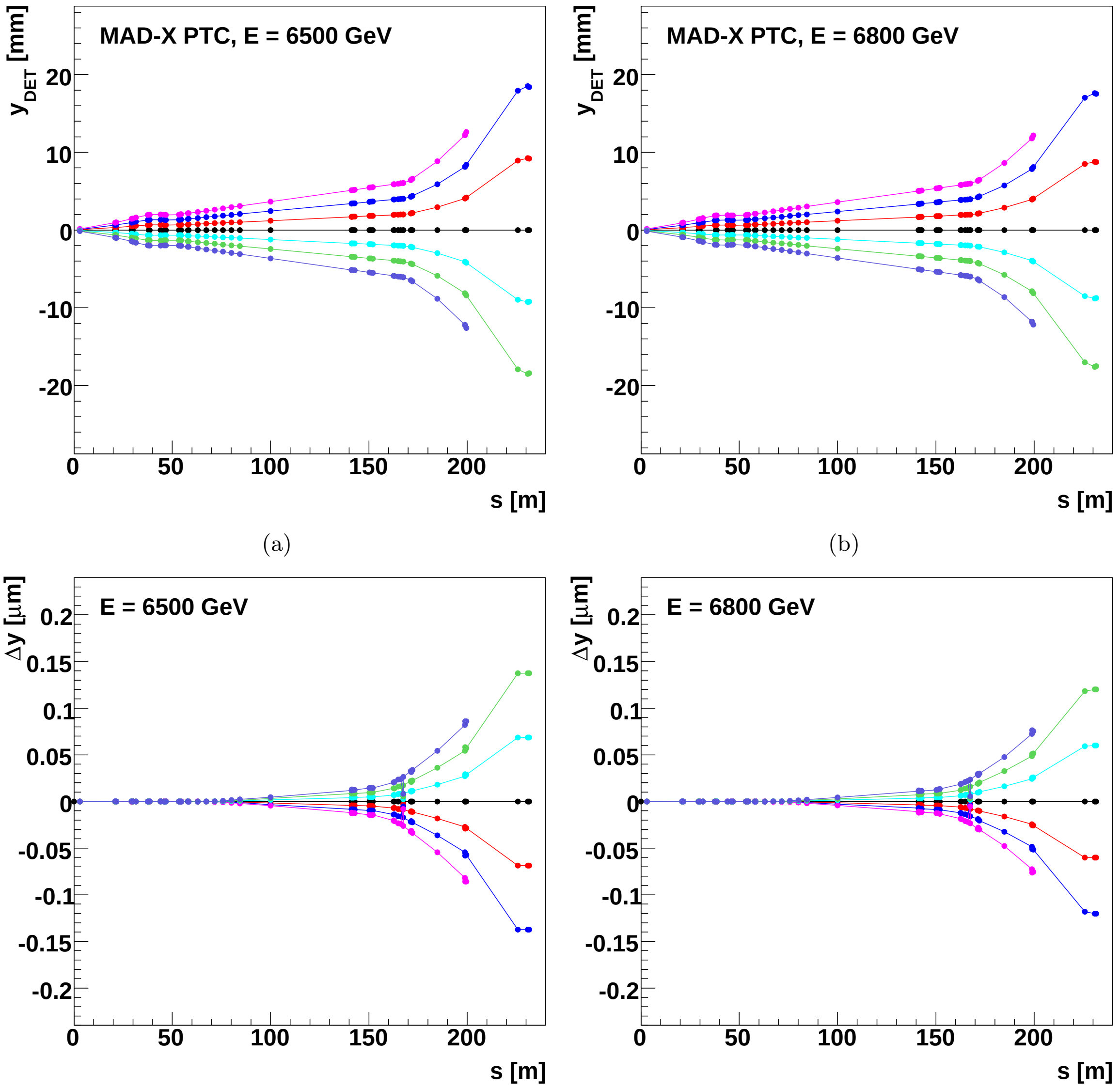

(a) (b)

(c) (d)

Figure A.4: **Top**: proton trajectory, as calculated by MAD-X PTC, for *beam*1 for different energies. **Bottom**: difference $\Delta x = x_{MADX} - x_{FPTracker}$ in transport between the MAD-X PTC and the FPTracker programs. The generated p_y momentum was ranging between -0.3 and 0.3 GeV, whereas the IP vertex coordinates and the p_x momentum were set to 0. Differences are much smaller than the ALFA or AFP detector spatial resolution.

A.2 Geometrical Acceptance

The geometrical acceptance calculated with MAD-X PTC at the location of the ALFA *beam*1 station is presented in Figure A.5(a). The explicit difference of the number of protons transported with MAD-X PTC and FPTracker is presented in Figure A.5(b). In calculations, the following factors were taken into account:

- the beam properties at the IP: the interaction vertex coordinates were assumed to have Gaussian distributions with zero means and the dispersions of $\sigma_x = \sigma_y = 0.612$ mm,
- the beam chamber and the detector geometries,
- the 1.5 mm distance between the detector edge and the beam centre.

It is worth noticing that at the beginning 10000 particles in each (E, p_T) bin were generated.

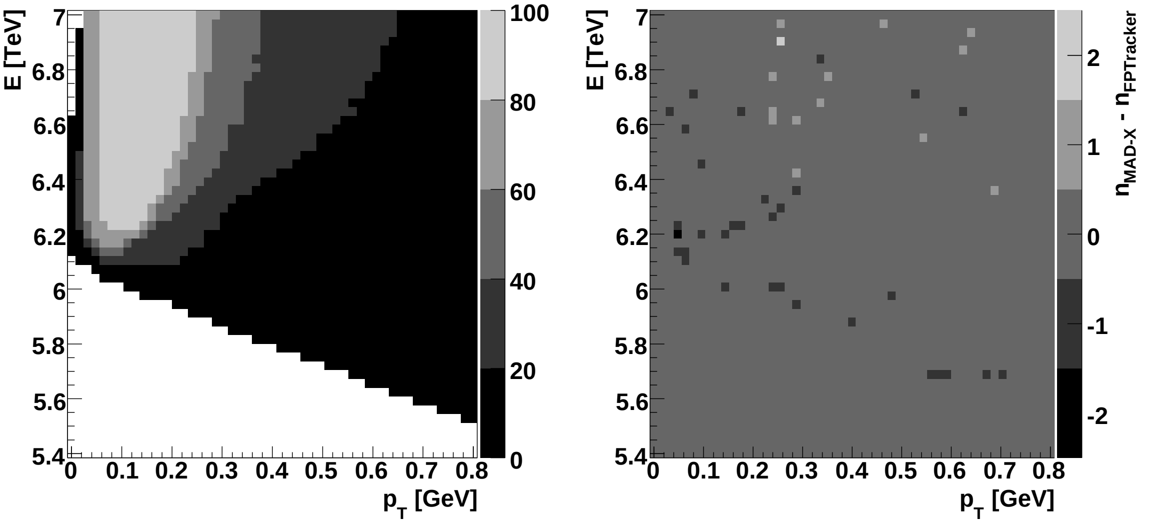

(a) MAD-X PTC (b) Difference: $n_{MAD-X} - n_{FPTracker}$

Figure A.5: **Left**: acceptance calculated by the MAD-X PTC program at 240 m for *beam*1. **Right**: difference of the number of particles transported by the MAD-X PTC and the FPTracker programs to the 240 m location for *beam*1. In the calculations the following factors were taken into account: the beam chamber geometry, the detector shape and its distance from the beam. The interaction vertex location was generated according to a proper Gaussian distribution (see text). In each (E, p_T) bin 10000 particles were generated. Observed differences are negligible.

Comparison of the results in Figure A.5(b) for the MAD-X PTC and FPTracker confirms that there are no major differences between acceptances calculated with both programs – the observed deviations are not larger than two particles per bin. In addition, they appear to be randomly distributed over the (E, p_T) plane. One can conclude that the observed differences are negligible.

A.3 Differences between MAD-X PTC and FPTracker

As was observed in the previous Sections, the differences seen in the results obtained with both codes are very small. However, to trace and understand their origin, more detailed studies of the trajectory position at the detector location were performed. The differences were quantified with $\Delta x = x_{MADX} - x_{FPTracker}$ and $\Delta y = y_{MADX} - y_{FPTracker}$ which measure the deviations in the (x, z) and (y, z) planes, respectively.

As an input, a set of particles uniformly distributed in energy, transverse momentum and vertex transverse position was generated. The generation parameters are summarised in Table A.1. They were chosen to cover all the area in the (E, p_T) plane in which the geometrical acceptance is larger than 50% (see *cf.* Figure A.5(a)).

Table A.1: The generation parameters.

Parameter	Min. value	Max. value	No. of bins
x_{IP} [mm]	-2.0	2.0	21
y_{IP} [mm]	-2.0	2.0	21
$p_{x_{\mathrm{IP}}}$ [GeV]	-0.6	0.6	25
$p_{y_{\mathrm{IP}}}$ [GeV]	-0.6	0.6	25
E_{IP} [TeV]	5.6	7.0	29

The Δy distribution is presented in Figure A.6. It is symmetric with respect to 0 and limited to $|\Delta y| < 0.22$ μm. One should again note that the limiting value is much smaller than the detector spatial resolution. The width of this distribution is related to the p_y distribution. The higher the average value of $p_{y_{\mathrm{IP}}}$ is, the larger is the value of Δy (*cf.* grey areas in Fig. A.6). Since only part of the $p_T = \sqrt{p_{x_{\mathrm{IP}}}^2 + p_{y_{\mathrm{IP}}}^2}$ distribution within the apparatus acceptance (*cf.* Fig. A.5), the Δy distribution is well localised.

The influence of the interaction vertex y-coordinate is small – see Figure A.7. The resulting Δy distribution is particularly narrow for $p_{y_{\mathrm{IP}}} = 0$. The multi-peak structure of the distribution in Fig. A.7 follows the discretisation of the vertex position assumed for the generated data sample.

The differences in the particle transport in the (y, z) plane outlined above can be attributed to the different methods used in the proton tracking through a quadrupole magnet in both codes (see Figures A.2 and A.4). In particular, different descriptions of magnetic fields – a treatment of the fringe fields and edge effects, applied approximations and numerical methods may result in the observed differences.

The studies were repeated for the (x, z) plane. The results are shown in Figures A.8 and A.9. The distribution of Δx, seen in Fig. A.8, is clearly asymmetric and defined for $\Delta x > 0$.

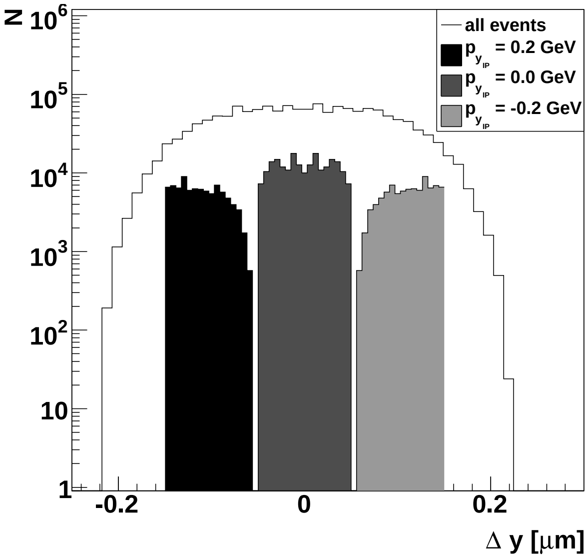

Figure A.6: Differences in protons transport in the case of the (y, z) plane, calculated as $\Delta y = y_{MADX} - y_{FPTracker}$. The shaded areas show the Δy values due to the different values of $p_{y_{\rm IP}}$.

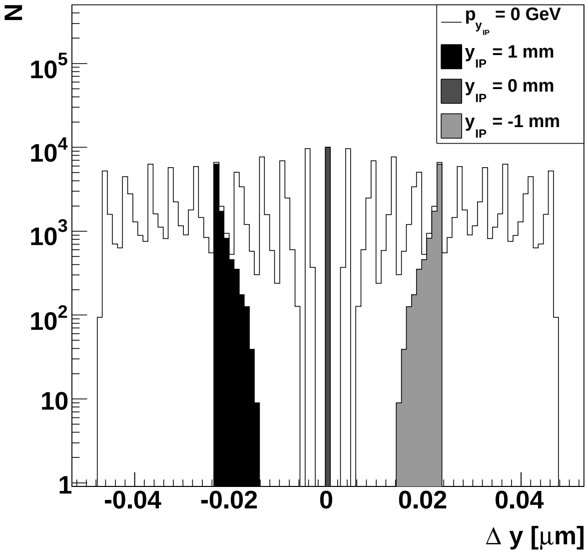

Figure A.7: $\Delta y = y_{MADX} - y_{FPTracker}$ distribution for $p_{y_{\rm IP}} = 0$ GeV. The shaded areas show the Δy regions due to the different values of the interaction vertex y-coordinate.

This shows that MAD-X PTC predicts that the scattered particles will be observed at larger values of x than those transported by FPTracker. Again, the values of Δx are much smaller than the ALFA detector spatial resolution. However, the differences between the results of both programs grow with decreasing energy of the scattered proton (see shaded areas which show contributions due to the different values of the scattered proton energy).

For a fixed energy of the scattered particle the width of the Δx distribution is determined by the value of $p_{x_{\mathrm{IP}}}$ (see Fig. A.9). The discontinuities observed for $p_{x_{\mathrm{IP}}} = -0.3$ GeV are due to the calculation precision. The x-coordinate distribution introduces a much smaller effect – it practically gives the width of the Δx distribution for a fixed value of $p_{y_{\mathrm{IP}}}$ (*cf.* Fig. A.9).

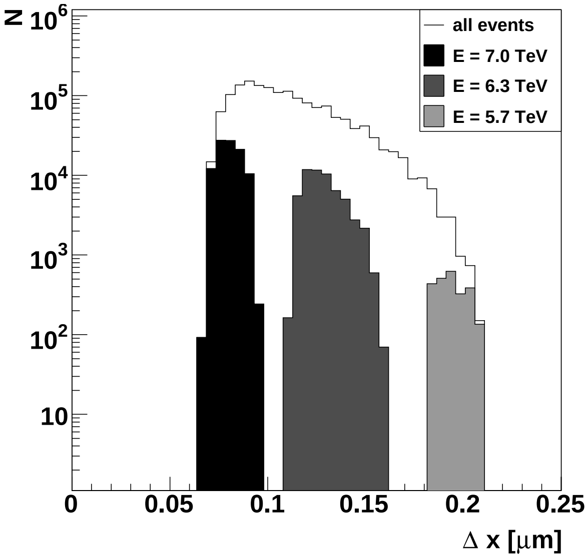

Figure A.8: $\Delta x = x_{MADX} - x_{FPTracker}$ distribution. The shaded areas show the contributions due to the selected values of the scattered particle energy.

The visible shift seems to be a consequence of bending of the protons trajectory. Note that all orbits, including the nominal one, are curved in the dipoles. Thus, the width of the Δx distribution can be attributed to the different numerical methods and approximations or the different description of the dipole magnets (the edge effects, the fringe fields) used in the tested tracking programs. Note that the nominal orbit positions in the (x, z) plane at the detector location are: $x_{MADX} = 0.0$ m and $x_{FPTrack} = -0.08$ μm. This is practically a negligible contribution to the systematics. The second and third order effects demonstrating the influence of the transverse momentum and the vertex position are caused by differences in the description of the quadrupole magnets.

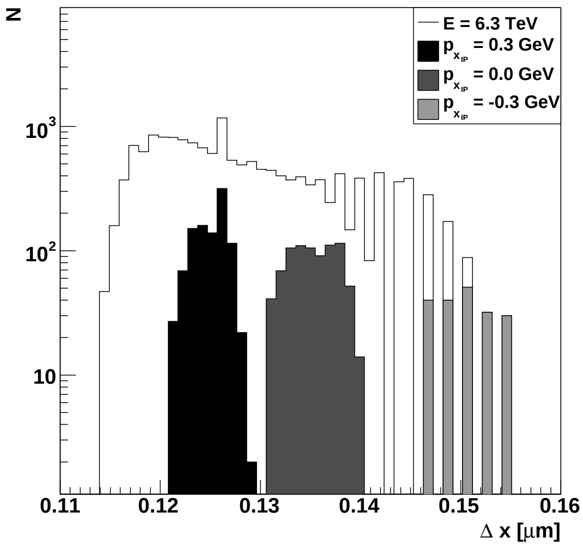

Figure A.9: $\Delta x = x_{MADX} - x_{FPTracker}$ distribution for $E = 6.3$ TeV. The shadowed areas show the contributions due to the selected p_x values.

A.4 Conclusions

The two sources causing the differences in the transport of protons as the function of energy loss through the LHC magnetic lattice were identified:

- the treatment of the LHC aperture,
- the transport calculation methods through the LHC beam line elements: dipole and the quadrupole magnets.

Discrepancies caused by the treatment of the LHC apertures, manifesting themselves *e.g.* in the geometrical acceptance ranges, were found to be very small. Moreover, they seem to be randomly distributed in the (E, p_T) plane and they can be neglected.

An examination of the differences in the particle positions at the detector plane revealed effects due to different descriptions of the dipole and quadrupole magnets in tested programs. These differences are caused by the fringe fields, the edge effects (absent in FPTracker) and applied approximations and numerical methods. They were found to be small and at least two orders of magnitude smaller than the ALFA detector spatial resolution. Therefore, the differences can be neglected.

In conclusion, both the differences caused by the treatment of the LHC beam chamber apertures and the transport calculation methods through the LHC beam line elements are found to be negligible. Therefore, the FPTracker package (based on the FPTrack) is in nearly perfect agreement with the official code of the LHC accelerator group and can be used without any doubts.

The calculations were performed for the $\beta^* = 2625$ m optic and $\sqrt{s} = 14$ TeV, but they were checked also for other machine settings with similar conclusions. Firstly, it is because the LHC apertures are independent of the LHC optics. Secondly, the magnet strengths in the LHC optics files scale with energy.

Appendix B

Parametrisation and Unfolding Tool

As it was mentioned in Appendix A, in order to compute a particle trajectory in a magnetic structure of an accelerator one of several dedicated transport programs can be used. The other method is to prepare a look-up table and interpolate the positions. The disadvantage of the above methods is either a long calculation time, as in the first case, or a very extensive use of the computer storage (since the size of the looking table grows with the required precision) for the latter.

The alternative is to use the transport parametrisation. This is a very fast method and requires only a limited amount of memory. The most important feature of the parametrisations is to provide an analytical representation of the proton position and momentum. This, in turn, allows to calculate the scattered proton momentum at the Interaction Point on the basis of the measurements at the forward detectors location. This idea was first proposed in [131] and was further evaluated in [1].

B.1 Transport Parametrisation

The LHC magnetic structure in the vicinity of the ATLAS detector is described only by the drift spaces, the dipole and the quadrupole magnets (*cf.* Section 2.1.1). Therefore, a linear transport approximation can be applied to describe the scattered proton transport [66].
Following [131], a transverse variable $\zeta \in \{x, y, x', y'\}$ the transport can be effectively described by the following equations:

$$\begin{aligned} \zeta &= A_\zeta + B_\zeta \cdot x_{\mathrm{IP}} + C_\zeta \cdot y_{\mathrm{IP}} + D_\zeta \cdot z_{\mathrm{IP}} + E_\zeta \cdot x'_{\mathrm{IP}} \\ &\quad + F_\zeta \cdot y'_{\mathrm{IP}} + G_\zeta \cdot z_{\mathrm{IP}} \cdot x'_{\mathrm{IP}} + H_\zeta \cdot z_{\mathrm{IP}} \cdot y'_{\mathrm{IP}}, \end{aligned} \tag{B.1}$$

where $A_\zeta, \ldots, H_\zeta$ are the polynomials in the reduced energy loss ($\xi = \Delta E/E_{beam}$) of rank $k_{A_\zeta}, \ \ldots, \ k_{H_\zeta}$:

$$A_\zeta = \sum_{n=0}^{k_{A_\zeta}} a_{\zeta,n} \cdot \xi^n, \quad \ldots, \quad H_\zeta = \sum_{n=0}^{k_{H_\zeta}} h_{\zeta,n} \cdot \xi^n.$$

The x_{IP}, y_{IP} and z_{IP} are the vertex coordinates, whereas x'_{IP}, y'_{IP} are the trajectory slopes.

In order to solve these equations and, thus, to find the parametrisation, the following algorithm was implemented:

1. find the A_ζ term – solve the $\zeta = A_\zeta$ equation,
2. find slopes of $\zeta = A_\zeta + B_\zeta \cdot x_{\mathrm{IP}}$ ($C_\zeta \cdot y_{\mathrm{IP}}$, …, $F_\zeta \cdot y'_{\mathrm{IP}}$) functions for different x_{IP} (y_{IP}, …, y'_{IP}),
3. using obtained slope values, fit the polynomial function of energy,
4. find slopes of $\zeta - B_\zeta \cdot x_{\mathrm{IP}} - E_\zeta \cdot x'_{\mathrm{IP}} = A_\zeta + G_\zeta \cdot z_{\mathrm{IP}} \cdot x'_{\mathrm{IP}}$ and $\zeta - C_\zeta \cdot y_{\mathrm{IP}} - F_\zeta \cdot y'_{\mathrm{IP}} = A_\zeta + H_\zeta \cdot z_{\mathrm{IP}} \cdot y'_{\mathrm{IP}}$ functions,
5. using the obtained slope values, fit the polynomial function of energy.

Once the parametrization coefficients are found, a check module is invoked. The difference between the value obtained from the parametrisation equations and from the transport program is calculated. If it is smaller than the required threshold, the calculated coefficients are written to disk. When this requirement is not fulfilled, the procedure restarts with $A_\zeta, \ldots, H_\zeta$ polynomials of higher ranks.

The absence of magnets with multipole field expansion moments higher than the quadrupole ones implies that the horizontal trajectory position (direction) does not depend on the vertical momentum component nor the vertical vertex coordinate, and *vice versa.* The best description of the scattered proton transport for the ALFA detectors (*high-β^** optics) is given by:

$$\left.\begin{array}{rcl}
x & = & \sum\limits_{n=0}^{k_{A_x}} a_{x,n} \cdot \xi^n + \sum\limits_{n=0}^{k_{B_x}} b_{x,n} \cdot \xi^n \cdot x_{\mathrm{IP}} + \sum\limits_{n=0}^{k_{E_x}} e_{x,n} \cdot \xi^n \cdot x'_{\mathrm{IP}}, \\
y & = & \sum\limits_{n=0}^{k_{C_y}} c_{y,n} \cdot \xi^n \cdot y_{\mathrm{IP}} + \sum\limits_{n=0}^{k_{F_y}} f_{y,n} \cdot \xi^n \cdot y'_{\mathrm{IP}}, \\
x' & = & \sum\limits_{n=0}^{k_{A_{x'}}} a_{x',n} \cdot \xi^n + \sum\limits_{n=0}^{k_{B_{x'}}} b_{x',n} \cdot \xi^n \cdot x_{\mathrm{IP}} + \sum\limits_{n=0}^{k_{E_{x'}}} e_{x',n} \cdot \xi^n \cdot x'_{\mathrm{IP}}, \\
y' & = & \sum\limits_{n=0}^{k_{C_{y'}}} c_{y',n} \cdot \xi^n \cdot y_{\mathrm{IP}} + \sum\limits_{n=0}^{k_{F_{y'}}} f_{y',n} \cdot \xi^n \cdot y'_{\mathrm{IP}},
\end{array}\right\} \tag{B.2}$$

For the AFP detectors (collision optics) the solution is:

$$\left.\begin{array}{rcl}
x & = & \sum\limits_{n=0}^{k_{A_x}} a_{x,n} \cdot \xi^n + \sum\limits_{n=0}^{k_{B_x}} b_{x,n} \cdot \xi^n \cdot x_{\mathrm{IP}} + \sum\limits_{n=0}^{k_{E_x}} e_{x,n} \cdot \xi^n \cdot x'_{\mathrm{IP}}, \\
y & = & \sum\limits_{n=0}^{k_{A_y}} a_{y,n} \cdot \xi^n + \sum\limits_{n=0}^{k_{C_y}} c_{y,n} \cdot \xi^n \cdot y_{\mathrm{IP}} + \sum\limits_{n=0}^{k_{F_y}} f_{y,n} \cdot \xi^n \cdot y'_{\mathrm{IP}}, \\
x' & = & \sum\limits_{n=0}^{k_{A_{x'}}} a_{x',n} \cdot \xi^n + \sum\limits_{n=0}^{k_{B_{x'}}} b_{x',n} \cdot \xi^n \cdot x_{\mathrm{IP}} + \sum\limits_{n=0}^{k_{E_{x'}}} e_{x',n} \cdot \xi^n \cdot x'_{\mathrm{IP}}, \\
y' & = & \sum\limits_{n=0}^{k_{A_{y'}}} a_{y',n} \cdot \xi^n + \sum\limits_{n=0}^{k_{C_{y'}}} c_{y',n} \cdot \xi^n \cdot y_{\mathrm{IP}} + \sum\limits_{n=0}^{k_{F_{y'}}} f_{y',n} \cdot \xi^n \cdot y'_{\mathrm{IP}},
\end{array}\right\} \tag{B.3}$$

B.2 Unfolding Procedure

The procedure of inferring the scattered proton momentum on the basis of the detector measurements is called the *unfolding.* This can be done in various ways. Here it is performed by means of the minimisation of the following χ^2 function:

$$\chi^2(\mathbf{p}) = \frac{\left(x_1^D - x_1(\mathbf{p})\right)^2}{\sigma_x^2} + \frac{\left(y_1^D - y_1(\mathbf{p})\right)^2}{\sigma_y^2} + \frac{\left(x_2^D - x_2(\mathbf{p})\right)^2}{\sigma_x^2} + \frac{\left(y_2^D - y_2(\mathbf{p})\right)^2}{\sigma_y^2},$$

where (x_1^D, y_1^D) denote the coordinates of the scattered proton trajectory position measured at the first station and $(x_1(\mathbf{p}), y_1(\mathbf{p}))$ – the coordinates calculated using the transport parametrisation for a proton with momentum $\mathbf{p}$. The variables x_2^D, y_2^D, $x_2(\mathbf{p})$ and $y_2(\mathbf{p})$ refer to the positions at the second station. The parametrisation does not describe correctly neither the losses of particles due to the beam pipe nor the collimators apertures, but this drawback is of minor importance for solving the unfolding problem.

The unfolding procedure is provided by the `SingleSideEvent` class. The constructor of this class takes as an argument the name of a file containing the parametrisation to be used for the unfolding and positions of the two detector stations that provide the measurement of proton trajectory.

A user needs to specify the information about the vertex position (or about the beam spot centre) and the positions of the proton trajectory measured by both stations. This is done by the `SetVertex` and `SetMeasurement` methods, respectively. If the information about the vertex is the same for all events, it can be specified only once, at the beginning.
The reconstruction is done by the `Reconstruct` method. It takes as an argument a string where the method of the reconstruction is specified:

- `"method=1"` uses a method developed for AFP, based on solving an equation created from the parametrisation formula,
- `"method=3"` uses Minuit minimisation and should be used for diffractive events,
- `"method=4"` also uses Minuit minimisation, but here the energy is fixed to the nominal one, so this method should be used for elastic events.

After calling the `Reconstruct` method, the obtained proton kinematics can be accessed with the following methods:

- `GetXi` returns the fractional energy loss,
- `GetPt` returns the transverse momentum,
- `GetT` returns the four-momentum transfer,
- `GetPhi` returns the azimuthal angle.

The results obtained by the unfolding procedure are shown in Section 2.2.6 and 2.2.7 for ALFA and AFP detectors, correspondingly.

Bibliography

[1] M. Trzebiński, R. Staszewski, and J. Chwastowski. *LHC High β^* Runs: Transport and Unfolding Methods*. ISRN High Energy Physics, vol. 2012 (2012) 491460.

[2] R. Staszewski, P. Lebiedowicz, M. Trzebinski, J. Chwastowski, and A. Szczurek. *Exclusive $\pi^+\pi^-$ Production at the LHC with Forward Proton Tagging*. Acta Physica Polonica B **42** (2011) 1861.

[3] R. Staszewski, M. Trzebiński, and J. Chwastowski. *Dynamic Alignment Method of the Forward-Proton Detectors at the LHC*. Adv. in High Energy Physics, vol. 2012 (2012), Article ID 428305.

[4] C. Marquet, C. Royon, M. Trzebiski, and R. Zlebcik. *Gaps between jets in double-Pomeron-exchange processes at the LHC*. Phys. Rev. D **87**, (2013) 034010.

[5] M. Trzebiński. *Towards a Total Cross Section Measurement with the ALFA Detector at ATLAS*.

[6] M. Trzebiński. *Probing the BFKL Pomeron with Future ATLAS Forward Detectors*. in Proceedings of the XI LISHEP – Workshop on High Energy Physics in the Near Future, Rio de Janeiro, 2013, edited by F. Caruso, V. Oguri and A. Santoro, eConf CC1303172.

[7] M. Trzebiński, J. Chwastowski, and T. Sykora. *Transport of Protons with High Energy Loss Through the LHC Magnetic Lattice for the High β^* Optics*. ATLAS-COM-LUM-2011-004.

[8] M. Trzebiński, R. Staszewski, and J. Chwastowski. *ForwardProtonParam: Tool for finding parametrisation equations and unfolding proton four-momentum at the IP*. in preparation.

[9] M. Trzebiński and J. Chwastowski. *Monte Carlo Studies for ALFA Runs at $\sqrt{s}$=8 TeV: Some Aspects of Optics, Beam Profiles, Elastic and Diffractive Event Patterns and Rates*. ATLAS-COM-LUM-2012-012.

[10] S. Jakobsen, O. Kepka, P. Newman, and M. Trzebiński. *Diffractive physics program with ALFA in low-β^* run in proton-proton interactions at $\sqrt{s}$=8 TeV*. ATLAS-COM-PHYS-2012-1435.

[11] L. Adamczyk *et al.* *AFP: A Proposal to Install Proton Detectors at 220 m around ATLAS to Complement the ATLAS High Luminosity Physics Program.* ATLAS-COM-LUM-2011-006.

[12] O. Kepka, C. Royon, L. Schoeffel, R. Staszewski, M. Trzebiński, and R. Zlebcik. *Physics Cases within the AFP project.* ATL-COM-PHYS-2012-775.

[13] ATLAS Collaboration. *Observation of a new particle in the search for the Standard Model Higgs boson with the ATLAS detector at the LHC.* Physics Letters B **716** (2012) 1.

[14] CMS Collaboration. *Observation of a new boson at a mass of 125 GeV with the CMS experiment at the LHC.* Physics Letters B **716** (2012) 1.

[15] R. P. Feynman. *The Theory of Positrons.* Phys. Rev. **76** (1949) 749759.

[16] Yu. L. Dokshitzer, V. A. Khoze, A. H. Mueller, and S. I. Troyan. *Basics of Perturbative QCD.* ISSN 0982-5657 (1991).

[17] R. P. Feynman. *Very High-Energy Collisions of Hadrons.* Phys. Rev. Lett. **23** (1969) 1415.

[18] G. Watt. *MSTW PDFs and impact of PDFs on cross sections at Tevatron and LHC.* Nucl. Phys. Proc. Suppl. 222-224 (2012) 61-80.

[19] H.-L. Lai *et al.* *New parton distributions for collider physics.* Phys. Rev. D **82** (2010).

[20] P. Jimenez-Delgado and E. Reya. *Dynamical NNLO parton distributions.* Phys. Rev. D **79**, 074023 (2009).

[21] H1 and ZEUS Collaboration. *Combined Measurement and QCD Analysis of the Inclusive ep Scattering Cross Sections at HERA.* JHEP **1001** (2010) 109.

[22] E. Predazzi. *Diffraction: Past, present and future.* Florianopolis 1998, Hadron physics 98.

[23] P. Collins. *An introduction to Regge theory and High Energy Physics.* Cambridge U.P., 1977.

[24] E. Levin. *Everything about Reggeons.* TAUP 2465-97, DESY 97-213.

[25] N. Cartiglia. *Measurement of the proton-proton total, elastic, inelastic and diffractive cross sections at* $\sqrt{s} = 2, 7, 8$ *and 57 TeV.* in Proceedings of the XI LISHEP – Workshop on High Energy Physics in the Near Future, Rio de Janeiro, 2013, edited by F. Caruso, V. Oguri and A. Santoro, eConf CC1303172.

[26] A. Donnachie and P. Landshoff. *Total cross-sections.* Phys. Lett. B **296**, 227, 1992.

[27] S. Donnachie, G. Dosch, P. Landshoff, and O. Nachtmann. *Pomeron Physics and QCD.* Cambridge Monographs on Particle Physics, Nuclear Physics and Cosmology, 2002.

[28] E. Levin. *An Introduction to Pomerons.* TAUP 2522/98, DESY 98-120.

[29] G. Ingelman and P. E. Schlein. *Jet Structure in High Mass Diffractive Scattering.* Phys.Lett. B **152** (1985) 256.

[30] UA8 Collaboration. *Evidence for Transverse Jets in High Mass Diffraction.* Phys. Lett. B **211** (1988) 239.

[31] UA8 Collaboration. *Cross-section measurements of hard diffraction at the SPS collider.* Phys. Lett. B **421** (1998) 395.

[32] H1 Collaboration. *Measurement and QCD analysis of the diffractive deep-inelastic scattering cross-section at HERA.* Eur. Phys. J. C **48** (2006) 715.

[33] H1 Collaboration. *Dijet Cross Sections and Parton Densities in Diffractive DIS at HERA.* JHEP **0710** (2007) 042.

[34] ZEUS Collaboration. *Deep inelastic scattering with leading protons or large rapidity gaps at HERA.* Nucl. Phys. B **816** (2009) 1.

[35] CDF Collaboration. *Diffractive dijets with a leading antiproton in* $\bar{p}p$ *collisions at* $\sqrt{s} = 1800\ GeV$. Phys. Rev. Lett. **84** (2000) 504.

[36] A. B. Kaidalov, V. A. Khoze, A. D. Martin, and M. G. Ryskin. *Probabilities of rapidity gaps in high energy interactions.* Eur. Phys. J. C **21** (2001) 521-529.

[37] O. Kepka, C. Marquet, and C. Royon. *Gaps between jets in hadronic collisions.* Phys. Rev. D **83** (2011) 034036.

[38] G. Altarelli and G. Parisi. *Asymptotic Freedom in Parton Language.* Nucl. Phys. B **126** (1977) 298.

[39] Yu. L. Dokshitzer. *Calculation of the Structure Functions for Deep Inelastic Scattering and* e^+e^- *Annihilation by Perturbation Theory in Quantum Chromodynamics.* Sov. Phys. JETP **46** (1977) 641-653, Zh. Eksp. Teor. Fiz. **73** (1977) 1216-1240.

[40] V. N. Gribov and L. N. Lipatov. *Deep inelastic ep scattering in perturbation theory.* Sov. J. Nucl. Phys. **15** (1972) 438.

[41] L. N. Lipatov. *Reggeization of the Vector Meson and the Vacuum Singularity in Nonabelian Gauge Theories.* Sov. J. Nucl. Phys. **23** (1976) 338.

[42] E. A Kuraev, L. N. Lipatov, and V. S. Fadin. *The Pomeranchuk Singularity in Nonabelian Gauge Theories.* Sov. Phys. JETP **45** (1977) 199.

[43] I. I. Balitsky and L. N. Lipatov. *The Pomeranchuk Singularity In Quantum Chromodynamics.* Sov. J. Nucl. Phys. **28** (1978) 822.

[44] C. Marquet and C. Royon. *Small-x QCD effects in forward-jet and Mueller-Navelet jet production.* Nucl. Phys. **B739** (2006) 13.

[45] F. Chevallier, O. Kepka, C. Marquet, and C. Royon. *Gaps between jets at hadron colliders in the next-to-leading BFKL framework.* Phys. Rev. D **79** (2009) 094019.

[46] C. Marquet and C. Royon. *Azimuthal decorrelation of Mueller-Navelet jets at the Tevatron and the LHC.* Phys. Rev. D **79** (2009) 034028.

[47] G. Corcella *et al. HERWIG 6.5: an event generator for Hadron Emission Reactions With Interfering Gluons.* JHEP **0101** (2001) 010.

[48] M. Bahr *et al. Herwig++ Physics and Manual.* Eur. Phys. J. C **58** (2008) 639-707.

[49] D0 Collaboration. *Probing hard color-singlet exchange in* $p\bar{p}$ *collisions at* $\sqrt{s} = 630$ *GeV and 1800 GeV.* Phys. Lett. B **440** (1998) 189.

[50] CDF Collaboration. *Dijet production by color-singlet exchange at the Fermilab Tevatron.* Phys. Rev. Lett. **80** (1998) 1156.

[51] Z. Nagy and Z. Trocsanyi. *Multi-jet cross sections in deep inelastic scattering at next-to-leading order.* Phys. Rev. Lett. **87** (2001) 082001.

[52] E. Gotsman, H. Kowalski, E. Levin, U. Maor, and A. Prygarin. *Survival probability for diffractive di-jet production at the LHC.* Eur. Phys. J. C **47** (2006) 655.

[53] A. Breskin (ed.) and R. Voss (ed.). *The CERN Large Hadron Collider: Accelerator and Experiments.* J. Instrum. **3** (2008) S08001.

[54] The LHC STUDY GROUP collaboration. *Design study of the Large Hadron Collider (LHC): a multiparticle collider in the LEP tunnel.* CERN-AC-91-03.

[55] M. Benedikt (ed.). *The PS complex as proton pre injector for the LHC – design and implementation report.* CERN-2000-003.

[56] A. Hilaire, V. Mertens, and E. Weisse. *Beam transfer to and injection into LHC.* Proceedings of the EPAC 1998, LHC-Project-Report-208.

[57] ATLAS Collaboration. *The ATLAS Experiment at the CERN Large Hadron Collider.* J. Instrum. **3** (2008) S08003.

[58] CMS Collaboration. *The CMS Experiment at the CERN Large Hadron Collider.* J. Instrum. **3** (2008) S08004.

[59] ALICE Collaboration. *The ALICE experiment at the CERN LHC: A Large Ion Collider Experiment.* J. Instrum. **3** (2008) S08002.

[60] LHCb Collaboration. *The LHCb Detector at the CERN Large Hadron Collider.* J. Instrum. **3** (2008) S08005.

[61] LHCf Collaboration. *The LHCf Detector at the CERN Large Hadron Collider.* J. Instrum. **3** (2008) S08006.

[62] TOTEM Collaboration. *The TOTEM Experiment at the CERN Large Hadron Collider.* J. Instrum. **3** (2008) S08007.

[63] MoEDAL Collaboration. *MoEDAL Technical Design Report.* CERN-LHC-2009-006.

[64] ATLAS Luminosity and Forward Detector Community. *ALFA Technical Design Report.* ATLAS TDR **018**, CERN/LHCC/2008-004.

[65] http://proj-lhc-optics-web.web.cern.ch/proj-lhc-optics-web/.

[66] K. Steffen. *High Energy Beam Optics.* Interscience Monographs and Texts in Physics and Astronomy vol. XVII, 1964.

[67] M. Aiba, H. Burkhardt, S. Fartoukh, and White S. *Optics Flexibility in the LHC at Top Energy.* LHC-PROJECT-Report-1106, 2008.

[68] S. White, H. Burkhardt, S. Cavalier, M. Heller, and P. Puzo. *Overall Optics Solutions for very high Beta in ATLAS.* LHC-PROJECT-Report-1135, 2008.

[69] H. Burkhardt and S. White. *High-β^* Optics for the LHC.* LHC-Project-Note-431, 2010.

[70] H. Burkhardt and S. Cavalier. *Intermediate 90m Optics for ATLAS-ALFA.* CERN-ATLAS-Note-2011-027, 2011.

[71] H. Burkhardt *et al. Un-squeeze to 90 m.* CERN-ATLAS-Note-2011-032, 2011.

[72] S. Cavalier, H. Burkhardt, M. Deile, M. Fitterer, S. Redaelli, R. Tomas, and G. Muller. *90 m Optics Commisioning.* CERN-ATLAS-2011-133, 2011.

[73] S. Cavalier, P. Puzo, H. Burkhardt, and P. Grafstrom. *90 m β^* Optics for ATLAS/ALFA.* CERN-ATLAS-2011-134, 2011.

[74] H. Burkhardt, A. Macpherson, S. Cavalier, and P. Puzo. *Plans for High Beta Optics in the LHC.* CERN-ATLAS-2012-141, 2012.

[75] F. Schmidt. *MAD-X User's Guide.* CERN 2005.

[76] E. Forest, F. Schmidt, and E. McIntosh. *Introduction to the Polymorphic Tracking Code.* CERN.SL.2002.044 (AP) KEK-Report 2002-3.

[77] ATLAS Collaboration. *ATLAS Inner Detector: technical design report 1.* CERN-LHCC-97-016.

[78] ATLAS Collaboration. *ATLAS Inner Detector: technical design report 2.* CERN-LHCC-97-017.

[79] ATLAS Collaboration. *ATLAS pixel detector: technical design report.* LHCC-98-013.

[80] ATLAS Collaboration. *Liquid argon calorimeter technical design report.* CERN-LHCC-96-041.

[81] ATLAS Collaboration. *Tile calorimeter technical design report.* CERN-LHCC-96-042.

[82] ATLAS Collaboration. *ATLAS Computing Technical Design Report.* CERN-LHCC 2005-022 (2005).

[83] I. Bird *et al. LHC computing Grid. Technical design report.* CERN-LHCC 2005-024.

[84] U. Amaldi *et al. The real part of the forward proton proton scattering amplitude measured at the CERN intersecting storage rings.* Phys. Lett. B **66** (1977) 390.

[85] T. Sjostrand, S. Mrenna, and P. Skands. *A Brief Introduction to PYTHIA 8.1.* Comput. Phys. Commun. **178** (2008).

[86] P. Bussey. *FPTrack Programme.*

[87] P. Sherwood. *FPTracker Programme.*

[88] A. H. Bethe. *Moliére's Theory of Multiple Scattering.* Phys. Rev. **89**, 1256 (1953).

[89] W. T. Scott. *The Theory of Small-Angle Multiple Scattering of Fast Charged Particles.* Rev. Mod. Phys. **35** 231 (1963).

[90] Particle Data Group. *Review of Particle Physics.* Phys. Rev. D **86**, 010001 (2012).

[91] Schneekloth U. Piotrzkowski, K. Proc. of the ZEUS Collaboration Meeting, March 1994, 2076, DESY, Hamburg.

[92] IBL Collaboration. CERN-LHCC-2010-013, ATLAS-TDR-019.

[93] A. Brandt *et al. The QUARTIC Detector.* In preparation.

[94] *Proceedings, Workshop on Timing Detectors, Cracow, Poland.* Acta Phys. Pol. B **4** Proc. Suppl. (2011).

[95] M. G. Albrow *at. al. Quartz Cherenkov Counters for Fast Timing: QUARTIC.* J. Instrum. **7** (2012) P10027.

[96] ATLAS Collaboration. *ATLAS Level-1 Calorimeter Trigger Algorithms.* ATLAS-DAQ-2004-011.

[97] ATLAS Collaboration. *Inclusive Jet Trigger Efficiencies for the Early 2011 Data.* ATLAS-COM-DAQ-2011-031.

[98] ATLAS Collaboration. *Charged-particle multiplicities in pp interactions at* $\sqrt{s} = 900$ *GeV measured with the ATLAS detector at the LHC.* Phys. Lett. B **688** (2010) 2142.

[99] M. Cacciari, P. G. Salam, and G. Soyez. *The anti-k_t jet clustering algorithm.* JHEP **04** (2008) 063.

[100] ATLAS Collaboration. *Measurement of jet production in 7 TeV proton-proton collision with the ATLAS detector.* ATLAS-COM-PHYS-2010-407, 2010.

[101] ATLAS Collaboration. *Central charged-particle multiplicities in pp interactions with* $|\eta| < 0.8$ *and pt > 0.5 and 1 GeV measured with the ATLAS detector at the LHC.* ATLAS-COM-CONF-2010-113, 2010.

[102] ATLAS Collaboration. *Charged-particle multiplicities in pp interactions at* $\sqrt{s} = 7$ *TeV and 900 GeV measured from pT > 100 MeV: Supporting the MinBias 2nd Publication.* ATL-COM-PHYS-2010-880, 2010.

[103] ATLAS Collaboration. *Measurement of inclusive jet and dijet cross sections in proton-proton collisions at 7 TeV centre-of-mass energy with the ATLAS detector.* Eur. Phys. J. **C71** (2011) 1512.

[104] M. Boonekamp *et al. FPMC: a generator for forward physics.* http://project-fpmc.web.cern.ch/project-fpmc/.

[105] H1 Collaboration. *Tests of QCD factorisation in the diffractive production of di-jets in deep-inelastic scattering and photoproduction at HERA.* Eur. Phys. J. C **51** 92007) 549.

[106] S. Frixione. *A general approach to jet cross-sections in QCD.* Nucl. Phys. B **507** (1997) 295.

[107] H. Jung. *Hard diffractive scattering in high-energy e p collisions and the Monte Carlo generator RAPGAP.* Comput. Phys. Commun. **86** (1995) 147.

[108] H1 Collaboration. *Measurement and QCD analysis of the diffractive deep-inelastic scattering cross-section at HERA.* Eur. Phys. J. C **48** (2006) 715.

[109] V. A. Khoze, A. D. Martin, and M. G. Ryskin. *Double-diffractive processes in high-resolution missing-mass experiments at the Tevatron.* Eur. Phys. J. **C19** (2001) 477, Err-ibid C20 (2001) 599.

[110] V. A. Khoze, A. D. Martin, and M. G. Ryskin. *Prospects for New Physics observations in diffractive processes at the LHC and Tevatron.* Eur. Phys. J. **C23** (2002) 311.

[111] V. A. Khoze, A. D. Martin, and M. G. Ryskin. *Central jet production as a probe of the perturbative formalism for exclusive diffraction.* Eur. Phys. J. **C48**, 467 (2006).

[112] V. A. Khoze, A. D. Martin, and M. G. Ryskin. *Insight into double-pomeron-exchange Higgs production and backgrounds.* Phys. Lett. B **650** (2007) 41.

[113] V. V. Sudakov. *Vertex parts at very high energies in quantum electrodynamics.* Zh. E. T. F. **30** (1956) 87 (Sov. Phys. J. E. T. P. **30** (1956) 65).

[114] ATLAS Collaboration. *Charged-particle multiplicities in pp interactions measured with the ATLAS detector at the LHC.* New J. Phys. **13** (2011) 053033.

[115] ATLAS Collaboration. *The ATLAS Simulation Infrastructure.* Eur. Phys. J. C **70** (2010) 823.

[116] ATLAS Collaboration. *Performance of the ATLAS Inner Detector Track and Vertex Reconstruction in the High Pile-Up LHC Environment.* ATLAS-CONF-2012-042.

[117] ATLAS Collaboration. *ATLAS measurements of the properties of jets for boosted particle searches.* Phys. Rev. **D86** (2012) 072006.

[118] ATLAS Collaboration. *Measurement of inclusive jet and dijet cross sections in proton-proton collisions at 7 TeV centre-of-mass energy with the ATLAS detector.* Eur. Phys. J. **C71** (2011) 1512.

[119] ATLAS Collaboration. *Jet energy resolution in proton-proton collisions at $\sqrt{s} = 7$ TeV recorded in 2010 with the ATLAS detector.* CERN-PH-EP-2012-191.

[120] The CDF Collaboration. *Observation of Exclusive Dijet Production at the Fermilab Tevatron p-pbar Collider.* Phys. Rev. D **77** (2008) 052004.

[121] O. Kepka and C. Royon. *Search for exclusive events using the dijet mass fraction at the Tevatron.* Phys. Rev. D **76** (2007) 034012.

[122] P. Lebiedowicz and A. Szczurek. *Exclusive $pp \to pp\pi^+\pi^-$ reaction: From the threshold to LHC.* Phys. Rev. **D81** (2010) 036003.

[123] P. Lebiedowicz and A. Szczurek. *Exclusive $pp \to nn\pi^+\pi^-$ reaction at LHC and RHIC.* Phys. Rev. **D83** (2011) 076002.

[124] P. Lebiedowicz, R. Pasechnik, and A. Szczurek. *Measurement of exclusive production of scalar χ_{c0} meson in proton-(anti)proton collisions via $\chi_{c0} \to \pi^+\pi^-$ decay.* Phys. Lett. **B701** (2001) 434.

[125] ABCDHW Collaboration. *Inclusive pomeron-pomeron interactions at the CERN ISR.* Z. Phys. **C42** (1989) 387.

[126] ABCDHW Collaboration. *The Reaction pomeron-pomeron* $\to \pi^+\pi^-$ *and an unusual production mechanism for the f2(1270).* Z. Phys. **C48** (1990) 569.

[127] AFS Collaboration. *A search for glueballs and a study of double pomeron exchange at the CERN Intersection Storage Rings.* Nucl. Phys. **B264** (1986) 154.

[128] CDF Collaboration. *Observation of Exclusive Charmonium Production and gamma gamma -¿ mu+ mu- in p anti-p Collisions at s**(1/2) 1.96 TeV.* Phys. Rev. Lett. **102** (2009) 242001.

[129] J. de Favereau, X. Rouby, and K. Piotrzkowski. *Hector, a fast simulator for the transport of particles in beamlines.* JINST **2**, P09005 (2007).

[130] S. Agostinelli *et al.* GEANT4 – *a simulation toolkit.* Nuclear Instruments and Methods in Physics Research A **506** (2003) 250-303.

[131] R. Staszewski and J. Chwastowski. *Transport Simulation and Diffractive Event Reconstruction at the LHC.* Nucl. Instrum. Meth. **A609** (2009) 136.